# Interferometric Radio Observations of the Interactive Winds of Massive Stars

by

**DIANE PATRICIA BROOKES**

**A thesis submitted to**
**The University of Birmingham**
**for the degree of**
**DOCTOR OF PHILOSOPHY**

**Astrophysics and Space Research Group**
**School of Physics and Astronomy**
**The University of Birmingham**
**February 2016**

## Abstract

Massive stars have very strong stellar winds which interact with their environment. This work has involved the study of these interactive winds at radio and other wavelengths. Radio observations have been made of the massive runaway star BD+43° 3654 and its bow shock which is interacting with the inter-stellar medium. These observations, together with archive data at other wavelengths, have revealed stratified dust and turbulent gas in this interaction zone.

Further radio studies have been undertaken of the interaction zones of the colliding winds of massive binary systems. Observations of the colliding wind binary WR 147 at 5 GHz have revealed a curved collision zone, suggestive of simple interactive models. Measurements of the flux from the Wolf-Rayet component of this massive binary system has allowed a mass-loss rate to be derived and though the companion O-star is not detected, an upper flux limit has allowed upper limits on the mass-loss rate and limits on the terminal velocity to be inferred. Also revealed is a curious 'bridge' feature previously observed in WR 147 which occurs between the two binary components. One mechanism is suggested to explain this anomalous feature, the ionising flux of one binary component, the O-star, may be ionising the wind of the other, the WR component. Modelling of the ionisation structure of the stellar winds has been undertaken to verify that this may be occurring.

Radio observations of massive stars made at low-frequency have produced detections of WR 147 and the brighter colliding wind binary, WR 146. These detections have allowed modelling of the non-thermal emission in order to deduce where the non-thermal absorption turn-over occurs in these systems. The resultant modelling has illustrated that these colliding wind regions are complex, with multiple absorption regions best describing their nature.

To Nye

## Acknowledgements

I would like to thank my supervisor, Dr. Ian Stevens, for his guidance and support. I would also like to thank the University of Birmingham for their part-time research bursary.

I am grateful for the staff at the GMRT and the e-MERLIN team at the University of Manchester who made these radio observations possible and I also thank them for their assistance with radio data reduction.

I would like to thank my collaborators for their inciteful and enormously helpful comments and particularly Prof. C.H. Ishwara-Chandra for his assistance with the BD+43° 3654 data reduction together with Dr. Danielle Fenech and Dr. Sean Dougherty for sharing with me their knowledge of MERLIN/e-MERLIN data reduction and the WR 147 system.

I am very grateful for the IT help and assistance from David Stops, who was always willing to assist with the vagaries of computer systems and software.

I would like to thank Nye for all the love and encouragement he has given me during my research. And to Andrea for believing in my ability from the beginning.

Thank you.

## Preface

The work that is presented in this thesis has been undertaken by the author between 2010 and 2016 at the University of Birmingham under the supervision of Dr. Ian R. Stevens. The research which is presented in the main chapters of this thesis is the work of the author, however, the work has involved collaboration with a number of co-authors which are noted below. These chapters have been prepared as stand alone research papers for publication in peer reviewed journals; they are, therefore, identical to the published papers with minor alterations for clarity and will, by their individual nature, also contain some duplication of material.

**Chapter 3** *New Observations of the Wolf-Rayet Colliding Wind Binary System WR 147 at 5 GHz with e-MERLIN* - This chapter was written by the author in collaboration with Dr. Danielle Fenech, Dr. Sean Dougherty, Dr. Ian R. Stevens, Dr. Peredur Williams, Dr. Ronny Blomme, Dr. Julian M. Pittard, Prof. Raman Prinja and Dr. Debra Wallace. The paper is to be submitted to *Monthly Notices of the Royal Astronomical Society* (MNRAS).

**Chapter 4** *Low-Frequency GMRT Observations of Massive Stars I: The Wolf-Rayet Colliding Wind Binary System - WR 147* - This chapter was written by the author in collaboration with Dr. Ian R. Stevens and Dr. Julian M. Pittard. The paper is to be submitted to *Monthly Notices of the Royal Astronomical Society* (MNRAS).

**Chapter 5** *Low-Frequency GMRT Observations of Massive Stars II: The Wolf-Rayet Colliding Wind Binary System - WR 146* - This chapter was written by the author in collaboration with Dr. Ian R. Stevens. The paper is to be submitted to *Monthly Notices of the Royal Astronomical Society* (MNRAS).

**Chapter 6** *Anatomy of a Bow Shock: Multi–Wavelength Observations of the Bow Shock Around The O4 Supergiant star BD+43° 3654* - This chapter was written by the author in collaboration with Dr. Ian R. Stevens, Dr. Paula Benaglia, Prof. C. H. Ishwara–Chandra and Dr.

Josep Martí. The paper is to be submitted to *Monthly Notices of the Royal Astronomical Society* (MNRAS).

**Chapter 7** *E-BOSS: an Extensive stellar BOw Shock Survey I* - This chapter is a summary of work as a co-author in collaboration with Dr. Cintia Peri, Dr. Paula Benaglia, Dr. Ian R. Stevens and N. L. Isequilla. This paper was published on 10 February 2012 in Astronomy & Astrophysics, volume 538, page A108.

# Contents

# List of Figures

# List of Tables

# Chapter 1

# Massive Stars - Drivers of Galactic Evolution

*"The light that comes to us from the starry Heavens is very weak. But what would human thought have been like if we could not perceive the stars, as would have been the case if the Earth had been, like our sister planet Venus, enveloped in a cloak of cloud?"* Paul Couderc, Preface to L'Architecture de l'Univers.

## 1.1 Massive Stars, Massive Effects

Massive stars have been found to have a huge influence on the evolution of their surrounding environment and beyond (Silk, 1997; Crowther, 2012). This occurs in a number of ways. The ionising radiation from massive stars influences their local stellar surroundings as well as local star formation. The strong stellar winds and final supernovae generated by massive stars add considerable amounts of energy and material to and interacting with the inter-stellar medium (ISM), having effects even on a Galactic scale (Woosley & Bloom, 2006; Crowther, 2012). They are also the source of high-energy objects in the Galaxy such as neutron stars and black holes (Kennicutt, 2005) and are thought to be the source of some gamma-ray bursts (Woosley & Bloom, 2006). This level of influence confirms that massive stars hold an important place in our understanding of the processes influencing the evolution of our Galaxy and in the Universe as a whole (Matzner, 2002; Zinnecker & Yorke, 2007). So what constitutes a massive star?

### 1.1.1 What is a massive star?

The current method of stellar classification is one first published by Annie Jump Cannon and Edward Charles Pickering of Harvard College Observatory, (Cannon & Pickering, 1925). In this Harvard spectral classification system a star is classified according to the observed surface

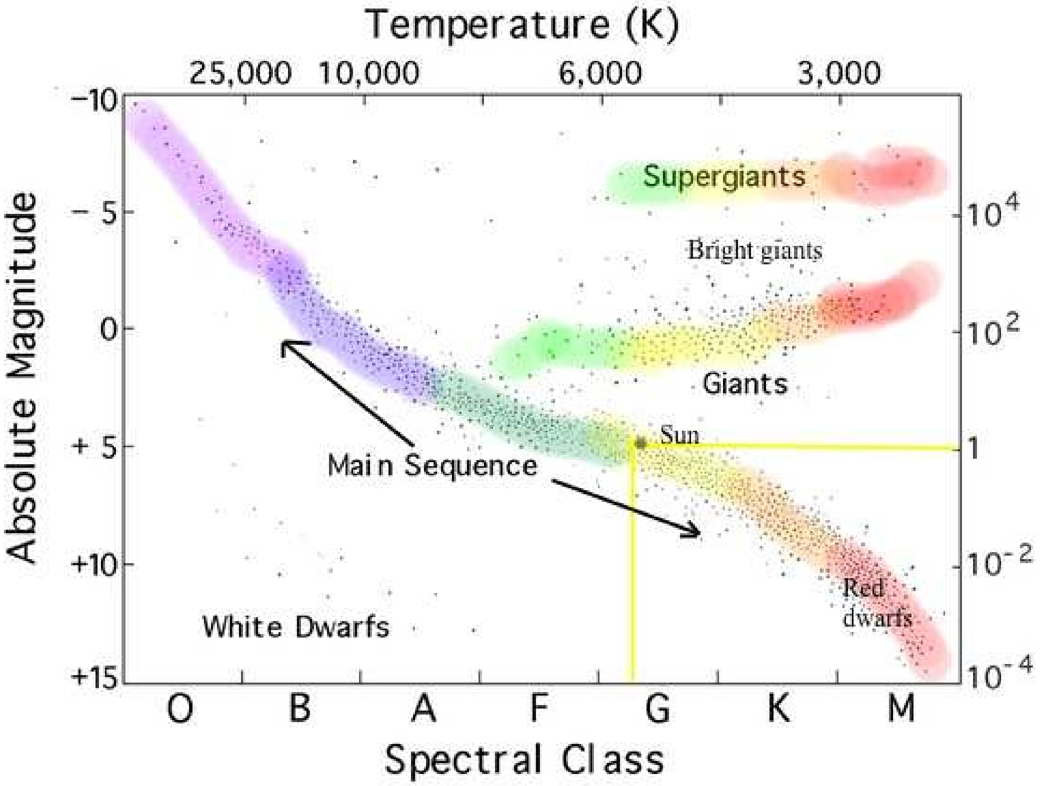

Figure 1.1: The Hertzsprung-Russell (HR) diagram. This diagram illustrates the spectral type at the base of the plot and the stellar temperature at the top, with absolute magnitude indicated along the left axis and stellar luminosity (in units of Solar luminosity) along the right axis. Massive stars are positioned in the upper left region of the HR diagram. Credit: http : //www.astro.washington.edu/users/anamunn/Astro101/Project1/ stellar_spectroscopy_procedure2_files/hrd.jpg.

temperature, where the hottest most massive stars (up to 100 solar mass - 100 $M_\odot$) are type O, with the next class being type B, with masses of $8 - 15$ $M_\odot$. The classification 'OB', therefore, encompasses both types, where they cannot be differentiated. These stars are positioned in the upper left portion of a Hertzsprung-Russell (HR) diagram, as illustrated in Fig. 1.1. Early theories of stellar evolution incorrectly suggested that all stars began their evolution here, later progressing down the main sequence as they aged. OB stars have, since this time, also been referred to as 'early-type' stars.

The mass range of all stars extends from these most massive stars to the smallest, which have the minimum mass required to sustain nuclear fusion, $\sim 0.08\,M_\odot$, these are referred to as brown dwarfs. Massive stars are, however, very rare. In the Milky Way stars of 100 $M_\odot$ are out-numbered a million to one by solar type stars, (Massey, 2003). They are also found to be

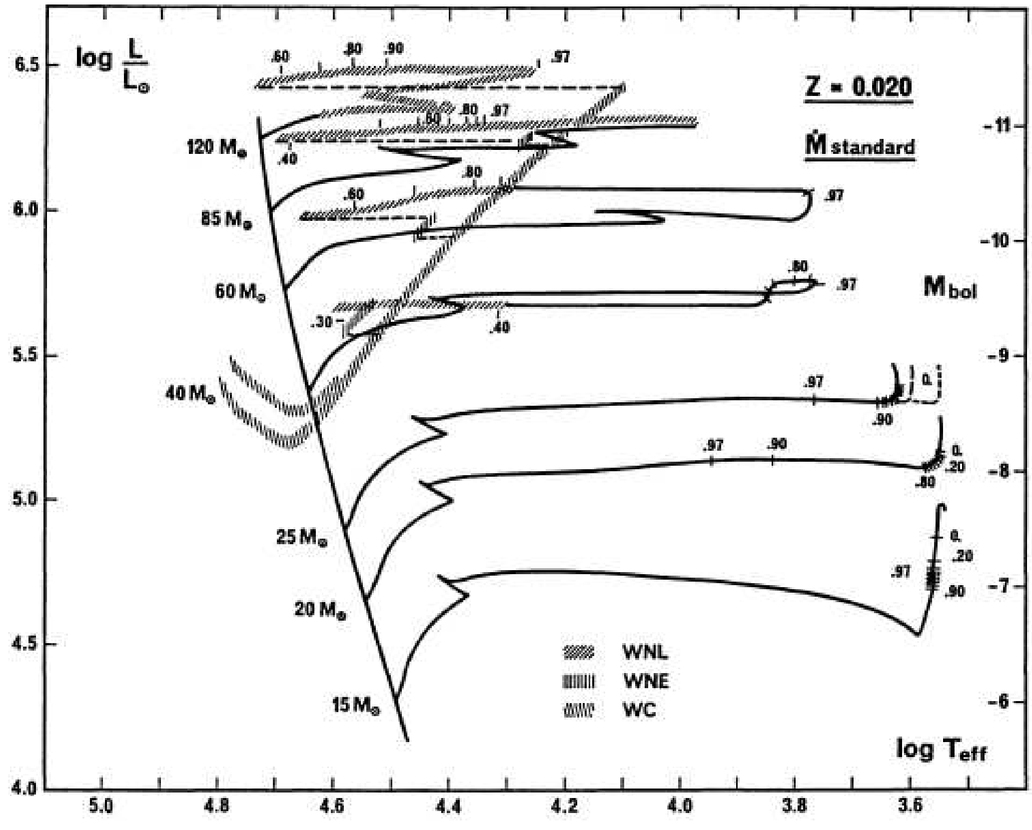

Figure 1.2: The evolution of massive stars across the HR diagram. The hatched lines indicate the evolution of different subtypes of WR-stars from the later stages of massive star evolution. (Schaller et al., 1992).

mainly formed in multiple associations, 70 per cent or more of massive stars are born and evolve in a binary system (Sana et al., 2012; Kobulnicky et al., 2014; Caballero-Nieves et al., 2014; Aldoretta et al., 2015).

O-stars are the most massive (15 - >100 $M_{\odot}$), luminous stars ($\sim 10^4 - 10^6$ times the solar luminosity ($L_{\odot}$) of 3.83 $\times 10^{26}$ J s$^{-1}$) and have the highest effective temperatures, ($T_{eff} > 28\,000$ K). These O-stars have strong, high velocity stellar winds with terminal velocities ($v_{\infty}$) of 1500 $-$ 4000 km s$^{-1}$ and subsequent mass-loss rates ($\dot{M}$) of $10^{-6} - 10^{-5}$ $M_{\odot}$ yr$^{-1}$(Lamers & Leitherer, 1993; Lamers & Cassinelli, 1999). They have a life-time in the region of 2-8 Myr (Maeder & Meynet, 1987).

B stars have masses of $\sim 8 - 15$ $M_{\odot}$, luminosities of $\sim 25 - 10^4$ $L_{\odot}$ with $T_{eff}$ of $\sim$ 11000 $-$ 28000 K with $v_{\infty}$ of 200 $-$ 2000 km s$^{-1}$ and $\dot{M}$ of $10^{-8} - 10^{-6}$ $M_{\odot}$ yr$^{-1}$ (Lamers & Leitherer, 1993; Lamers & Cassinelli, 1999). Their life-times are $\sim 12 - 30$ Myr (Schaller et al., 1992).

Stars with masses of 8 - 25 $M_{\odot}$ evolve to the Red Giant Stage (RGS) before ending their lives as supernova, (Yoon & Cantiello, 2010).

Wolf-Rayet (WR) stars are the descendants of massive stars of $\sim 25 - >100$ $M_{\odot}$(Georgy et al., 2015), which evolve to masses of $\sim 10 - 20$ $M_{\odot}$. They are hot ($T_{\mathrm{eff}}$ =25 000 − 50 000 K), luminous ($10^5 - 10^6 L_{\odot}$), massive stars which consequently have high mass-loss rates and characteristic broad emission lines, they are considered to be the later evolutionary stage of massive stars (Zeilik et al., 1992; Vink, 2015). One of the few mass values obtained for a WR-star is that of the WR star in the V 444 Cyg eclipsing binary system, which is given as 12.4±0.5 $M_{\odot}$ (Hirv et al., 2006).

These massive WR-stars are divided into subclasses of WN, WC and WO (with further subclasses) denoting their enrichment in nitrogen, carbon and oxygen respectively. These enrichments are considered to be due to the products of the CNO cycle of H-burning and triple-$\alpha$ He burning as the WR-star evolves. These elements are mixed from the core throughout the star due to turbulence caused by stellar rotation (massive star rotational rates are $\sim$ 200 km s$^{-1}$, Crowther, 2012; de Mink et al., 2013). These subclasses of WR-stars have parameters that range from WN stars having $v_{\infty}$=700 − 2000 km s$^{-1}$ and $\dot{M}$=$10^{-5} - 10^{-6}$ $M_{\odot}$ yr$^{-1}$, WC stars are found to have $v_{\infty}$=1200 − 3000 km s$^{-1}$, with $\dot{M}$=$\sim 10^{-5}$ $M_{\odot}$ yr$^{-1}$ with WO stars having $v_{\infty}$=4000 km s$^{-1}$ and $\dot{M}$=$10^{-5}$ $M_{\odot}$ yr$^{-1}$ (Maeder & Meynet, 1987; Crowther, 2007). The lifetimes of the WR sequence of massive stars are $\sim 10^5$ yr, approximately 10 per cent of the main sequence stage, (Crowther, 2008).

These subtypes of WR-stars are considered to represent further evolutionary stages of massive stars, their evolution from O and B stars is illustrated in Fig. 1.2 which contains the upper section of the HR diagram with evolutionary paths detailed for high mass stars as they evolve away from the main sequence and their progression towards WR classes, marked with hatched lines towards the end of the evolutionary paths. The progression through these evolutionary types depends upon the mass of the the original massive star. For example higher mass O-stars (¿75 $M_{\odot}$) evolve through a WN H rich stage to a WN H poor stage to a WC stage, ending their life as a supernova:

O → WN→ WC → supernova (type SN Ic).

Stars whose initial mass is $\sim$ 40 - 75 $M_{\odot}$ evolve to a WN H poor stage to a WC stage, ending their life with a supernova and those of a lower mass range advance through WN H poor stage to the supernova stage, (Crowther, 2007).

The composition of these WR subgroups is illustrated by generic examples of their spectra shown in Fig. 1.3 and 1.4 indicating nitrogen present in WN types and carbon in WC types.

These high mass, high luminosity stars, although rare, contribute greatly to their environment and the Universe as a whole. They generate huge amounts of ionising Ultra-Violet (UV) radiation, heating gas and dust in the ISM and also their high velocity stellar winds and mass-loss rates enrich their environment with carbon, nitrogen and oxygen (Massey, 2003) at a consequential loss to the star, influencing its evolution also. These winds interact with their surrounding environment creating high energy shocked regions and are responsible for driving stellar evolution within the stellar cluster and more (Gerola & Seiden, 1978; Zinnecker & Yorke, 2007). The winds originate from within the star, the structure of which is discussed in the next section.

### 1.1.2 The structure of massive stars

Energy transport within a star is by two mechanisms, radiative transport and convection. Radiative transport is where there is a continuous process of photon energy being scattered, absorbed and re-emitted in random directions over distances of approximately the photon mean free path ($l_{ph}$), e.g. for the interior of the Sun $l_{ph}$=1 cm. That is, stellar interiors are opaque to radiation.

Convection in stellar interiors occurs when the temperature gradient increases to create instabilities leading to convection. The stability criteria for the onset of convection is given by the Schwarzschild criteria, where the temperature gradient is greater than the adiabatic (no energy exchange) gradient, convection becomes the dominant energy transport mechanism (Phillips, 1999).

In stars with solar type masses ($\sim 0.25 - 8\ M_{\odot}$) the core is radiative with a convective envelope and even lower mass stars are fully convective.

In massive stars (greater than $\sim 8\ M_{\odot}$) the higher temperature and pressure in the core creates a greater temperature gradient and instabilities where convection is found to be the preferred, efficient method of heat transfer (see Maeder & Meynet (1987) their Figure 3). Here hot cells rise and expand adiabatically to reach equilibrium into a cooler environment. As the

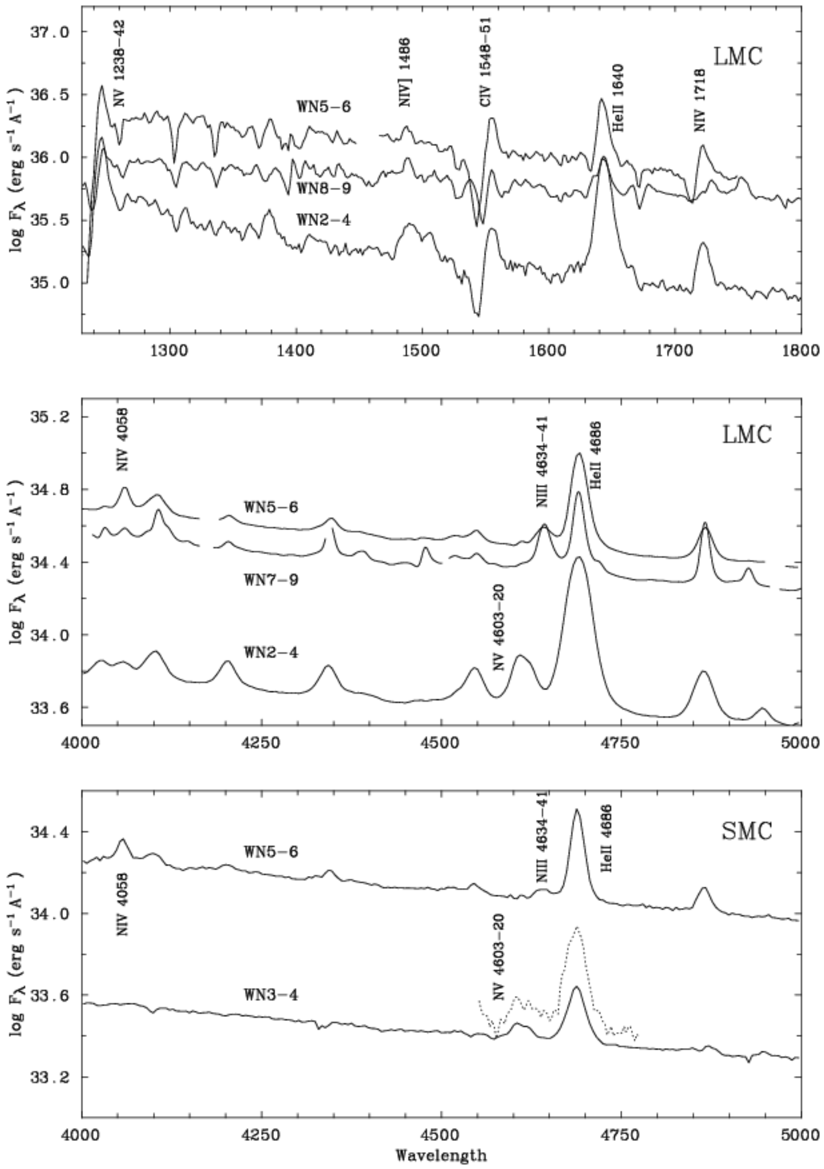

Figure 1.3: An example of WR stellar spectra illustrating their elemental content, a generic WN spectra with peaks of NIII at 46364 Å and NIV peaks at 1718 Å (Crowther & Hadfield, 2006).

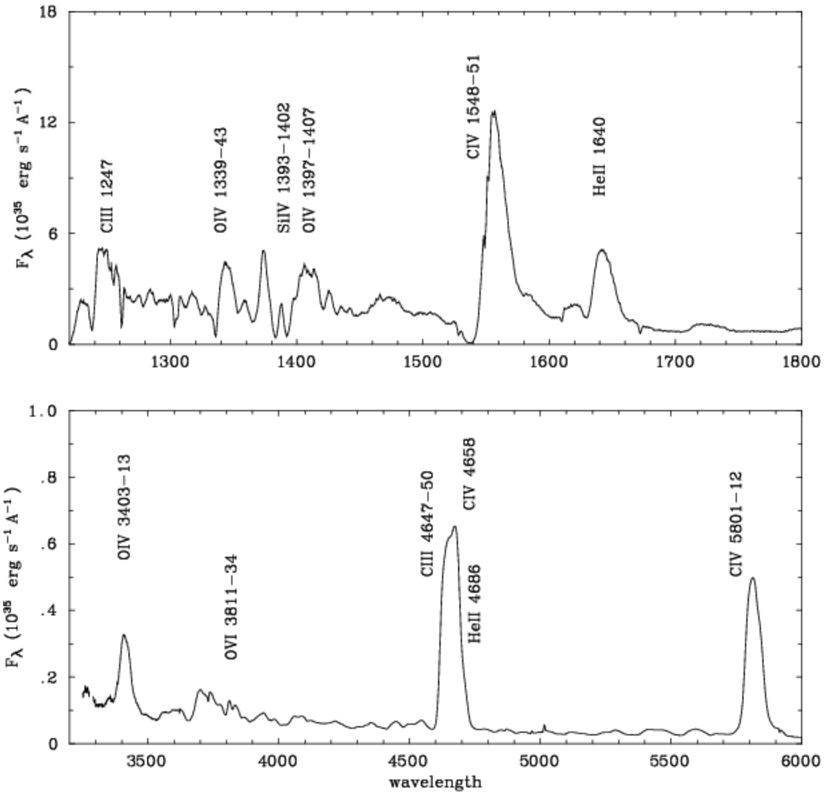

Figure 1.4: An illustration of WR spectra, a generic WC spectra with CIV peaks at 1548-51 and 5801-12 Å and CIII peaks at 1247 and 4647-50 Å (Crowther & Hadfield, 2006).

opacity reduces towards the outer layers due to lower density and expansion, radiative processes dominate.

Internal structure has been modelled simulating non-rotating massive stars (Maeder & Meynet, 1989) and also rotating models (Meynet & Maeder, 2000; Ekström et al., 2012). The structure and evolution of massive stars are also affected by their winds (which are affected by metallicity) and binarity (due to mass transfer).

In addition to convective cores and radiative envelopes, there is evidence for a small outer convective zone associated with iron opacity (FeCZ). These regions may be responsible for photometric variations and possible wind clumping, see Cantiello & Braithwaite (2011) and also a very recent study by Moravveji (2016).

The origin and birthplace of massive stars is from within large stellar clusters. This is discussed in the next section.

## 1.2 Massive Star Formation in Stellar Clusters

### 1.2.1 Star birth

The birthplace of stars is in cold, dense, giant, molecular clouds. In this environment dense cores of gas (density=$10^5\,\mathrm{cm}^{-3}$, $T$=10–15 K) are formed by gravitational turbulence within the cloud, some of which will remain gravitationally bound (McKee & Tan, 2003).

These cores develop into sites of gravitational collapse, becoming proto-stellar embryos which then begin accreting material as they progress towards the main sequence (Black & Bodenheimer, 1975; Klein et al., 2004). These high mass proto-stars will begin to burn hydrogen and develop their stellar radiation-driven winds whilst still accreting material (Zinnecker & Yorke, 2007).

The most massive stars will evolve quickly, in ∼3 Myr. For a finale, these stars go out with a bang, the resultant supernovas from these first stars will dissipate the molecular cloud, leaving a cluster or an association of several clusters of OB stars (Zinnecker et al., 1993).

Within a star forming region, a spherically symmetric accreting system has an upper limit to the luminosity that it can generate before it is able to overcome the gravitational attraction of the accreting particles and prevent the formation of a proto-star. This limit occurs when the outward force exerted by photons emitted by the accreting body acting upon electrons

Figure 1.5: A *Herschel* satellite image of the massive star forming region Cygnus X. Cygnus X holds the massive star association Cygnus OB2 (Credit: ESA/PACS/SPIRE/ Martin Hennemann & Frdrique Motte, Laboratoire AIM Paris-Saclay, CEA/Irfu - CNRS/INSU - Univ. Paris Diderot, France).

Figure 1.6: A Hubble Space Telescope image of the massive young starburst cluster NGC 3603. (Credit: NASA, ESA and the Hubble Heritage (STScI/AURA)-ESA/Hubble Collaboration) and Brandner et al. (2000).

and, due to the electrostatic Coulomb force between them, protons, is greater than the inward gravitational attraction. At this limiting point accretion will halt, this limit is described by the Eddington Limit ($L_{edd}$):

$$L_{edd} = \frac{4\pi G M_* m_p c}{\sigma_T} \tag{1.1}$$

where $G$ is the gravitational constant, $M_*$ is the mass of the accreting body, $m_p$ is the proton mass, $c$ is the speed of light and $\sigma_T$ is the Thomson cross-section of the electron (Frank et al., 2002). It follows that this limit equates to:

$$L_{edd} \cong 3.2 \times 10^4 \left(\frac{M_*}{M_\odot}\right) L_\odot \tag{1.2}$$

which when combined with the mass luminosity relationship of:

$$L_* \propto M_*^\alpha \tag{1.3}$$

where $\alpha = 3.5$ for massive stars (Phillips, 1999), leads to a stellar luminosity ($L_*$) of $10^6$ $L_\odot$ for a 100 $M_\odot$ star, with a corresponding $L_{edd}$ of $\sim 10^6$ $L_\odot$. This indicates that a maximum stellar mass is in the region of $100 - 200$ $M_\odot$.

An accreting body that achieves a luminosity equal to or greater than the Eddington limit will, therefore, be unable to form a proto-star, those that acquire a luminosity lower than the Eddington limit remain bound and continue their evolution.

A recent study by Johnston et al. (2015) has uncovered a disk around a young O-type star with the Atacama Large Millimeter Array (ALMA), illustrating that massive stars form via accretion from disks as do low mass stars.

The masses of these massive stars can be determined, in the case of spectroscopic and eclipsing binaries, from their orbital parameters (Rauw et al., 2005). The general case is when mass is deduced from spectroscopic and evolutionary models (Crowther et al., 2010).

### 1.2.2 Massive Stars in Stellar clusters

Studies of the early development of stellar clusters and their star formation have suggested that there are two general types of clusters which develop; starburst clusters and leaky (or mass-loss) clusters, (Pfalzner, 2009). For example Fig. 1.5 shows the massive star forming region Cygnus X, including Cygnus OB2, an association of star clusters observed by the *Herschel* satellite in infrared (IR).

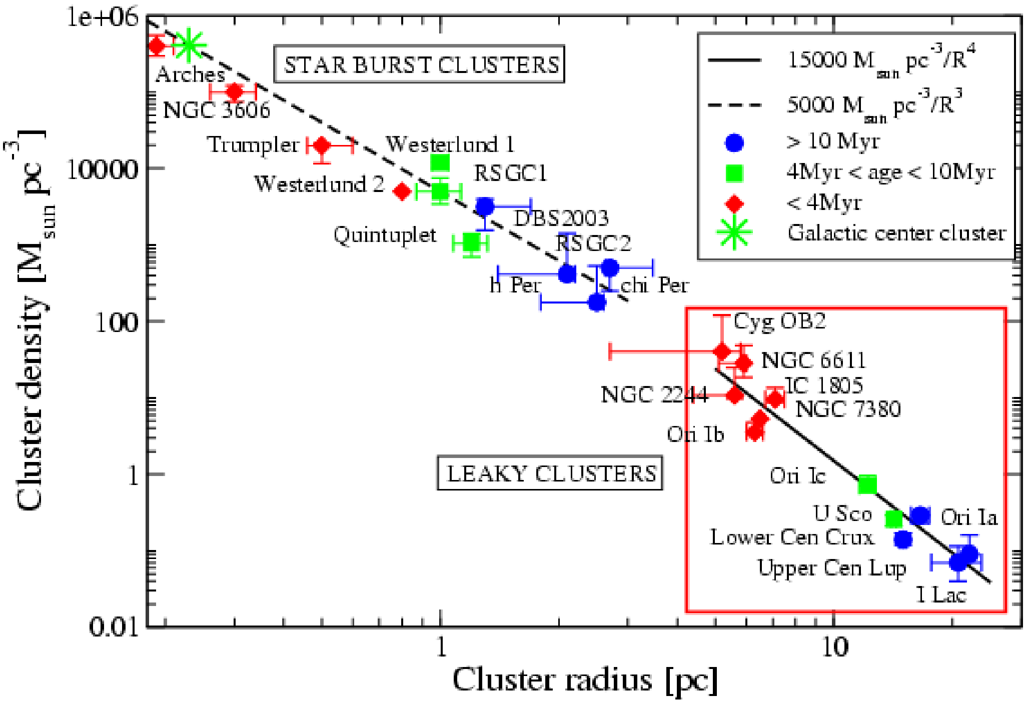

Figure 1.7: Cluster density-radius function showing upper left, star burst clusters and lower right, mass-loss or leaky clusters, (Pfalzner (2009), Figure 2).

Starburst clusters appear to be born with a density of $\gtrsim 10^5\, M_\odot\, \mathrm{pc}^{-3}$ and then material within the cluster will diffuse, or expand, without further mass-loss, giving an expansion velocity of approximately 0.2 km s$^{-1}$ ($\sim$0.2 pc Myr$^{-1}$). This indicates that cluster evolution involves expansion at a considerable rate, compared to cluster size ($\sim$pc).

Leaky clusters, however, form at a different point on the density-radius function given by Pfalzner, (reproduced in Figure 1.7). Analysis of this function by Pfalzner (2009) suggests that leaky cluster types diffuse with rates greater than just expansion, this suggests leaky cluster mass-loss via different processes, such as out-gassing, stellar mass-loss, tidal evaporation and stellar ejection via n-body encounters, (Pfalzner, 2009). The expansion velocity of leaky clusters is given as $\sim 1-2$ km s$^{-1}$($\sim 1-2$ pc Myr$^{-1}$), further analysis with cluster expansion models due to gas expulsion suggest that 75 per cent of cluster gas is expelled suggesting a star formation efficiency of $\sim$ 25 per cent.

Simulations of the dynamics of clusters embedded in molecular clouds show strong correlations between the kinetic energy of cluster stars and of those leaving the cluster, suggesting the latter have been ejected from the cluster and that they share a common origin, (Kroupa, 2008;

Pfalzner, 2009). These ejected stars are known as runaways and will be discussed further in Section 1.5.4.

Massive star formation in stellar clusters has been modelled by Bonnell & Bate (2002) and Vine et al. (2004). A young (∼2 Myr) star cluster can be seen as NGC 3603 (see Fig. 1.6) and the Cygnus OB2 region is a well studied example of a 3-5 Myr association of star clusters, seen in Fig. 1.5 (Wright et al., 2014; Kobulnicky et al., 2014; Caballero-Nieves et al., 2014; Drake et al., 2015).

Understanding the winds of massive stars is crucial to understanding their structure and evolution, this is discussed in the next section.

## 1.3 The Winds of Massive Stars

### 1.3.1 Radiatively driven stellar winds

All stars lose mass through their stellar winds and many stars are radio emitters, as shown in the radio HR diagram in Figure 1.12. However, massive, high luminosity stars produce strong radiation driven stellar winds and consequently have high mass-loss rates of approximately $10^{-7}$ to $10^{-4}$ $M_{\odot}$ yr$^{-1}$.

The theory of radiatively driven winds was first detailed by Castor, Abbott and Klein, 1975, and is refered to as CAK theory. This theory indicates that the force driving the winds of massive stars is derived from the stellar radiation which imparts momentum when it interacts with particles in the wind. Photons radiated from the star's core are absorbed by ions in the wind, which have bound electrons, absorb then emit energy, producing lines in the stellar spectra.

The two equations describing the flow of the stellar wind by Castor et al. (1975b) are the conservation of mass:

$$\dot{M} = 4\pi r^2 \rho v = constant \tag{1.4}$$

where $\dot{M}$ is the mass-loss rate, $r$ is distance from the centre of the star, $\rho$ is the wind density, and the distribution of the wind velocity $v$, with distance $r$ from the star can be approximated by the velocity law;

$$v_r = v_\infty \left(1 - \frac{R_*}{r}\right)^{\beta} \tag{1.5}$$

where $R_*$ is the stellar radius, $v_\infty$ is the wind terminal velocity and $\beta$ indicates how steep the velocity law is. For hot stars with a fast, accelerating wind, as a point source $\beta$ is $\sim 0.5$. Where a star is assumed not to be a point source, (including a Finite Disk Correction factor) $\beta$ is found to be $\sim 0.8$, (Pauldrach et al., 1986; Lamers & Cassinelli, 1999).

The second equation given by Castor et al. (1975b) is that of momentum balance:

$$v\frac{dv}{dr} = -\frac{GM_*}{r^2} + \frac{\sigma_e L_*}{4\pi r^2 c}[1 + M(t)] - \frac{1}{\rho} \cdot \frac{dp}{dr} \tag{1.6}$$

where $c$ is the speed of light, $G$ is the gravitational constant, $M_*$ is stellar mass, $\sigma_e$ is the electron scattering opacity, $L_*$ is stellar luminosity, and $M(t)$ is the force multiplier as a function of the optical depth variable, $t$. The force multiplier is given in the form of:

$$M(t) = kt^{-\alpha}. \tag{1.7}$$

The power law ($\alpha$) is found to be $\sim 0.7$ and $k$ is a constant (Castor et al., 1975b) with the optical depth parameter ($t$) given as:

$$t = \sigma_e \rho v_{th} \left| \frac{dv}{dr} \right|^{-1} \tag{1.8}$$

where $v_{th}$ is the random thermal velocity of the atoms.

From Eq. 1.6 it can be seen that momentum balance is subject to the force of gravity, stellar luminosity and density. The force imparted to particles in the stellar wind is considerable, as indicated by the large mass-loss rates of massive stars (Castor et al., 1975b; Owocki, 1994, 2014).

### 1.3.2 Mass-loss from massive stars

The high mass-loss rates of massive stars will, consequently, reduce the mass of a star as it evolves and also will alter the star's chemical composition and structure, through mixing, (Maeder & Meynet, 2010). Also material such as carbon, nitrogen and oxygen from and formed by massive stars, is ejected via their stellar winds and also supernovae, and added to the ISM affecting its chemical composition. The addition of momentum and energy from the wind will also affect the evolution of the ISM. The reliable determination of mass-loss rates, therefore, is valuable to accurately describe the evolution of massive stars and the surrounding ISM.

Optical studies first revealed mass-loss from these massive stars, (Beals, 1929), radio observations (Wright & Barlow, 1975) and ultraviolet spectroscopy (Morton, 1967; Howarth & Prinja, 1989) have since led to more detailed studies. The winds from hot OB stars are now understood to be driven by the transfer of momentum from the stellar radiation field through the scattering in metallic, (principally C, N and O) resonance lines, (Castor et al., 1975b; Fullerton et al., 2006) as previously described.

The standard model for mass-loss from stellar winds assumes that it is a uniform, spherically symmetric flow of ionized gas with velocity ($v$), that is related to the gas number density ($n$) by;

$$\dot{M} = 4\pi r^2 n \mu m_{\mathrm{H}} v \tag{1.9}$$

where $\dot{M}$ is the mass-loss rate; $r$ is radial distance from the star; $\mu$ is the mean atomic weight of the gas and $m_{\mathrm{H}}$ is the mass of a hydrogen atom, (Wright & Barlow, 1975).

The distribution of the velocity with distance from the star is related to the velocity law, Eq.1.5. However stellar winds are not found to be perfectly symmetric and models need to state when this assumption is made or include adjustments. Current results suggest that small-scale clumping in the stellar wind may be a common feature, clumps in the winds of massive stars have been detected in spectral studies of HeII 4686 Å by Eversberg et al. (1998) and some models are now including this process, (see for example Fullerton et al. (2006) and references therein).

There are several methods of measuring stellar mass-loss rates, these methods and the parameters that each uses are described in the next section.

#### Mass-loss rates from thermal radio emission

Wright & Barlow (1975) have studied the radio and infra-red spectrum of early-type stars and other radio studies of mass-loss have been undertaken by Abbott et al. (1980, 1981). Wright and Barlow determined that the radio spectra are predicted to be of the form $S_\nu \propto \nu^{0.6}$, where $S$ is the flux and $\nu$ is the frequency. They derived a relation between the measured flux and mass-loss rates of;

$$\dot{M} = 0.095\, \frac{\mu v_\infty S_\nu^{3/4} d^{3/2}}{Z \gamma^{1/2} g^{1/2} \nu^{1/2}}\ (M_\odot\ \mathrm{yr}^{-1}) \tag{1.10}$$

where $\mu$ is the mean atomic weight of the gas, $v_\infty$, the terminal velocity of the mass-loss flow is in km s$^{-1}$; $S_\nu$, the flux observed at frequency $\nu$ is in Janskys (see Section 1.4.1 for a description of flux density); $d$, distance is in kpc; $Z$ is the rms charge, $\gamma$ is the ratio of the electron number density and the ion number density, $g$ is the free-free Gaunt factor and the frequency $\nu$ is in Hz. This model assumes the standard wind model of uniform spherical mass-loss, that the flux is from thermal free-free emission and the measured flux should obey the relationship of $S_\nu \propto \nu^{0.6}$, which is true in the radio region, (Wright & Barlow, 1975). Typical radio fluxes from early-type stars are $S_\nu \sim$ milli Janskys (mJy), for example HD 210839 a type O6 star has been observed at 3.6 cm (8.3 GHz) to have a flux of, $S_\nu = 0.38\,\mathrm{mJy}$, (Lamers & Leitherer, 1993).

The benefit of using this model is that it uses the free-free thermal integrated emission of all ion species that originates from the outer, rarefied, constant velocity region of the stellar wind, (Fullerton et al., 2006). This relationship can be used on nearby stars whose distance parameters are more accurately measured, (Wright & Barlow, 1975). Radio emission from massive stars will be discussed in more detail in Section 1.4.1.

### Mass-loss rates from ultraviolet resonance lines

The following are two studies of mass-loss from ultraviolet resonance lines,

1. C IV, N V and Si IV resonance doublets

   In an ultraviolet survey of 203 O-type stars, Howarth & Prinja (1989) have studied observed wind velocities derived from C IV, N V and Si IV resonance doublets, Figure 1.8 shows resonance lines for 8 of the sample O-stars from Howarth & Prinja (1989). From their studies they proposed the following relationship between mass-loss and stellar luminosity;

   $$\log_{10}\,(\dot{M}/\,M_\odot\ \mathrm{yr}^{-1}) = 1.69\ \log_{10}\,(L_*/L_\odot) - 15.4 \tag{1.11}$$

   This survey of UV spectra was at high resolution and assumed a spherically symmetric mass flow. The mass-loss predictor was estimated to be accurate to a factor of 2 (rms), (Howarth & Prinja, 1989).

2. P v resonance doublet

   Fullerton, Massa & Prinja (2006) determined mass-loss rates of 40 O-type stars from the ion fraction of $P^{+4}$ from ultraviolet observations of the P v resonance doublet which has a rest wavelength of $\lambda_{0\ blue}$ of 1117.77 Å and $\lambda_{0\ red}$ of 1128.008 Å utilising the Far Ultraviolet Spectroscopic Explorer (FUSE), Berkeley Extreme and Far-UV Spectrometer (ORFEUS BEFS) and Copernicus, (Figure 1.9 shows examples of fits to P v wind profiles,

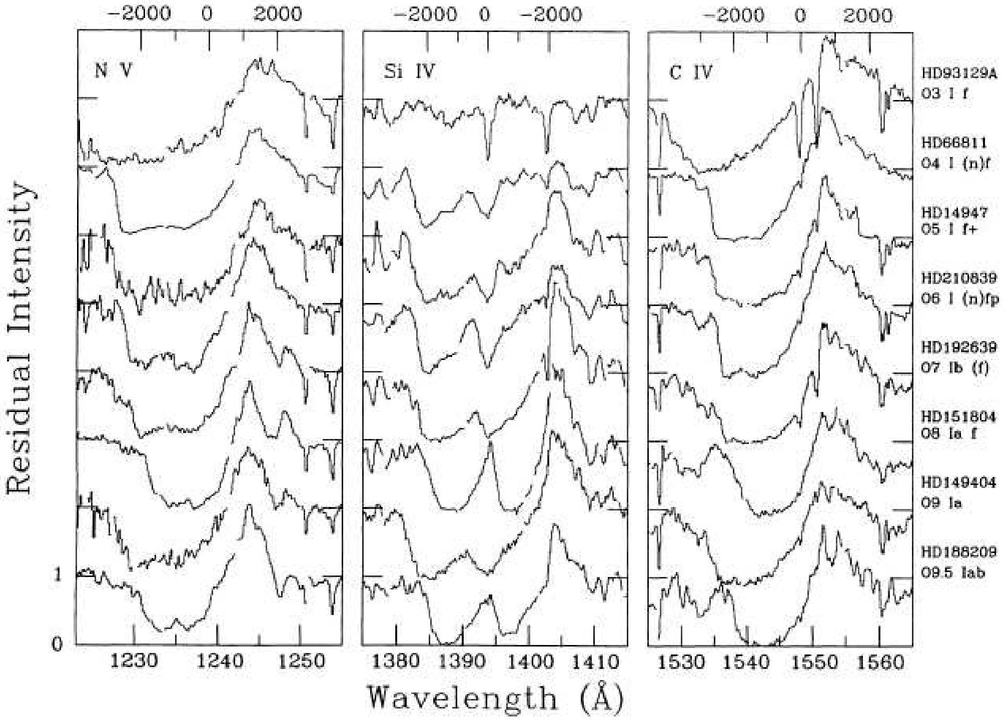

Figure 1.8: Resonance line profiles of 8 O-stars, upper scale is velocities ( km s$^{-1}$) (Howarth & Prinja, 1989).

(Fullerton et al., 2006)). These mass-loss rates were derived from their following relation:

$$\dot{M}_q(P^{+4}; w) = \left(\frac{m_e c}{\pi e^2}\right) \frac{4\pi \mu m_H}{f_{ij}\lambda_0 A_p}\ R_* v_\infty^2 x^2 w \,\frac{dw}{dx}\ \tau_{rad}(w) \tag{1.12}$$

where $f_{ij}$ is the oscillator strength of the component of the P v resonance line; $A_p$ is the abundance of P relative to hydrogen; $\mu$ is the mean molecular weight of the plasma; $x$ is the radial distance in units of stellar radius; and $w$ is the normalised velocity, (Fullerton et al., 2006). This relationship is effectively $\dot{M}=$ constant $\times\ r^2 \times v\ dv/dr$ derived from the radiative wind momentum equation 1.6.

This mass-loss model assumes the standard wind model and a spherically symmetric steady flow. This data was then compared with mass-loss rates derived from radio and H$\alpha$ observations.

### Mass-loss rates from H$\alpha$ recombination radiation

Many massive stars show strong H$\alpha$ emission at 6563 Å. Using H$\alpha$ emission lines Lamers & Leitherer (1993) derived the mass-loss rates of 28 selected O-type stars. They proposed mass-loss

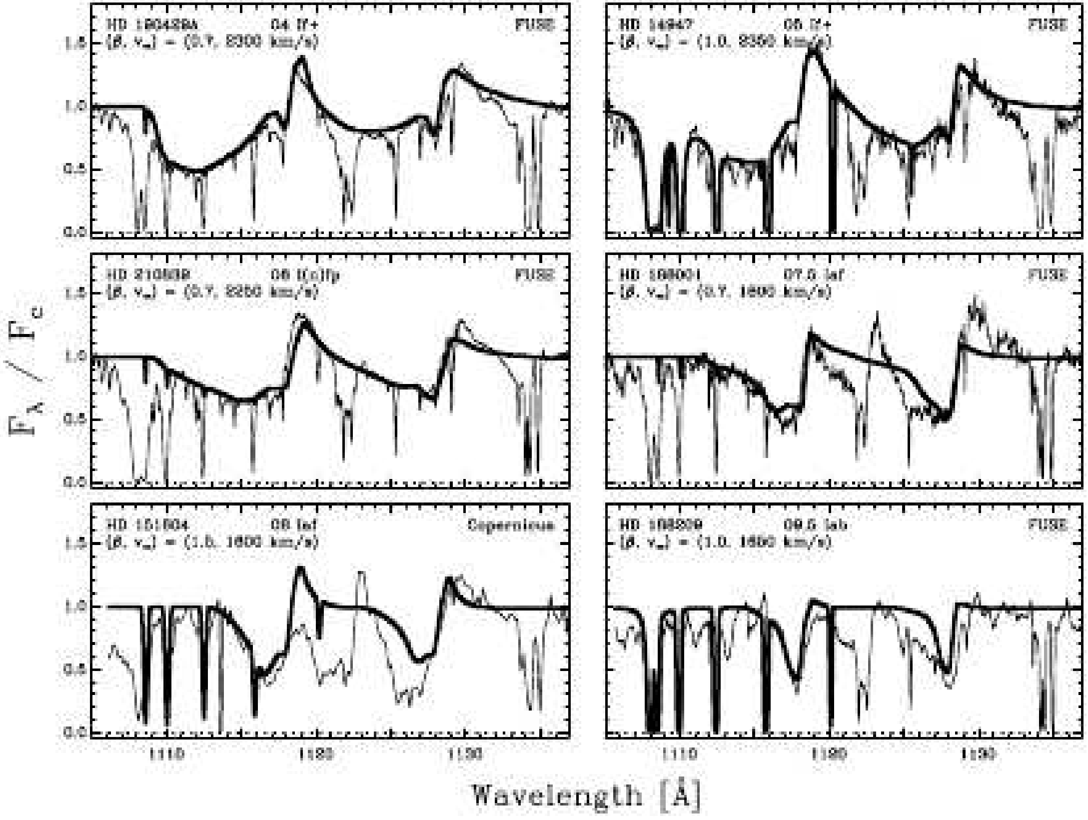

Figure 1.9: Examples of P v wind profiles, from Fullerton et al. (2006).

rates as a determination of the luminosity of the wind in H$\alpha$ due to optically thin recombination radiation of hydrogen originating in the wind, $L(H\alpha)$, and the effective temperature, $T_{eff}$:

$$\log_{10}\ \dot{M} = 0.5\ \log_{10}\ L(H\alpha)\ +\ \log_{10}\ v_{\infty}\ + 0.5\ \log_{10}\ R\ -\ 0.5I\ -\ 0.5c(T_{eff})\ -\ 12.563 \quad (1.13)$$

where $\dot{M}$ is in $M_{\odot}$ yr$^{-1}$; $L(H\alpha)$ is in $L_{\odot}$; $v_{\infty}$ is in km s$^{-1}$; $R$ is the empirical radius of the star in $R_{\odot}$ multiplied by $I$, the distance-integrated velocity law relating the initial and terminal velocity of the wind, (see Leitherer, 1988) and $T_{eff}$ is in Kelvin, (Lamers & Leitherer, 1993). These results were then compared with rates derived from thermal radio emission and UV observations. A dependence of mass-loss rates on stellar parameters was also proposed, with a fitting formula relating $\dot{M}$ to $L$ and $T_{eff}$:

$$\log_{10}\ \dot{M} = 1.738\ \log_{10}\ L\ -\ 1.352\ \log_{10}\ T_{eff}\ -\ 9.547 \quad (1.14)$$

where $L$ is in $L_{\odot}$, (Lamers & Leitherer, 1993).

**Mass-loss rates from metallicity function**

Vink et al. (2001) added a parameter relating metallicity ($Z$) to their earlier, theoretically derived formula from Vink et al. (2000), the authors propose a recipe to calculate mass-loss from O and B type stars as a function of $Z$ together with $L, M,\ v_\infty,\ v_{esc}$ and $T_{eff}$, allowing for the mass-loss rate relating to $Z$, $\dot{M}_Z$, being dependent upon the temperature around the bi-stability jump. The bi-stability jump is seen as a steep decrease in the wind terminal velocity with a corresponding rise in $\dot{M}$ at around $T_{eff}$ of 25 000 K (Vink et al., 1999).

In cooler B stars the wind and mass-loss is related to the iron content in the wind which increases at $25\ 000 - 27\ 500\,$K causing an increase of mass-loss, (Vink et al., 1999).

On the hot side of the bi-stability jump, $27\,500 < T_{eff} \leq 50\,000\,$K, their recipe is:

$$\begin{aligned}
\log_{10}\ \dot{M}_Z \ = \ & - \ 6.697\ (\pm 0.061) \\
& + \ 2.194\ (\pm 0.021)\ \log_{10}\ (L_*/10^5) \\
& - \ 1.313\ (\pm 0.046)\ \log_{10}\ (M_*/30) \\
& - \ 1.226\ (\pm 0.037)\ \log_{10}\ \left(\frac{v_\infty/v_{esc}}{2.0}\right) \\
& + \ 0.933\ (\pm 0.064)\ \log_{10}\ (T_{eff}/40\,000) \\
& - \ 10.92\ (\pm 0.90)\ \{\log_{10}\ (T_{eff}/40\,000)\}^2 \\
& + \ 0.85\ (\pm 0.10)\ \log_{10}\ (Z/Z_\odot)
\end{aligned} \tag{1.15}$$

where $\dot{M}_Z$ is in $M_\odot\,\mathrm{yr}^{-1}$, $L_*$ and $M_*$ are in solar units, $T_{eff}$ is in Kelvin and $Z_\odot$ is the Solar metallicity. Using a Galactic ratio $v_\infty/v_{esc} = 2.6$, Vink et al. (2001) calculated a grid of wind models and mass-loss rates for a range of metallicities and found that mass-loss and metallicity relate as $\dot{M} \propto Z^{0.69}$ for O-stars and $\dot{M} \propto Z^{0.64}$ for B stars.

### 1.3.3 A comparison of different methods of mass-loss determination

A summary of published mass-loss data for a sample of 18 O-stars, derived from different methods are displayed in Figure 1.10 (Howarth & Prinja, 1989; Lamers & Leitherer, 1993; Fullerton et al., 2006). This figure illustrates that some UV derived mass-loss rates are considerably lower than those derived from radio and H$\alpha$.

The different wavelengths used to calculate mass-loss rates originate from different regions of the wind and this, therefore, needs to be considered when evaluating different methods. The

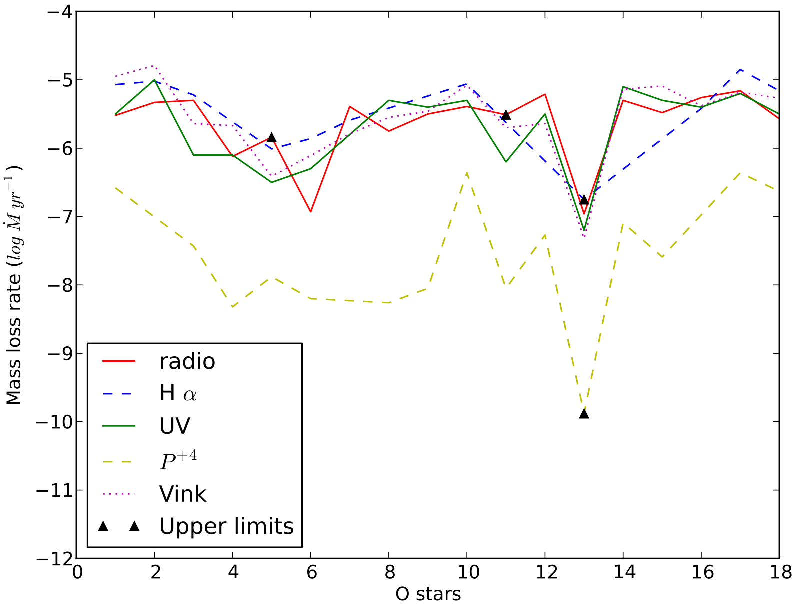

Figure 1.10: Comparison of mass-loss rates from the sample of 18 O-stars indicating lower rates from the $\dot{M}_{\mathrm{P}+4}$ method.

observed H$\alpha$ emission originates from the rapidly accelerating dense region near the star, radio emission is from free-free thermal emission from the outer, rarefied, constant velocity region and the UV emission originates from between these two, (Fullerton et al., 2006).

The $\mathrm{P}^{+4}$ ion is thought to be the dominant ion in some winds, the doublet is rarely saturated as the cosmic abundance of P is so small and, as it is not formed in stellar hydrogen burning, it will remain at the same level throughout the star's lifetime, (Fullerton et al., 2006). This would suggest that this is a good indicator to use.

Mass-loss rates derived from free-free radio emission have been considered the most reliable, though the thermal emission can be contaminated with non-thermal (NT, see Section 1.4.1) emission causing overestimations. Many (~25 per cent) O-type stars exhibit NT emission, (Fullerton et al., 2006), and many have only been observed at one frequency which is insufficient to determine a spectral index to indicate if the emission is thermal or NT, therefore, care needs to be taken to ensure radio data are from thermal emission alone.

The comparison by Fullerton et al., (2006) shows that $\mathrm{P}^{+4}$ derived mass-loss rates for their sample of O-stars are lower than those derived from radio and H$\alpha$ by a factor of 10 or more, see Figure 1.10, they suggest small-scale clumping in the winds as one explanation for this. If

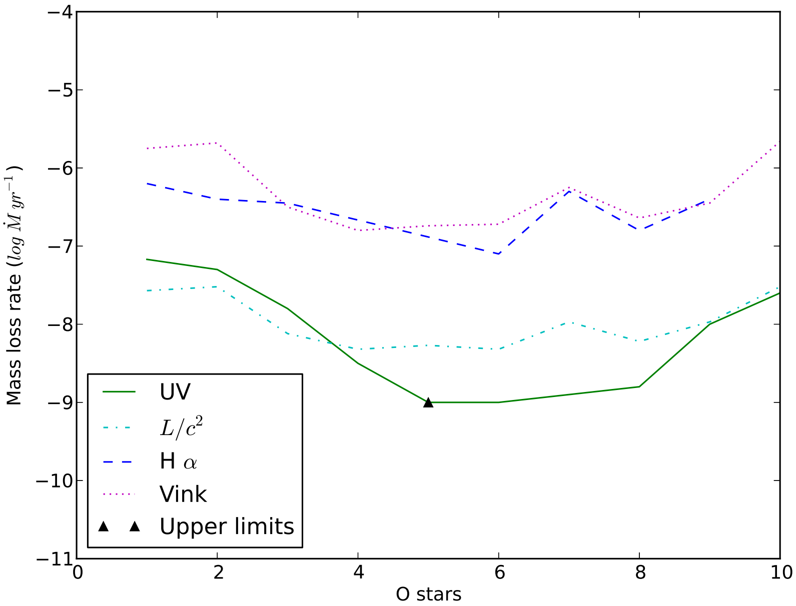

Figure 1.11: Comparison of mass-loss rates of O-stars, from Martins et al. (2012), indicating lower mass-loss rates for UV and $L/c^2$ methods, see text for details.

this is so, they suggest that mass-loss measurements using radio and H$\alpha$ will be overestimated, but using volume filling factors these rates can be reduced, (Fullerton et al., 2006). Another consideration is whether clumping is expected to depend on the distance from the star, if not, then using different emission should not produce differences due solely to clumping.

In a study Martins et al. (2012) have observed 10 OB stars at UV and H$\alpha$ and derived and compared mass-loss rates from these observations. These have then been compared with the theoretical rates of Vink et al. (2001), which relate to metallicity and also compared their observations to $L/c^2$ values. $L/c^2$ values correspond to rates obtained if the driving is due to a single line in the emission peak of the spectral energy distribution (SED) and gives a lower limit to mass-loss rates as expected by radiation-driven wind theory, (Martins et al., 2012). Indeed the rates from $L/c^2$ and also UV are lower than those obtained from H$\alpha$ and metallicity, see Figure 1.11.

A recent review by Smith (2014) underlines the uncertainty in our knowledge of mass-loss rates, with models including clumping within the stellar wind 2-3 times lower than non-clumping models.

Work has been undertaken by Pauldrach et al. (2012) who conclude that Very Massive Stars

(VMS) with low metallicity evolve without losing much of their mass, for example a 3 000 $M_\odot$ VMS with $Z = 0.005\ Z_\odot$ is predicted to lose 120 $M_\odot$ in total, compared with 1105 $M_\odot$ lost by a similar mass VMS with $Z$ equal to $Z_\odot$. Pauldrach et al. (2012), Table 15, suggests that early, low metallicity, population III stars did not contribute a substantial amount of helium to the early ISM.

## 1.4 Multi-Wavelength Properties of Massive Stars

### 1.4.1 Radio emission

Radio emission from the hot stellar winds of massive early-type stars has been detected since the early 1980's, (Abbott et al., 1980, 1981; White & Becker, 1983). Figure 1.12 illustrates the radio HR diagram indicating radio luminosity from a range of different spectral types. This figure is an older diagram, with more radio sources now detected. For example a recent survey of Westerlund1 has detected radio emission from a number of cool hypergiants, (Dougherty et al., 2010).

The radio emission detected by radio telescopes is a combination of two forms of emission, indicated in Figure 1.12 by open and closed circles:

1. Thermal emission - A continuous emission, thought to derive from a spherically symmetrical mass-loss flow, producing thermal free-free emission at a brightness temperature of around $10^4$ K, (Wright & Barlow, 1975), and
2. Non-thermal emission - A mainly non-steady, possibly variable emission with a higher brightness temperature of around $10^6 - 10^7$ K: thought to be produced by NT synchrotron radiation from accelerated electrons in shocked regions of the stellar wind, (De Becker, 2007).

Examples of these types of emission are shown in Figure 1.13, the thermal emission is represented by the dashed line which shows a flux with $S_\nu \propto \nu^{0.6}$ and the NT emission is shown by the dotted line which has a power law of $\nu^{-0.5}$, the solid line illustrates the observed total flux, which is the sum of both types of emission. The turn-over in the NT flux at low frequency is due to absorption, this property is discussed at the end of this section.

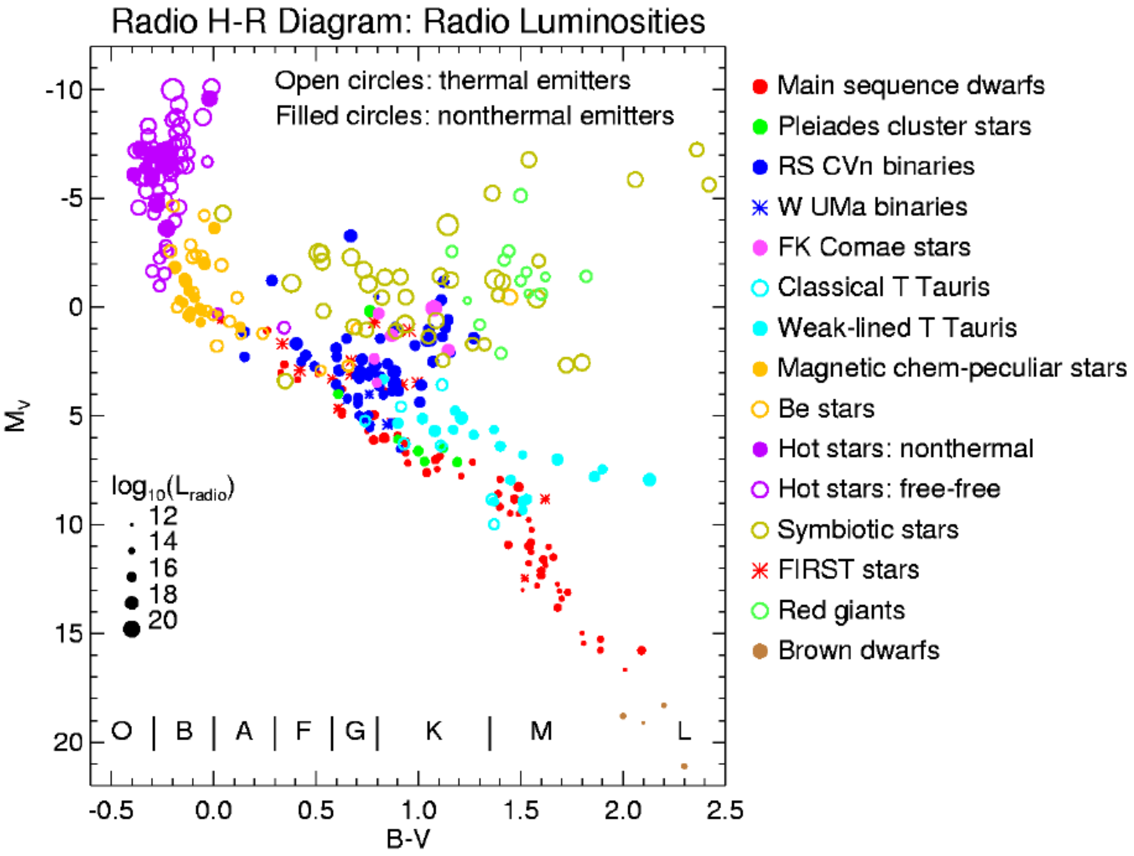

Figure 1.12: The radio HR diagram, indicating radio luminosity by the size of the circles from different spectral types and thermal and non-thermal emission by open and filled circles, see Section 1.4.1 for a description of this emission (Credit: www.astro.umd.edu/∼white).

The intensity of radio emission is measured in units of flux density, at frequency $\nu$ ($S_\nu$), expressed as $\mathrm{W\,m^{-2}\,Hz^{-1}}$. This is, in practice, an inconveniently large unit, therefore, flux densities are normally expressed in the smaller unit of Jansky (Jy) defined as $10^{-26}\,\mathrm{W\,m^{-2}\,Hz^{-1}}$. Flux density $S_\nu$, at wavelength $\nu$, is related to the stellar mass-loss rate ($\dot{M}$) by equation 1.10. Observations of radio emission and processes that may produce them will now be examined further.

### Thermal radio emission

Thermal or black-body emission is produced by free-free, Bremsstrahlung or braking radiation, which has been found to have a flux density:

$$S_\nu \propto \nu^\alpha, \tag{1.16}$$

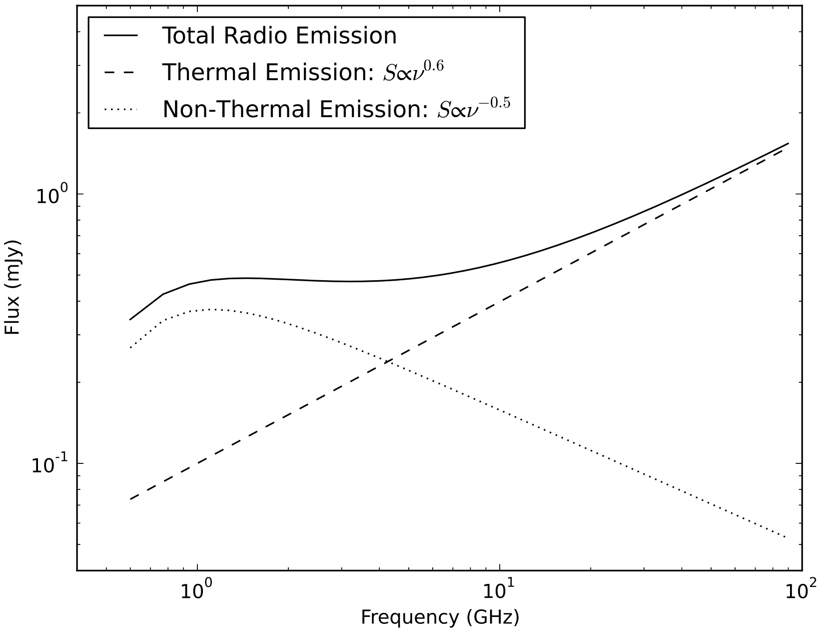

Figure 1.13: Model radio emission: the observed total flux (solid line), the thermal emission (dashed line) with $\alpha$=+0.6 and NT emission (dotted line) with $\alpha$=-0.5. Note the turn-over of the NT flux at low frequencies. See text for details.

where $\alpha = 0.6$, this is presuming an homogeneous stellar mass-loss with constant or accelerating velocity, (Wright & Barlow, 1975). This emission is produced when a charged particle is deflected by another charged particle, it was free before the interaction and remains free afterwards, hence free-free. This interaction is predominately between an electron being deflected by an ion. The electron slows or brakes due to the interaction and radiates the excess energy. In massive stars, primarily, accelerated electrons are thought to be the photon producers originating in the plasma of the extended stellar envelope, (Seaquist & Gregory, 1973; De Becker, 2007).

The mass-loss rate for early-type stars is found to be in the order of $10^{-7}$ to $10^{-5}$ $M_{\odot}$ yr$^{-1}$, with luminosity in the order of $10^6\,L_{\odot}$, with a correlation suggested by Scuderi et al. (1998) of:

$$\log_{10}\dot{M} \;\propto (1.25 \pm 0.30)\log_{10} L \tag{1.17}$$

although other studies suggest the correlation is $\sim 1.69$, (Howarth & Prinja, 1989; Lamers & Leitherer, 1993).

The black-body, or brightness temperature, $(T_B)$ of thermal emission is related to the radio brightness, $(B)$ or flux density per unit solid angle, by Rayleigh's classical approximation to the radiation law, (Christiansen & Högbom, 1987):

$$B \approx \frac{2kT_B}{\lambda^2}\ (\mathrm{Wm^{-2}Hz^{-1}sterad^{-1}}). \qquad (1.18)$$

(for $h\nu \ll kT_B$), (Christiansen & Högbom, 1987). In thermal emission the brightness temperature is typically found to be $\sim 10^4$ K, (De Becker, 2007).

In the stellar environment this emission, given the brightness temperature of $\sim 10^4$ K, is thought to be produced in stellar winds, as opposed to originating directly from the star. The theory of wind production in early-type stars was developed by Castor, Abbott & Klein, (1975) (CAK theory) as described earlier. The observed emission is closely related to the mass-loss rates of massive stars with radio flux being used to determine mass-loss rates, (see equation 1.10). For example a mass-loss of 3 x $10^{-6}$ $M_\odot$ yr$^{-1}$ is derived for the O2 type star, 30 Dor016, (Evans et al., 2010).

### Non-thermal radio emission

Non-thermal emission is found to have a spectral index ($\alpha$) differing from that of thermal emission (where typically $\alpha = 0.6$), having significantly lower or negative values and can also present strong flux variations. The radio emission is found to be non-steady or variable and to have a brightness temperature of $\sim 10^6 - 10^7$ K, considerably greater than that observed from thermal emission, (White & Becker, 1983; Abbott et al., 1984).

This emission is thought to be produced by synchrotron radiation (White, 1985; Rauw et al., 2002). This is produced by charged particles as they gyrate around magnetic field lines, (Matzner, 2001). The spectra of individual electrons combine to create the power-law spectra observed, as illustrated in Fig. 1.14. The observed NT emission is illustrated as a dotted line in the model spectra in Fig. 1.13.

In order to produce this type of emission, therefore, the stellar environment needs to have; (i) a magnetic field and (ii) a source of relativistic electrons. If synchrotron radiation is the cause of this NT radio emission, the contributing magnetic field could originate from;

1. A fossil field; a remnant magnetic field from the molecular cloud that the star formed from (Walder et al., 2012).

2. Another source for the magnetic field may be the dynamo effect. In the convective core

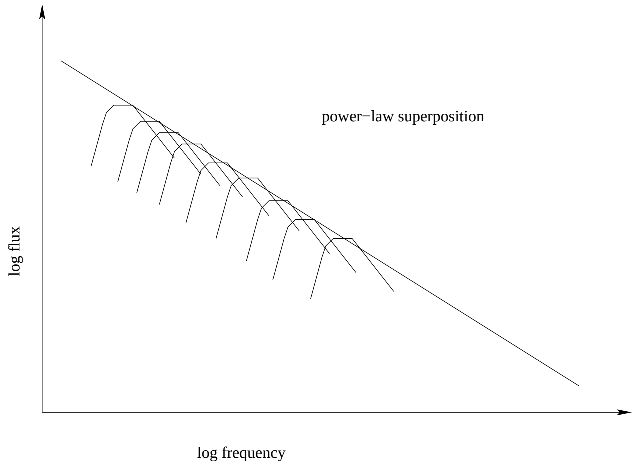

Figure 1.14: Diagram illustrating the superposition of individual electron spectra, (after Shu (1991), Fig 18.4). See text for details.

of massive stars a magnetic field is unlikely to survive, though in the radiative envelope a fossil magnetic field may survive. Dynamo action may be maintained by turbulence caused by the Coriolis force creating convection and rising cells of fluid, (De Becker, 2007). The dynamo could be driven by differential rotation or the Tayler - Spruit dynamo, (Spruit, 2002).

In massive stars the magnetic field may be located at the core-envelope interface, (De Becker, 2007). This field may reach the surface via the following two proposed methods;

1. Meridional circulation models have been investigated, though this effect acts to impede the dynamo action and proved difficult to yield surface magnetic fields, (Charbonneau & MacGregor, 2001).

Table 1.1: List of non-thermal emitting WR and O-type stars showing binarity.

| Star | Spectral Type | Multiplicity | Period | Ref. |
|---|---|---|---|---|
| WR11 | WC8 | binary | 78.5 day | 1,2 |
| WR98a | WR+OB | binary | 1 year | 1,3 |
| CygOB2#8A | O6If+O5.5III(f) | binary | 21.908 days | 1,4 |
| 9 Sgr | O3.5V((f$^+$)) + O5-5.5V((f)) | binary | 9.1 years | 5 |
| WR 140 | WC7+O4-5 | binary | 7.9 years | 6 |

Refs. 1: De Becker (2007); 2: Dougherty & Williams (2000); 3: Monnier et al. (2002); 4: Bieging et al. (1989); 5: Blomme & Volpi (2014); 6: Dougherty et al. (2005).

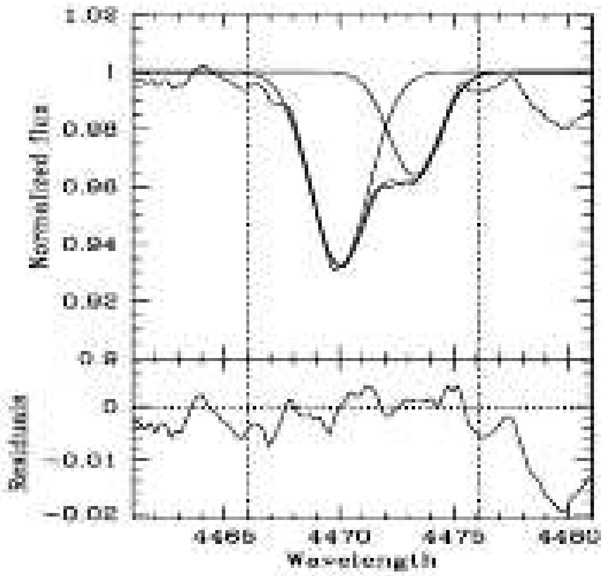

Figure 1.15: He I Spectra of Cyg OB2#8A, with Gaussians fitted to show 2 orbital components, De Becker et al. (2004). Repeated observations show changes in these components, allowing a determinant of the orbit.

2. The buoyant rise of magnetic tubes, symmetric rings around the stellar axis.

Either of these methods may act in massive stars, (De Becker, 2007).

A study of magnetic spots on massive stars has been undertaken by Cantiello & Braithwaite (2011) who suggest that localised magnetic fields may be the source of variability and clumping in the winds.

Perturbations in the stellar wind can produce instabilities that generate hydrodynamical shocks. In addition, in binary systems the interaction of both stellar winds produce additional shocked regions in the collision zone, resultant brightness temperatures of $\sim 10^7\,$K can be indicative of such binarity, (De Becker, 2007). Confirmation of the occurrence of binarity in NT radio emitting Wolf-Rayet (WR) and O-type stars is given in Table 1.1, see also a spectra showing binary components in Figure 1.15. A recent analysis of massive stars in six Galactic stellar clusters has concluded that more than 70 per cent of O-stars are binaries, (Sana et al., 2012, 2014).

This thesis has studied the radio emission from binary and runaway massive stars investigating the thermal and NT components of the received flux. These studies are detailed in the following chapters.

### Absorption of radio emission

There are a number of absorption mechanisms which can act on radio flux, at source and along the line of sight, these are:

1. Free-free absorption: When NT emission occurs in the presence of a thermal plasma, free-free absorption of the NT emission by the plasma may occur, (Allen, 1968). The free-free opacity is described by Equation 1.21

2. Synchrotron Self-Absorption: There is a mechanism of Synchrotron Self-Absorption (SSA) which occurs when the brightness temperature of the source approaches the kinetic temperature of the relativistic electrons and re-absorption occurs, modifying the spectrum at low frequencies, (Pittard et al., 2006).

3. Razin effect: In the presence of a thermal plasma and when the refractive index of the medium equates to less than 1, synchrotron radiation is suppressed. This is the Tsytovich-Razin effect which produces a characteristic cut-off frequency, $\nu_R$, given by;

   $$\nu_R = 20\,\frac{n_e}{B} \tag{1.19}$$

   where $B$ is magnetic field strength in Gauss, $n_e$ is the electron number density in $\mathrm{cm}^{-3}$ (Melrose, 1972; Dougherty et al., 2003; Pittard et al., 2006).

4. Inverse Compton scattering: A mechanism which absorbs NT emission at higher frequencies is Inverse Compton scattering (IC). This occurs where low energy photons are scattered to high energies by interactions with highly relativistic electrons, (Pittard et al., 2006).

### The non-thermal turn-over

The effect of one or a combination of the above absorption mechanisms is to cause the spectra of the NT emission to turn down or over. The position of this turn-over is likely to be different for each source/star, see this effect at low frequency in Fig. 1.13 illustrating model emission.

The absorption of emission can indicate the opacity in the region of the source. The Emission Measure $EM$, is the integral of the electron number density $\int n_e^2 dl$, given in units of $\mathrm{cm}^{-6}\,\mathrm{pc}$. The total emitted specific intensity, $I_\nu$, is related to the $EM$ by;

$$I_\nu \propto \int n_e^2 T^{-1/2} dl. \tag{1.20}$$

The free-free optical depth $\tau_{ff}$ can be deduced from the $EM$:

$$\tau_{ff} = 3.3 \times 10^{-7} T_4^{-1.35} \nu_9^{-2.1} \int_0^{\infty} n_e^2 dl. \tag{1.21}$$

The NT turn-over occurs when the optical depth is approximately = 1. See Chapters 4 and 5 for further discussions on low frequency emission and NT turn-overs.

### 1.4.2 Infra-red emission

IR wavelengths span the range from the red edge of the visible region, 700 nm to ∼1 mm. This emission originates from the Rayleigh-Jeans tail of the blackbody radiation, also from dust in the Universe that has been heated by UV radiation which then re-radiates this energy at IR wavelengths. In massive star forming molecular clouds the UV radiation from young massive stars is absorbed by surrounding gas and dust, then re-emitted at IR wavelengths which is able to pass through these regions without being scattered. This enables the study of massive star formation in these dense regions, (see for example Kraus et al., 2010).

This emission is largely filtered by the Earth's atmosphere as seen in Fig. 2.1. Some near IR emission is observed at ground level, e.g. by the Isaac Newton telescope at La Palma (Stevens & Howarth, 1999). The study of far IR emission in the Universe is more easily conducted above the atmosphere by satellite telescopes. The first IR space telescope was the Infra-red Astronomical Satellite (IRAS: Neugebauer et al. 1984) and one of the latest IR satellites, the Wide-field Infra-red Survey Explorer (WISE: Wright et al. 2010), has opened windows on the IR structure of the Universe, see Fig. 1.22 for example. IR observations are also important for the detection of elements in the spectra of stars, e.g. Helium and Neon.

The study of IR surveys of the Galactic plane first identified the presence of Infra-Red Dark Clouds (IRDC: Egan et al. 1998). It is in these IRDCs that massive stars are thought to evolve (Kauffmann & Pillai, 2010). The recent release of data from the WISE survey has revealed structure such as bubbles and bow shocks around massive stars (Peri et al., 2012). This thesis includes studies of WISE data of massive stars, see Chapter 6.

#### Galactic extinction/absorption

The absorption and/or scattering of photon energy by interstellar matter is a mechanism responsible for reduction or extinction of the received IR flux. The extinction, $R(V)$, is described by:

$$R(V) = A(V)/E(B-V), \tag{1.22}$$

Gordon et al. (2003), where

$$E(B-V) = A_B - A_V = (B-V) - (B-V)_0, \tag{1.23}$$

and where $(B-V)_0$ = intrinsic value for the colour index of the star, $A_B$ = total extinction in the photometric B (450 nm) band, $A_V$ = total extinction in the photometric V(550 nm) band, $B = B_0 + A_B$, $V = B_0 + A_V$. $V_0$ and $B_0$ are intrinsic values for the magnitudes of the star.

At 2175 Å (0.2175 $\mu$m) this extinction curve includes a bump feature, thought to be absorption by a form of carbon, ie graphite. The average figure for the Milky Way is an $R(V)$ of 3.1 (Gordon et al., 2003).

### 1.4.3 Optical and H$\alpha$ emission

At optical wavelengths ($400 - 700\,$nm) spectroscopic studies have been made of massive stars, see for example Lépine et al. (2001), together with massive star surveys, see Maíz Apellániz et al. (2012). At this wavelength mass-loss rates can be deduced from the luminosity in H$\alpha$ due to recombination radiation, see Section 1.3.2

In this thesis, work has included studies of spectroscopic and continuum data from the Hubble Space Telescope (HST), see Chapter 3, together with H$\alpha$ (656.28 nm) images from the Int Photometric H$\alpha$ Survey of the northern Galactic plane (IPHAS: Drew et al. 2005), see Chapter 6. The IPHAS survey was conducted from the ground based 2.54 m diameter Isaac Newton Telescope (INT), situated at the Roque de los Muchachos Observatory, La Palma.

### 1.4.4 Ultraviolet emission

Due to atmospheric absorption, ultraviolet (UV) emission can only be detected above the atmosphere. This has been accomplished by rocket studies in the 1960's and later by satellites, such as *Copernicus* and the International Ultraviolet Explorer (*IUE*). Howarth & Prinja (1989) have conducted a survey of over 200 O-stars with the *IUE*, estimating some of their fundamental parameters, see Fig. 1.8.

From UV emission resonance doublets, stellar wind $v_\infty$ can be derived and from luminosities, $\dot{M}$ can be deduced (Howarth & Prinja, 1989), see Section 1.3.2.

### 1.4.5 High energy emission - X-rays and Gamma-rays

Observations of massive stars at high energy wavelengths has been undertaken since the 1970's with the *EINSTEIN* satellite, (Stevens, 2005). More recently the *Chandra* and *XMM-Newton* X-ray satellite telescopes launched in 1999 (Nazé, 2009) and in 2003 the gamma-ray satellite *INTEGRAL* was launched. These satellite observatories have given a more detailed look at this energetic region of the spectrum (De Becker et al., 2007).

The X-ray luminosity ($L_X$) of massive stars scales with bolometric luminosity, with a scaling relation for the O-stars in Cyg OB2 given by Rauw et al. (2015) as:

$$\log_{10} \frac{L_X}{L_{bol}} = -7.2 \pm 0.2. \tag{1.24}$$

Typical $L_X$ are $\sim 10^{30} - 10^{34}$ erg s$^{-1}$ with X-ray emission having a temperature ($kT$) of $\sim$ 0.5 – 2 keV (Stevens, 2005). This emission is thought to originate from shocks within the winds of massive stars. In single stars, for example $\zeta$-Puppis, the emission is thought to be from the stellar wind near the star, 1.5 $R_*$, (Hervé et al., 2013), whilst in binaries the emission is believed to originate from the wind collision zone (Corcoran et al., 2011).

The source of high energy emission from massive stars is thought to be from shocks and colliding wind regions within the strong stellar winds. An illustration of X-ray emission from the Eta Carina Nebula, is seen in a montage of images in Fig. 1.16. This figure shows some of the sources within this nebula, the open star cluster Trumpler 14 which contains the massive binary system HD 93126A whose wind collision region has recently been studied by Benaglia et al. (2015), also shown is an X-ray light curve of the Wolf-Rayet system WR 25 indicating an orbital period of 207 days (Pandey et al., 2014) and the bright massive binary system Eta Carina seen with optical HST data together with gamma-ray *INTEGRAL* data and X-ray *Fermi* data. This binary system has a strange X-ray light curve, seen in the figure, that is thought to represent a merger event (Farnier et al., 2011; Portegies Zwart & van den Heuvel, 2015). See further studies of this region by Leutenegger et al. (2003); Pandey et al. (2014).

The following section gives a description of shocks in stellar winds.

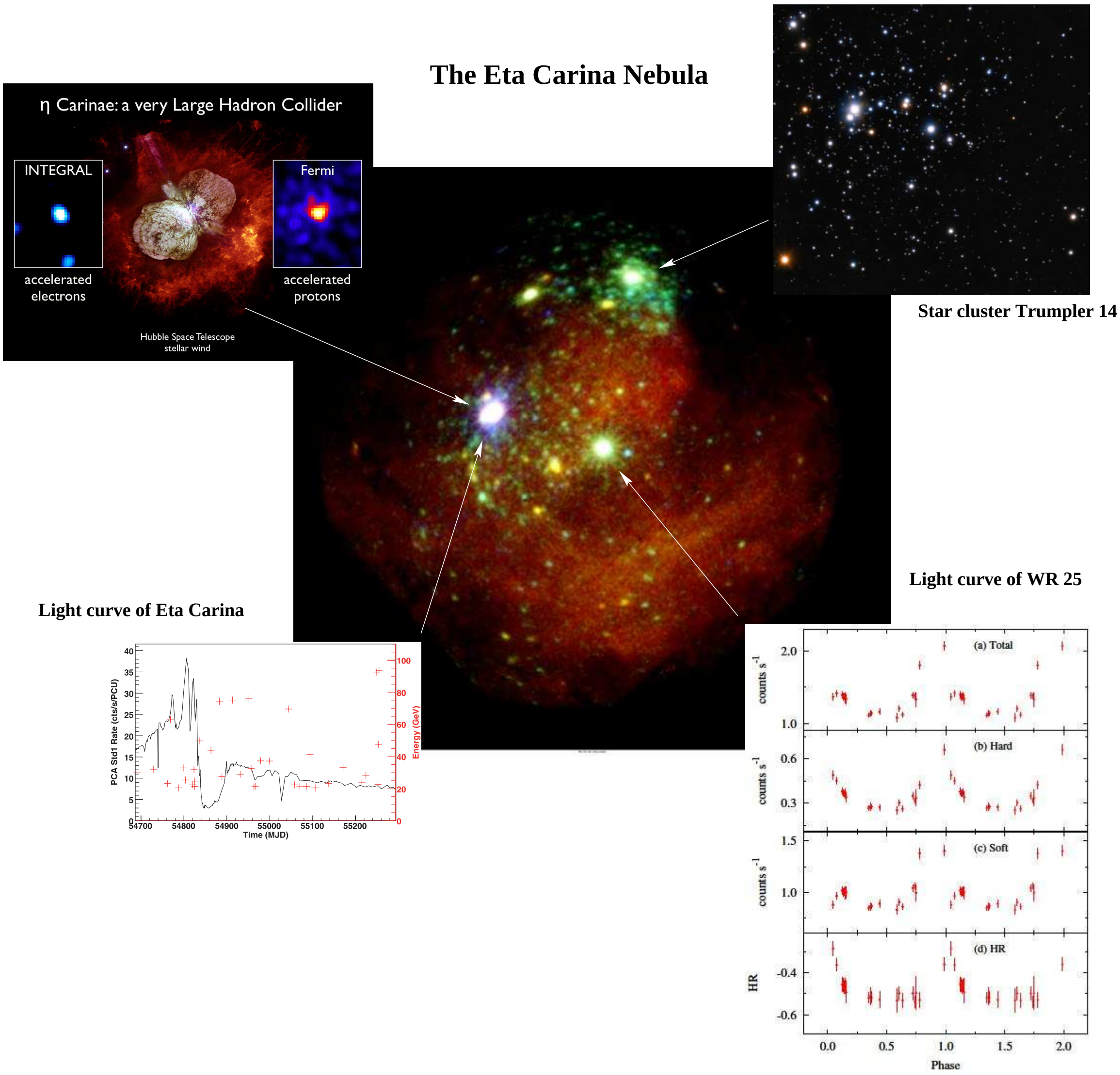

Figure 1.16: Montage of sources within the Eta Carina Nebula. Centre: *XMM-Newton* image of the Eta Carina Nebula (32 by 32 arcmin). The energy bands are coloured as: low energy (0.2–1.0 keV) in red, medium energy (1.0–2.0 keV) in green and high energy (2.0–12 keV) in blue. Image courtesy of Rosemary Willatt (ESAC) and ESA, (Raassen et al., 2003). With surrounding images, Top left: The Eta Carina, a bright massive star binary system illustrating a central HST image with *INTEGRAL* gamma-ray data and *Fermi* X-ray data (Farnier et al., 2011), Top right: An optical images of the open star forming cluster Trumpler 14 (Sana et al., 2010), which includes the bright massive binary system HD 93126A (see study by Benaglia et al. 2015), Bottom right: *XMM-Newton* light curve of the Wolf-Rayet star WR 25, displaying periodic emission giving an orbital period of ∼207 days (Pandey et al., 2014) and Bottom left: An X-ray light curve of Eta Carina indicating a high flux period thought to indicate a merger event (Farnier et al., 2011; Portegies Zwart & van den Heuvel, 2015) .

Figure 1.17: A wind blown bubble around the Wolf-Rayet star WR 6. The bubble is approximately 18 parsec in diameter, with the WR-star being the almost central bright source.
Credit: http : //apod.nasa.gov/apod/image/1506/sh308_simon_960.jpg.

## 1.5 Shocks in Stellar Winds

### 1.5.1 Wind blown bubbles

The strong winds from massive stars add mechanical energy to their environment and create spectacular wind blown bubbles around their star (Castor et al., 1975a; Weaver et al., 1977; McKee et al., 1984; Mackey et al., 2015). Figure 1.17 shows a beautiful example of a wind blown bubble around the Wolf-Rayet star WR 6.

### 1.5.2 The anatomy of shocks

When the velocity of a stellar wind is greater than the sound speed of the surrounding ISM a shock can form. The material ahead of the wind cannot respond to the shock until it arrives, whereupon the shock will compress, heat and accelerate the ISM. This then cools in the post shock region. The analytical study of bow shocks in stellar winds has been made by Baranov et al. (1971); Dyson (1975) and Wilkin (1996), who stressed the importance of the conservation

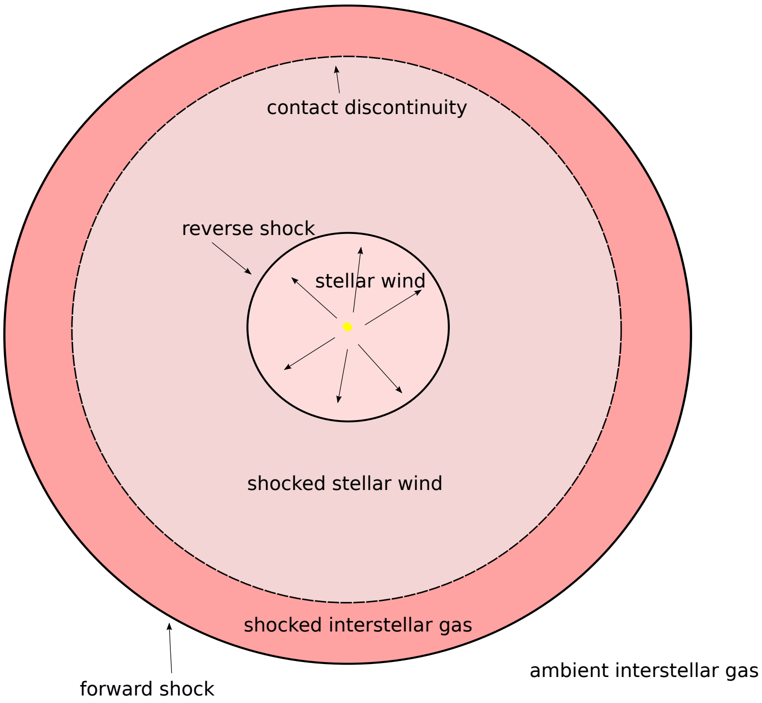

Figure 1.18: A stellar wind blown bubble. Diagram illustrating the wind-flow structure of a stellar bubble, showing the central star and surrounding stellar wind, the reverse shock with the shocked wind region, the contact discontinuity, the outer, shocked interstellar gas region and the forward shock.

of momentum across the shock. A further discussion of analytical bow shock shape follows in Chapter 6.

The anatomy of a shock wave is determined by the conservation of 3 quantities across the shock; the pressure, $P_0$, density, $\rho_0$ and velocity, $v_0$ of the supersonic gas before the shock and equivalent parameters for the subsonic post-shock gas, $P_1, \rho_1, v_1$. The thickness of the shock is relatively small, in the region of the mean-free-path of the particles, it can, therefore, be considered a discontinuity (Shu, 1992). A schematic of a stellar bubble is shown in Fig. 1.18 indicating stellar wind shock structure, from the stellar wind region, the reverse shock, the shocked stellar wind region, the point of momentum balance - the contact discontinuity, the shocked ISM region, the outer forward shock and the ambient ISM.

To understand the conditions that are present in the shock, there are 2 types of shocks to consider, a fast shock with velocity, $v \gtrsim 40$ km s$^{-1}$, which interacts with the ISM and is slowed down and heated quickly producing a thin shock front. The conditions before and after are refered to as jump conditions, and these shocks are called J-shocks. Slower, weaker shocks have a thicker shock and are explained by a continuous process of heating and cooling. These continuous shocks are known as C-shocks. Within stellar winds shocks are high velocity J-shocks.

The J-shocks are subject to the following conservation conditions:

1. The conservation of mass dictates that the same mass that flows into the shock will flow out, hence a flow rate per unit area:

$$\rho_0 v_0 = \rho_1 v_1 = constant \tag{1.25}$$

2. The conservation of momentum states that mass entering the shock, $(\rho_0 v_0)\ v_0$, leaves with the same mass, but with momentum altered by the net force:

$$P_0 + \rho_0 v_0^2 = P_1 + \rho_1 v_1^2 = constant \tag{1.26}$$

3. The energy of the gas either side of the shock will be conserved though there is work done on the gas by pressure in the shock, hence:

$$\frac{1}{2} v_0^2 + \frac{5}{2}\frac{P_0}{\rho_0} = \frac{1}{2} v_1^2 + \frac{5}{2}\frac{P_1}{\rho_1} = constant. \tag{1.27}$$

These three jump conditions are known as the Rankine-Hugoniot conditions, mostly related to high Mach number shocks, and these conditions determine the ‘jumps’ in $P, v$ and $\rho$ (Frank et al., 2002; Tielens, 2005). Figure 1.19 illustrates the changes in conditions across the shock, Draine & McKee (1993).

The Mach number, $M_0$, is defined as the ratio of the velocity, $v_0$, and the sound speed, $c_s$:

$$M_0 = \frac{v_0}{c_s} \tag{1.28}$$

where the sound speed, $c_s$, is related to the Boltzmann constant, $k$, the temperature, $T$ and the mean mass per particle, $m$ by:

$$c_s = \sqrt{kT/m}. \tag{1.29}$$

We can then derive that in a strong adiabatic shock, with a pre-shock Mach number, $M_0 \gg 1$, that the velocity of the gas as it crosses the shock drops by a quarter, (Frank et al., 2002):

$$\frac{v_1}{v_0} = \frac{1}{4} \tag{1.30}$$

which from the conservation of mass equation above indicates that the gas is compressed by a factor of 4 by the shock;

$$\frac{\rho_1}{\rho_0} = 4 \tag{1.31}$$

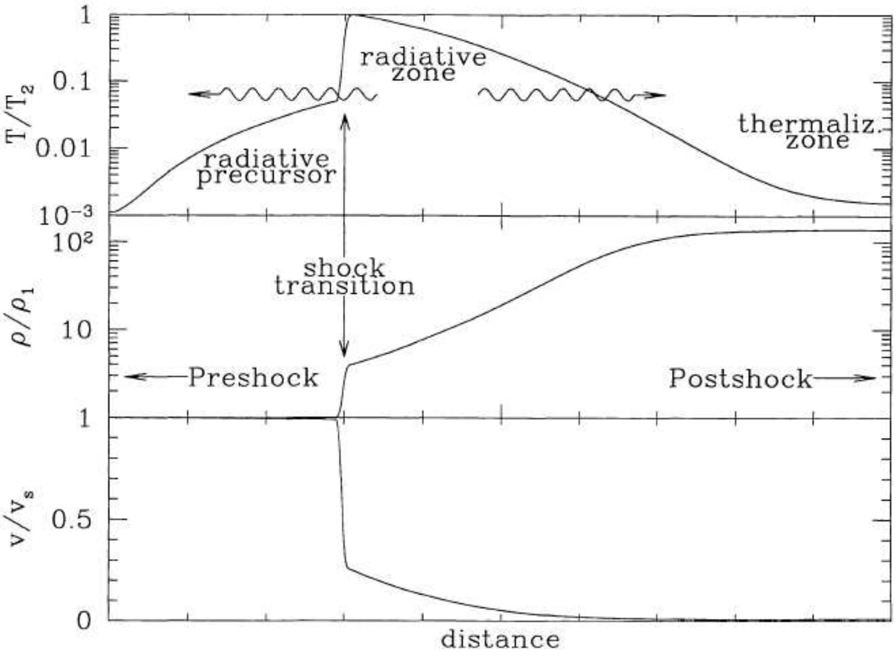

Figure 1.19: An illustration of 'jump' conditions as described by Draine and McKee, 1993, their Fig. 1.

(Frank et al., 2002; Tielens, 2005).

If radiative cooling is occurring in the shocked gas; i.e. the shock is isothermal, this needs to be considered and here the post-shock pressure ($P_2$) is related to the initial density $\rho_0$ and the shock velocity $V_s$:

$$P_2 = \rho_0 V_s^2 \tag{1.32}$$

where $P_2$ is dependent on the upstream Mach number. In a collision-less shock particle collisions are rare, with interactions predominately due to a small number of particles accelerated by magnetic field - charged particle interactions, carrying a substantial amount of energy out of the system.

When a magnetic field is present in a J-shock, flux freezing occurs, i.e. compression as the gas cools leads to an increase in the magnetic field which acts as a cushion for the shock (Tielens, 2005). Note that magnetic pressure is less than gas pressure which is less than the ram pressure.

Magnetic disturbances propagate though an ionised fluid as Alfvén waves, with a speed or Alfvén velocity ($v_A$) of:

$$v_A = \left(\frac{B^2}{4\pi\rho}\right)^{1/2} (\mathrm{cm\,s^{-1}}) \tag{1.33}$$

where $B$ is the magnetic field strength in Gauss, and $\rho$ is the plasma density in units of electron number cm$^{-3}$ (Tielens, 2005).

In Magneto Hydro-Dynamics (MHD) there are 3 shock types; intermediate (non-compressive), slow and fast-mode, (both compressive) - slow mode have a tangential component of the magnetic field which decreases across the shock, fast-mode increase.

Magnetic shocks are an important consideration in stellar winds, when the magnetic field, $B$, is parallel to the shock front:

$$B_1 v_1 = B_2 v_2 \tag{1.34}$$

though when the field is perpendicular the situation is more complicated, (McKee & Hollenbach, 1980; Draine & McKee, 1993).

In shocks that occur in the stellar winds of massive stars the ionised gas and magnetic fields present enable electrons to be accelerated by the first-order Fermi mechanism, (Bell (1978) and Benaglia et al. (2006)). The Fermi mechanism accelerates charged particles via repeated reflection from the magnetic field. Therefore these high energy shock fronts provide a mechanism, via Fermi acceleration, to accelerate electrons to relativistic velocities, producing X-rays and possibly high energy $\gamma$-rays, (Fermi, 1949; Blandford & Ostriker, 1978).

### 1.5.3 The Solar bow shock: in-situ measurements of a bow shock

First hand results of in-situ measurements of the Solar bow shock have been made by the Voyager spacecraft. Initial reports indicate that the heliopause, the boundary between the solar plasma and the ISM has been crossed by the Voyager 1 spacecraft. On 20th August 1977 Voyager 2 was launched and a few days later on the 5th September Voyager 1 was also launched, both spacecraft embarking on a trip to the outer reaches of the Solar system.

The Voyager craft have now travelled to the edge of the Solar system, through the termination shock, with Voyager 1 confirmed as passing through the Solar bow shock into the ISM on the 9th April, 2013, see Fig 1.20. The plasma wave instrument on board Voyager 1 detected electron plasma oscillations corresponding to an electron density of approximately 0.08 cm$^{-3}$, close to the density expected from the ISM, indicating that the craft has crossed the heliopause into the interstellar plasma on 25 August 2012. Magnetic field measurements indicated similar Solar and interstellar magnetic fields, although no linkage between the two was found (Gurnett et al., 2013).

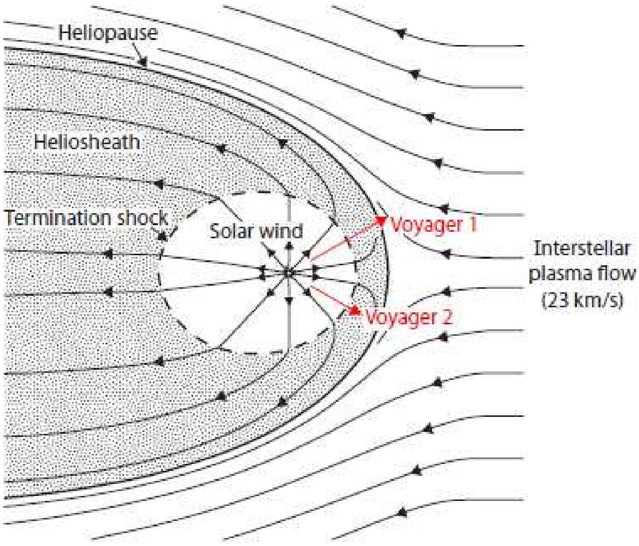

Figure 1.20: Diagram showing the heliopause and the current location of the Voyager spacecraft (Gurnett2013).

### 1.5.4 Runaway stars and stellar bow shocks

#### Runaway stars

Many massive, early-type stars have been found to show large peculiar space velocities, $\gtrsim$40 km $s^{-1}$, (Blaauw, 1961) with respect to their local ISM and are thought to have been ejected from their birth cluster. There are two current theories describing the formation of these high velocity stars:

1. The Binary Supernova Scenario (BSS; Blaauw, 1961), suggests that when the primary star in a binary system becomes a supernova, the secondary star is ejected from the system with a velocity comparable to its former orbital velocity ($\sim$100 km $s^{-1}$) and a kinematic age smaller than the age of its parent association, (Tetzlaff et al., 2010).

2. The Dynamical Ejection Scenario (DES; Poveda et al., 1967), suggests that runaways may be ejected from dense young stellar clusters by gravitational interactions occurring soon after formation, consequently having a kinematic age similar to its parent association, (Tetzlaff et al., 2010).

Current thinking is that both of these scenarios do occur, see Tetzlaff et al. (2010) and references therein. These ejected, or runaway stars are studied further in the Chapter 6 and 7.

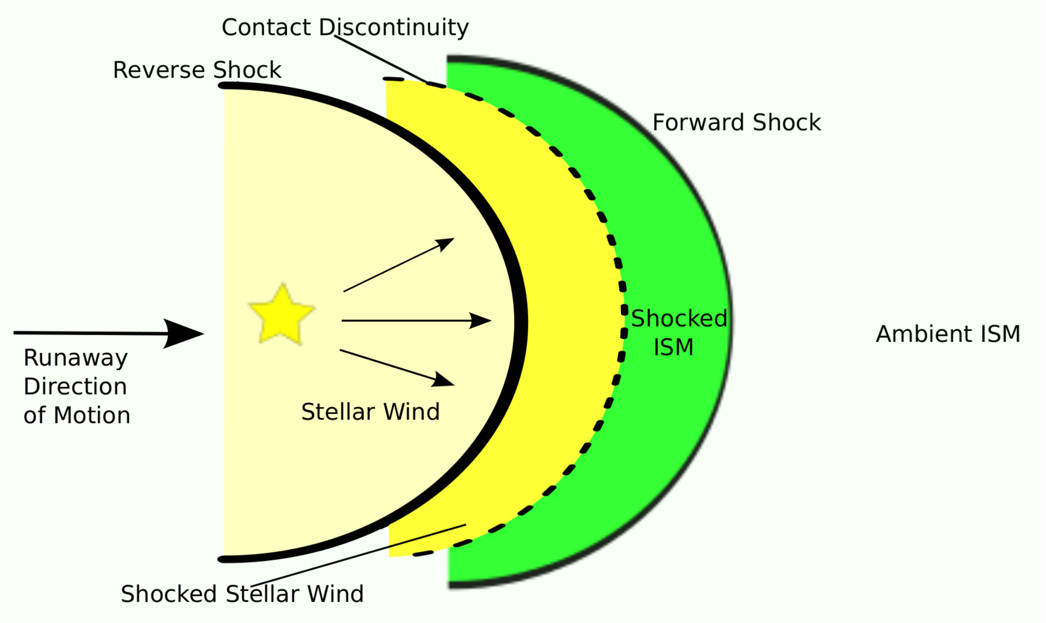

Figure 1.21: A stellar bow shock. Sketch of the bow shock structure of a runaway massive star, illustrating the hot stellar wind region, the reverse shock and the shocked stellar wind region, the momentum balance indicated by the dashed line - the contact discontinuity - and then the shocked ISM region, with the forward shock meeting the unshocked ISM.

### Stellar bow shocks

In the case of massive runaway stars which are found to possess high spatial velocities and large stellar winds, these winds interact with the ISM and sweep up material, dust and gas, creating a contact discontinuity where the momentum flux of the stellar wind and the ISM balance. When the relative velocity between the stellar wind and the ISM is higher than the sound speed in the ISM a bow shock may occur (van Buren & McCray, 1988; Noriega-Crespo et al., 1997; Cox et al., 2012a). The structure of the resultant bow shock from these interactions is detailed in Fig. 1.21. Here the contact discontinuity separates the shocked and unshocked stellar wind from the shocked and unshocked ISM. When viewed moving in the plane of the sky the bowed shock wave tails back towards the runaway. However if the runaway is moving in the line of sight the bow shock will appear circular around the star, see for example del Valle & Romero (2012).

See also examples of observed bow shocks from runaways, Fig.1.22 is an image of $\zeta$ Ophiuchi, thought to be ejected by the BSS method and now producing a distinctive bow shock shape in the direction of motion. Also, shown in Fig.1.22, is $\alpha$ Camelopardalis, an O-type supergiant whose ejection method is uncertain. These figures show infra-red images illustrating the emission

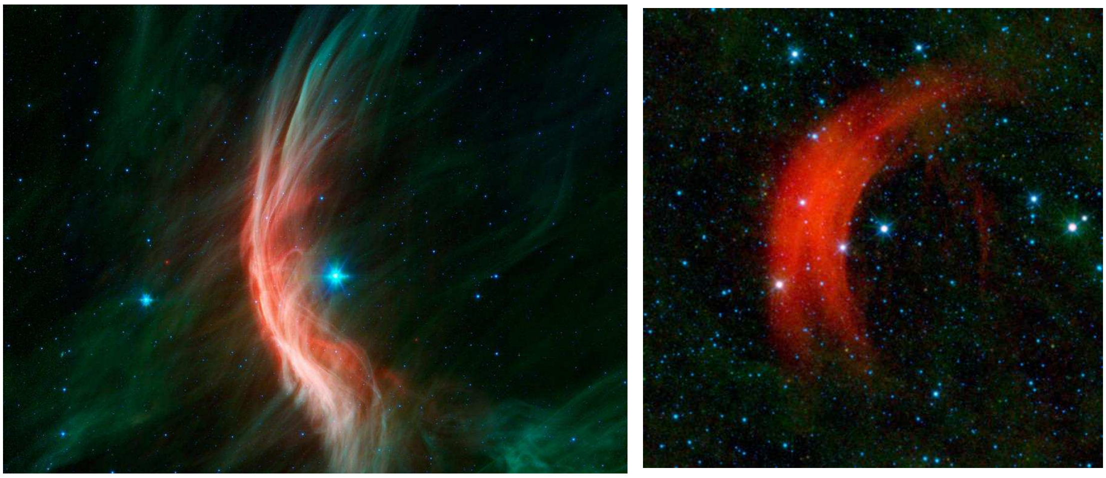

Figure 1.22: Examples of stellar bow shocks, Left: An infra-red Spitzer image of Zeta Ophiuchi showing the bowed shape of the shock and the runaway star visible behind the shock. 3.6 and 4.5 $\mu$m are coloured blue, 8.0 $\mu$m is green and 24 $\mu$m is red. Image Credit: NASA, JPL-Caltech, Spitzer Space Telescope. See also a WISE image of this bow shock in Peri et al. (2012). Right: An infra-red WISE image of Alpha Camelopardalis, revealing the bowed shape of the shock and the parent star positioned before the reverse shock front. 3.4 and 4.6 $\mu$m are coloured blue, 12.0 $\mu$m is green and 22 $\mu$m is red. Image Credit: NASA, JPL-Caltech, WISE Team and see also this bow shock imaged in Peri et al. (2012).

from dust swept up by the bow shocks.

The distance from the star to the bow shock momentum balance, the standoff distance ($R_0$) is given by the momentum flux of the stellar wind ($\dot{M}\, v_\infty$), the density of the ISM ($\rho_{ISM}$) and the velocity of the star ($v_*$) is given by Wilkin (1996) as:

$$R_0 = \sqrt{\frac{\dot{M}\, v_\infty}{4\pi \rho_{ISM} v_*^2}}. \tag{1.35}$$

Wilkin (1996) has studied the interaction zone for stellar wind bow shocks, giving analytical solutions to predict the distance $R$, at an angle $\theta$, to give the shape of the interaction zone. This theoretical interaction zone and the bow shocks of runaway stars are discussed further in Chapter 7 which details a survey of bow shocks from runaways and also in Chapter 6 where one runaway, BD+43° 3654, is studied in detail.

### 1.5.5 Massive binary systems and colliding wind shocked regions

Many massive stars are now known to be part of binary systems (Sana et al., 2014). In such a binary system containing two massive stars, their strong highly ionised stellar winds will

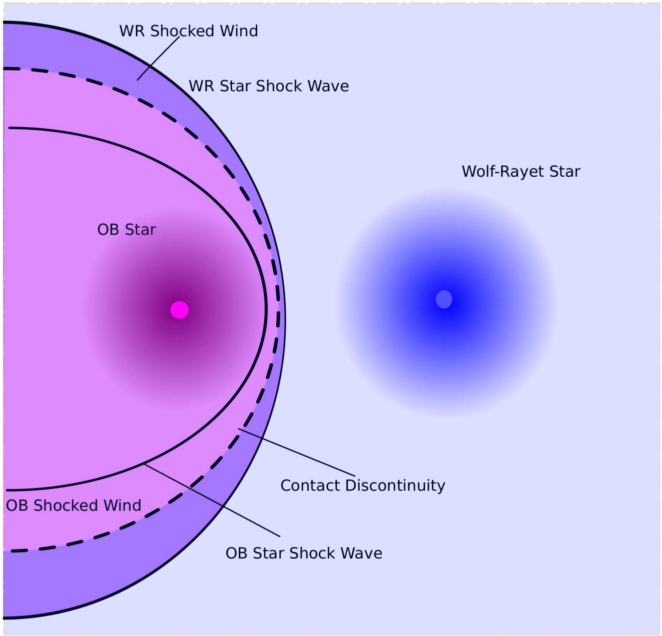

Figure 1.23: A colliding wind binary. Sketch of the interaction zone around a colliding wind binary system. The component stars and their surrounding stellar winds are indicated, left - the OB star and right - the WR-star. The primary shock of the WR-star is indicated by a solid line, tailing back around the companion. The contact discontinuity is shown as a dashed line and the secondary shock of the OB star is shown as a solid line.

collide, creating a shocked region where their momentum flux is balanced (Stevens et al., 1992, 1995; Corcoran et al., 1996; Reitberger et al., 2014). In a survey of the young massive cluster Westerlund 1, studies of radio spectra have suggested the presence of colliding wind binaries (Dougherty et al., 2010).

This wind collision zone between two massive binary components creates a shock structure where each star creates a shock front and shocked wind region, with a contact discontinuity where the momentum fluxes balance. The shock shape will be determined by the winds of the stars, a stronger wind will dominate and shape the interaction zone. This shape has been studied by Canto et al. (1996) who provide solutions for the distance from each star to the interaction zone, $r$, at angles of $\theta$, to obtain the shape of the thin shell of the interaction zone.

The distance from each of the stars to the interaction zone between them is given by $\eta$, the ratio of their momentum flux:

$$\eta \equiv \frac{[\dot{M}(O)\ v_\infty(O)]}{[\dot{M}(WR)\ v_\infty(WR)]} \equiv \left(\frac{r(O)}{r(WR)}\right)^2 \tag{1.36}$$

(Stevens et al., 1992; Usov, 1992), where $r(O)$ is the distance from the O-star to the interaction

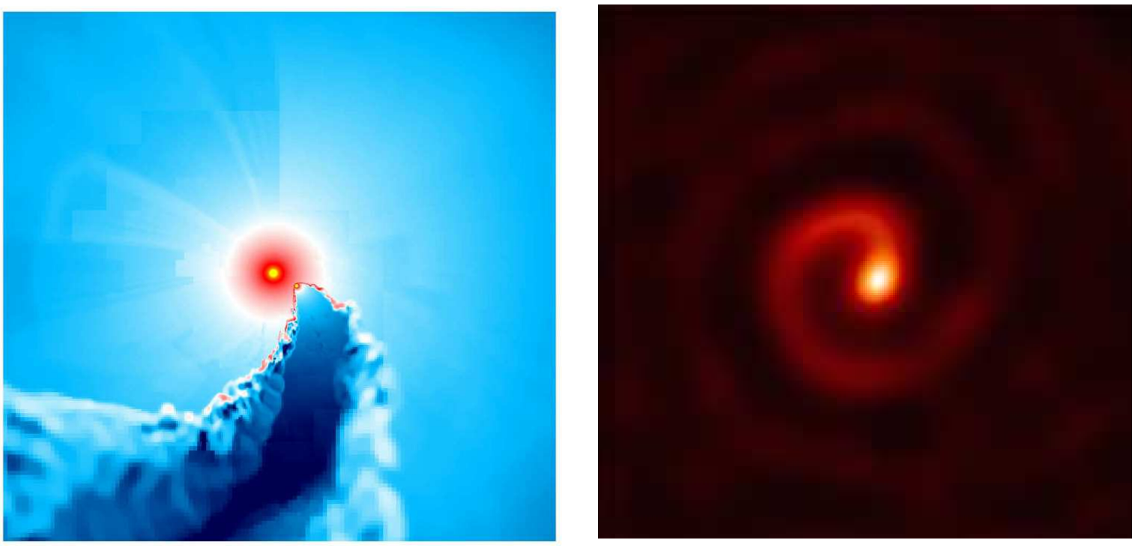

Figure 1.24: Colliding wind binaries. Left: Model of the colliding wind system WR 22. The WR-star is the yellow central object, surrounded by its stellar wind, the companion star is the small yellow point with the wind collision plume tailing behind, see text for details, Parkin & Gosset (2011). Right: The colliding wind binary system WR 104, also known as the pin-wheel nebulae, revealed in the IR by Tuthill et al. (2008)

zone and $r(WR)$ is the distance from the WR-star to the same (Usov, 1992; Benaglia et al., 2015). The structure of these regions is illustrated in Fig. 1.23 indicating the shock structure between the strong wind of a WR-star, together with an OB star with the shock structure tailing behind the weaker OB component.

This structure is illustrated by a detailed model of the WR 22 system in Fig.1.24. Here the central Wolf-Rayet component has the stronger wind which collides with the lesser wind of the companion and the resulting plume from the collision is seen tailing behind (see this link for an illuminating movie of this simulation:
http://www.esa.int/spaceinvideos/Videos/2012/10/Colliding_winds_at_WR_22).

The winding or pin-wheel effect created by this two-wind interaction has been observed in WR 104, in the IR by Tuthill et al. (2008) also illustrated in Fig. 1.24 (see a movie of this multi-epoch observation here: http://www.physics.usyd.edu.au/~gekko/pinwheel.html).

Colliding winds are also known to occur in low mass binary systems, where the interaction zone is more a deflection of the stellar winds. This is illustrated in simulations by Johnstone et al. (2015).

The study of colliding wind binaries is detailed further in Chapters 3 and 4 which detail two observations of the Wolf-Rayet colliding wind system WR 147 and in Chapter 5 with details of observations of a brighter Wolf Rayet system, WR 146.

## 1.6 Conclusion

As outlined in this section, massive stars are very influential in “galactic ecology”, as their winds, their energy and metal pollution are added to their galactic environment affecting its evolution greatly.

The following chapter gives an introduction to radio interferometry, with subsequent chapters detailing radio observations of the massive runaway star BD+$43^o$ 3654 and the colliding wind binaries WR 147 and WR 146.

# Chapter 2

# An Introduction to Radio Interferometry

*"The discovery of a new dish does more for human happiness than a new star."* Anthelme Brillat-Savarin 1755-1826, Physiologic du Goût 1825, IX.

## 2.1 Summary

This chapter is a description of what can be gleaned from the radio portion of the electromagnetic spectrum. It includes a description of what emission can be detected from the ground, the various types and arrangements of radio telescopes and how the received data is analysed to produce final images.

## 2.2 An Introduction to Radio Astronomy

### 2.2.1 The transparency of the sky

Photons of light from the Sun, Moon and from the stars of our Galaxy and also extra galactic sources in the night sky have been observed by mankind for thousands of years. We now know that this visible light forms part of the electromagnetic spectrum, with wavelengths ranging from very small gamma-rays, $10^{-12}\,$m, to long radio waves, $\sim$km. The atmosphere around the Earth absorbs a large portion of incoming electromagnetic radiation, although 'windows' of transparency do occur, as illustrated in Figure 2.1. These windows allow us to detect visible light with our naked eyes and radio wavelengths, ranging from millimetres to kilometres, can be detected by radio telescopes on the ground.

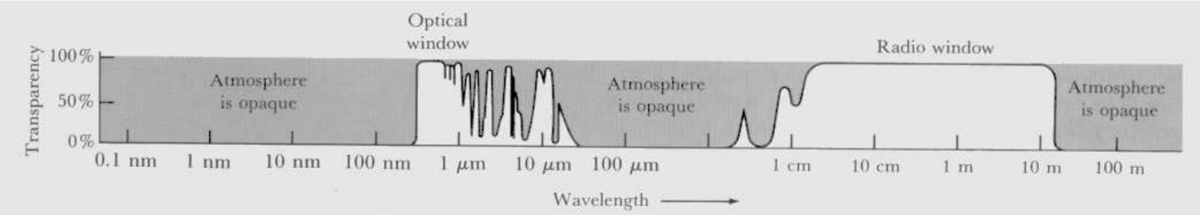

Figure 2.1: The transparency of the Earth's atmosphere, revealing windows at optical and radio wavelengths. (Credit: NASA FUSE project. http://www.astro.rug.nl/∼ndouglas/teaching/ObservingTechniques/atmosphere.html).

### 2.2.2 A brief history of radio telescopes

The first detection of radio emission was made in 1932 by Karl G. Jansky at the Bell Telephone Laboratories, Holmdel, New Jersey, with a dipole array which received radio waves at 14.6 m or at a frequency of 20.5 MHz. This detection came from the direction of the centre of the Galaxy (Jansky, 1933). Shortly afterwards Grote Reber built his own 9 m parabolic radio receiver dish in Wheaton, Illinois and in 1941 he had completed a radio map of the sky at 160 MHz, indicating, for the first time, the existence of Cygnus A and Cassiopeia A as individual radio sources (Reber, 1944).

In the 1950's the Cambridge Interferometer, an array of four fixed elements, was built by Martin Ryle and Antony Hewish. This early interferometer was used to produce early catalogues of radio sources, see for example the second Cambridge (2C) catalogue at 81 MHz, (Shakeshaft et al., 1955).

The unit of source intensity used in radio astronomy is flux density, $S_\nu$ (defined in Section 1.4.1) with units of $\mathrm{W\,m^{-2}\,Hz^{-1}}$, though normally the smaller unit of Jansky (Jy) is used, defined as $10^{-26}\,\mathrm{W\,m^{-2}\,Hz^{-1}}$.

## 2.3 What is an Interferometer?

### 2.3.1 Interferometer design

A single antenna radio telescope absorbs power from incoming signals which is then measured by the 'total power' receiver. The resolution of a telescope is limited by the Rayleigh criterion. This states that the angular separation (in radians) of two point sources should be greater than the distance between the maximum and first zero of the diffraction pattern, or Airy disc, see

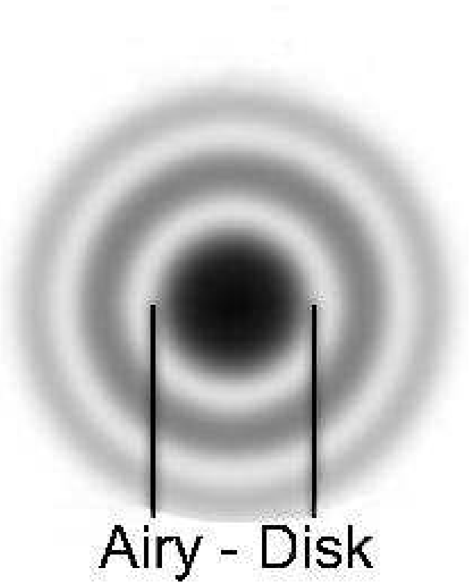

Figure 2.2: An example of an Airy disc. source: http://www.jb.man.ac.uk.

Fig. 2.2. This gives the resolving power or the angular resolution ($\theta$) in radians, of a telescope of diameter $D$, as being equal to;

$$\theta = 1.22\,\frac{\lambda}{D} \tag{2.1}$$

where $\lambda$ is the wavelength of the observation, (Christiansen & Högbom, 1987). For example, at an optical wavelength of 500 nm an angular resolution of 1 arcsec would require a telescope of ~13 cm. A similar resolution at a radio frequency of 5 GHz would require a radio dish of ~15 km, which is not feasible to construct.

Therefore, to increase the resolving power of a radio telescope, that is to resolve smaller sources, it follows from the Rayleigh criterion (Equation 2.1) that a larger aperture is needed. With some radio wavelengths in the order of many metres or kilometres a single telescope dish is not feasible and the solution is a collection or array of radio telescopes. This consists of two or more antennas that observe a source simultaneously and send signals to a 'correlation' receiver, this gives an output proportional to the average of the voltages from all antennas.

Figure 2.3 illustrates a two element interferometer, where the time delay ($T$) between the two telescopes or antennas is given by the distance or baseline ($B$) between the two antennas and the angle ($\theta$), between the baseline and the source wave-front ($b$). Therefore the propagation

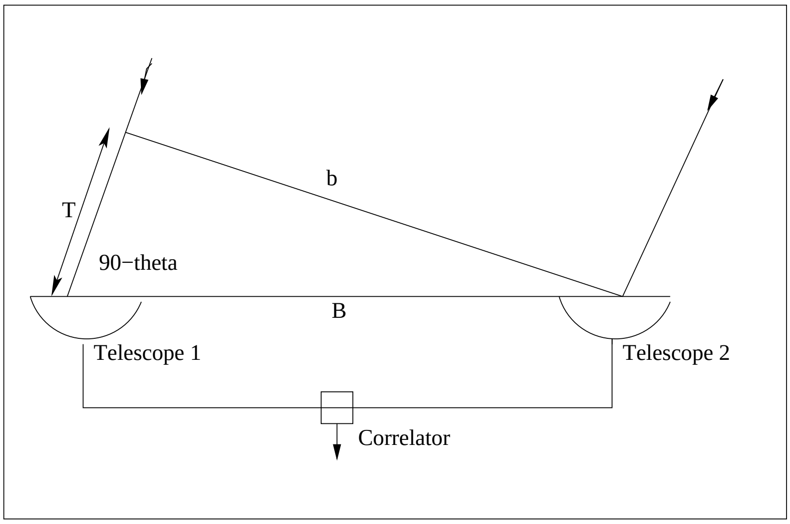

Figure 2.3: A diagram illustrating a two element interferometer. Telescope 1 and 2 are separated by distance $B$, the incoming signal arrives at an angle $\theta$, with the time delay of the signal arriving at telescope 1 equal to $T$.

delay between wave-fronts ($T$), is given as;

$$T = \frac{B\ \sin\theta}{c}. \tag{2.2}$$

To illustrate this delay, consider the time delay for a two element interferometer such as Fig. 2.3 where the baseline, $B = 1\,\mathrm{km}$ and the angle of the incident wave front, $\theta = 0$ degrees, here $T$ = 0, that is, there is no time delay from an overhead source. Where $\theta = 40$ degrees, $T$ becomes $\sim 2\mu$s and at a greater baseline distance of 10 km, $T$ becomes 10 $\times$ greater at $\sim 20\,\mu$s.

### 2.3.2 What is a correlator?

From these numerous elements of the interferometer, or antennas, a final signal is required. To obtain this the voltage output of all the signals are fed to a correlator which multiplies the voltages, allowing for time delays, and then time averages the signal to give a final output. The correlator output voltage ($R$) is related to the baselines in the interferometer array as a sinusoidal output;

$$R = (V^2/2)\ cos(\omega T) \tag{2.3}$$

where $V$ is the voltage, $\omega$ is the phase difference of the wavefront between the antennas and $T$ is the time delay of the received wavefronts. The sinusoids that represent the interference of the wavefronts are called fringes, with amplitude and phase (Christiansen & Högbom, 1987).

The relevant intensity for a source per unit solid angle is the radio brightness ($B$), which is related to emission from a black-body and the brightness temperature ($T_B$), by Rayleigh's classical approximation to the radiation law by Equation 1.18

The effective area of an antenna, $A(l,m)$, (where l,m are directional cosines) is determined by the shape of the reception pattern, $P(l,m)$, or 'beam' of the antenna and $A_{max}$, the maximum effective area:

$$A(l,m) = A_{max}P(l,m) \tag{2.4}$$

(Christiansen & Högbom, 1987).

### 2.3.3 Baselines and u-v coverage

The positioning and the number of antennas in an array has an effect on the visibility or *u-v* coverage of the source. The greater the number of antennas, the more baselines between them are available, creating a more complete effective coverage, see Fig. 2.4 for an example of coverage by a 30 element Y shaped array. A *u-v* plane is measured in distances on the ground, not the sky and is defined according to the observing wavelength $\lambda$, where $u$ is measured from west to east and $v$ is measured south to north, i.e:

$$u = (x_2 - x_1)/\lambda \tag{2.5}$$

and

$$v = (y_2 - y_1)/\lambda. \tag{2.6}$$

An observation of a few seconds with a two element interferometer, such as that illustrated in Fig. 2.3, will produce a *u-v* plane with just two coverage points. Over a longer time-scale, around 12 hours, the rotation of the Earth has the effect of increasing the *u-v* coverage, also known as Earth's rotation synthesis. This has the effect of a circular coverage, as shown in Fig. 2.5. Positioning of the array elements in two dimensions in a 'Y' or a spiral configuration increases the *u-v* coverage over the effective telescope area, this is illustrated also in Fig. 2.5. These images are produced by the graphical simulator The Pynterferometer (Avison & George, 2013), see also Fig. 2.4 which shows the *u-v* plane coverage at 610 MHz of the Y shaped array at the Giant Meterwave Radio Telescope (GMRT).

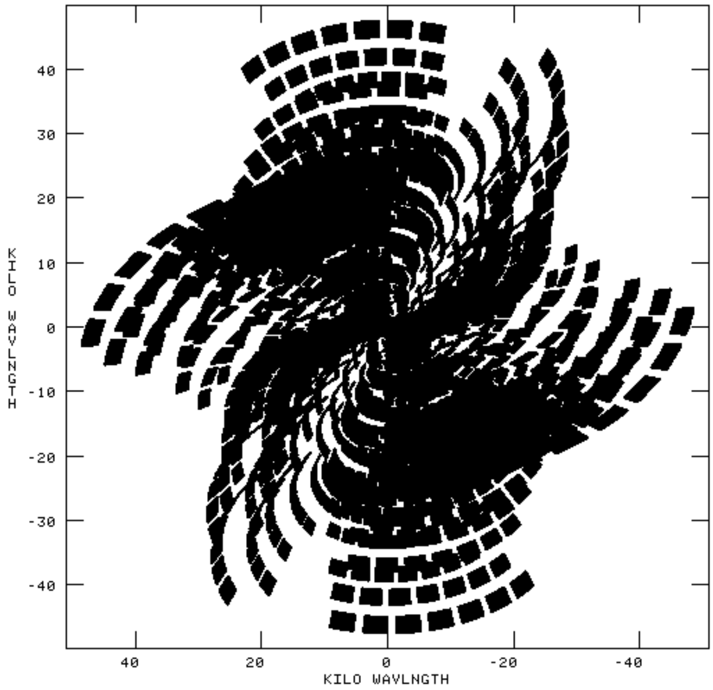

Figure 2.4: Coverage of the *u*-*v* plane at 610 MHz by the GMRT 'Y' shaped array.

The *u*-*v* plane of 6 antennas of the Multi-Element Radio Linked Interferometer Network (MERLIN) array is shown in Fig. 2.6, (see Fig. 2.12 for a plan of the layout of this telescope). Fig. 2.6 illustrates the benefit of a longer observation time and a source at high declination, hence the top left panel illustrates an observation for 24 hours of a source which remains above the horizon (circumpolar). The bottom right panel illustrates a low declination source with considerably less coverage. The *u*-*v* coverage of the upgraded e-MERLIN array is increased as the array now has an increased bandwidth, currently 512 MHz, see for example Fig. 3.1.

A greater number of long baselines will better resolve a point source, with shorter baselines better able to resolve diffuse, extended sources. At lower frequencies, radio interference or Radio Frequency Interference (RFI) becomes more intrusive. This RFI originates from terrestrial radio sources, such as TV transmissions, air traffic control, mobile phones, short wave, FM and digital radio signals, also unintentional radio signals from power lines, TV boosters and electronic instruments. The problems that these signals cause are illustrated in Fig. 2.7. To counter this problem, the removal of some bands may be necessary to avoid the RFI affected data, see Fig.2.8

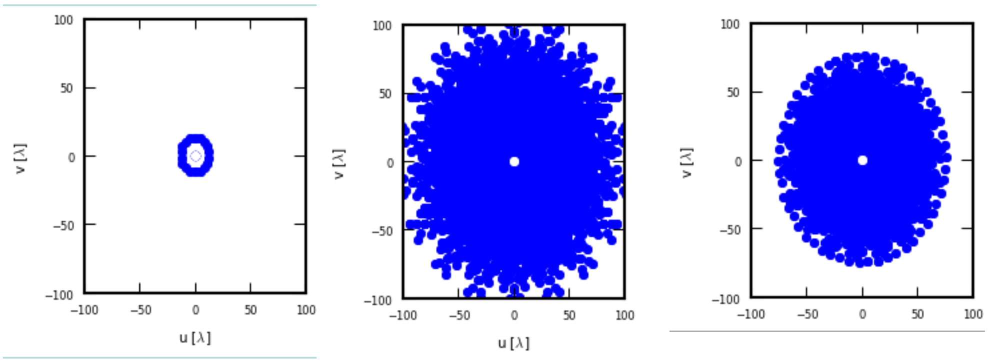

Figure 2.5: Simulated $u$-$v$ planes of 3 different arrays with Earth rotation; Left: A 2 element interferometer with a 1 km baseline. Middle panel: A 30 element array in a Y configuration with a max. 14 km diameter. Right panel: A 30 element array in a spiral configuration, 14 km baseline.

for example.

### 2.3.4 Telescope sensitivity

The minimum flux level that a telescope can detect, its point-source sensitivity ($\sigma_S$), can, for an interferometer with $n$ number of antennas, be derived from:

$$\sigma_S = \frac{\sqrt{2}kT_{sys}}{\eta_a \eta_c A\sqrt{(n_b)n_{IF}\Delta\nu\tau}} \text{ (Jy)} \tag{2.7}$$

where $[(\eta_a A)/(2k)] = G$ the antenna gain, in K Jy$^{-1}$ (antenna gain is related to the effects of elevation on the shape of the antenna), $k$ is the Boltzmann constant, $T_{sys}$ is the system noise in K, $A$ is the effective mean collecting area of the antennas in m$^2$, $\eta_a$ is aperture efficiency, $\eta_c$ is correlator efficiency, $n_b$ is the number of baselines (given by $n_b$=[$\frac{n}{2}$ $(n-1)$]), $n_{IF}$ is the number of IF's or intermediate frequency bands which make up the bandwidth, $\Delta\nu$ is the bandwidth in Hz and $\tau$ is the time on source in seconds. The point source sensitivity is indicative of the ability of a telescope to detect a source.

This difference in theoretical and achieved sensitivity for the low frequency range of the GMRT for a range of observing conditions for the GMRT, together with approximate values for the sensitivity of the e-MERLIN array, is illustrated in Table 2.1.

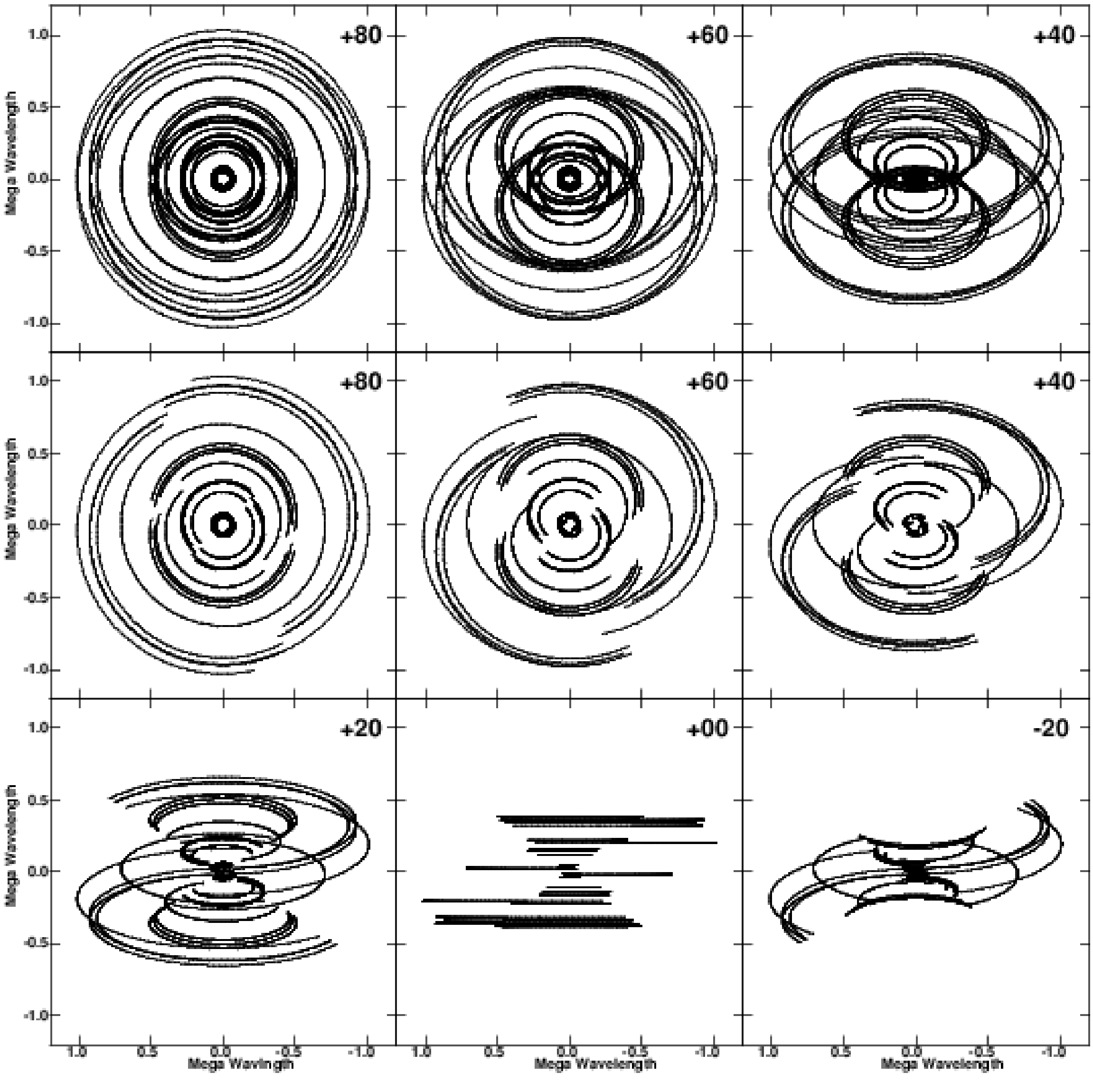

Figure 2.6: Examples of coverage of the *u*-*v* plane by the MERLIN array for 6 telescopes for a range of elevation and length of observation. Top row: ∼ 24 hours tracks for a circumpolar source. Middle row: ∼ 12 hours tracks for a circumpolar source. Bottom row: Full tracks for a low declination source. Credit: MERLIN User Handbook, 2003, http : //www.merlin.ac.uk/user_guide/.

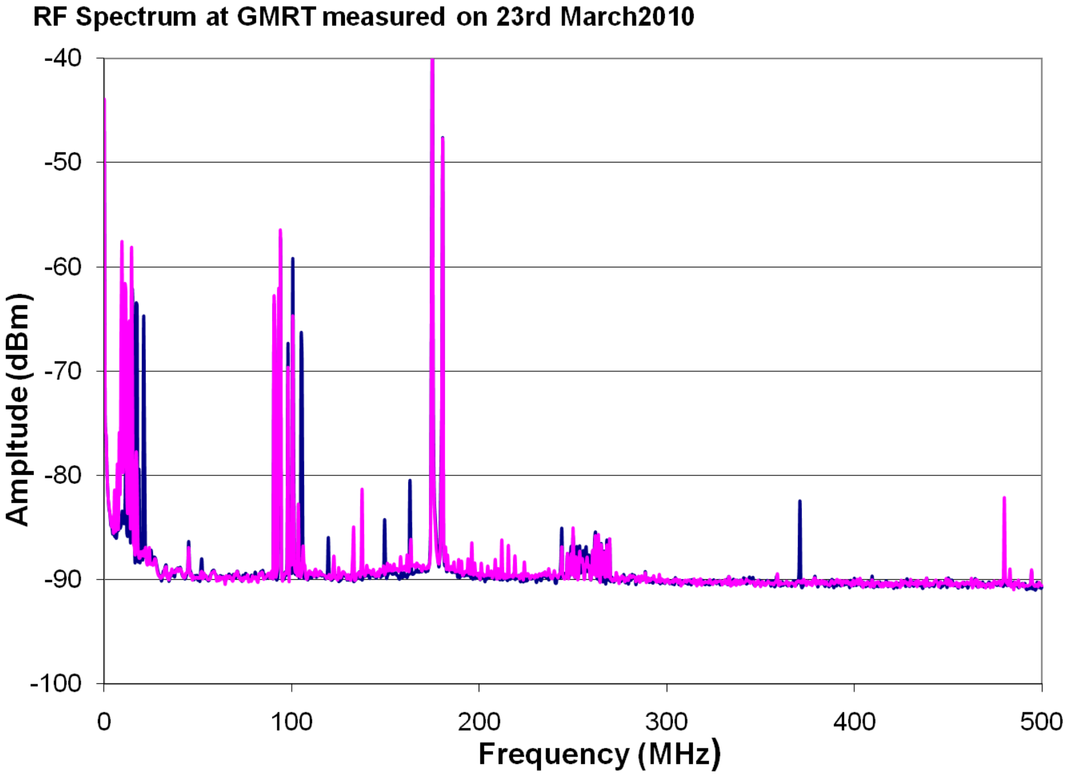

Figure 2.7: The radio spectrum of the GMRT from 0-500 MHz. The RFI peaks include 3 main peaks representing short wave and FM radio signals, police and TV signals, with satellite signals at ∼250 MHz. The blue signals are at 12.00 hr and the pink signals are 22.00 hr.
(Credit: www.astron.nl/rfi/presentations/RFI2010.session.2.1.Pravin.ppt)

Table 2.1: Comparison of theoretical sensitivity of the GMRT and e-MERLIN interferometers (best achieved values from the GMRT handbook).

| Telescope | Frequency (MHz) | Duration (hrs) | Theoretical $\sigma_S$ (mJy) |
|---|---:|---|---|
| GMRT | 610 | 1 | 0.013 |
| GMRT | 610 | 5.5 | 0.0056 |
| GMRT best achieved | 610 | | 0.02 |
| GMRT | 235 | 1 | 0.031 |
| GMRT | 235 | 5.5 | 0.013 |
| GMRT best achieved | 235 | | 0.25 |
| e-MERLIN | 5000 | 1 | 0.00035 |
| e-MERLIN | 5000 | 9 | 0.00012 |

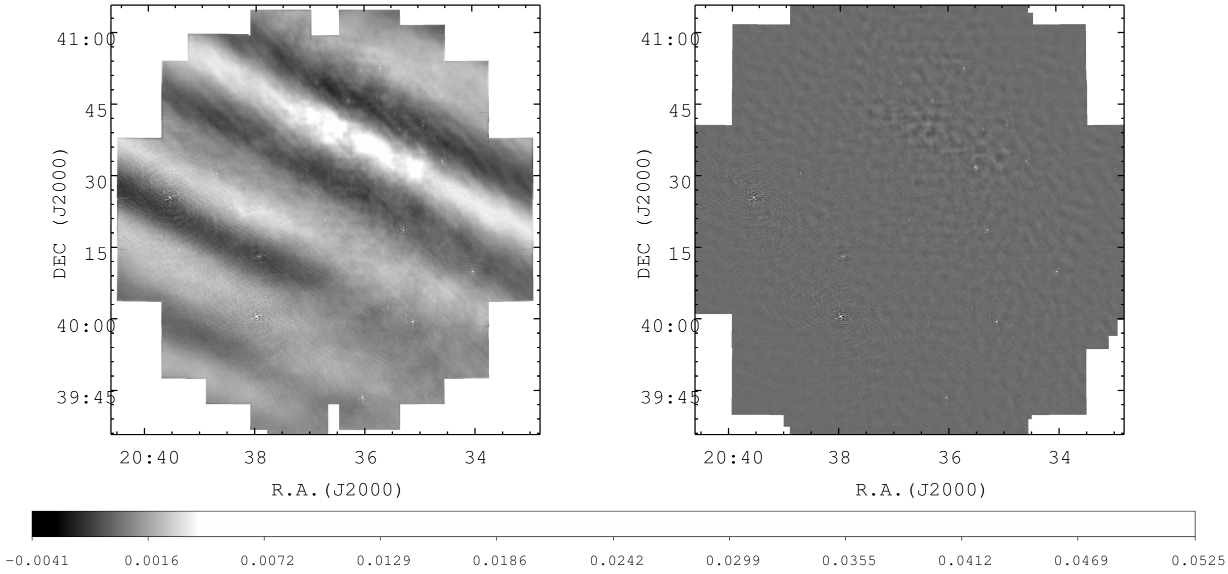

Figure 2.8: Examples of baseline removal from 610 MHz GMRT data. Top left panel: Image including all baselines, showing ‘stripes’ caused by RFI. Top right Baselines up to 1 k$\lambda$ removed. The flux scale is in Jy bm$^{-1}$

## 2.4 Current Radio Interferometers

The study of radio emission now covers the full range of radio wavelengths from millimetre to kilometre. The latest generation of radio telescopes will allow much improved imaging capability, for example the Atacama Large Millimeter Array (ALMA) (200 $\mu$m – 1 mm) in Chile, the updated Multi-Element Radio Linked Interferometer Network (e-MERLIN) (1.5 – 22 GHz) in the UK and the LOw Frequency ARray (LOFAR) in northern Netherlands. LOFAR is a low frequency array of 25 000 small dipole antennas observing at 10 – 250 MHz, with an effective diameter of about 100 km. Also the proposed Square Kilometre Array (SKA) (50 MHz – 14 GHz) to be situated in Australia and South Africa.

The characteristics of different arrays enable different science to be studied. This is illustrated in Fig. 2.9 where the sensitivity and resolution characteristics of the Jansky Very Large Array (JVLA), GMRT and e-MERLIN arrays are compared.

In Fig. 1.13 it can be seen that a study of NT emission is best directed at 0.5 to 5 GHz frequency range, where low frequency absorption is less apparent and any thermal emission is relatively low. Therefore a telescope with high sensitivity is required, i.e the GMRT. See

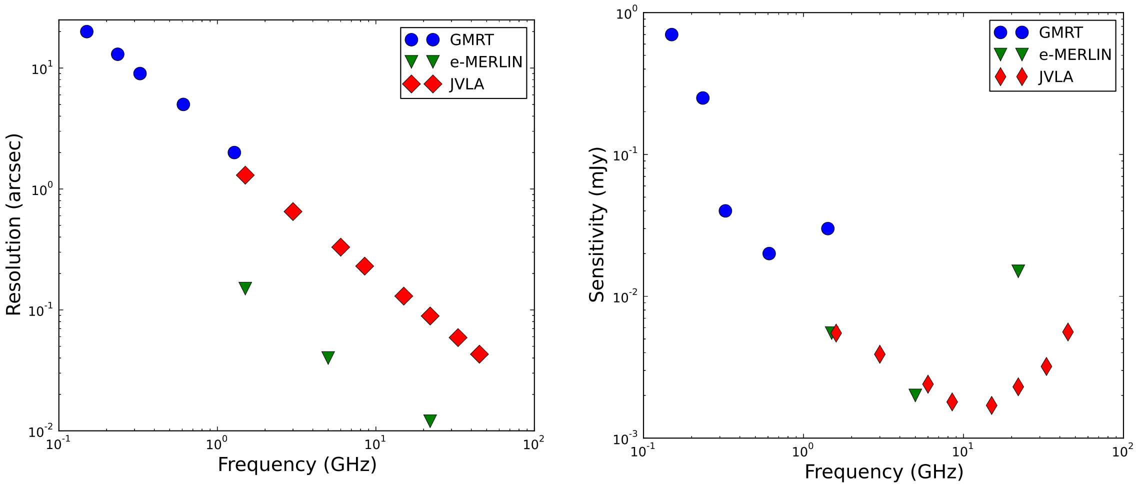

Figure 2.9: Plots revealing, left panel: the resolution and right panel: the sensitivity of the GMRT, e-MERLIN and JVLA (at the A configuration) arrays.
Credit : http : //www.e − merlin.ac.uk/tech/,
http : //www.gmrt.ncra.tifr.res.in/gmrt_hpage/Users/doc/ob s_manual.pdf,
https : //science.nrao.edu/science/meetings/presentation/JVLAcapabilities − web.pdf.

Chapter 6 for a study of NT emission observations at 0.610 and 1.28 GHz with the GMRT array.

However if the position of the turn-over of NT emission is being studied, low frequency observations will reveal where NT absorption begins to take effect. In this regard high sensitivity at low frequency is needed, i.e. the GMRT. See Chapter 4, 5 for a study searching for NT turn-overs with observations with the GMRT at 235 and 610 MHz.

The resolution of a binary source requires a telescope with a resolution and sensitivity able to reveal both sources and their separation. See Chapter 3 for a study of binary components separated by 0.65 arcsec observed at 5 GHz with the high resolution and sensitive e-MERLIN array. The GMRT and e-MERLIN arrays are described further in the next section.

### 2.4.1 The Giant Metrewave Radio Telescope

The Giant Metrewave Radio Telescope (GMRT) is situated near Pune, India at a latitude of 19.1 degrees north, longitude 74.05 degrees east and an altitude of 588 m. It consists of 30 × 45 m diameter parabolic dishes, of which 14 are arranged in a central random array of approximately 1 km, with the remaining 16 antennas arranged along three arms in a Y configuration with a maximum baseline of around 25 km, this layout is illustrated in Fig. 2.10. The dishes are constructed from light-weight stainless steel wire/ropes stretched between frames of tubular steel. This light-weight open structure reduces wind forces and does not need to contend with

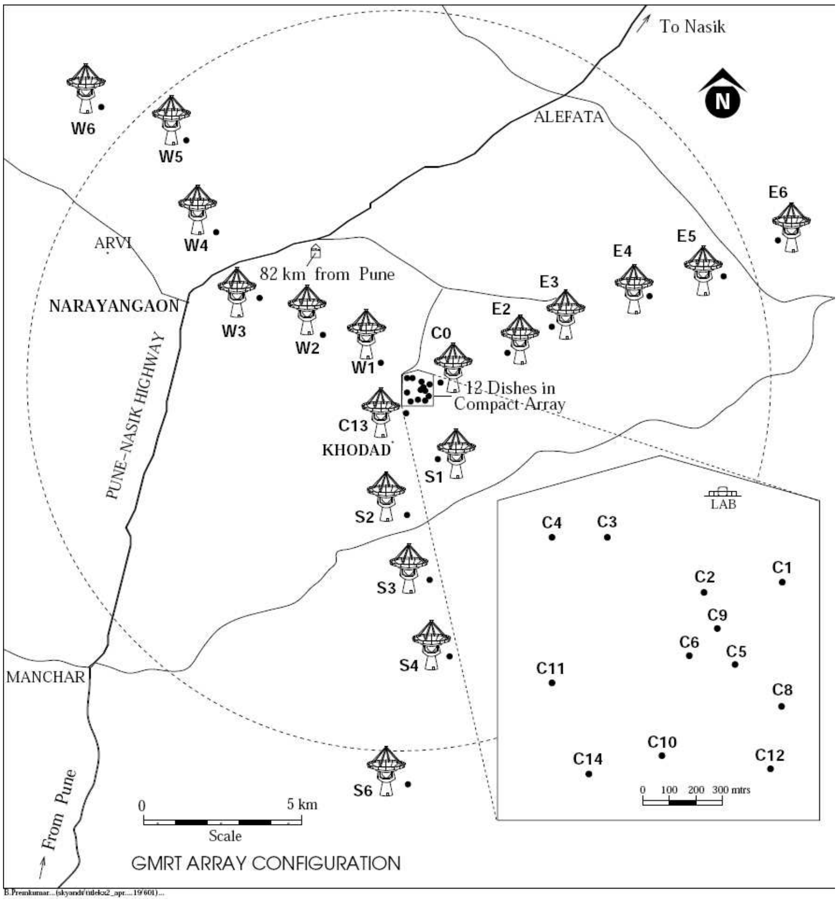

Figure 2.10: The layout of the GMRT array, near Pune, India.
Credit: http : //gmrt.ncra.tifr.res.in/gmrt_hpage/Users/Help/sys/array.html.

Table 2.2: Specifications of the Giant Meterwave Radio Telescope.

| | Frequency (MHz) | | | | |
|---|---|---|---|---|---|
| | 150 | 235 | 325 | 610 | 1420 |
| Resolution (arcsec) | ∼20 | ∼13 | ∼9 | ∼5 | ∼2 |
| Largest detectable structure (arcmin) | 68 | 44 | 32 | 17 | 7 |
| Field of view (arcmin) | 186±6 | 114±5 | 81±4 | 43±3 | $(24\pm2)\times(1400/f)$ |
| System temperature (K) | 615 | 237 | 106 | 102 | 73 |
| Antenna gain (K Jy$^{-1}$) | 0.33 | 0.33 | 0.32 | 0.32 | 0.22 |

Credit: http://www.gmrt.ncra.tifr.res.in/gmrt hpage/Users/doc/obs manual.pdf.

Figure 2.11: The GMRT antennas, illustrating the light-weight construction of the dishes.
Credit: http://ncra.tifr.res.in/ncra/for-public/picture-gallery/gmrt/gmrt-dishes/019GMRTPune.jpg.

snow fall in this area of India. This design can be seen in Fig. 2.11.

The frequency range of the GMRT is 150 to 1420 MHz, with a 32 MHz bandwidth see Table 2.2 for details of the specifications of the array. (See the GMRT website for further details: http://www.gmrt.ncra.tifr.res.in)

### 2.4.2 The Multi-Element Radio Linked Interferometer Network, e-MERLIN

The e-MERLIN array is a seven telescope interferometer situated across the middle of the UK. This array consists of a number of different telescope designs connected to a central correlator situated at the Jodrell Bank Observatory (JBO), see Fig. 2.12 which illustrates the location of the seven antennas. Four of the antennas are 25 m dishes, the Cambridge antenna is a 32 m dish, while at JBO is the 78 m Lovell Telescope with the 32×25 m Mark II. This interferometer has a maximum baseline of 217 km.

e-MERLIN array is an upgrade of the Multi-Element Radio Linked Interferometer Network. The upgrade has seen the links now made via optical-fibre, new receivers and a new correlator at

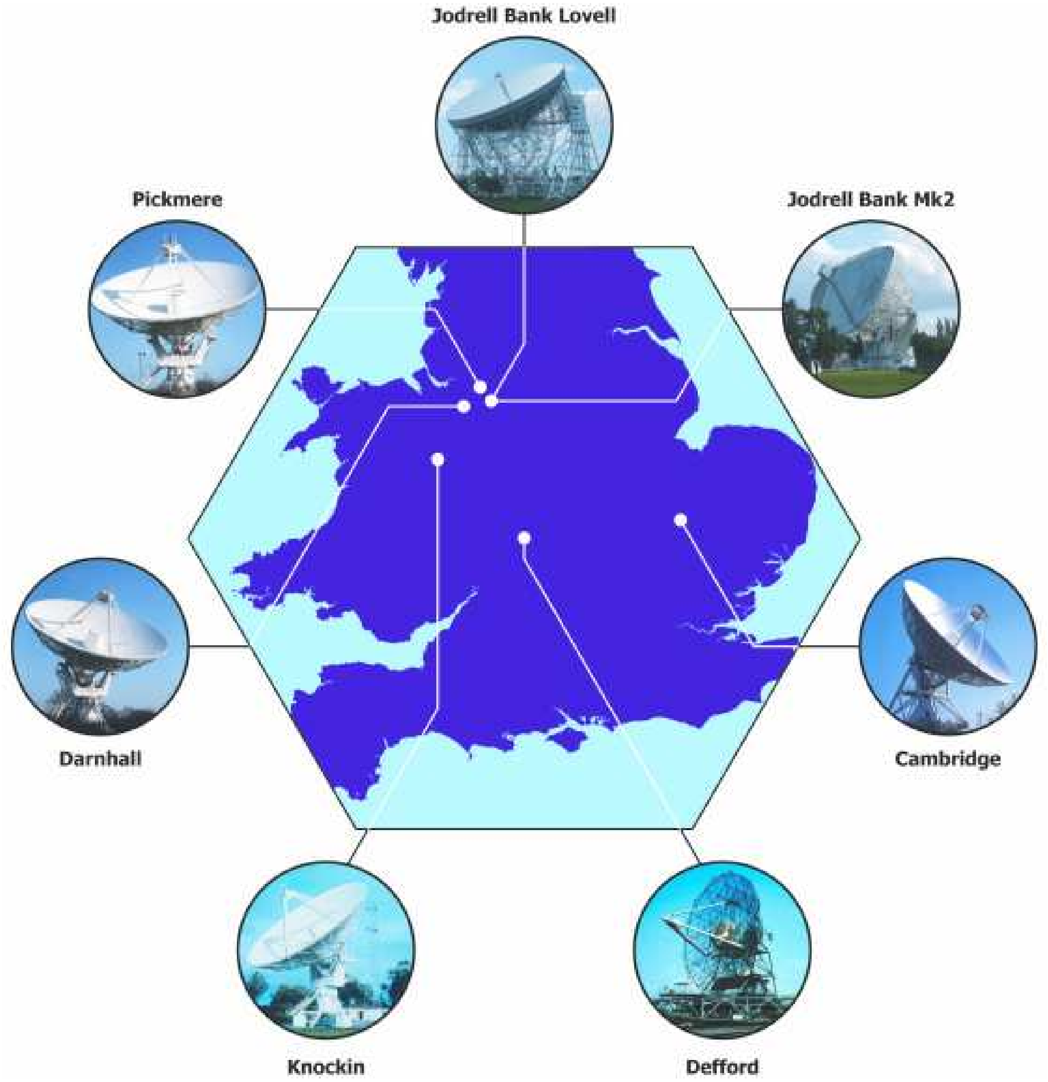

Figure 2.12: A map indicating the locations in the UK of the 7 telescopes in the e-MERLIN array. Credit: http://www.merlin.ac.uk.

JBO. This upgrade has included an increased sensitivity and bandwidth of the telescope, with further improvements planned. The telescope will, in the future observe at a frequency range of 1.5–22 GHz, see Table 2.3 for the technical capabilities of e-MERLIN post upgrade. (See the e-MERLIN website for further details and updates: http://www.e-merlin.ac.uk.)

Table 2.3: Current (February 2016) technical capabilities of the e-MERLIN array.

| Frequency | 1.5 GHz (L-band) | 5 GHz (C-band) | 22 GHz K-band) |
|---|---|---|---|
| Resolution(mas) | 150 | 40 | 12 |
| Field of view(arcmin) | 30 | 7 | 2.0 |
| Freq.range(GHz) | 1.3–1.7 | 4–8 | 22–24 |
| Bandwidth(GHz) | 0.4 | 2 | 2 |
| Sensitivity($\mu$m/bm) | 5–6 | 1.8–2.3 | $\sim$15 |
| Surface brightness sensitivity(K) | $\sim$190 | $\sim$70 | $\sim$530 |
| Astrometric performance(mas) | $\sim$2 | $\sim$ 1 | $\sim$2 |

Credit: http://www.e-merlin.ac.uk

## 2.5 Radio Data Reduction

The radio data received from the interferometer is in need of data reduction to remove as much RFI as possible and to calibrate the signals from each antenna, before finally producing an image. This process has, in this work, been completed using the NRAO Astronomical Image Processing System (aips) software package.

### 2.5.1 A History of AIPS

The development of the aips software package originated in Charlottesville, Virginia in 1978. In 1983 aips was selected as the main data reduction software for the Very Long Baseline Array (VLBA), at which time the software was expanded to cover all stages of radio calibration covering a comprehensive range of calibrating and editing functions, this now consists of over 467 operating "tasks". The software provides the operator with windows displaying text output results and a "TV window" displaying plots and images, with input commands and "help" information displayed in a terminal window (aips COOKBOOK, http://www.aips.nrao.edu/cook.html).

### 2.5.2 The sequence of data reduction

Radio data consists of the source data, the flux calibrator; a nearby bright source used usually at the beginning and end of the observation as a flux reference, and also a phase calibrator; a nearby well know source observed throughout the observation alternating with the source to record atmospheric flux variations throughout the observation otherwise known as the phase amplitude. The coverage by the array of antennas will depend on the positions of the antennas (see Fig. 2.4) and the time on source. The more antenna coverage and the longer the observation time, the greater the coverage of the *u*-*v* plane.

The process of data reduction begins with the loading of the data set into AIPS where it is indexed and listed to sort and display the contents. Initially the first and last few seconds of the data is flagged using the task QUACK to remove problems affecting the start and end of the observation scans. Next the flux density of the flux calibrator is set from known measurements using the task SETJY. The process of removing RFI from the calibrators then begins, where one method is to plot the data with AIPS function UVPLT to scan through the baselines and remove RFI with function UVFLG.

When the calibrators have been flagged, then calibration can be applied to the data to re-scale flux for the known flux calibrator at this frequency and phase variations during the observation. This is performed with function CALIB, followed by GETJY to examine the flux of the phase calibrator. Following this the function CLCAL calibrates all sources followed by a bandpass to calibrate one channel and apply it to all. The data is then examined to observe the result with task UVPLT and/or POSSM. Further flagging can then be applied if required and calibration repeated. When happy with the RFI removal/calibration, the data can be imaged using the function IMAGR. This function is a CLEAN algorithm, first devised by Högbom (1974), which assumes that the radio sky is seen as a small number of point sources or clean components, which then cleans the image by performing deconvolution on clean components from the data iterating over a number of cleaning cycles. This process of data reduction with AIPS is schematically illustrated in Fig 2.13

One further method to clean up a dirty/noisy image and reveal a point source is to remove short baselines (see Section 2.3.3) or tapering during the imaging process to smooth the background of the data. The process of tapering involves using a gaussian taper during imaging

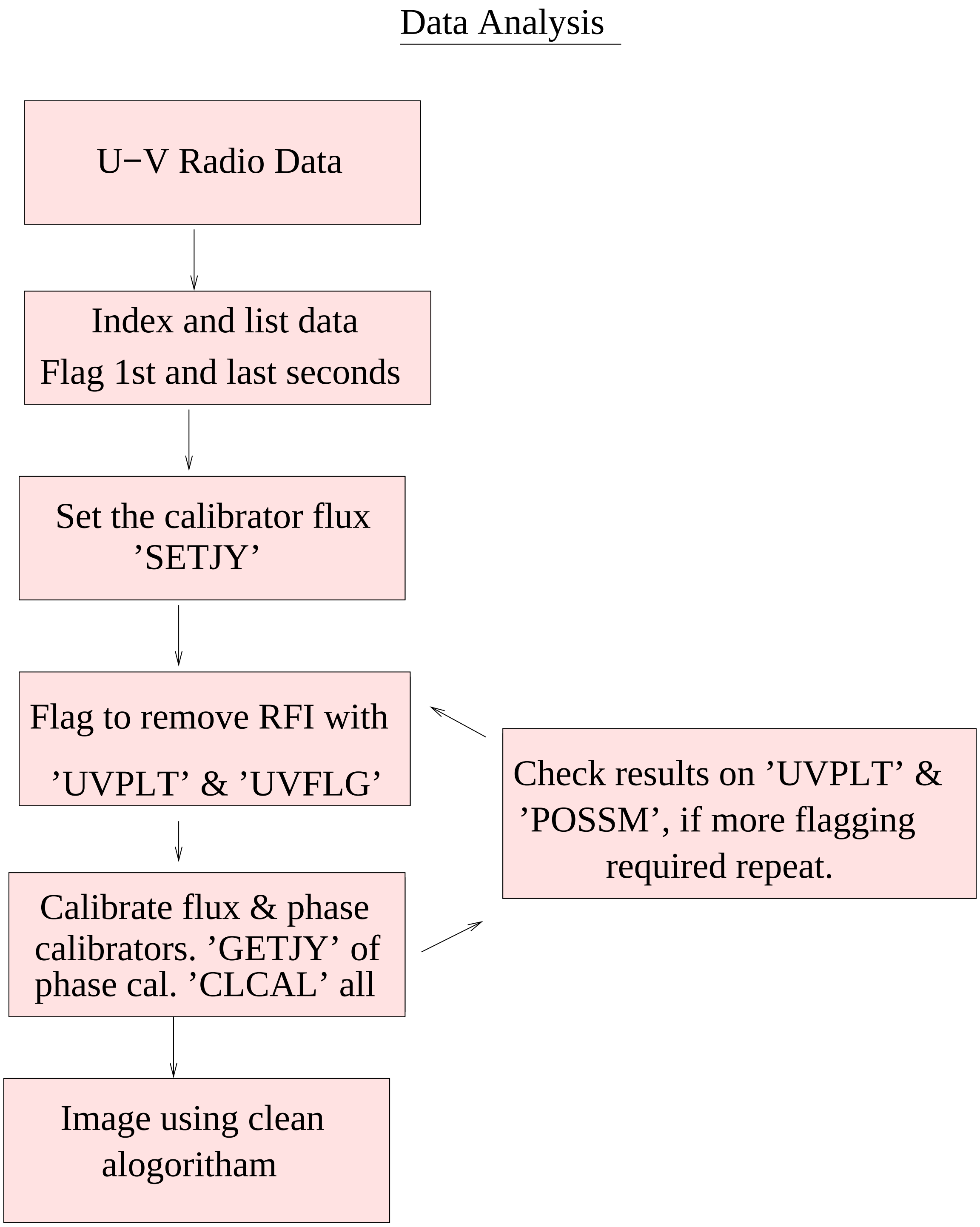

Figure 2.13: A Schematic illustrating the sequence of radio data analysis with AIPS.

to smooth these variations. The e-MERLIN array has 6 antennas, or 7 if the Lovell telescope is included, therefore removing baselines reduces the received flux considerably, so in this case tapering is the preferred method.

If enough flux is present in the source, self-calibration may be performed to improve the image, though a low flux source may not allow this process to succeed. Self-calibration involves defining ‘real’ structure in the image and using flux from this point as a model to calibrate the data, then re-imaging the data. This process can be repeated until the image quality is improved.

## 2.6 Conclusion

This chapter has given an introduction to how radio frequencies are detected and a brief history of the development of interferometers. It has included descriptions of the GMRT and e-MERLIN arrays that have been used in this research and a summary of performing radio data reduction.

The following chapters include details of research undertaken on the Wolf-Rayet colliding wind binary systems, WR 147 - see Chapters 3 and 4, and also WR 146 - see Chapter 5. In Chapter 6 there is a study of the massive runaway star BD+43° 3654 and its bow shock, with a survey of bow shocks detailed in Chapter 7.

# Chapter 3

# New Observations Of The Wolf-Rayet Colliding Wind Binary System WR 147 At 5 GHz With e-MERLIN

*"We do our best to increase the sum of human knowledge as pertains to the story of starlight."*
Annie Jump Cannon: Celestial Computer 1863-1941.

**Abstract**

We present new 5 GHz e-MERLIN observations of the important colliding wind binary WR 147. We resolve the two radio components, the Wolf-Rayet star and the colliding wind region, together with emission from the intervening 'bridge' region.

The companion O-star is not detected, enabling us to put a constraint on the mass-loss rate of the star. We derive an upper flux limit of 0.36 mJy. From this and from our estimated location of the wind collision shock, we derive a minimum O-star terminal velocity of 350 km s$^{-1}$, with a more probable 2000 km s$^{-1}$ with a mass-loss rate in the range of 0.05–1.6 $\times 10^{-6}$ $M_\odot$ yr$^{-1}$.

We discuss a mechanism to account for the puzzling 'bridge' feature located between the two stars, as being possibly due to the ionising radiation from the O-star interacting with the less ionised Wolf-Rayet stellar wind.

## 3.1 Introduction

The study of massive stars has indicated that although they are relatively low in number, they contribute significantly to their environment. Massive stars have strong winds and high mass-loss rates that re-cycle large proportions of the parent star's mass to their local inter-stellar medium (ISM). Recently confirmation has been made that many massive stars are found in binary systems (Sana et al., 2012) and it follows that the two winds from these binary companions will collide. It has been found that these collision regions are sources of non-thermal (NT) emission, suggesting particle acceleration in very energetic regions. This NT emission can be detected at radio frequencies, (see for example Dougherty et al. 2011), giving a window to study this collision region. The wind collision region of some massive colliding wind binaries has been detected, including WR 140 (Williams, 2011), HD 93129A (Benaglia et al., 2015) and Cyg OB2 No.5 (Kennedy et al., 2010).

The Wolf-Rayet (WR) binary system WR 147 is the nearest WR-star and colliding wind system to observe in the northern hemisphere, at a distance of 650 parsec (pc) (Morris et al., 2000), thus giving us the best opportunity to study such a system.

The system is composed of two radio sources; a southern, thermal radio source, the WR-star, of spectral type WN8(h), (Caillault et al., 1985; Smith et al., 1996; Morris et al., 2000). This classification is now generally accepted. The northern NT radio source is considered to be the region where the stellar winds of the component massive stars reach a momentum balance; the wind collision region (WCR).

The binary companion (an O or B star) has not been observed at radio frequencies. We can make a simple estimate of what its flux should be, using results from Wright & Barlow (1975). For an O-star with a mass-loss rate of $\dot{M}$(O)=$10^{-6}$ $M_{\odot}$ yr$^{-1}$ and a wind terminal velocity of $v_{\infty}(O)$ = 2000 km s$^{-1}$, we estimate an expected radio flux of ~0.2 mJy. We will discuss this later and provide limits on the mass-loss rate (and nature) of the companion (see Section 3.3).

The companion has been observed at infra-red (IR) wavelengths by Williams et al. (1997) who suggest the companion is a type B0.5 and also at optical wavelengths by Niemela et al. (1998), using *HST* observations, who proposed a type O8-O9 V-III. A spectral analysis has also been made by Lépine et al. (2001) who give a type O5-7 I-II(f). The IR (Williams et al., 1997) and optical (Niemela et al., 1998) classifications were from inferred magnitudes, the visual magnitude suggesting a more luminous type, however the Lépine et al. (2001) spectral study is more rigorous, though still described by the author as tentative as the O-star was only faintly detected in their study.

In their spectroscopic observations Lépine et al. (2001) detect an angular separation of the stellar components of 624 mas while the differential speckle survey by Horch et al. (2011) detects an angular separation of 644.9 mas. Making the assumption of reasonable stellar masses, and that the system was being viewed face-on and that the binary eccentricity was zero, Setia Gunawan et al. (2001) made a very rough estimate that the binary period was of order 1350 years. This estimate should be regarded as very approximate, given that the system will have some inclination, and as it is a wide binary it is very likely to be quite eccentric.

WR 147 was first resolved as two radio sources by Moran et al. (1989) who observed the system at C band (5 GHz) with the Multi-Element Radio Linked Interferometer Network (MERLIN). Observations have also been made with the Very Large Array (VLA) by Churchwell et al. (1992) at 4 frequencies (1.46, 5, 15 and 22.5 GHz) on 3 different epochs and at 8.3 GHz on 2 epochs by Contreras & Rodríguez (1999). Studies by Churchwell et al. (1992) confirmed those of Moran et al. (1989) that WR 147 is composed of two radio sources, a southern thermal source and a northern NT component, with suggestions of a 'bridge' structure between the two radio components. The WR 147 system has also been detected during X-ray observations by Skinner et al. (1999) and as an extended source by Pittard et al. (2002), with a double X-ray source observed by Zhekov & Park (2010b). WR 147 is considered a classic example of a Particle-Accelerating Colliding Wind Binary (PACWB) (De Becker & Raucq, 2013). Further MERLIN observations at C band and L band (1.6 GHz) have been made by Williams et al. (1997), which confirmed the presence of a 'bridge' structure. These data also show the northern radio source to have a shape consistent with a WCR and that the stellar wind of the southern WR-star has an apparent non-spherical appearance. The 'bridge' structure is an unexpected feature and is not consistent with colliding wind theory as the WR stellar wind is unaware of a companion until their winds collide. It is only when they do meet that the two stellar winds collide and form an interaction zone with shock fronts and a contact discontinuity where their wind momentum balance, (Luo et al., 1990; Eichler & Usov, 1993; Stevens et al., 1992).

Given that in this system both radio sources have been observed and that the companion O-star has been detected at IR and optical wavelengths this work attempts to observe both stellar binary components and the wind collision region together for the first time and detect any structure in the emission.

The ongoing upgrade of the MERLIN array, including connection by a fibre optical network, has an ultimate goal to increase the bandwidth by more than 2 orders of magnitude to 4 GHz and a sensitivity increase of 10 × to 2-15 $\mu$Jy beam$^{-1}$. The previous bandwidth of the MERLIN observations was 16 MHz.

This bandwidth is not yet fully available, but we have been able to observe WR 147 with the upgraded e-MERLIN array, with a bandwidth of 512 MHz, to investigate the structure of the WR stellar wind at this greater sensitivity, to attempt to obtain a radio detection of the O-star and to detect again any emission between the two components.

In Section 3.2 we detail our observations and data reduction methods, in Section 3.3 we show and discuss our results, and in Section 3.4 we conclude and discuss future work.

## 3.2 e-MERLIN Observations and Data Reduction

The WR 147 system was observed by the e-MERLIN array at C band on 2014 February 24 for approximately 9 hrs on source. The bandwidth was 512 MHz, with 4 frequency bands (IFs) of 128 MHz centred at 4.8165, 4.9455, 5.07245 and 5.2005 GHz. The Lovell telescope was not included in the array, the Pickmere antenna was included for only the first 7 hours and the Defford antenna was included for only the final 3.5 hours. The zero-polarization calibrator 3C84 (0319+415) was observed for approximately 1 hour at the beginning of the observation, then 3 minute scans by the phase calibrator J2007+4029 alternating with 6 minute scans of the source continued for 3 hours. The flux calibrator 3C286 (1331+305) was then scanned for 30 minutes followed by the bright point source calibrator OQ208 (1407+284, Mrk 668) for 30 minutes, after which the source and phase calibrator scans continued for another 6 hours to complete the observation. The limited extent of the $u$-$v$ plane coverage for the observation is illustrated in Fig. 3.1

Data reduction was performed initially at the University of Manchester, with assistance from the e-MERLIN team, using the Astronomical Image Processing System (AIPS). We have further analysed the data which involved recalibrating and flagging the phase calibrator. This calibration was applied to the target source with individual telescope weighting applied and used to produce the images presented in this paper. We attempted self-calibration on the source data, but this did not improve the results reliably due to the low flux levels of this source.

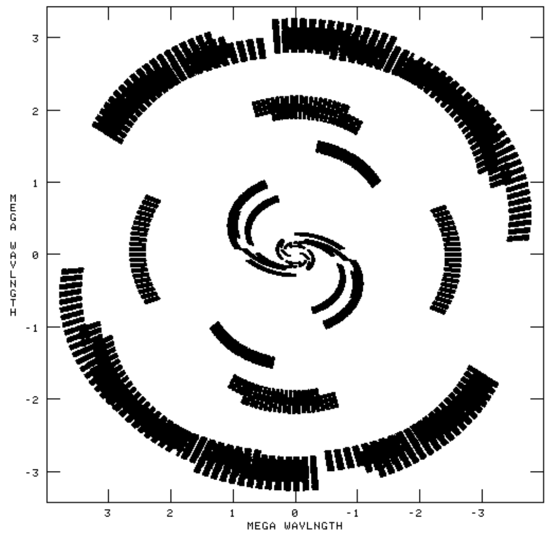

Figure 3.1: The u-v plane coverage of the six antennas used in the e-MERLIN observation. The Pickmere telescope was available for the first seven hours and the Defford telescope was available for the final three hours.

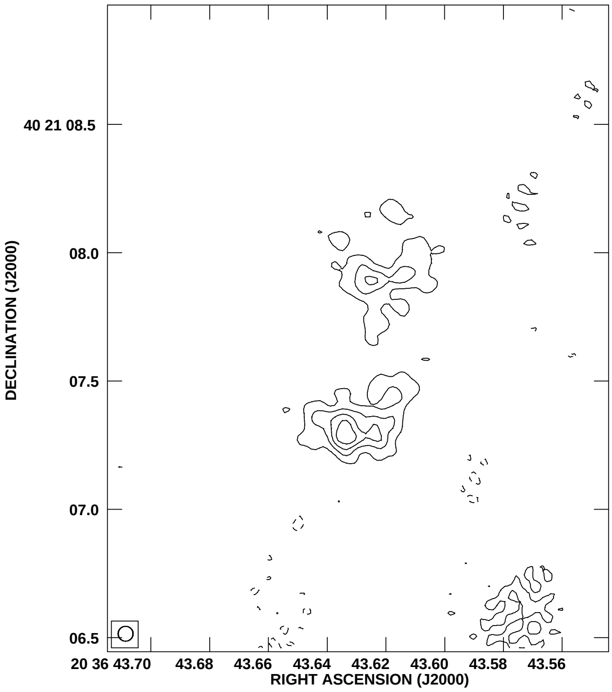

Figure 3.2: The e-MERLIN 5 GHz data of WR 147, with a $\sigma$ of 58 $\mu$Jy beam$^{-1}$ and contours at $\sigma$ × -3, 3, 6, 9, 12, 15. A simulated beam of 58×58 mas is shown in the bottom left of the image.

The images presented here were produced using the AIPS task IMAGR using natural weighting. There was no tapering applied and the restoring beam size was chosen to be $58 \times 58$ mas in order to match the previously published MERLIN images (Williams et al., 1997).

## 3.3 Results

### 3.3.1 New e-MERLIN data

These new e-MERLIN data of WR 147 are shown in Fig. 3.2. The data shown in this image has had no taper applied. The image has $\sigma = 58$ $\mu$Jy beam$^{-1}$. The contours shown are at values of $\sigma\times$ -3, 3, 6, 9, 12, 15 and with a beam size of $58 \times 58$ mas, illustrated at the bottom left corner of the image. The pixel size is 15 mas. These new results indicate a clear detection of the southern component, namely the WR-star and of the WCR which displays a clear curved, but complex shape, as seen in previous MERLIN observations. We also detect flux from the previously observed 'bridge' feature located between the two sources.

The emission from the wind of WR-star has a peak pixel at $\alpha_{J2000} =$ 20 36 43.6334, $\delta_{J2000} =$ +40 21 07.285, though it does not appear spherically symmetrical, exhibiting an elongated shape, with an alignment approximately NW to SE. The WCR shows peak pixels or hotspot at $\alpha_{J2000} =$ 20 36 43.6242, $\delta_{J2000} =$ +40 21 07.885. These peak positions are listed with positions from previous observations in Table 3.4 We have not been able to determine the spectral index across the bandwidth of this data. However, when the proposed final bandwidth of e-MERLIN is available, we should be better able to determine the spectral index of the emission.

We note that it is extremely unlikely that the northern radio source is an unrelated background object. From Giommi et al. (2006), at 5 GHz we expect around 20 sources deg$^{-2}$ for sources with a flux $S_\nu > 4$mJy, which translates to $1.5 \times 10^{-6}$ sources in a region of $1 \times 1$ arcsec. We also see that the previously detected emission below the southern component is not present.

### 3.3.2 Stellar fluxes and mass-loss rates

#### Stellar fluxes

We have measured the fluxes from three distinct regions of this system – the WR-star (the southern source), the wind collision region (WCR), (the northern source), and the 'bridge'

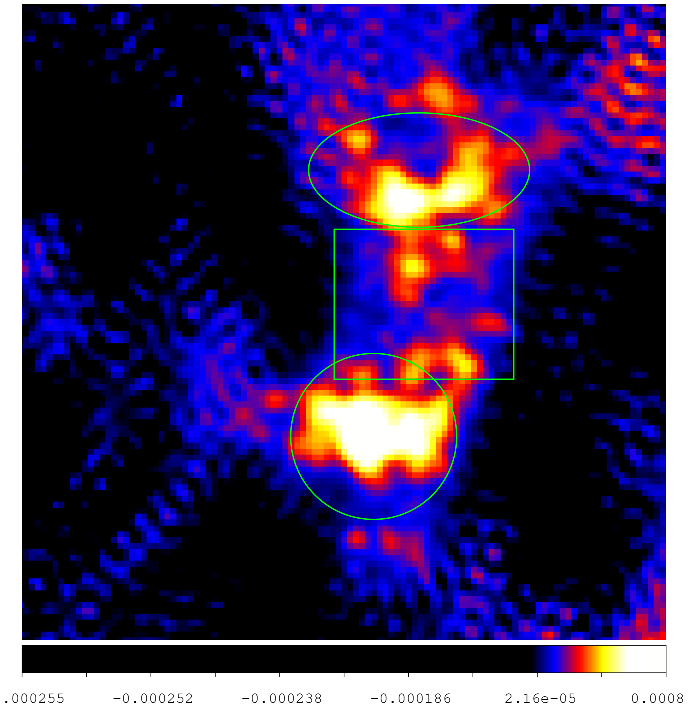

Figure 3.3: The WR 147 e-MERLIN data, with boxes illustrating the areas encompassing emission measured for each region. Top region: the WCR, Centre region: the ‘bridge’, Lower region: WR-star.

region between the two stars. These regions are illustrated in Fig. 3.3. The WCR is an ellipse centred at $\alpha_{J2000}$ = 20 36 43.622, $\delta_{J2000}$ = +40 21 07.97 with radii of 280 and 146 mas. The WR-star region was a circle centred at $\alpha_{J2000}$ = 20 36 43.632, $\delta_{J2000}$ = +40 21 07.29 with a radius of 211 mas. The ‘bridge’ region was a box centred at $\alpha_{J2000}$ = 20 36 43.621, $\delta_{J2000}$ = +40 21 07.63, of 457 by 382 mas.

The flux of the WR-star was initially measured using the AIPS IMFIT package, which fits the emission with a 2D Gaussian function, which gave a flux value of 8.1±0.6 mJy, centred at a location of $\alpha_{J2000}$ = 20 36 43.6318, $\delta_{J2000}$ = +40 21 07.308, with a major axis of 0.269±0.019 arcsec (17.96±1.27 pixels) and a minor axis of 0.149±0.0105 arcsec (9.90±0.70 pixels). The centroid of the fitted Gaussian is located slightly north-west of the peak pixel. We also measured the flux of the WR-star with the AIPS TVSTAT function, which gave a measured integrated flux of 9.1 ± 0.2 mJy. This is the preferred method used in this work.

The flux from the WCR was measured with TVSTAT. Here, the integrated flux value was 3.8± 0.1 mJy. We also measured the flux from the ‘bridge’ region between the two radio components (this region is seen in Fig. 3.3) giving an integrated flux of 4.2 ± 0.06 mJy. These values are

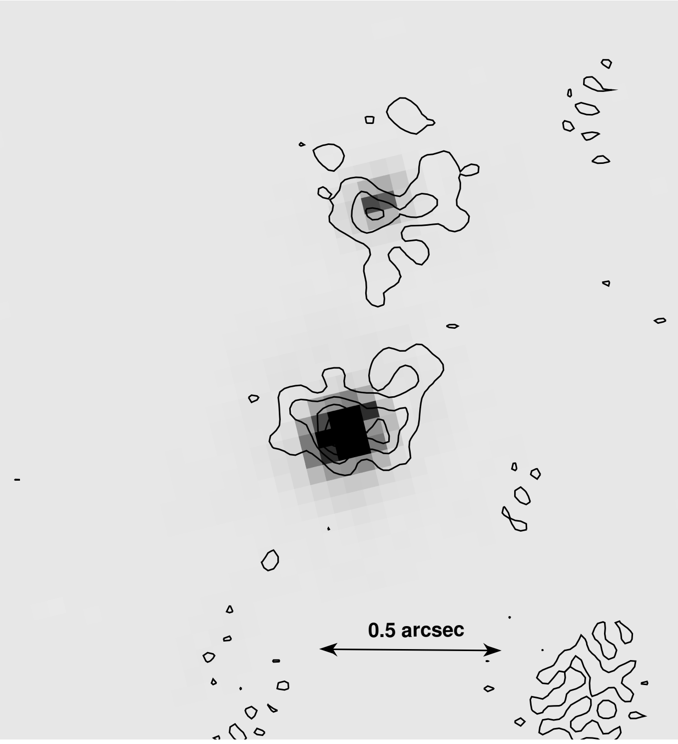

Figure 3.4: This e-MERLIN data contours overlain onto the HST data detection of both binary components, revealing the position of the O-star (Wallace, 2003).

Table 3.1: The measured e-MERLIN 5 GHz fluxes from 3 regions of the WR 147 system.

| epoch | $S_{WR}$ (mJy) | $\sigma$ | $S_{WCR}$ (mJy) | $\sigma$ | $S_{bridge}$ (mJy) | rms (mJy) | method |
|---|---|---|---|---|---|---|---|
| 2014 Feb 24 | 9.1 | 0.2 | 3.8 | 0.1 | 4.2 | 0.06 | TVSTAT |

listed in Table 3.1.

Importantly, the O-star is not clearly detected in these e-MERLIN observations. It is important to locate where the O-star is in these observations. The optical position of the O-star, with respect to the WR-star, was determined by Horch et al. (2011) in 2010, to have a separation of 0.6449 arcsec and a Position Angle (PA) of 350.2 deg. For the e-MERLIN data, the WR position was taken to be the measured Gaussian centroid of the higher flux of the southern source, at $\alpha_{J2000}$ = 20 36 43.634, $\delta_{J2000}$ = +40 21 07.29. This gave an O-star position of $\alpha_{J2000}$ = 20 36 43.624, $\delta_{J2000}$ = +40 21 07.93, within the wind collision zone, illustrated in Fig. 3.7.

We have overlaid contours of this e-MERLIN data onto the 1996 HST detection of the O-star by Wallace (2003). The centre coordinates for the HST data were corrected to the centre of the e-MERLIN data (by altering CRVAL1, CRVAL2) with the HST data having pixels of 50 mas. This overlay also reveals the position of the O-star within the wind collision zone.

At this position we detect a pixel value of 0.35 mJy beam$^{-1}$. In order to estimate the noise in the immediate vicinity of the O-star position, we measured the flux density from an area surrounding this position (approximately 350 pixels), from which we detect a flux density of 4.1 mJy with an rms of 0.12 mJy beam$^{-1}$. We therefore propose an upper flux limit for the O-star of 3 × this localised $\sigma$ of 0.36 mJy, (see De Becker & Raucq (2013); Blomme & Volpi (2014) for similar use of this method).

We can estimate the expected flux from the O-star from the seminal Wright & Barlow (1975) paper and their equation:

$$S_\nu = 23.2 \left(\frac{\dot{M}}{\mu\, v_\infty}\right)^{4/3} \frac{\nu^{2/3}}{d^2} \gamma^{2/3} g^{2/3} Z^{4/3} \text{ (Jy)} \tag{3.1}$$

where $\mu$ is the mean atomic weight of the gas, $v_\infty$ is the terminal wind velocity in km s$^{-1}$, $S_\nu$ is the thermal flux observed at frequency $\nu$ in Jy, $\nu$ is in Hz, $d$ is the distance in kpc, $Z$ is the rms charge, $\gamma$ is the ratio of the electron number density and the ion number density and $g_{ff}$ is the free-free Gaunt factor approximated by Lamers & Cassinelli (1999) as:

$$g_{ff} = 10.6 + 1.90\ \log_{10}\ T_e - 1.26\ \log_{10}\ (\nu\ Z)\,. \tag{3.2}$$

We assume the following values, $\mu = 1.27$, $Z = 1.13$, $\gamma = 1.09$, $T_e$ estimated at 10 000 K (Setia Gunawan et al., 2001). This gives a theoretical O-star flux of ~0.2 mJy.

### Mass-loss rates

We can now obtain estimates of the mass-loss rates of the WR-star, $\dot{M}$(WR) and O-star, $\dot{M}$(O), from these fluxes by rearranging eqn. 3.1:

$$\dot{M} = 0.095 \frac{\mu v_\infty S_\nu^{3/4} d^{3/2}}{Z \gamma^{1/2} g_{ff}^{1/2} \nu^{1/2}}\ (M_\odot \text{ yr}^{-1}) \tag{3.3}$$

For the WR-star the mass-loss rate, $\dot{M}$(WR), is calculated assuming a He dominated wind (singly ionised), with no allowance made for wind-clumping (which would reduce the value) and, as we are unable to detect a spectral index from the data at this bandwidth, all flux from the

Table 3.2: Published mass-loss rates of the WR-star, together with rates derived in this work and derived O-star mass-loss rates for a range of $v_\infty$, as illustrated in Fig. 3.5. Also listed is $v_\infty(O) = 2000$ km s$^{-1}$suggested by the spectral type derived by Lepine et al. (2001), with a range of corresponding $\dot{M}$(O).

| component | $v_\infty$<br>( km s$^{-1}$) | $\dot{M}$<br>( $M_\odot$ yr$^{-1}$) | ref. |
|---|---|---|---|
| WR-star | | 3.9 $\times 10^{-4}$ | Caillault et al. (1985) |
| WR-star | | 2.1 $\times$ $10^{-4}$ | Moran et al. (1989) |
| WR-star | | 4.2 $\times$ $10^{-5}$ | Churchwell et al. (1992) |
| WR-star | | 4.6 $\times$ $10^{-5}$ | Williams et al. (1997) |
| WR-star | | 1.9–4.0 $\times$ $10^{-5}$ | Skinner et al. (1999) |
| WR-star | | 1.5–3.7 $\times$ $10^{-5}$ | Morris et al. (2000) |
| WR-star | | 6.5 $\times$ $10^{-4}$ | Lépine et al. (2001) |
| WR-star | | 1.6. $\times$ $10^{-4}$ | Hamann et al. (2006) |
| WR-star | 1000 | 3.4 $\times$ $10^{-5}$ | this work |
| O-star | >350 | 3 $\times 10^{-7}$ | this work |
| O-star | 2500 | 0.04–2.0 $\times 10^{-6}$ | this work |
| O-star | 2000 | 0.05–1.6 $\times 10^{-6}$ | this work |

WR-star is assumed to be thermal. Using the above integrated flux value obtained with TVSTAT, with $\mu = 4.0$, $v_\infty(WR) = 1000$ km s$^{-1}$(Williams et al., 1997), $d = 650$ pc (Morris et al., 2000), $Z = 1.0$, $\gamma = 1.0$ and $T_e$ estimated at 9400 K (Churchwell et al., 1992), we obtain a spherically smooth $\dot{M}$(WR) = 3.4 $\times$ $10^{-5}$ $M_\odot$ yr$^{-1}$.

See Table 3.2 for a listing of previous determinations. From this table it can be seen that the two earliest values are higher, these were derived from a $v_\infty$ of 2000 km s$^{-1}$ by Caillault et al. (1985) and both assume a distance to the system on ~2 kpc. The latter two values were derived from momentum balance by Lépine et al. (2001) and from models in a larger study of WN stars by Hamann et al. (2006). The value derived in this work is comparable to the remainder which give values determined from radio flux assuming $v_\infty$ of ~1000 km s$^{-1}$ and a distance of 650 pc.

We can now also make some estimates of the O-star wind parameters, in spite of not having detected the source, by making use of the location of the WCR and the upper limit on the O-star flux. We note the uncertainty in the value of $v_\infty(O)$ in the literature, from 800 km s$^{-1}$ (Williams et al., 1997) to 2000 km s$^{-1}$ (Lépine et al., 2001).

For a colliding wind system, the location of the interaction region between the two stars is determined the the wind momentum ratio, $\eta$, given by;

$$\eta \equiv \frac{[\dot{M}(O)\ v_\infty(O)]}{[\dot{M}(WR)\ v_\infty(WR)]} \equiv \left(\frac{r(O)}{r(WR)}\right)^2 \tag{3.4}$$

where $r(O)$ is the distance from the O-star to the interaction zone and $r(WR)$ is the distance from the WR-star to the same. We acknowledge that it is reasonable to accept that both stars will have some clumping within the wind, therefore these $\dot{M}$ rates are maximum values, clumping could reduce these values by a factor of two or three. In addition, we are assuming that we are viewing the system face-on, and inclination effects will alter these results.

From these e-MERLIN data, we measure the distance from the Horch position of the O-star (as discussed earlier) to the centre of the WCR (defined as the brightest pixel in the northern source) to be $r(O) = 35.0\,\mathrm{mas}$, and $r(WR) = 609.9\,\mathrm{mas}$, and hence $\eta$=0.003 (we will return to discuss $\eta$ in Section 3.3.3).

From the upper flux limit of 0.36 mJy for the O-star and assuming cosmic abundances, we calculate an upper limit of the $\dot{M}$(O) for different values of $v_\infty(O)$ and $\eta$. We assume $\mu = 1.27$, $Z = 1.13$, $\gamma = 1.09$, and $T_e = 10^4$K (Setia Gunawan et al., 2001).

The assumed value of $\eta$ provides an estimate of the value of the quantity $\dot{M}(\mathrm{O})\, v_\infty(\mathrm{O})$ (via eqn. 3.4), while the upper limit on the detected flux from the O-star provides a limit on the value of $\dot{M}(\mathrm{O})/\, v_\infty(\mathrm{O})$ (eq. 3.3). Putting these two constraints together leads to an upper limit of $\dot{M}$(O) as a function of $v_\infty(O)$ and $\eta$ that is shown in Fig. 3.5.

Using the value of $\dot{M}$(WR) derived earlier and the quoted $v_\infty(WR)$, we can provides constraints on the O-star mass-loss rate and wind velocity. This is displayed in Fig. 3.5 for a range of $\eta$ from 0.003 to 0.03, illustrating $\dot{M}$(O) plotted against a range of $v_\infty(O)$.

For $\eta$=0.003, the constraint of non-detection, merely implies that the O-star wind velocity $v_\infty(O) > 350$ km s$^{-1}$(which is undoubtedly true). For an assumed O-star wind velocity of $v_\infty(O) = 2000$ km s$^{-1}$, a value of $\eta = 0.003$ implies an O-star mass-loss rate of $\dot{M}$(O)=$5\times10^{-8}\,M_\odot$ yr$^{-1}$, which is comfortably consistent with the non-detection of the O-star (see Fig. 3.5).

For larger values of $\eta$ (see discussion in Section 3.3), the constraint on the O-star mass-loss rate is a bit tighter, but only if the O-star wind velocity is $< 1000\,\mathrm{km\ s^{-1}}$ does it put real constraints on the O-star mass-loss rate.

Comparisons with the spectral types derived by Lépine et al. (2001) from spectral analysis,

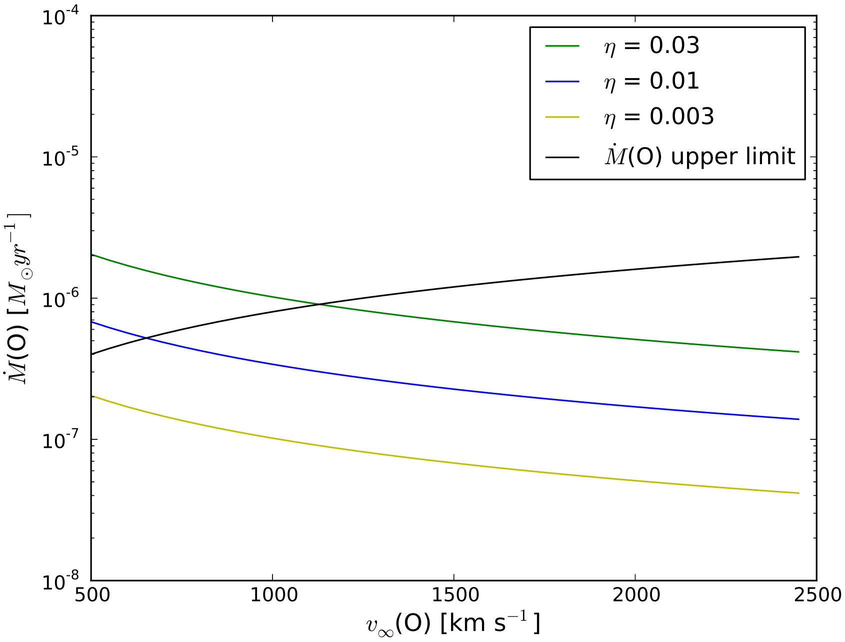

Figure 3.5: Plot of O-star $\dot{M}$ vs $v_{\infty}$ derived from the momentum flux of the system, for a range of values of $\eta$, from 0.003 to 0.03. 0.003 is measured from this data. Also plotted is the O-star $\dot{M}$ vs $v_{\infty}$ derived from the flux upper limit from the e-MERLIN data. See text for details.

suggests that the O-star, of type O5-7 I-II(f), has a $v_{\infty}(O)$ in excess of 2000 km s$^{-1}$, (Prinja et al., 1990). The conclusion from this is that these e-MERLIN observations do not put strong constraints on the wind properties of the O-star. We need better constraints on the orbit of the system in order to understand the wind collision. In the following sections, we will discuss more the system orientation, the shape and nature of the wind collision shock and the bridge feature.

### 3.3.3 System orientation and location of the wind collision region

The relative PA and separation of the two binary components (in the optical/IR) has been recorded since the first detection of the O-star in 1996 (Niemela et al., 1998). These positions are shown in Table 3.3.

Over the time-scale of these observations (both radio and optical) the orbital motion of the system may be detectable. For example, using the previously quoted separation of the stellar components and an estimated combined mass of 40 $M_{\odot}$, (O-star mass 15-20 $M_{\odot}$, Morris et al. 2000, plus a WR-star mass of 23 $M_{\odot}$, Setia Gunawan et al. 2001) assuming a circular orbit that

Table 3.3: PA and separation of the stellar binary components of WR 147. The errors included for the 2001, 2008, 2010 are systematic and may be considered a minimum error value.

| epoch | separation (arcsec) | PA (deg) | reference |
|---|---|---|---|
| 1996.145 | 0.643± 0.157 | 350±2 | Niemela et al. (1998) |
| 1996.145 | 0.64 | 352.1 | Wallace (2003) |
| 1996.405 | 0.64± 0.02 | 350.9±2 | Williams et al. (1997) |
| 2001 | 0.624±0.015 | 360.2 | Lépine et al. (2001) |
| 2001.4991 | 0.627±0.001 | 350.7±0.11 | Mason et al. (2009) |
| 2008.4589 | 0.631±0.001 | 349.4±0.11 | Mason et al. (2009) |
| 2010.471 | 0.6449±0.0006 | 350.2±0.17 | Horch et al. (2011) |

Table 3.4: Co-ordinates (J2000) of the WR 147 radio components observed at 5 GHz, with one 1.6 GHz, after Watson et al. (2002).

| epoch | WR-star | | WCR | |
|---|---|---|---|---|
| | RA (h m s) | Dec (◦ ’ ”) | RA (h m s) | Dec (◦ ’ ”) |
| 1992 Jun 24 | 20 36 43.635 | +40 21 07.45 | 20 36 43.633 | +40 21 07.99 |
| 1993 Apr 11 (1.6GHz) | 20 36 43.638 | +40 21 07.40 | 20 36 43.629 | +40 21 08.02 |
| 1995 Apl 29 | 20 36 43.634 | +40 21 07.43 | 20 36 43.624 | +40 21 07.98 |
| 1998 Dec 05 | 20 36 43.635 | +40 21 07.41 | 20 36 43.631 | +40 21 07.93 |
| 2014 Feb 24 | 20 36 43.633 | +40 21 07.29 | 20 36 43.624 | +40 21 07.89 |

is in the plane of the sky, an orbital period of ∼1360 yr is obtained. With this orbital period an approximate 5° change in the PA would occur during time period (∼ 20 yr), which should be visible in the data. However, in the optical data in Table 3.3 there does not appear to be any discernible trend, within the errors. This perhaps implies that the system may well have a longer orbital period.

Next we consider the situation regarding the radio data. The positional information from radio data of the WCR and the WR-star is listed in Table 3.4 and an overlay of the e-MERLIN data from 2014 (shown as contours) on the MERLIN 1992 data is shown in Fig. 3.6. The data in this image is separated by 21.672 yrs and some trends are apparent.

In the figure the peak pixels of the WCR and the WR-star are joined by lines in each data set. If these lines can be assumed to be lines joining the two stars, the angle between the two

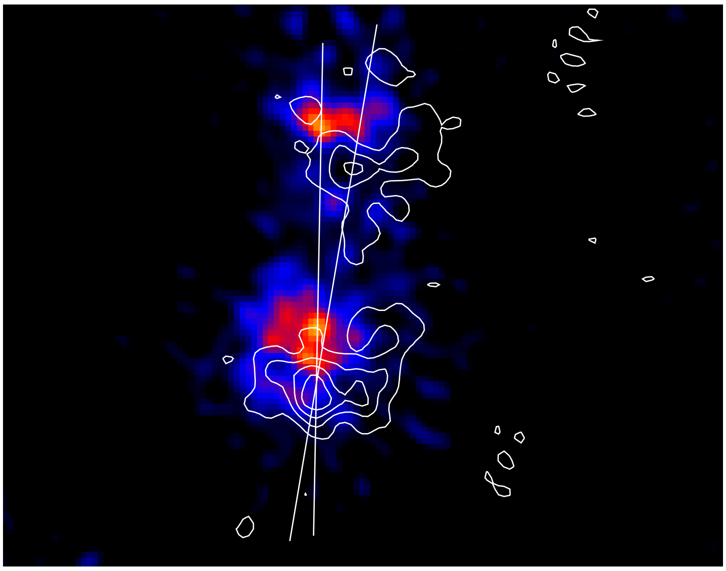

Figure 3.6: The 1992 MERLIN data overlaid with the 2014 e-MERLIN contours (levels as Fig.2). Also shown are lines connecting the peaks of the northern and southern components of each data set, suggesting possible orbital motion. See text for details.

lines is 8.5°. Such a large motion seems to be at odds with the optical constraints discussed above. It is much more likely to be due to intrinsic variations in the collision zone rather than genuine orbital motion.

In addition, the peak pixels of the two radio components can also be seen in Fig. 3.6 to have moved between the 1992–2014 time-frame. The peak pixels of the WR-star are displaced by 185 mas, which at a distance of 650 pc corresponds to a velocity in the plane of the sky of ~26 km s$^{-1}$. This is only the apparent velocity on the plane of the sky, but such a velocity is unremarkable for massive stars, for example, compared with the known runaway star BD+43° 3654, which has an apparent velocity on the plane of sky of 40 km s$^{-1}$.

It is clear that proper account of the proper motion of the system will be needed before any orbital motion can be reliably detected at radio wavelengths.

As previously mentioned there is no emission detected from the northern O-star, but its position may be inferred from the shape of the WCR and the latest known position of the O-star, (Horch et al., 2011), this is indicated with a white cross on Fig. 3.7.

In order to compare the shape of the NT emission from the WCR with a theorised interaction zone, we have constructed a model of this wind interaction zone, (see also modelling by Contreras & Rodríguez 1999). The two wind interaction model of Canto et al. (1996) obtains solutions for

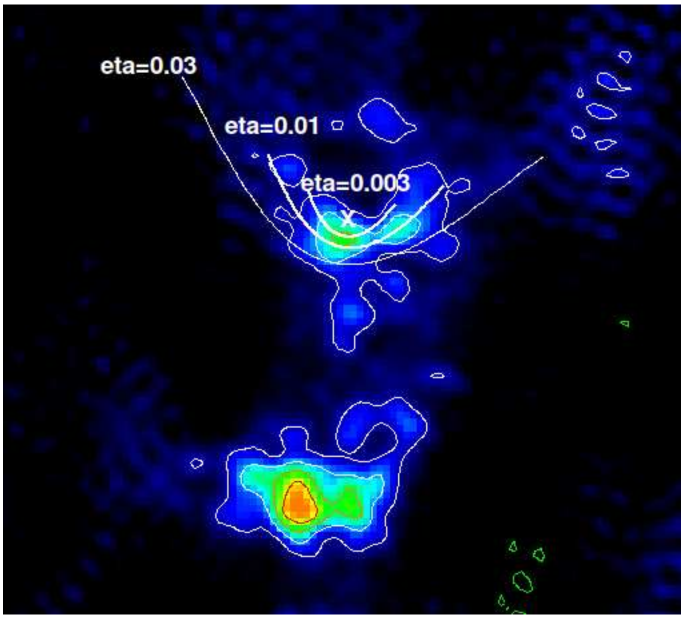

Figure 3.7: The Cantó wind-wind interaction model added to the e-MERLIN data, contour levels are as Fig.3.2. The O-star position as given by Horch et al. (2011) is indicated by a white cross with interaction zones shown with $\eta$=0.03, 0.01, 0.003. (See text for details.).

the position of the collision zone of two interacting winds.

We assume an inclination of 0° and use the Horch et al. (2011) PA and separation to locate the O-star. From the e-MERLIN data, given the locations of the O-star and the WR-star, if we identify the peak pixel in the WCR as being the location of the wind-wind interface, this leads to a value of $r_O(\theta = 0) = 35\,\mathrm{mas}$. We obtain a corresponding value of $\eta$ from Canto et al. (1996):

$$r_O = \frac{\eta^{1/2} D}{1 + \eta^{1/2}} \tag{3.5}$$

of 0.003. Having defined a value of $\eta$, then the shape of the wind collision zone is unambiguously (and numerically) determined by the solution of Canto et al. (1996) Eq.23 for the radius, $r_O(\theta)$:

$$r_O(\theta) = D \ \sin \ \theta_1 \ \csc \ (\theta + \theta_1) \tag{3.6}$$

for the angle $\theta_1$, their Eq.24:

$$\theta_1 \cot \, \theta_1 = 1 + \eta(\theta \cot \, \theta - 1), \tag{3.7}$$

where $D$ is the angular separation between the two stellar components, $\theta$ and $\theta_1$ are angles from the line of centres to the location on the interaction zone for the O-star and WR-star respectively (see Fig. 3.8).

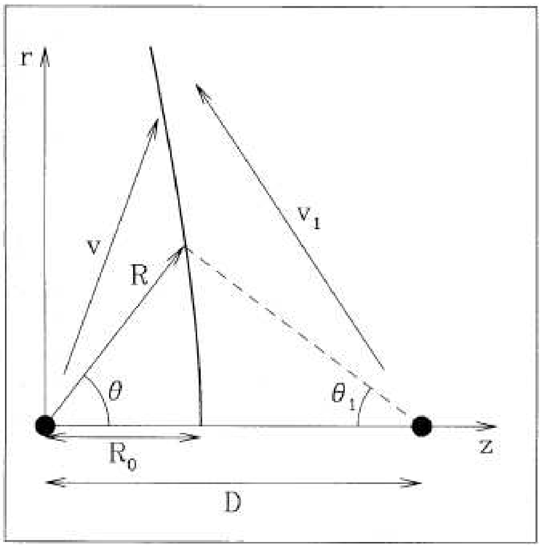

Figure 3.8: Sketch of a two wind interaction, where the two massive stars are indicated by dots, their separation and distance to the wind interaction zone is along the $x$ axis, from Canto et al. (1996).

Here we shall assume that the angular binary separation $D = 644.9\,\mathrm{mas}$ (Horch et al., 2011) and obtain $\theta$ from the approximation of by Canto et al. (1996) Eq.26

$$\theta_1 \approx \left\{\frac{15}{2}\left[-1+\sqrt{1+\frac{4}{5}\,\eta(1-\theta\ \cot\ \theta)}\right]\right\}^{1/2} \tag{3.8}$$

valid for low values of $\eta$ (Canto et al., 1996).

The position of this modelled interaction zone can be seen overlain onto the e-MERLIN data in Fig. 3.7. On this figure we also include interaction models for $\eta$=0.01 ($r_O$=60 mas) and $\eta$=0.03 ($r_O$=90 mas). This figure displays the e-MERLIN data with the same contours as Fig. 3.2 (Fig. 3.7 was compiled using GAIA [1] ).

These model interaction zones do not clarify where the contact discontinuity lies, although the WCR peak flux appears near the apex of the interaction model. We note that modelling of this interaction zone by Dougherty et al. (2003) showed that the large extent of the WCR seen in theoretical intensity distributions, diminishes to just a small spot at the apex where the brightest emission is, see their Fig. 17. See also modelling of another colliding wind binary, HD 93129A, by Benaglia et al. (2015), who also study the WCR and momentum balance for a range on $\eta$ values.

---

[1] Graphical Astronomy and Image Analysis tool, part of the Starlink software project, http : //starlink.jach.hawaii.edu/starlink.

This modelling illustrates that the WCR of WR 147 is complex and a simple Cantó model is a poor representation of the region.

### 3.3.4 Archive MERLIN data

Observations at 5 GHz of WR 147 have previously been undertaken with the MERLIN array. The first was by Moran et al. (1989), subsequently observations by Williams et al. (1997) in 1992 and a multiple epoch study by Watson et al. (2002) in 1995 and 1998. The 1992, 1995 and 1998 data are available in the MERLIN archive and are shown in Fig.3.9 together with the e-MERLIN data, (using DS9, Joye & Mandel 2003). The 'bridge' feature between the two radio components is apparent in all the data, this feature is discussed further in the Section 3.3.5.

### 3.3.5 The bridge

In the e-MERLIN data the region between the two radio sources does reveal connecting emission which confirms previous observations that suggest the existence of a 'bridge', see Fig.3.9. This emission is not easily explained as it is in the region of the WR stellar wind and is not connected to the shocked region. If this emission originates from clumps in the WR wind, the flow could be detected. The wind flow time from the WR to the O-star can be deduced from the separation; assuming an orbit in the plane of the sky, a separation of 644.9 mas (Horch et al. 2011 at a distance of 650 pc (Williams et al., 1997) which corresponds to a minimum separation, $D$, of $\sim$ 420 AU and $v_\infty$= 1-2000 km s$^{-1}$ (Williams et al., 1997). This gives a wind flow time of $\sim$1-2 yrs. As there have been observations of a 'bridge' structure from 1992 by Williams et al. (1997) to 2014, this emission cannot be one large clump, moving in the wind, but must be a constant and persistent feature.

In the INT/WFC Photometric H$\alpha$ Survey of the Northern Galactic Plane (IPHAS Drew et al. (2005)) WR 147 is a point source with low background emission. This is near the Cygnus OB2 star forming region, but WR 147 is positioned in a region of low diffuse emission. This suggests that the bridge is unlikely to be background emission and must be associated with the binary system. The possibility of an optical effect creating the 'bridge' is unlikely as this would produce emission elsewhere, other than the region adjoining the two component stars.

It may be that the emission is from material in the WR stellar wind that is partly un-ionised,

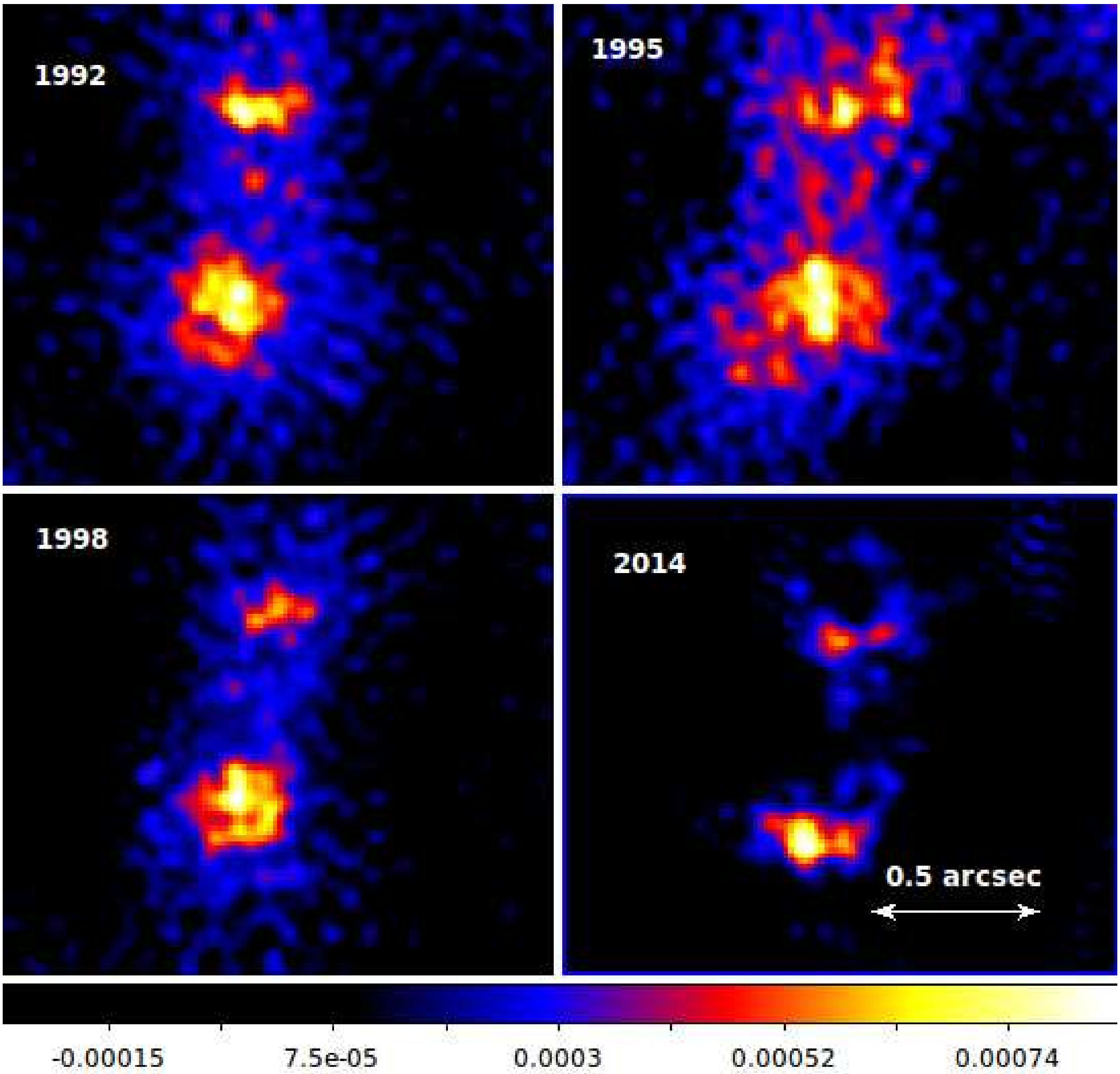

Figure 3.9: Archive 5 GHz MERLIN data from 1992 to 1998 and 2014 e-MERLIN data revealing emission from a ‘bridge’ feature in all data. Co-ordinates and flux scales (Jy) are matched, see text for details.

which is then ionised by the O-star. To test this hypothesis we have studied the ionisation spheres around both stellar components.

The WR-star is known to have a hydrogen (H) depleted wind of ~9 per cent H to 91 per cent helium (He), by mass, with cosmic abundances of other elements, and spectroscopic studies reveal the wind has singly ionised He (Morris et al., 2000; van der Hucht, 2001).

In order to analyse the ionisation properties of the O-star we have modelled the region between the two binary components using the CLOUDY spectral synthesis code, (Ferland et al., 2013). Initially we created a density table to simulate the WR wind, using a density law where the wind density, $\rho = \dot{M}/(4\pi v_\infty \mu D^2)$, where $\mu$ is the atomic mass unit and $D$ is the separation of the binary components. To obtain an appropriate density profile for the WR-star we used the following parameters: $\dot{M}$(WR) deduced above of 3.4 $\times 10^{-5}$ $M_\odot$ yr$^{-1}$; $v_\infty(WR)$ of 1000 km s$^{-1}$(Williams et al., 1997); $D$ ~420 AU, as before.

This density table was then added to the CLOUDY input file, together with an O-star black body temperature of 28 500 K, (Crowther et al., 1995) and luminosity of $10^{39}$ erg s$^{-1}$, (derived from an $\dot{M}(O)$ of $10^{-6}$ $M_\odot$ yr$^{-1}$and the relationship of Howarth & Prinja (1989)), thus giving an O-star stellar radius of 1.5 $\times 10^{12}$ cm. We assume Solar elemental abundances with all but H scaled by 30 to replicate H depletion.

The results of this CLOUDY simulation are displayed in Fig. 3.10. In this figure the top plot displays the WR stellar wind density that was stipulated by the density table, together with the electron density, the electron temperature ($T_e$) is shown in the centre plot and the lower plot displays the helium ionisation states as a ratio to hydrogen. All plots are shown against distance from the O-star. These results show that the O-star is able to fully ionise He to 1.5 $\times 10^{15}$ cm (~100 AU from the O-star, which is just past the WCR) and is able to singly ionise He up to the WR-star, see Fig. 3.10.

These results (with these parameters) suggests that there is a possibility that the O-star could be ionising He between the two binary components and creating the emission that is detected as a ‘bridge’.

Varying the input parameters to CLOUDY alters the positions of the He ionisation boundary. Such variations imply that this simple model would benefit from detailed modelling to understand the fine detail of what may be occurring within this ‘bridge’ region.

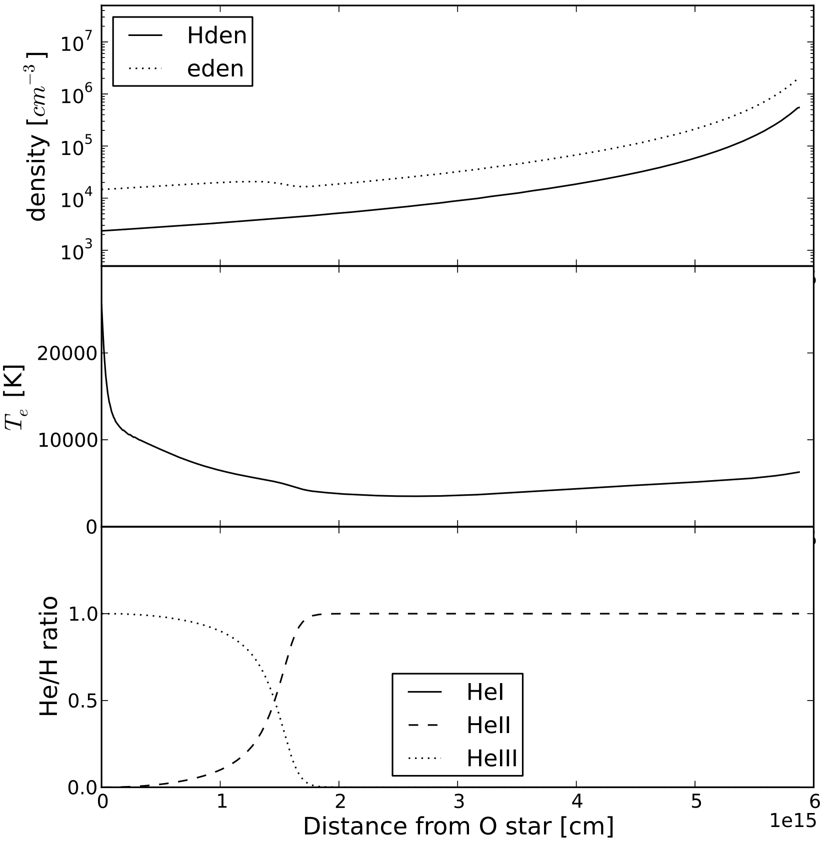

Figure 3.10: The ionisation structure of the O-star wind as modelled with the CLOUDY simulation. All plots describe conditions from the O-star at distance 0, to the WR-star at approximately 6 $\times 10^{15}$ cm. Top frame: the density profile added to the input file and the electron density, 2nd frame: Electron temperature ($T_e$) profile, 3rd frame:He ionisation structure, illustrating where fully ionised He becomes singly ionised, occurring at around $1.5 \times 10^{15}$ cm.

## 3.4 Conclusion

The new e-MERLIN observation has revealed the WR-star that has an apparent irregular structure. We measure a WR flux of 9.1 ±0.2 mJy and derive a $\dot{M}$ of $3.4 \times 10^{-5}$ $M_{\odot}$ yr$^{-1}$. We did not detect the O-star in the data, but have proposed an upper flux limit of 0.36 mJy for the O-star and derive an upper limit for the O-star $\dot{M}$ for a range of $v_{\infty}$. A probable $v_{\infty}(O)$ for the Lépine et al. (2001) spectral type of O5-7 I-II(f) is 2000 km s$^{-1}$(Prinja et al., 1990) which corresponds to a $\dot{M}$ range of 0.05 to $1.6 \times 10^{-6}$ $M_{\odot}$ yr$^{-1}$.

Modelling the interaction zone and comparing with the e-MERLIN data suggests that the position of the interaction zone and value of $\eta$ is difficult. Untangling the orbital motion, possible inclination or any possible proper motion, (Dzib & Rodríguez, 2009), will entail further detailed study.

The e-MERLIN data also reveals the ‘bridge’ emission between the two radio sources. We propose one mechanism to account for this emission, that the ionising radiation from the O-star may be interacting with the WR wind and increasing the ionisation of He within it.

Although these e-MERLIN observations have a significantly broader bandwidth than earlier MERLIN observations, there are still some major uncertainties in understanding this key colliding wind system. We have not been able to identify the position of the O-star in these radio observations and also the uncertainties in the optical position of the O-star means that we have very limited knowledge of the orbit (i.e. period, eccentricity, inclination). This makes locating the wind-wind collision zone (and determining the appropriate values of $\eta$) very difficult, and limits what we can learn about the wind collision.

Further observations will be very important. Ongoing optical observations have the possibility of beginning to detect orbital motion of the system, and in future e-MERLIN will have a 2 GHz bandwidth. This will will improve the sensitivity further and enable the study of the evolution of the wind-wind collision region (and perhaps see evidence of instabilities in the wind-wind collision region) and possibly detect the O-star at radio wavelengths.

Further work will involve further analysis of the positional and orbital status of the system, together with more detailed modelling of the ionisation states of both stellar winds.

# Chapter 4

# Low-Frequency GMRT Observations Of Massive Stars I: The Wolf-Rayet Colliding Wind Binary System - WR 147

*"A straight line can readily be drawn among each of the two series of points corresponding to maxima and minima, thus showing that there is a simple relation between the brightness of the variables and their periods."* Henrietta Swan Leavitt, 1868-1921.

**Abstract**

We present results from simultaneous low-frequency GMRT observations, at 235 MHz and 610 MHz, of the key colliding wind system WR 147. WR 147 is strongly detected at 610 MHz, but is not detected at 235 MHz, indicative of a strong turn-down at low-frequency.

We model the low-frequency radio emission using simple synchrotron plus free-free absorption models. We find that a single component model is unable to fit the data, but that a two component model is better able to fit the data. We discuss the low-frequency turn-over of the spectrum of this star in terms of the expected free-free absorption and find evidence for substantial clumping in the wind of WR-star.

We also discuss these results in the light of more complex synchrotron emission models, based on numerical hydrodynamic simulations of colliding winds and including a range of absorption mechanisms. These multi-component models can reproduce the general shape of the low-frequency spectrum of WR 147.

We conclude by discussing the importance of low-frequency observations of massive stars in constraining the energetics and structure of colliding winds.

## 4.1 Introduction

Massive stars have dense, ionised stellar winds, with high mass-loss rates ($\dot{M}$) of $\sim 10^{-7}$ to $10^{-4}$ $M_\odot$ yr$^{-1}$and terminal wind velocities ($v_\infty$) of ~500-3000 km s$^{-1}$. Emission from these energetic winds is seen at radio frequencies as thermal and/or non-thermal (NT) emission. Many massive stars are in binary systems and the wind-wind collision is an important component at many wavelengths (see the review by De Becker, 2007).

The thermal radio emission from massive stars comes from free-free emission from the ionised stellar wind. This emission has a positive spectral index, i.e. $\alpha \sim +0.6$, where $S_\nu \propto \nu^\alpha$, (Wright & Barlow, 1975). The NT emission is thought to originate from synchrotron emission from electrons accelerated by shocks either within the wind or from the wind-wind collision and is seen to have a flat or negative spectral index (De Becker, 2007). The presence of NT emission is, therefore, indicative of the presence of highly accelerated particles and of a magnetic field in the emission region.

Very few observations exist of massive stars at frequencies below 1.4 GHz (see the review by Benaglia, 2010). Thermal emission will generally be harder to detect at lower frequencies (as $\alpha > 0$), while detection of NT emission is more likely. However, we expect that the NT spectrum, rising towards lower frequencies, will eventually turn-over due to free-free absorption and possibly other effects (Pittard et al., 2006). The spectral location of this turn-over is largely unknown and will vary from star to star and will potentially provide important insights into the emission and absorption processes in stellar winds (i.e. location within the wind etc.).

In a binary system where the NT emission comes from the wind-wind collision, if the orbital period is short (say, a few days) then the NT production region will be sufficiently buried by the overlying wind that free-free absorption will be strong and the result is a turn-over at higher frequencies (probably$>$ 1 GHz). However, if the period is longer (years to many years), then free-free absorption becomes increasingly weak and other absorption mechanisms may come into play, such as Synchrotron Self Absorption (SSA); caused when the source brightness approaches the kinetic temperature of the relativistic electrons, or the Razin effect; which occurs in the presence of a thermal plasma with a correspondingly lower refractive index suppressing synchrotron radiation. Both of these mechanisms absorb emission at low-frequency. Inverse Compton (IC) processes affect the radio spectra at higher frequencies (Pittard et al., 2006; Dougherty et al., 2003).

Fitting the broadband radio spectra of massive stars like WR 147, is necessary to understand the emission processes going on in the system. As is evident from the work of Skinner et al. (1999), the low-frequency portion of the spectrum is key to constraining in the emission models.

We have undertaken a series of observations at low-frequency of several massive OB/Wolf-Rayet (WR) stars which are known NT emitters. WR 147 is the first of these to be analysed. A subsequent paper will include results of the WR binary WR146. In this paper we present low-frequency radio observations of WR 147 with the Giant Metrewave Radio Telescope (GMRT) to investigate the emission processes in this key colliding wind system. In Section 4.2 we detail the WR 147 system, in Section 4.3 we present our new GMRT observations of WR 147. In Section 4.4 we discuss the Spectral Energy Distribution (SED) of WR 147 and in Section 4.5 we present results of our spectral fitting. In Section 4.6 we discuss the consequences of our findings on the energetics of colliding wind systems and conclude in Section 4.7.

## 4.2 The WR 147 System

### 4.2.1 The components of WR 147

The WR 147 binary system consists of a WN8 type WR-star and an OB type companion. The nature of the system has been extensively discussed in Williams et al. (1997), Setia Gunawan et al. (2001), Pittard et al. (2006) and Skinner et al. (1999).

At radio wavelengths, the system was resolved into two components by Moran et al. (1989) using the *MERLIN* array. The southern radio component WR147S, associated with the WR-star and the northern radio component WR147N, thought to be the colliding wind region (CWR), with the OB star situated just to the north of WR147N (Williams et al., 1997; Niemela et al., 1998). The separation between the two stellar components has been estimated as 624 mas by Lépine et al. (2001) and around 645 mas by Horch et al. (2011). The system is at an assumed distance of $650(+130, -110)$ pc, (Morris et al., 2000). If we assume that the system is to be face-on (and an inclination of $i = 0°$) and to have a circular orbit, then for reasonable stellar masses, the binary period is around 1350 years, (Setia Gunawan et al., 2001). If, as is highly likely, the system has an eccentric orbit then the true period could be quite different from this.

The spectral type of the WR component was given as WN8(h) by Caillault et al. (1985) and Smith et al. (1996) and this is now generally accepted. The OB star was classified as B0.5V by Williams et al. (1997), later classifications include O8-O9 V-III (Niemela et al., 1998) and O5-7 I-II(f), (Lépine et al., 2001), indicating that there is considerable uncertainty in this case.

Skinner et al. (1999) studied WR 147 at radio and X-ray wavelengths. At radio wavelengths, Skinner et al. (1999) decomposed the emission into thermal and non-thermal components and found that the thermal wind emission has a spectral index, $\alpha = +0.62$ ($\pm 0.1$), and fitted the non-thermal emission with a range of different models, but were unable to come to any strong conclusions as to the emission model. In this paper, we will show that the inclusion of low-frequency data significantly improves the situation.

The WR-star and the wind collision zone were resolved at X-ray energies with the *Chandra* satellite in Pittard et al. (2002). The X-ray emission was seen to peak close to the position of the wind collision shock and north of the WN8 star. Further results from X-ray observations of WR 147 with both the *XMM-Newton* and *Chandra* satellites have been presented by (Skinner et al., 2007), Zhekov & Park (2010b,a).

Setia Gunawan et al. (2001) monitored WR 147 at radio wavelengths over an 8 year period and their results suggested clumps were present in the stellar winds and reported a possible sinusoidal variation of ~8 years. Changes in the structure of both the thermally emitting WR stellar wind component and the NT CWR were observed by Watson et al. (2002) with the *MERLIN* array, possibly indicating clumps in the wind.

The WR component has a mass estimated as $M(WR) = 30\ M_\odot$ (Hamann & Koesterke, 1998), a wind terminal velocity $v_\infty(WR) = 1000$ km s$^{-1}$, (Williams et al., 1997), an effective temperature $T_{\rm eff}(WR) = 26000\,$K, (Setia Gunawan et al., 2001) and mass-loss rate $\dot{M}(\mathrm{WR}) = [1.5\text{-}3.7]\times10^{-5}\ M_\odot\ \mathrm{yr}^{-1}$, (Morris et al., 2000).

The mass of the OB star has been very tentatively estimated as $M(O) = 15 - 20 M_\odot$ by Morris et al. (2000), with $v_\infty(O) = 800$ km s$^{-1}$, (Williams et al., 1997), $T_{\rm eff}(O) = 28500\,$K, (Setia Gunawan et al., 2001) and $\dot{M}(\mathrm{O}) = 6\times10^{-7}\,M_\odot\ \mathrm{yr}^{-1}$ (Williams et al., 1997). However, because the spectral type is poorly known, these values are very uncertain. Table 4.1 includes a summary of these values.

### 4.2.2 Colliding wind binary considerations

In WR 147 we have two massive stars both with winds. These winds will collide and the location of the northern radio source (believed to be the prime source of the NT emission) will be determined by the wind momentum balance (Stevens et al., 1992; Williams et al., 1997).

For WR 147, if we assume that the wind collision zone, on the line of centres, is located at a distance $r(OB)$ from the OB star and $r(WR)$ from the WR-star, then the ratio of distances $r(OB)/r(WR)$ is given by the ratio of the wind momenta, such that (Stevens et al., 1992; Usov, 1992):

$$\eta = \left[\frac{r(OB)}{r(WR)}\right]^2 = \frac{\dot{M}(OB)v_\infty(OB)}{\dot{M}(WR)v_\infty(WR)}\,. \tag{4.1}$$

From Niemela et al. (1998), we obtain a distance ratio, $r(OB)/r(WR)$ of 0.17, or $\eta = 0.029$. Using the *MERLIN* radio flux for the WR component (Williams et al., 1997) with the Wright & Barlow (1975) mass loss formula, we find $\dot{M}$(WR)=$1.30\times10^{-5}\,M_\odot$ yr$^{-1}$ for the WR-star. In turn this suggests $\dot{M}$(OB)=$4.7\times10^{-7}\,M_\odot$ yr$^{-1}$.

### 4.2.3 Previous radio observations

WR 147 has been previously observed several times at a range of radio frequencies.

Radio observations have been previously made of WR 147 with the VLA by Churchwell et al. (1992) 1.5, 5, 15 and 23 GHz resolving the two radio components. Also 5 GHz VLA observations by Contreras et al. (1996) resolved the two sources and Skinner et al. (1999) resolved the two radio sources at 15 and 22 GHz.

Using the Westerbork Synthesis Radio Telescope (WSRT) Setia Gunawan et al. (2003) surveyed the Cygnus OB2 region at 350 MHz and 1.4 GHz, including WR 147. WR 147 was clearly detected at 1.4 GHz, but the situation was more complex at 350 MHz. The Cygnus OB2 region has considerable extended emission spread through the region and Setia Gunawan et al. (2003) noted weak extended emission at 350 MHz at the location of WR 147, see Figs. 4.1 and 4.2. This may not be point source emission and we do not include this data point in our analysis. We shall refer to the sources detected in this survey by their SHBW number.

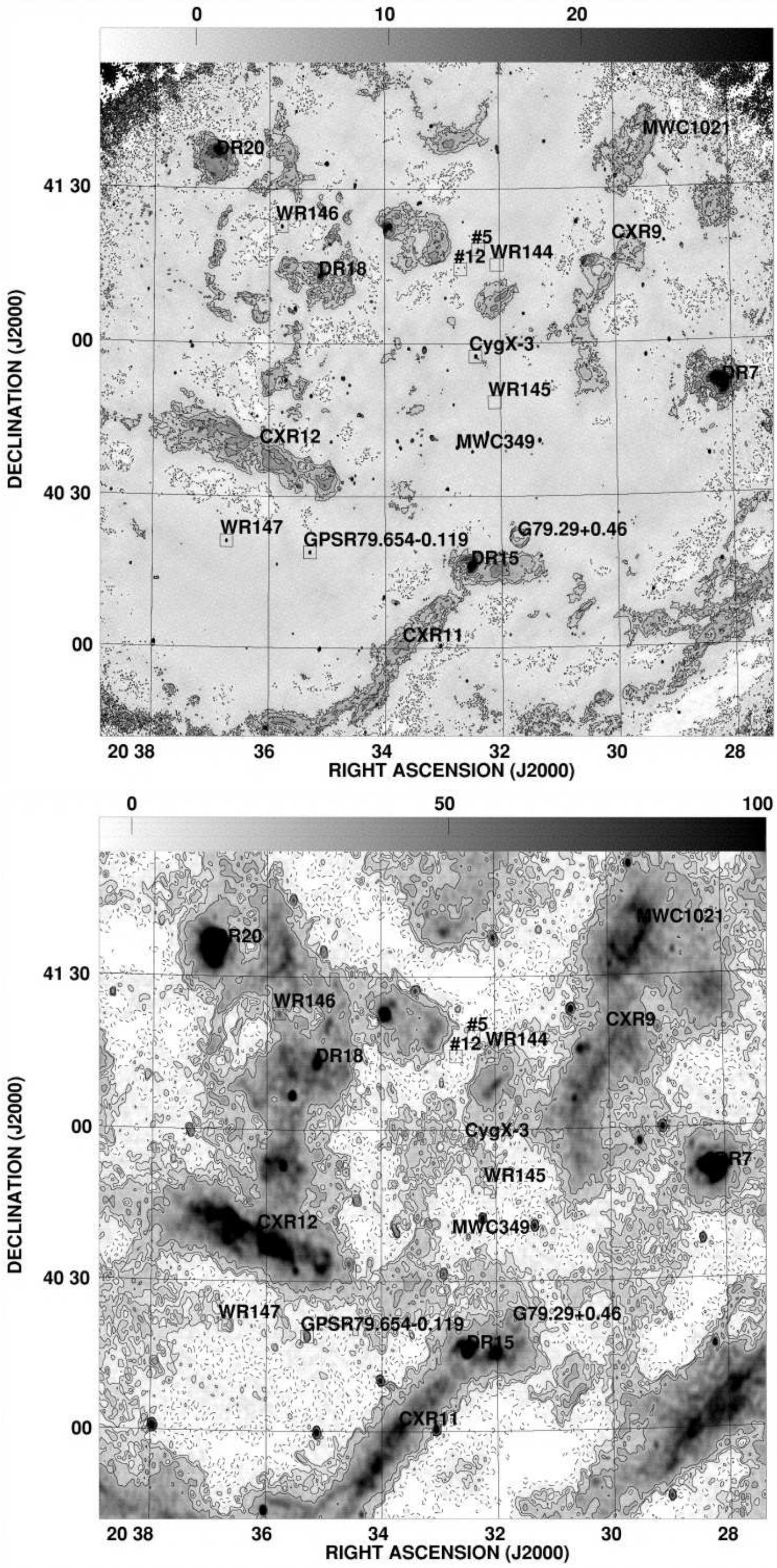

Figure 4.1: The Cygnus OB2 survey by Setia Gunawan et al. (2003), Top panel: 1400 MHz, Lower panel: 350 MHz.

Table 4.1: Assumed parameters of the WR 147 system

| Parameter | Value | Ref |
|---|---:|---|
| System: | | |
| Distance | 650 (+130-110) pc | 1 |
| Period | > 1350 yr | 2 |
| Inclination | 0° (face on) | assumed |
| Separation (A) | 645 mas | 4 |
| OB star: | | |
| spectral type | O5-7 I-II(f) | 7 |
| mass | 15-20 $M_\odot$ | 1 |
| $v_\infty$ | 800 km $s^{-1}$ | 6 |
| $T_{\rm eff}$ | 28500 K | 2 |
| $\dot{M}$ | $4.7\times10^{-7}\,M_\odot$ $yr^{-1}$ | derived |
| WR-star: | | |
| spectral type | WN8(h) | 3 |
| mass | 30 $M_\odot$ | 5 |
| $v_\infty$ | 1000 km $s^{-1}$ | 6 |
| $T_{\rm eff}$ | 2600 K | 2 |
| $\dot{M}$ | $1.30\times10^{-5}\,M_\odot$ $yr^{-1}$ | derived |

References: (1) Morris et al. (2000), (2) Setia Gunawan et al. (2001), (3) Caillault et al. (1985), (4) Horch et al. (2011), (5) Hamann & Koesterke (1998), (6) Williams et al. (1997), (7) Lépine et al. (2001)

The observed fluxes from the Skinner observations are shown in Table 4.3, together with the 43.3 GHz VLA flux of Contreras et al. (1996).

Recent observations have been made of the WR 147 system at 15 – 44 GHz with the JVLA by Carlos Carrasco-Gonzalez et al.(in preparation) who suggest that the thermal spectral index of ∼0.6 is solid.

## 4.3 Low-frequency GMRT Observations and Results

### 4.3.1 Observations

WR 147 has been observed with the GMRT, located near Pune, India, at 235 MHz and 610 MHz. Importantly, these two bands can be observed simultaneously with the GMRT (which removes the issue of any variability of the source). The system was observed on 2012 November 4. The field was centred on WR 147 for a period of 5.5h.

The flux density calibrator was 3C48 and the phase calibrator was 2052+365. The bandwidth

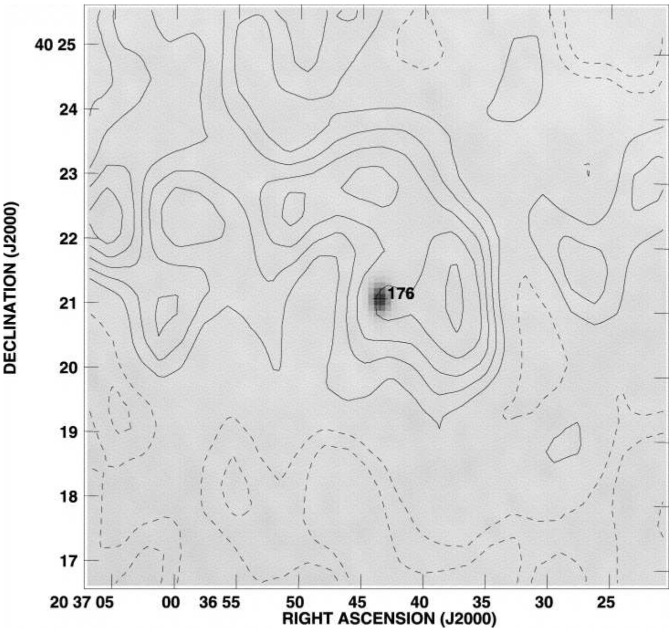

Figure 4.2: 350 MHz emission from the Cygnus OB2 survey in the region of WR 147 (SBHW 176) (Setia Gunawan et al., 2003).

Table 4.2: Details of the GMRT observations of WR 147.

| Band (MHz) | B/width (MHz) | Date | Time (UT) (hr) | Flux calibrator | Phase calibrator | Resolution (arcsec) | rms (mJy beam$^{-1}$) |
|---|---|---|---|---|---|---|---|
| 610 | 32 | 2012 Nov 4 | 13:00-18:20 | 3C48 | 2052+365 | 5.0 | 0.11 |
| 235 | 32 | 2012 Nov 4 | 13:00-18:20 | 3C48 | 2052+365 | 13.0 | 1.9 |

was 32 MHz with 256 channels. The time on source in a single scan was 30 minutes, moving to the phase calibrator for 10 minutes, with the flux calibrator observed at the beginning and end of the observation. Three antennas were unavailable (leaving 27 usable for most of the observations), with a maximum baseline of approximately 25km and a nominal resolution of $\sim 5.0$ arcsec at 610 MHz and $\sim 13.0$ arcsec at 235 MHz. The achieved noise levels were 0.11 mJy beam$^{-1}$ at 610 MHz and 1.9 mJy beam$^{-1}$ at 235 MHz (see Table 4.2 for details).

Data reduction was performed using standard proceedures, with the Astronomical Image Processing System (AIPS). Because the Cygnus OB2 region has a substantial amount of extended emission from HII regions (Setia Gunawan et al., 2003) and as we are interested in point source emission from WR 147 we have excluded short baselines (those with $< 1\ k\lambda$) from the analysis (such a procedure was also done by Martí et al. (2007) in their analysis of a nearby field).

With these low-frequency observations, we are not able to resolve WR 147 into two components at either frequency.

### 4.3.2 GMRT results

The wide-field GMRT data on WR 147 at 235 MHz and 610 MHz are shown in Fig. 4.3, along with zoomed-in images around the source in Fig. 4.4. WR 147 was strongly detected at 610 MHz, with a total flux of 13.0 mJy (determined using the AIPS Gaussian fitting function IMFIT).

For comparison, we also show sources detected by Setia Gunawan et al. (2003) at 350 MHz and 1.4 GHz, which are labelled with their SHBW number. These other sources are mainly point sources plus a diffuse HII region above WR 147, CXR12.

At 235 MHz no emission was evident at the position of WR 147. In the spectral fitting described later, we use an upper limit value of $3\sigma$, as in Blomme & Volpi (2014), with $\sigma = 1.9$ mJy beam$^{-1}$ at 235 MHz.

We note that three other sources are present at 235 MHz that also appear in the 610 MHz data and in the Setia Gunawan et al. (2003) survey, these are indicated in Fig. 4.3.

The brightest source in the field is source SHBW 195 which has a total flux of $122 \pm 0.5$ mJy at 610 MHz and $360 \pm 9.2$ mJy at 235 MHz indicating a negative spectral index which consistent with the Setia Gunawan et al. (2003) survey, but with lower GMRT fluxes (in the Setia Gunawan et al. (2003) survey this source has fluxes of 535 mJy at 350 MHz and 122 mJy at 1.4 GHz).

The fluxes (detected and upper limit), which we will use to fit the spectra, are listed in Table 4.3 along with those obtained at higher frequencies with the VLA by Skinner et al. (1999) and Contreras et al. (1996).

## 4.4 WR 147 Spectral Energy Distribution

Analysis of the thermal and NT radio emission from WR 147 has previously been undertaken by Skinner et al. (1999), using data taken near contemporaneously at higher frequencies.

Here we add our low-frequency GMRT data to the VLA data from Skinner et al. (1999), and this allows us to fit models to the NT emission from the system, to better constrain the emission models. We note that we are implicitly assuming that the system is reasonably constant over a period of $> 10$ years. This is an assumption that has been considered by Setia Gunawan et al.

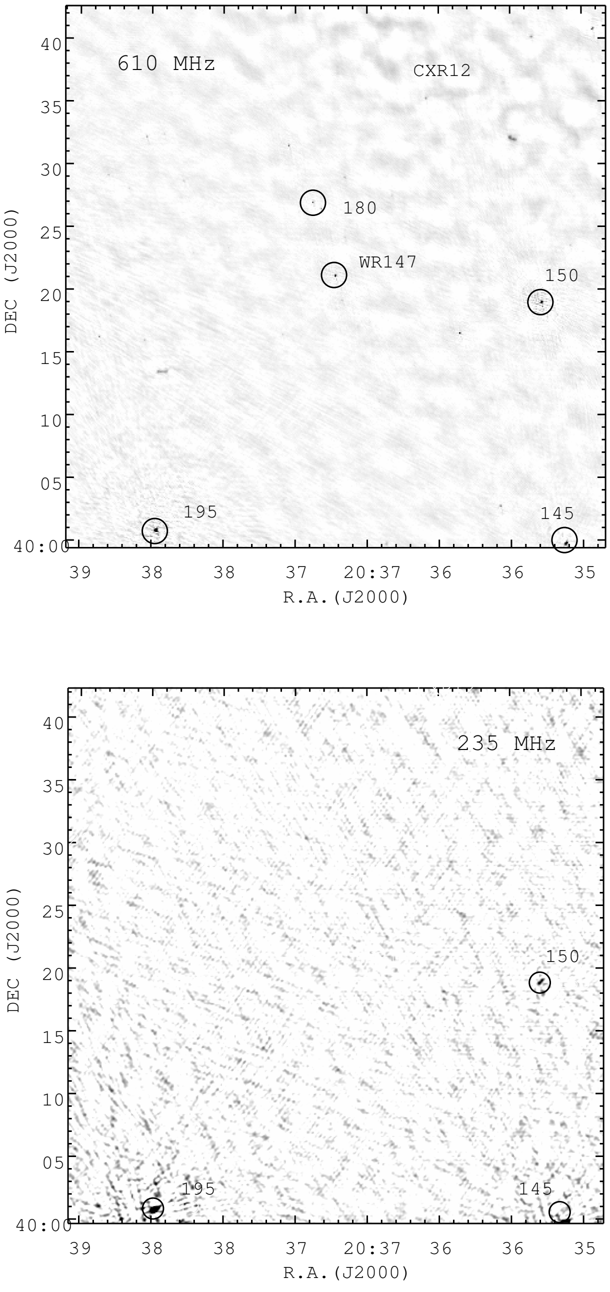

Figure 4.3: Top panel: The GMRT 610 MHz observations of the WR 147 field. This image is labelled with some of the nearby SBHW sources. For all images baselines of length $< 1k\lambda$ have been excluded. Bottom panel: The 235 MHz data on the WR 147 field, also labelled with some of the SHBW sources. See text for further details.

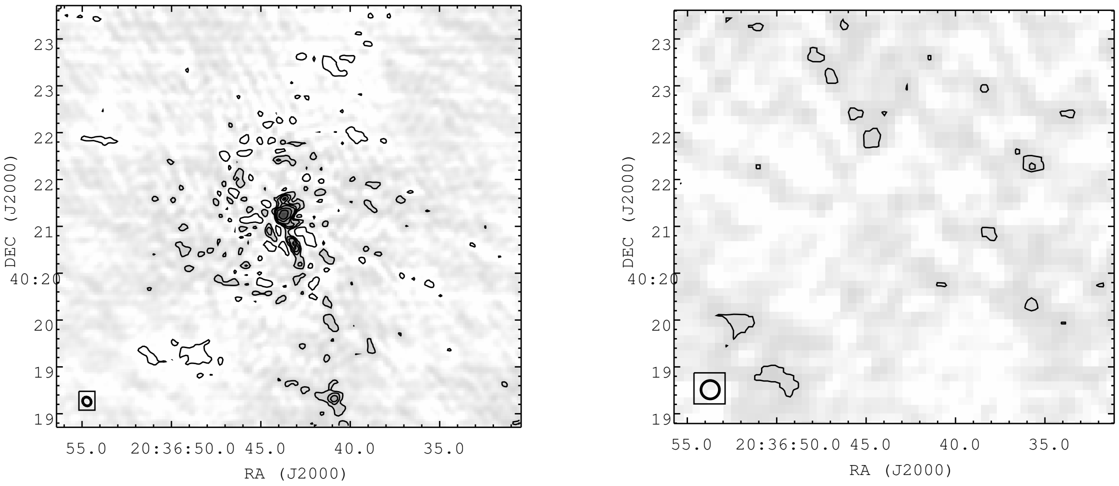

Figure 4.4: Left panel: Zoomed-in image around WR 147 at 610 MHz. For this image $\sigma = 0.11$ mJy beam$^{-1}$ and the contours are at $\sigma\times$ -3, 3, 6, 9, 12, 24, 48. The synthesised beam size of $5.9'' \times 5.2''$ is shown bottom left. Right panel: Zoomed-in image around WR 147 at 235 MHz. WR 147 is not detected. For this image $\sigma = 1.9$ mJy beam$^{-1}$ and the contours are at $\sigma\times$ 2, 3. The synthesised beam size of $11.8'' \times 11.8''$ is shown. See text for further details.

Table 4.3: The GMRT and VLA fluxes of WR 147. The fluxes are all for the total flux from WR 147, except where it is possible to resolve the two components.

| Freq | $\lambda$ | $S_{tot}$ | $\sigma$ | $S_{WR}$ | $S_{NT}$ | reference |
|---|---|---|---|---|---|---|
| (GHz) | (cm) | | (mJy) | | | |
| 0.235 | 128 | <6.0 | 2.0 | | | GMRT |
| 0.610 | 50 | 13.1 | 0.22 | | | GMRT |
| 1.42 | 21.1 | 25.4 | 0.19 | | | VLA 1 |
| 4.86 | 6.2 | 38.9 | 0.09 | | | VLA 1 |
| 8.44 | 3.6 | 44.7 | 0.08 | | | VLA 1 |
| 14.94 | 2.0 | 49.6 | 0.25 | 41.8 | 7.8 | VLA 1 |
| 22.86 | 1.3 | 57.3 | 0.35 | 53.9 | 3.4 | VLA 1 |
| 43.3 | 0.7 | 82.8 | 1.1 | | | VLA 2 |

References: GMRT, this paper; VLA 1, Skinner et al. (1999); VLA 2, Contreras et al. (1996).

Table 4.4: Observed flux values of WR 147, derived thermal flux($\alpha$=0.62) and NT flux derived from total – thermal, (see text for details).

| Frequency(GHz) | 0.235 | 0.610 | 1.42 | 4.86 | 8.44 | 14.94 | 22.86 | 43.3 |
|---|---|---|---|---|---|---|---|---|
| | | | | (mJy) | | | | |
| Total emission | <6.0 | 13.1 | 25.4 | 38.9 | 44.7 | 49.6 | 57.3 | 82.8 |
| $\sigma$ | 2.0 | 0.22 | 0.19 | 0.09 | 0.08 | 0.25 | 0.35 | 1.1 |
| Thermal | 3.2 | 5.8 | 9.7 | 20.8 | 29.3 | 41.8 | 53.9 | 80.9 |
| $\sigma$ | 0.4 | 0.6 | | | | | | |
| NT | <2.8 | 7.3 | 15.7 | 18.1 | 15.4 | 7.8 | 3.4 | 1.9 |

(2001), who found that WR 147 showed smaller scale variability over 8-10 yr.

### 4.4.1 Total radio SED and NT emission

The GMRT total flux data is shown in Fig. 4.5 (top) together with the VLA total flux data of Skinner et al. (1999) and Contreras et al. (1996), see Table 4.3 for flux values. The VLA observations at 14 and 22 GHz have resolved the WR147S emission, thought to be thermal emission from the stellar wind of the WR component. The thermal data is indicated by crosses in Fig. 4.5 where we show the results of fitting this data to a power law model, $S \propto \nu^{\alpha}$, this gives $\alpha = 0.62 \pm 0.03$. Also indicated are models fitted to the $2\sigma$ range, i.e $\alpha = 0.56$ and 0.68.

From this, we estimate the thermal flux from WR 147 using $S_\nu$ (mJy) $= 41.8(\nu/14.94\text{GHz})^{0.62}$. This thermal flux is then deducted from the total flux to give the NT emission (Skinner et al., 1999). These values are listed in Table 4.4 and plotted in Fig. 4.5 (lower).

## 4.5 Spectral Fitting

### 4.5.1 Introduction - fitting the radio spectrum

We have attempted to understand the NT emission by fitting our data (including the upper limit at the 235 MHz) data to models of synchrotron emission with absorption mechanisms (see Appendix A for details of the fitting).

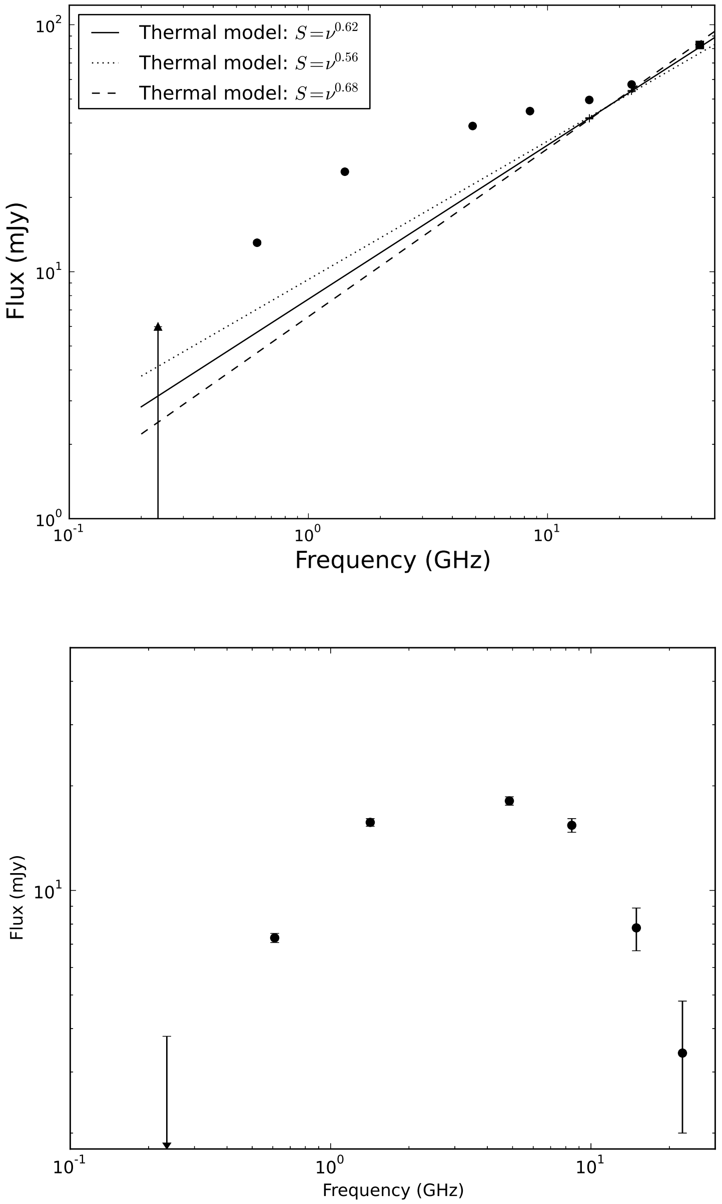

Figure 4.5: Top panel: GMRT and VLA total flux, plus power law fitting to the thermal flux, with $\alpha$=0.62 plus a $2\sigma$ range of 0.56 and 0.68 see text for details. Lower panel: The NT emission from WR 147, resulting from subtracting the thermal emission.

Table 4.5: The best fit values for 1 and 2 component models for the NT emission from WR 147. Shown are the best fit parameters and the $1\sigma$ error range (see text for details).

| 1-component | | 2-component | |
|---|---|---|---|
| Parameter | Best fit | Parameter | Best fit |
| $C$ | $57.4^{58.4}_{56.4}$ | $C_1$ | $32.1^{32.9}_{31.3}$ |
| | | $C_2$ | $108.6^{112.5}_{104.7}$ |
| $\alpha$ | $-0.68^{-0.69}_{-0.67}$ | $\alpha_1$ | $-1$ |
| | | $\alpha_2$ | $-1$ |
| $\tau_1$ | $2.27^{2.33}_{2.22}$ | $\tau_{1,1}$ | $0.83^{0.88}_{0.79}$ |
| | | $\tau_{1,2}$ | $18.9^{20.13}_{17.7}$ |
| $\chi^2$ (d.o.f) | 26.6 (4) | $\chi^2$ (d.o.f) | 3.19 (3) |

### 4.5.2 A one component model

We initially assume a one component model, with synchrotron emission and free-free absorption. The model form assumed is:

$$S_{mod}(\nu) = C\nu^{\alpha}e^{-\tau_1/\nu^{2.1}} \tag{4.2}$$

where $S_{mod}(\nu)$ is the model flux at a frequency $\nu$ and $C$, $\alpha$ and $\tau_1$ are the model parameters to be fitted, with $\tau_1$ the free-free absorption optical depth at 1 GHz. Given the model fluxes in Table 4.4 we can derive the best fit model, including the 235 MHz upper limits and results are shown in Fig. 4.6 and Table 4.5. As can be seen, this is a very poor fit, and the 610 MHz detection and 235 MHz are key to showing that the model is a poor representation of the data.

### 4.5.3 A two component model

The next logical step is to include a second component. Mathematically this can represented as follows:

$$S_{mod}(\nu) = \sum_{i=1,2} C_i\nu^{\alpha_i}e^{-\tau_{1,i}/\nu^{2.1}} \tag{4.3}$$

This can be imagined as one region of NT emission that is more buried than another. We have chosen to fix $\alpha_1 = \alpha_2 = -1.0$. Allowing $\alpha$ values to range freely allows for better fits, but leads to unrealistic values of $\alpha$.

This model gives a much superior fit to a one component model, the results are also shown in Fig. 4.6 and Table 4.5. This improved fit strongly suggests different regions of absorption are

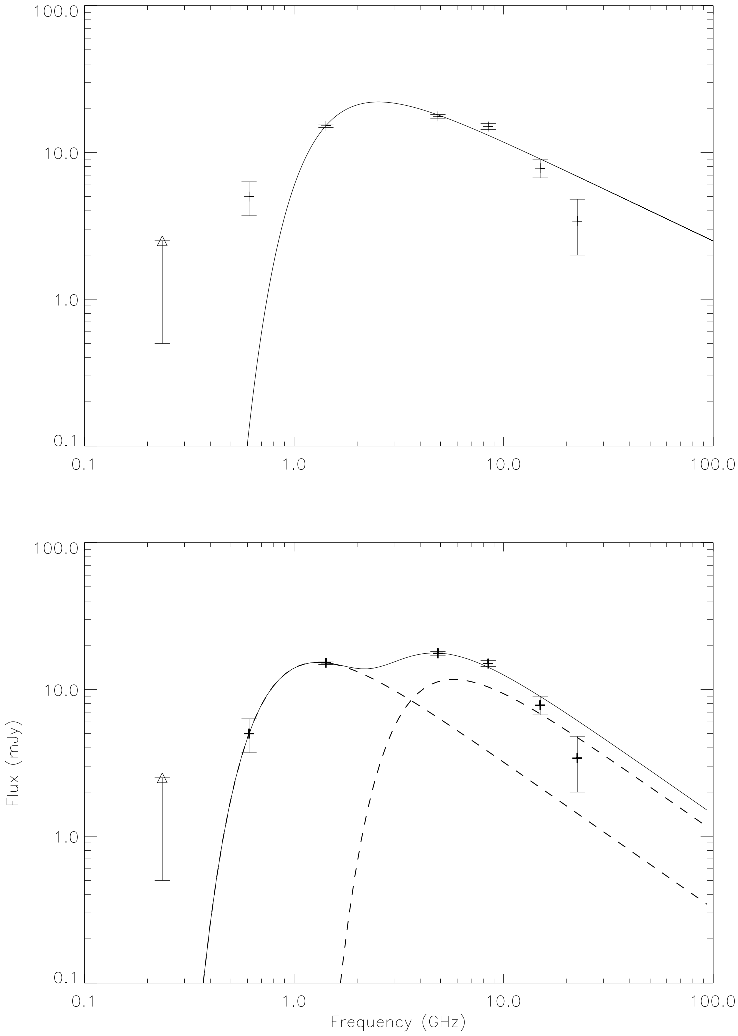

Figure 4.6: Top panel: A 1-component NT model fitted to GMRT and VLA data. Lower panel: A 2-component NT model where $S_\nu = C\nu^\alpha e^{-\tau/\nu^{2.1}}$ fitted to the Skinner VLA data and this GMRT data, see text for details.

present.

### 4.5.4 A numerical model

Pittard et al. (2006) performed numerical calculations of the expected radio spectrum of colliding wind systems. In this model the emission comes from an extended region associated with the wind collision shock and the absorption likewise comes from a range of different depths and the line of sight passes through the wind. Here we repeat those calculations accounting for the new low-frequency data and we refer you to that paper for more details. Here we are not attempting to fit the spectra, but are rather calculating models for reasonable values and seeing how the resulting spectra compare.

The parameters assumed in this calculation are as follows. The mass-loss rate are assumed to be $\dot{M}(WR) = 4.2{\times}10^{-5}\,M_{\odot}$ yr$^{-1}$ and $\dot{M}(O) = 6.0{\times}10^{-7}\,M_{\odot}$ yr$^{-1}$. The wind terminal velocities are assumed to be $v_{\infty}(WR) = 1000\,$km s$^{-1}$ and $v_{\infty}(OB) = 800\,$km s$^{-1}$. The separation between the two stars is assumed to be $D_{sep} = 7.05 \times 10^{15}$ cm (which corresponds to an apparent separation of $D_{sep} = 624$mas at 650 pc. The assumed luminosities are $L_{*}(WR) = 5 \times 10^{4}\,L_{\odot}$ and $L_{*}(OB) = 1 \times 10^{5}\,L_{\odot}$. We have calculated models for 2 inclinations ($i = \pm 30°$).

Further, we assume solar abundances for the OB star, and mass fractions of $X = 0.094$, $Y = 0.89$, and $Z = 0.016$ for the WR-star. We also assume that the winds are smooth.

The models shown in Fig. 4.7 are for $\eta_{rel,e} = \zeta_B = 1.0 \times 10^{-2}$, where $\zeta_B$ controls the number of NT electrons and the strength of the magnetic field.

The resulting spectra are shown in Fig. 4.7, where the thermal free-free emission (dashed line), non-thermal synchrotron emission (dotted line) and the total emission (solid line) are shown.

For $i = +30°$ (when the OB star is in front of WR-star) the low-frequency turn-over is at too low a value. Things improve for $i = -30°$ (where the WR-star is in front of OB, so that the line of sight passes through more of the WR wind) but the turn-over is still too weak.

There are various conclusions from this modelling that may be used to explain the discrepancies between the model and the data. We could investigate models with a higher inclination, which would give rise to more free-free absorption. However, given the observed location of the wind collision, a lower inclination is perhaps preferred. It is possible that the inclusion of the

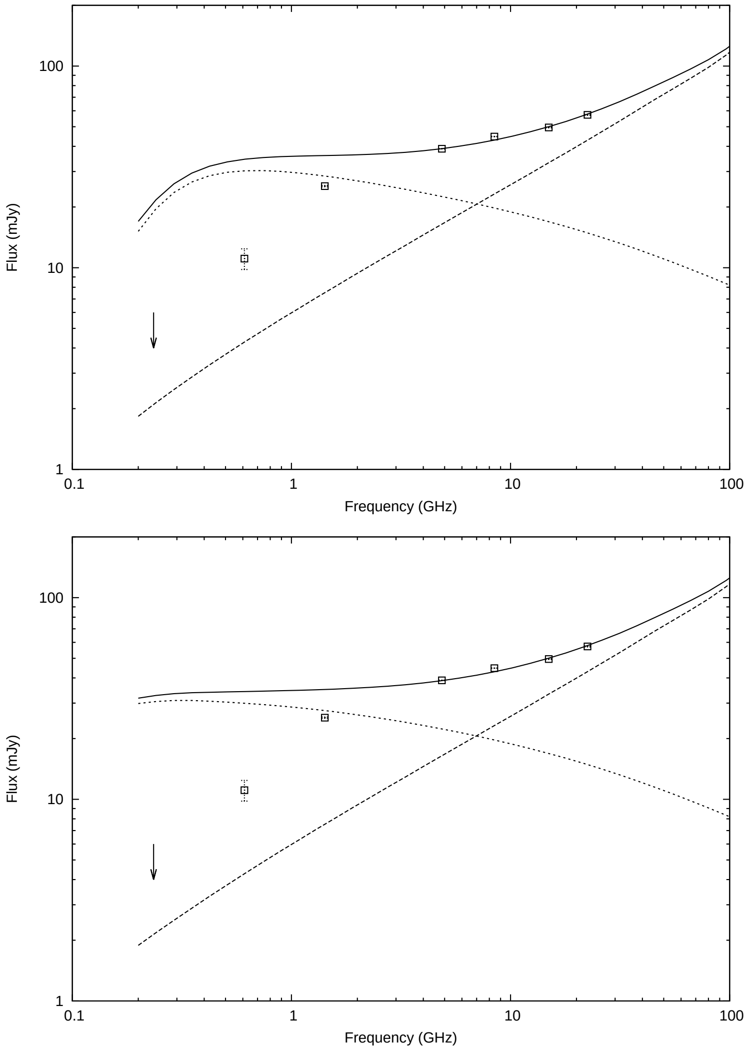

Figure 4.7: Numerical modelling of the emission. Top panel for for $i = 30°$. Lower panel for for $i = -30°$.

Razin effect could also give rise to the observed turn-over. The Razin turn-over occurs at a frequency of $\nu_R(\mathrm{GHz}) = 20\mathrm{n_e}/\mathrm{B}$, with $n_e$ in units of $\mathrm{cm}^{-3}$ and $B$ in Gauss (Pittard et al., 2006). This indicates a $B$-field of $\sim$20 $\mu$Gauss is required at a turn-over of 1 GHz, the WR 147 $B$-field is derived by Setia Gunawan et al. (2001) at 5 mGauss. Clumping will increase the free-free emission and also increase the low-frequency absorption of the synchrotron emission. It will mean that the synchrotron emission can be reduced in strength somewhat (in order to match the high frequency total flux). We shall explore this more in a subsequent section.

## 4.6 Discussion

### 4.6.1 Summary

The improved fit of the multiple component model suggests that there are regions of WR 147 with different degrees of absorption. A recent study by Benaglia et al. (2015) of the spectra of the massive binary system HD 93219A has revealed a low frequency turn-over in the emission from this system at ~1.4 GHz, though their study does not include data below 1.4 GHz. This illustrates the paucity of low frequency data that would more easily reveal the position of a turn-over.

In this section we examine the optical depth of WR 147 and the effects of clumping.

### 4.6.2 The free-free optical depth in WR 147

The free-free absorption optical depth, $\tau_{ff}$, can be written as:

$$\tau_{ff} = 3.3 \times 10^{-7} T_4^{-1.35} \nu_9^{-2.1} \int_0^{\infty} n_e^2 dl \tag{4.4}$$

where the Emission Measure, $EM$ ($\int_0^{\infty} n_e^2 dl$), is in units of cm$^{-6}$ pc, appropriate for interstellar absorption. In this expression $\nu_9$ is the frequency in GHz and $T_4$ the gas temperature in units of $10^4$ K. We shall assume that $T_4 \sim 1$.

Initially we assume that the NT emission comes from a small region located at the wind-wind interface of the system and calculate the expected free-free absorption given the estimated wind parameters of the component stars. Given the geometry of the system we expect the free-free absorption to be dominated by the WR wind.

We use parameters from Table 4.1, for the WR-star mass-loss rate $\dot{M}$(WR) and wind terminal velocity $v_\infty$(WR) (and corresponding values for the O-star, $\dot{M}$(O) and $v_\infty$(O)). We assume the system is at a distance $d$ and the stellar components are separated by a distance $A$ and that the NT emission source is at a distance $A_{NT}$ from the WR-star. We assume that the winds are at terminal velocity (reasonable because WR 147 is a very wide system and the assumed geometry).

The wind density, $\rho$, at a radius, $r_{WR}$, from the WR-star is given by

$$\rho = \frac{\dot{M}(WR)}{4\pi r(WR)^2 v_(WR)} \tag{4.5}$$

and the electron number density $n_e = \rho/\mu_e$, where $\mu_e$ is the mean mass per electron in the wind. Assuming fully ionised H and singly ionised He - this leads to a value of $\mu_e \sim 3.15 m_H$.

If we assume that we are viewing the system from the side and that the separation between the WR-star and NT emission region is $A_{NT}$ then it can be shown that along the line of sight from the NT emission:

$$\begin{aligned} EM &= \left(\frac{\dot{M}(WR)}{4\pi\mu_e\, v_\infty(WR)}\right)^2 A_{NT}^{-3} \int_0^{\pi/2} \cos^2\theta \, d\theta \\ &= \left(\frac{\dot{M}(WR)}{4\pi\mu_e\, v_\infty(WR)}\right)^2 A_{NT}^{-3} \left(\frac{\pi}{4}\right). \end{aligned} \tag{4.6}$$

Given the assumed values, we have that $EM = 2.2 \times 10^4 \text{ cm}^{-6}\,\text{pc}$ and hence $\tau_{ff} = 0.0074$ at 1 GHz (assuming $T_4 = 1$). This value is considerably below that from the fitting.

Further, if we assume that the system is not being viewed at $i = 0°$ (i.e. face-on) then we can again calculate the change in the Emission Measure as a function of inclination.

Note that the apparent separation stays constant, so that the true separation increases as $A_{NT,proj} = A_{NT} \sin i$. This means that the increase in $\tau_{ff}$ is not as marked as it would otherwise be.

Consequently, orientation effects cannot lift the inferred free-free absorption, unless quite large values of the inclination are assumed.

### 4.6.3 Clumping

Assuming the wind is smooth, we have a mass-loss rate of $\dot{M}_{sm}$. However, assume we have a clumped wind, with a clumped mass-loss rate of $\dot{M}_{cl}$ and a clumping factor $f_{cl}$, defined as

$$f_{cl} = \frac{<\rho^2>}{<\rho>^2}$$

where $\rho$ is the density in the wind.

Consider a wind where the material consists of 2 densities, $\rho_1$ and $\rho_2$, with $\rho_1 > \rho_2$. The denser material has a filling factor $f$ and the less dense material therefore has a filling factor $(1 - f)$. The mean density is then (and this is the equivalent density if all the material was smoothly distributed - i.e. $\rho_1 = \rho_2$.

$$<\rho> = f\rho_1 + (1-f)\rho_2$$

and

$$< \rho^2 >= f \rho_1^2 + (1-f) \rho_2^2$$

As an extreme case, let $\rho_1 / \rho_2$ be very large, then

$$f_{cl} = \frac{< \rho^2 >}{< \rho >^2} = \frac{1}{f}$$

From the scaling of the free-free radio flux, we have that

$$\dot{M}_{sm} = \dot{M}_{cl} f_{cl}^{1/2}$$

The free-free optical depth has been defined above. Assuming the same level of free-free flux from winds with clumping and no-clumping, the ratio of the free-free optical depth in the clumped wind to the free-free optical depth in a smooth wind can be written as:

$$\frac{\tau_{ff}(clump)}{\tau_{ff}(smooth)} = f_{cl}$$

Consequently, we can fairly easily raise the expected level of free-free absorption by invoking a clumping factor. Previous observational evidence of clumping in the winds of massive stars have been made by Lépine & Moffat (2008), whilst Najarro (2001) obtain a clumping filling factor of 0.5 for the massive B type star P Cygni and a study by Crowther et al. (2002) suggest O-star clumping factors of 1-0.1.

We note that in the theoretical wind calculations of Runacres & Owocki (2002) show that clumping factors in excess of 10 could be generated in their calculations. These authors note a number of provisos regarding their results, but nonetheless, these observations could be taken as evidence for such strongly clumped winds, though the observational evidence above reveal lower values.

## 4.7 Conclusion

We have presented new GMRT observations of the important colliding wind system WR 147. We detect the system at 610 MHz, but not at 235 MHz. Having made an estimate of the thermal emission from the ionised winds, we model the NT emission from the wind interaction region. We find that the NT emission can not be explained by a simple one component model consisting of synchrotron emission plus free-free absorption. We find that a two component model can better explain the emission. More detailed numerical modelling of the system suggested that clumping or the Razin effect may well play a role in the emission/absorption process in colliding wind systems. Although these GMRT observation have provided some further insight into these systems, it is clear that observations with broader band receivers, such as are being developed for the GMRT and eventually on the SKA-Low telescope, will enable us to locate the turn-over and spectral shape of colliding wind systems and revolutionise our view of the wind emission processes in such systems.

We also have GMRT data on the WR146 system and that will be presented in a subsequent paper. The GMRT was not able to spatially resolve the individual wind components in WR 147. Note that we have recently observed WR 147 with the *e-MERLIN* array and that paper is in preparation.

## 4.8 Appendix A

### 4.8.1 Fitting the radio spectra - including upper limits

A common problem in fitting radio spectra is the inclusion of upper limits in an appropriate manner, and here we adopt the approach described by Sawicki (2012).

Assuming we have only detections then we can use a $\chi^2$ methodology to find the best-fit parameters for a given spectral model. Suppose we have $N$ measured detections of flux $S_i$ at frequencies $\nu_i$, with uncertainties of $\sigma_i$. Given an assumed model (for instance, a power-law + free-free absorption) we can calculate model fluxes $S_{mod,i}$ at the same frequencies. We can then write the $\chi^2$ as:

$$\chi^2 = \sum_{i=1}^{N} \frac{(S_i - S_{mod,i})^2}{\sigma_i^2} .$$

If in addition to the detections, we have $M$ upper limits of $S_j^{upp}$ at frequencies $\nu_j^{upp}$, with errors $\sigma_j^{upp}$ (and corresponding model values $S_{mod,j}$), we can define an updated expression for $\chi^2$ (as in Sawicki, 2012), so that:

$$\begin{aligned}\chi^2 &= \sum_{i=1}^{N} \frac{(S_i - S_{mod,j})^2}{\sigma_i^2} \\ &- 2\sum_{j=1}^{M} \ln\left(\sqrt{\frac{\pi}{2}}\sigma_j^{upp}\left[1 + erf\left(\frac{S_j^{upp} - S_{mod,j}}{\sqrt{2}\sigma_j^{upp}}\right)\right]\right)\end{aligned}$$

where $erf(x)$ is the error function.

For an assumed spectral model, we minimize this $\chi^2$ expression using an IDL program incorporating the *AMOEBA* algorithm. In our implementation of this formalism, we also calculate asymmetric error bars for the best fit parameters.

# Chapter 5

# Low-Frequency GMRT Observations Of Massive Stars II: The Wolf-Rayet Colliding Wind Binary System - WR 146

*"However long we live, life is short, so I work. And however important man becomes, He is nothing compared to the stars. There are secrets, dear sister, and it is for us to reveal them."*
Caroline Herschel, 1750-1848.

**Abstract**

We present simultaneous, low-frequency observations at 235 and 610 MHz of the bright colliding wind binary, WR 146. We detect WR 146 at both frequencies.

We model the low frequency non-thermal radio emission and use simple synchrotron plus free-free absorption models to fit the data. A one component model is not able to fit the data well, but using a two component model obtains better results. We discuss the low frequency turn-over of the spectrum with regards to free-free absorption. We conclude that the models reveal a complex region of absorption which required more complex models to explain the structure. We examine the emission measure and opacity of the wind, with $\tau$=0.55 at 1 GHz which is consistent with the two component model.

We conclude that low frequency observations are an important tool to understand the dynamics of colliding wind systems.

## 5.1 Introduction

The stellar winds from massive stars generate large amounts of energy which is detected at radio frequencies as free-free, thermal emission, thought to originate in the stellar wind, together with Non-Thermal (NT) emission thought to originate from synchrotron emission from electrons accelerated in shocks within the stellar wind. This emission is subject to absorption processes within the wind such as free-free absorption and the Razin effect, this is particularly relevant for NT emission at low frequencies where a turn-over in the received flux is thought to occur. Few observations have been made of massive stars below 1.4 GHz (see Benaglia (2010), Setia Gunawan et al. (2003)), therefore this study has been made at low frequencies to search for a better understanding of low-frequency turn-overs in massive stars.

In this paper we present the second of a low frequency programme of study investigating the NT emission of massive stars; observations of the radio bright Wolf-Rayet (WR) colliding wind binary system, WR 146, (see Chapter 4 and Brookes et al., in preparation for paper 1 and further details of this study). This binary system is thought to be in the Cyg OB2 massive star association, of which Wright et al. (2015) have conducted a census of component stars indicating $\sim$ 200 OB massive stars, 3 WR-stars, with star forming over a period of 1 - 7 Myr ago, consistent with the age of 2-4 Myr for WR 146 (Wright et al., 2015).

The WR 146 system has been detected by Setia Gunawan et al. (2003) in their radio survey of the Cygnus OB2 region at 327 MHz and 1.4 GHz, these results are illustrated in Fig. 5.1.

We present 235 and 610 MHz radio observations of WR 146 made with the Giant Metrewave Radio Telescope (GMRT) to study the NT emission and possible low frequency turn-over in this system. Section 5.2 describes WR 146 system, Section 5.3 details our observations, Section 5.4 we present the results of our observation, in Section 5.5 we model the NT emission, we discuss these results in Section 5.6 and conclude with Section 5.7.

## 5.2 A Description of the WR 146 system

The WR 146 system ($\alpha_{J2000}$= 20 35 47.09, $\delta_{J2000}$= +41 22 44.7) was first identified as a WR-star by Herbig & Mendoza (1960), who classified it as a type WC6. Radio emission was first detected from WR 146 in a radio survey by Zoonematkermani et al. (1990) with the VLA at 1.4 GHz.

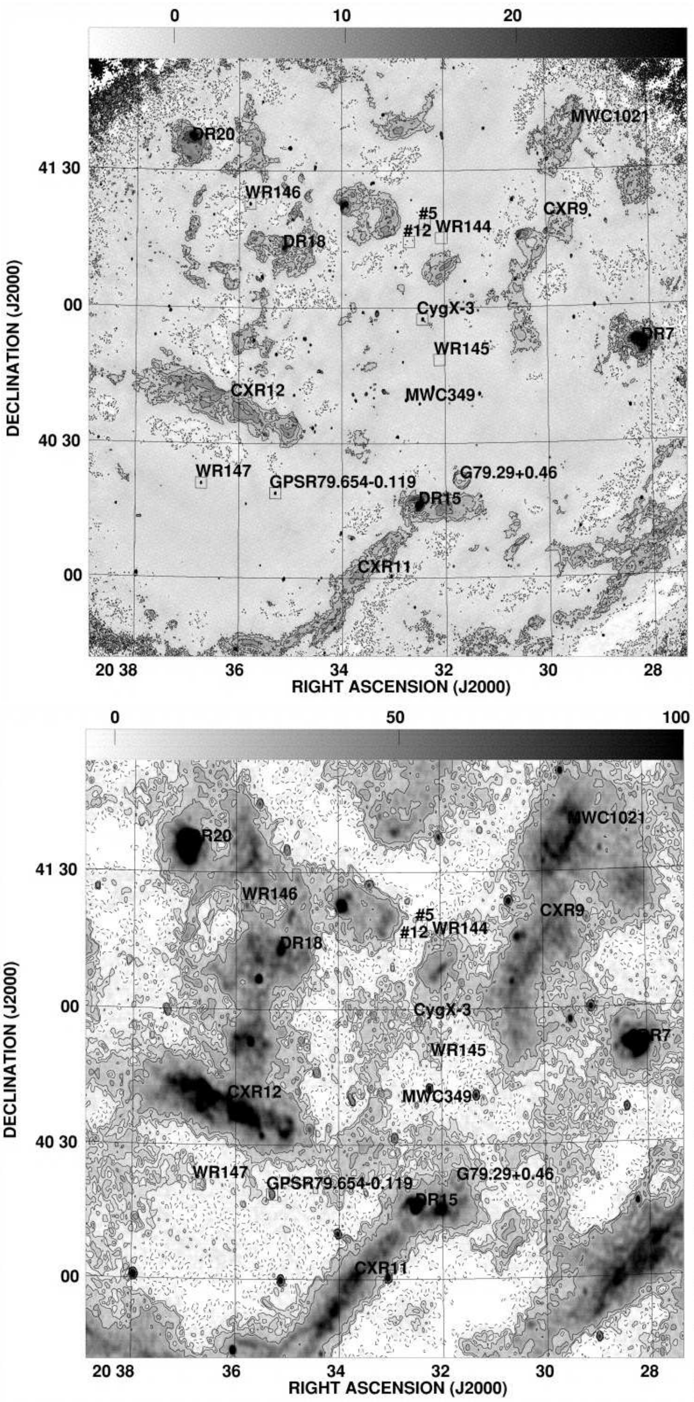

Figure 5.1: The Cygnus OB2 survey region of Setia Gunawan et al. (2003). Top panel: at 1400 MHz and Lower panel: at 350 MHz, indicating the position of the colliding wind binary WR 146.

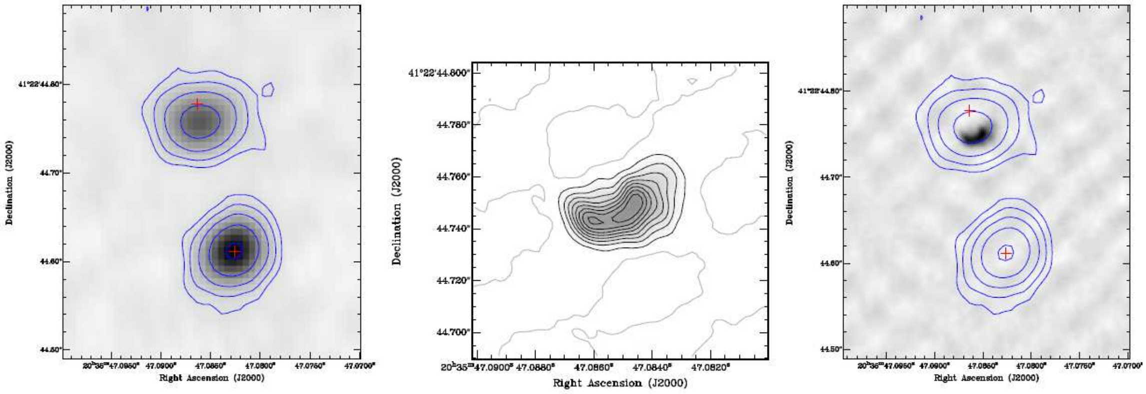

Figure 5.2: VLA and EVN data of WR 146. Left: VLA data at 43 GHz, Centre: EVN data at 5 GHz, and Right: Contours of the 43 GHz data overlaid onto the 5 GHz data. HST positions of the stars are marked with crosses (O'Connor et al., 2005)

Further observations by Felli & Massi (1991) with the EVA and VLA suggested that there were two radio components, a thermal source from the WR stellar wind and a non-thermal (NT) source, thought to be the stellar wind interaction or colliding wind region (CWR). The two stellar components have been spatially resolved by the Hubble Space Telescope (HST) by Niemela et al. (1998) and spectroscopically by the HST STIS spectrograph by Lépine et al. (2001).

Further radio observations have been made with the Westerbork Synthesis Radio Telescope (WSRT) 327 MHz survey of the Galactic plane (Taylor et al., 1996) and the Dominion Radio Astrophysical Observatory Synthesis Telescope at 1.42 GHz (Wendker et al., 1996). Also observations have been made at 1.6 and 5 GHz with the MERLIN array (Dougherty et al., 1996) and at 1.4 to 43 GHz with the VLA European VLBI Network (EVN) and VLBA (Dougherty et al., 2000; O'Connor et al., 2005), where two radio components have been resolved, though at 22 GHz the two components have been identified as thermal emission from each of the stellar winds of the two binary stars (Dougherty et al., 2000), see this detection of WR 146 in Fig. 5.2.

The distance to the system is given by Dougherty et al. (1996) as 1.2 kpc, and by Willis et al. (1997) as 0.75 kpc and 1.25 kpc by Setia Gunawan et al. (2000). WR 146 is likely in the Cyg OB2 association, given a distance of 1.45 kpc by Wright et al. (2015) and Hanson (2003), which is assumed in this work. A binary separation of 168 milli-arcsec (mas) is given by Niemela et al.

(1998), with the northern OB companion classified as an O8 I-IIf spectral type (Lépine et al., 2001). The O-star is given a terminal wind velocity, $v_\infty$(O), of 2000 km s$^{-1}$and a mass-loss rate, $\dot{M}$(O), of 1×10$^{-5}$ $M_\odot$ yr$^{-1}$ by Lépine et al. (2001).

The separation of the WR-star to the NT CWR ($r(WR)$) is given as 135 mas (O'Connor et al., 2005), suggesting a separation between the O-star and the NT CWR ($r(OB)$) of approximately 33 mas.

The terminal velocity of the southern, WR component, $v_\infty$(WR), is given by Eenens & Williams (1994) as 2900 km s$^{-1}$, Willis et al. (1997) state a value of 2700 km s$^{-1}$and give a $\dot{M}$(WR) of 2.6×10$^{-5}$ $M_\odot$ yr$^{-1}$(derived from 5 GHz radio data), where Lépine et al. (2001) give an $\dot{M}$(WR) of 6.9×10$^{-5}$ $M_\odot$ yr$^{-1}$(derived from the momentum flux). These parameters are listed in Table 5.1.

## 5.3 Observation

WR 146 was observed by the GMRT, near Pune, India, using the dual frequency setting which observed simultaneously at 235 and 610 MHz. The flux density calibrator used was 3C48 and the phase calibrator was 2052+365. The bandwidth was 32 MHz with 256 channels. The observation was made on 2012 November 4 for approximately 5 hrs and was on source for ∼3.5 hrs. The time on source was 30 mins, moving to the phase calibrator for 10 mins with the flux calibrator being observed for 10 mins at the beginning and the end of the observation. There were 4 antennas unavailable, leaving 26 used. The maximum baseline was approximately 25 km giving a resolution of ∼5.0 arcsec at 610 MHz and ∼13.0 arcsec at 235 MHz, see Table 5.2.

The data was reduced using the Astronomical Image Processing System (AIPS), with shorter wavelength baselines (<1 k$\lambda$) omitted, with self-calibration applied in order to reduce noise in the data.

## 5.4 Results

The final results reveal the detection of WR 146 at both frequencies. The resultant images of WR 146 from the data are illustrated in Fig. 5.4 and 5.5 which reveal the detections at both frequencies. The fluxes of WR 146 measured from the GMRT data were 56.8 mJy at 610 MHz

Table 5.1: Parameters of WR 146.

| parameter | value | unit | ref. |
|---|---|---|---|
| Northern O-star: | | | |
| spectral type | O8 I-IIf | | 1 |
| $v_\infty$ | 2000 | km $s^{-1}$ | 1 |
| $\dot{M}$ | $1\times10^{-5}$ | $M_\odot$ $yr^{-1}$ | 1 |
| $r_{OB}$ | 45 | mas | deduced |
| Southern WR-star: | | | |
| spectral type | WC6 | | 2 |
| $v_\infty$ | 2900 | km $s^{-1}$ | 3 |
| $v_\infty$ | 2700±200 | km $s^{-1}$ | 8 |
| $\dot{M}$ | $2.6\times10^{-5}$ | $M_\odot$ $yr^{-1}$ | 8 |
| $\dot{M}$ | $6.9\times10^{-5}$ | $M_\odot$ $yr^{-1}$ | 1 |
| $\dot{M}$ | $6.3\times10^{-5}$ | $M_\odot$ $yr^{-1}$ | 11 |
| $T_e$ | $10^4$ | K | 4 |
| $r_{WR}$ | 135±6 | mas | 5 |
| System: | | | |
| distance | 1.2±0.3 | kpc | 4 |
| distance | 0.75±0.1 | kpc | 8 |
| distance(min) | 1.25 | kpc | 9 |
| distance(CygOB2) | 1.45 | kpc | 10 |
| binary separation | 168 ±31 | mas | 7 |
| position angle | 21±4 | deg | 7 |
| period | ∼300 | years | 4 |
| period | >550 | years | 6 |

1: Lépine et al. (2001), 2: Herbig & Mendoza (1960), 3: Eenens & Williams (1994), 4: Dougherty et al. (1996), 5: O'Connor et al. (2005), 6: Setia Gunawan et al. (2003), 7: Niemela et al. (1998), 8: Willis et al. (1997), 9: Setia Gunawan et al. (2000), 10: Wright et al. (2015), 11: this paper.

Table 5.2: Details of the GMRT observations of WR 146

| Band (MHz) | B/width (MHz) | Date | Time (UT) (hr) | Flux calibrator | Phase calibrator | Resolution (arcsec) | rms (mJy $beam^{-1}$) |
|---|---|---|---|---|---|---|---|
| 610 | 32 | 2012 Nov 3 | 12:21-18:24 | 3C48 | 2052+365 | 5.0 | ∼0.2 |
| 235 | 32 | 2012 Nov 3 | 12:21-18:24 | 3C48 | 2052+365 | 13.0 | ∼2.0 |

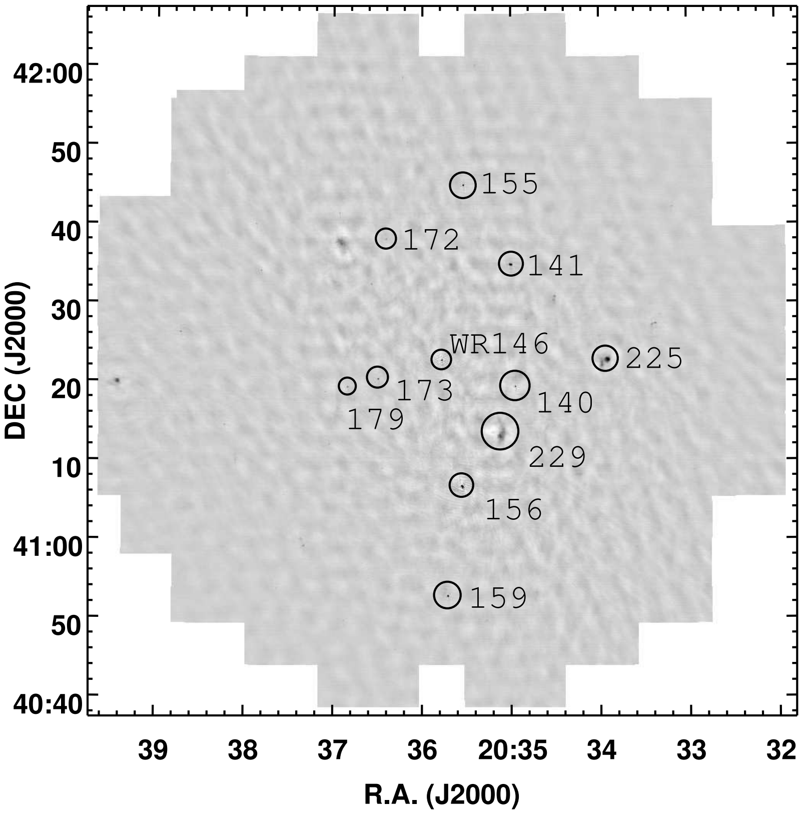

Figure 5.3: Detail of the full field of the 610 MHz observation indicating some of the SBHW sources also detected. See text for details

with an rms of 0.2 mJy beam$^{-1}$ and 32.5 mJy at 235 MHz with an rms of 2.0 mJy beam$^{-1}$, see Table 5.3.

Also detected are many sources at 610 MHz that also appear in the Setia Gunawan et al. (2003) survey, though only one other source appeared at 235 MHz (SBHW 156). Fig. 5.3 displays the whole field at 610 MHz detailing sources detected in the Setia Gunawan et al. (2003) survey, these are indicated by their SBHW survey reference numbers.

## 5.5 Non-Thermal Modelling

Previous radio and infra-red (IR) observations have resolved the southern WR component (Dougherty et al., 1996; Dougherty & Williams, 1999; Dougherty et al., 2000; O'Connor et al., 2005) and give fluxes which confirm a positive spectral index, $\alpha$, where the thermal flux $S \propto \nu^{\alpha}$

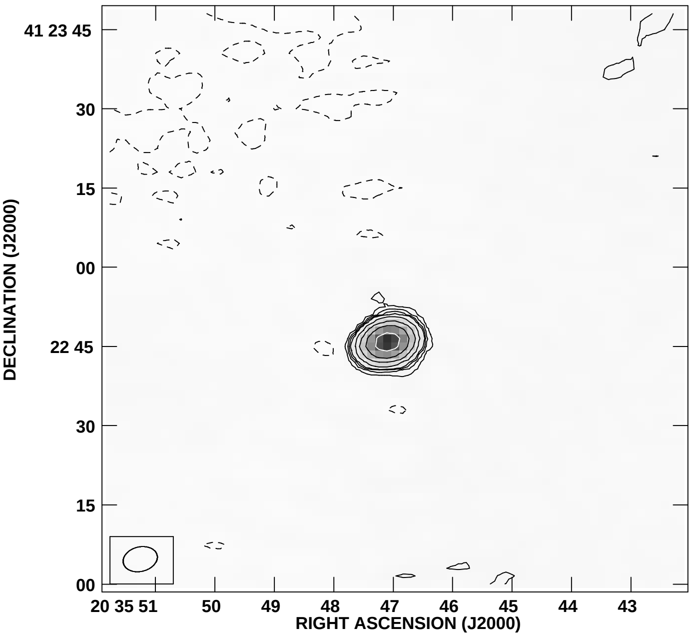

Figure 5.4: The 610 MHz GMRT data of WR 146, with $\sigma_{rms}$=0.2 mJy beam$^{-1}$, and contours at $\sigma_{rms}\times$ –3, 3, 6, 9, 12, 24, 48, 96, 192, 384. A synthesised beam of approx. 6.6 × 4.6 arcsec is shown bottom left. See text for details.

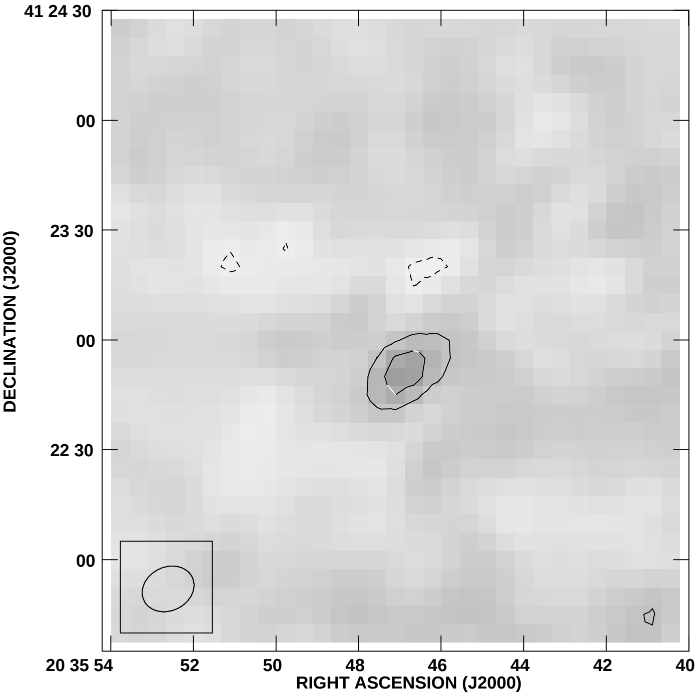

Figure 5.5: The 235 MHz GMRT data of WR 146, with $\sigma_{rms}$=2.0 mJy beam$^{-1}$ and contours at $\sigma_{rms}\times$ −3, 3, 6, 9, 12. A synthesised beam of approx. 14 × 12 arcsec is shown bottom left. See text for details.

Table 5.3: The fluxes measured from the GMRT observations of WR 146

| Freq (GHz) | $S_\nu$ (mJy) | error (mJy) | rms (mJy) |
|---|---|---|---|
| 0.610 | 56.8 | ±0.33 | 0.2 |
| 0.235 | 24.5 | ±4.8 | 2.0 |

Table 5.4: Previously published fluxes of WR 146, the 43 GHz values are estimated from O'Connor et al. (2005) Fig. 2.

| Epoch | Freq (GHz) | $S_{Total}$ | error | $S_S$ (mJy) | error | $S_N$ | error | ref & telescope |
|---|---|---|---|---|---|---|---|---|
| 1994 | 0.327 | 53 | 4 | – | – | – | – | 1 WSRT |
| 1996-7 | 1.4 | 66 | 2 | – | – | – | – | 1 WSRT |
| 1996 Oct 26 | 1.465 | 78.4 | 0.2 | – | – | – | – | 2 VLA |
| 1992 Dec 26 | 4.885 | 33.9 | 0.4 | 2.5 | 0.3 | 31.4 | 0.4 | 2 MERLIN |
| 1995 Apr 29 | 4.885 | 30.1 | 0.3 | 1.6 | 0.3 | 28.5 | 0.3 | 2 MERLIN |
| 1996 Oct 26 | 8.435 | 29.8 | 0.8 | – | – | – | – | 2 VLA |
| 1996 Oct 26 | 22.46 | 17.4 | 1.3 | 7.0 | 1.3 | 10.4 | 1.0 | 2 VLA |
| 2004 Oct 01 | 43 | ∼12 |  | ∼ 7 |  | ∼ 5 |  | 3 VLA |

1: Setia Gunawan et al. (2003), 2: Dougherty et al. (2000), 3: O'Connor et al. (2005)

(Wright & Barlow, 1975), suggesting that this is thermal emission from the WR stellar wind. Fluxes from these previous radio observations are plotted in Fig. 5.6, together with fluxes from this GMRT observation, these are also listed in Table 5.4.

Also shown on Fig. 5.6 are the results of fitting a power law model, $S \propto \nu^{\alpha}$, to the fluxes for the southern WR component, (the flux used for the fitting at 4.8 GHz was the average of the '92 and '95 data as in Dougherty et al. (2000)). This gives $\alpha$=0.8 in agreement with Dougherty et al. (2000) who give 0.82 ±0.14, the range of errors are also plotted.

### 5.5.1 A one component model

As detailed in paper 1, from the thermal fitting we calculate the theoretical thermal flux using the relationship $S_\nu = 7.0(\nu/22.46\mathrm{GHz})^{0.82}$ (mJy), from Skinner et al. (1999) and paper 1. To extract the NT fluxes from the total flux data, following the method in paper 1, we deduct the thermal flux from the observed total fluxes, these are listed in Table 5.5 and illustrated in Fig. 5.7. Using this NT data we have initially fitted a single component model with synchrotron

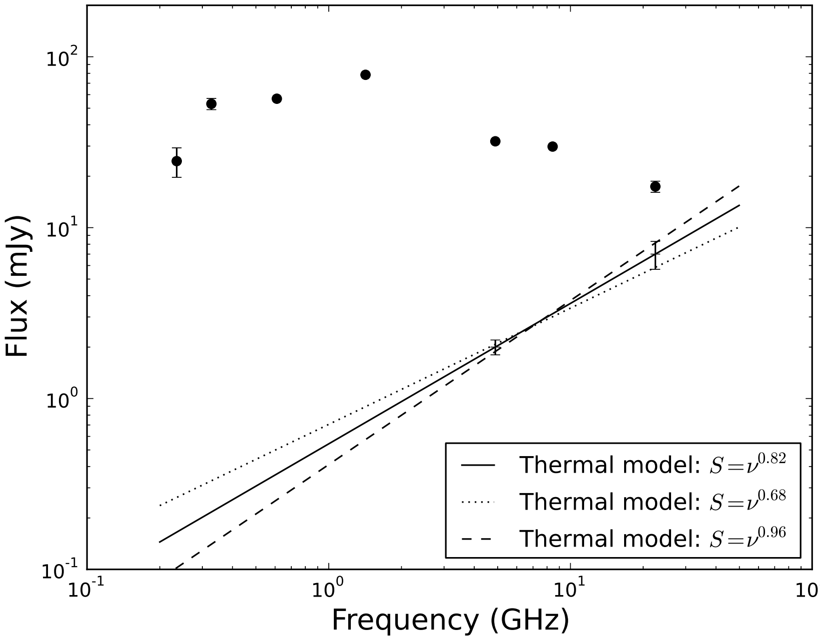

Figure 5.6: Plot of total fluxes for WR 146. Also shown are fluxes for the southern, thermal component, with a power law model fitted indicating a spectral index of 0.82±0.14 with the error range also plotted. Note some error bars are smaller than the points.

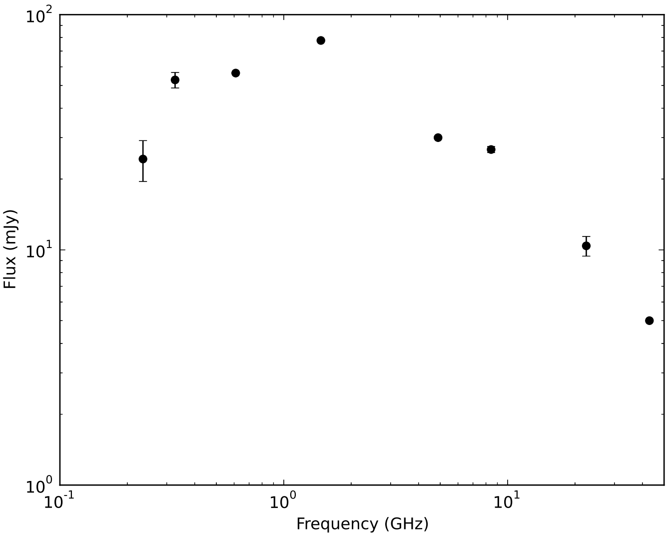

Figure 5.7: Plot of NT fluxes of WR 146, i.e. total minus thermal fluxes. Note some error bars are smaller than the points.

Table 5.5: Total observed fluxes of WR 146, $S_{total}$, together with flux from the observed resolved components at 4.8, 22 and 43 GHz, with the theoretical thermal flux $S_{thermal}$, and Non-thermal flux, $S_{NT}$, (NT=total – thermal flux). See text for details.

| Epoch | Freq (GHz) | $S_{total}$ | error | $S_{thermal}$ (mJy) | error | $S_{NT}$ | error | ref |
|---|---|---|---|---|---|---|---|---|
| 2012 Nov 04 | 0.235 | 24.5 | 4.8 | 0.17 | – | 24.33 | 4.8 | 3 |
| 1994 | 0.327 | 53 | 4 | 0.22 | – | 52.78 | 4 | 1 |
| 2012 Nov 04 | 0.610 | 56.8 | 0.33 | 0.36 | – | 56.44 | 0.33 | 4 |
| 1996 Oct 26 | 1.465 | 78.4 | 0.2 | 0.75 | – | 77.65 | 0.2 | 2 |
| 1992/1995 | 4.885 | 32.0 | 0.4 | 2.0 | 0.2 | 30.0 | 0.4 | 2 |
| 1996 Oct 26 | 8.435 | 29.8 | 0.8 | 3.1 | – | 26.7 | 0.8 | 2 |
| 1996 Oct 26 | 22.46 | 17.4 | 1.3 | 7.0 | 1.3 | 10.4 | 1.0 | 2 |
| 2004 Oct 01 | 43 | $\sim 12$ | 1.0 | $\sim 7$ | 1.0 | $\sim 5$ | 1.0 | 3 |

1: Setia Gunawan et al. (2003), 2: Dougherty et al. (2000), 3: O'Connor et al. (2005), 4: This paper

emission and free-free absorption of the form:

$$S_{mod}(\nu) = C\nu^{\alpha} e^{-\tau_1/\nu^{2.1}} \tag{5.1}$$

where $S_{mod}(\nu)$ is the model flux at frequency $\nu$ and constant $C$, spectral index $\alpha$ and $\tau_1$, the free-free absorption at an optical depth of 1 GHz, are the model parameters to be fitted. The best fit of this one component model is shown in Fig.5.8 with parameters listed in Table 5.6. This model suggests a turnover at $\sim$ 1 GHz, but does not produce a good fit to the data.

Benaglia et al. (2015) have fitted a similar one component model to a massive binary system, HD 93129A, with a separation between the two O type components of 2.7 arcsec. This result indicates a turnover at $\sim$ 3 GHz.

### 5.5.2 A two component model

We then added an extra component to the model to represent two regions of free-free absorption, of the form:

$$S_{mod}(\nu) = C1\,\nu^{\alpha_1}\,e^{-\tau_{1.1}/\nu^{2.1}} + C2\,\nu^{\alpha_2}\,e^{-\tau_{1.2}/\nu^{2.1}} \tag{5.2}$$

and then fitted this two component model to the data. We fitted this model fixing $\alpha_1$=$\alpha_2$=–1.0 to allow better fitting. The two component model produces a much better fit, see Fig. 5.9, with parameters listed in Table. 5.6. This is suggestive of turnovers at $\sim$ 0.4 and 1.4 GHz.

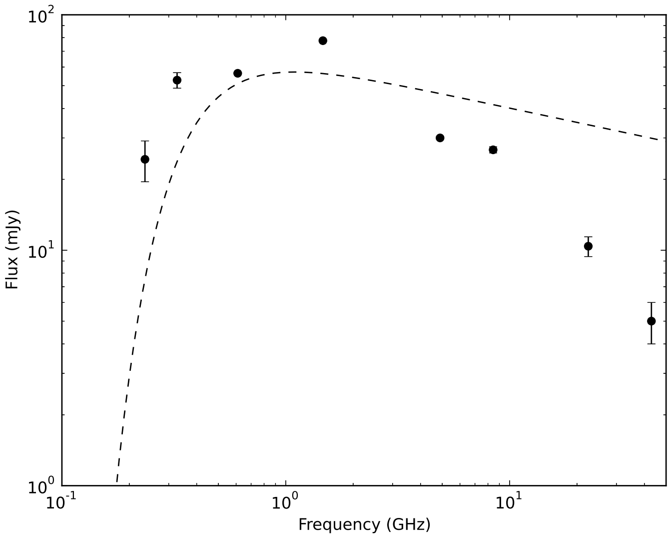

Figure 5.8: Plot of a 1-component model fitted to NT fluxes of WR 146. This suggests a turnover at ~1 GHz, though the model does not fit the data very well, see text for details.

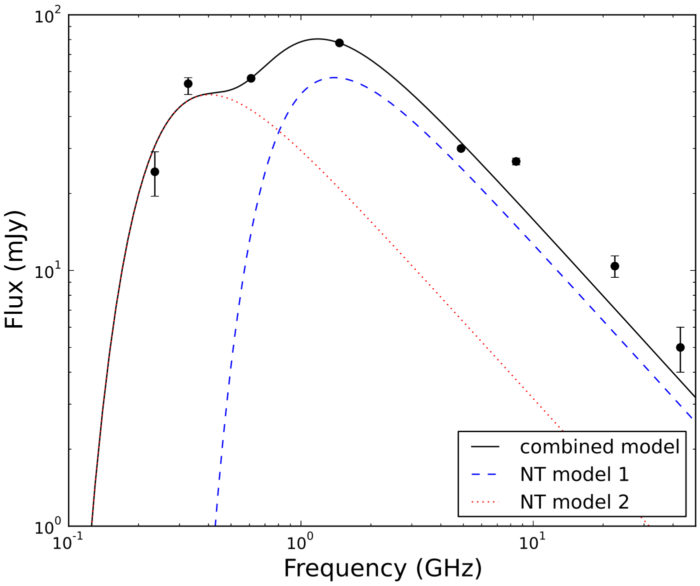

Figure 5.9: A Plot of the 2-component model fitted to the NT fluxes of WR 146.

Table 5.6: The one and two component model parameters

| Parameter | Best fit |
|---|---|
| One component model: | |
| $C1$ | 64.1 |
| $\alpha 1$ | $-0.20$ |
| $\tau_{1.1}$ | 0.12 |
| Two component model: | |
| $C1$ | 128 |
| $\tau_{1.1}$ | 0.96 |
| $C2$ | 31.6 |
| $\tau_{1.2}$ | 0.071 |

## 5.6 Discussion

Having determined approximate model parameters for the opacity of WR 146 we then attempt to determine opacity values from the calculated thermal flux, from which initially, we determined the $\dot{M}$(WR).

### 5.6.1 Mass-loss rates

From the thermal flux deduced above for the WR-star we calculated the mass-loss rate, $\dot{M}(WR)$, from the equation in the seminal paper by Wright & Barlow (1975):

$$\dot{M} = 0.095\,\frac{\mu\, v_\infty\, S_\nu^{3/4}\, d^{3/2}}{Z\, \gamma^{1/2}\, g^{1/2}\, \nu^{1/2}}\,(M_\odot \mathrm{yr}^{-1}) \tag{5.3}$$

where $\mu$ is the mean atomic weight of the gas, $v_\infty$ is the terminal velocity of the mass-loss flow in km s$^{-1}$, $S_\nu$ is the flux observed at frequency $\nu$ in Janskys, $d$, distance is in kpc, the frequency, $\nu$ is in Hz, $Z$ is the rms charge, $\gamma$ is the ratio of the electron number density to the ion number density and $g$ is the Gaunt factor as approximated by Allen (1973) as:

$$g_{ff} = 10.6 + 1.90\ \log_{10}\ T - 1.26\ \log_{10}\ (\nu\ Z). \tag{5.4}$$

At 610 MHz with $Z$=1.2, $\mu$=5.29, $\gamma$=1.15, as in Willis et al. (1997), $v_\infty(WR)$=2900 km s$^{-1}$, Eenens & Williams (1994), $d$=1450 pc, Wright et al. (2015), and $T$=10$^4$ K, Dougherty et al. (1996), we calculate a $\dot{M}(WR)$ of 7.9 $\times 10^{-5}$ $M_\odot$ yr$^{-1}$. This compares well with a previously published value of 6.9 $\times 10^{-5}$ $M_\odot$ yr$^{-1}$ by Lépine et al. (2001), which was derived from the momentum flux.

### 5.6.2 The free-free optical depth in WR 146

We repeat the method used in paper 1 to obtain the optical depth of WR 146. The free-free absorption optical depth, $\tau_{ff}$, can be written as:

$$\tau_{ff} = 3.3 \times 10^{-7} T_4^{-1.35} \nu_9^{-2.1} \int_0^\infty n_e^2 dl \tag{5.5}$$

where the Emission Measure, $EM$, ($\int_0^\infty n_e^2 dl$) is usually given in units of cm$^{-6}$ pc, appropriate for interstellar absorption, where $\nu_9$ is the frequency in GHz, $n_e$ is the electron number density and $T_4$ is the gas temperature in units of $10^4$ K. We shall assume that $T_4 \sim 1$.

As in paper 1, we assume that the NT emission originates from the region of the wind-wind interaction zone and calculate the expected free-free absorption using the estimated parameters of the component stars assuming that the WR wind dominates the free-free absorption.

Using our $\dot{M}(WR)$ value of 7.9 $\times 10^{-5}$ $M_\odot$ yr$^{-1}$, and assuming the wind is at terminal velocity with $v_\infty(WR) = 2900$ km s$^{-1}$, (Eenens & Williams, 1994). The distance to the system is assumed to be 1.45 kpc, (Wright et al., 2015), the stellar components are separated by a distance $r = 168$ mas, (Niemela et al., 1998), and the NT emission is $r_{NT} = 135$ mas from the WR-star, (O'Connor et al., 2005).

The wind density, $\rho$, at a radius $r_{WR}$ from the WR-star is given by:

$$\rho = \frac{\dot{M}(WR)}{4\pi r_{WR}^2 v_\infty(WR)} \tag{5.6}$$

and the electron number density $n_e = \rho/\mu_e$, where $\mu_e$ is the mean mass per electron in the wind:

$$\mu_e = \frac{1}{X + Y/2 + Z/2} \tag{5.7}$$

where $X$ is the hydrogen mass fraction, $Y$ is the helium mass fraction and $Z$ is the mass fraction of the remainder (Allen, 1973). Assuming a wind consisting of fully ionised helium, then $\mu_e = 2$ amu. This is most likely to be true in the inner wind of the WR component of WR 146. However, at some point in the wind, the helium will recombine to the singly ionised state and then $\mu_e = 4$ amu (Dessart et al., 2000).

From equation 5.8, the emission measure $EM \propto \mu_e^{-2}$, then this recombination potentially has a big effect on the free-free absorption. Because WR 146 is not a single star, the presence of the O-star and ionisation radiation from the wind collision will change the ionisation structure of the WR wind. This will limit what we can infer from simple modelling of the system.

If we assume that we are viewing the system from the side then we can show that:

$$\begin{aligned} EM &= \left(\frac{\dot{M}(WR)}{4\pi\mu_e\, v_\infty(WR)}\right)^2 A_{NT}^{-3} \int_0^{\pi/2} \cos^2\theta \, d\theta \\ &= \left(\frac{\dot{M}(WR)}{4\pi\mu_e\, v_\infty(WR)}\right)^2 A_{NT}^{-3} \left(\frac{\pi}{4}\right). \end{aligned} \tag{5.8}$$

Given the above values we have $EM = 1.7\ \times 10^6$ cm$^{-6}$ pc and $\tau_{ff} = 0.55$ at 1 GHz.

## 5.7 Conclusion

We have presented new simultaneous, low frequency detections of the colliding wind binary system, WR 146, at 235 and 610 MHz. We have modelled the NT turnover using a one component free-free absorption, synchrotron model which was not a good fit to the data. We then used a two component model, this was a better fit to the data illustrating that the region is complex with a number of different absorption regions. From the calculated thermal flux we derive a mass loss rate for the WR-star, $\dot{M}$(WR), of 7.9 $\times 10^{-5}$ $M_\odot$ yr$^{-1}$and an optical depth $\tau_{ff} = 0.55$ at 1 GHz.

The fitting of absorption models to the NT flux suggests more than one region of absorption, with turnovers between $\sim 0.4$ and 1.4 GHz.

This GMRT observation has improved our knowledge of the low frequency spectrum, observations with broad band receivers such as the planned SKA will further enable us to locate the turnover and spectral shape, increasing our understanding of processes in wind collision regions.

# Chapter 6

# Anatomy Of A Bow Shock: Multi-Wavelength Observations Of The Bow Shock Around The O4 Supergiant BD+43° 3654

*"In nature nothing exists alone."* Rachel Carson (1907-1964).

**Abstract**

We present results of a multi-wavelength analysis of the bow shock associated with the O4If supergiant, BD+43° 3654, a runaway star located near the Cygnus OB2 cluster and probably ejected from that cluster. New low-frequency radio Giant Metrewave Radio Telescope (GMRT) observations at 610 and 1.28 GHz show the bow shock clearly at both frequencies. We present and discuss multi-wavelength observations of the bow shock around BD+43° 3654, including IR data from the Wide-field Infra-red Survey Explorer (*WISE*) and *Herschel* as well as H$\alpha$ data from the INT/WFC Photometric H-Alpha Survey (IPHAS). We discuss the dynamics of the stellar wind/ISM interaction that gives rise to the bow shock, and the thermal and non-thermal emission associated with the bow shock and how multi-wavelength observations of bow shocks are key to understanding these important objects.

## 6.1 Introduction

### 6.1.1 Runaway stars and bow shocks

Many O–type stars ($\sim$ 25 per cent) have high spatial velocities ($30 - 200$ km s$^{-1}$) and lie far from the associations in which they were born (Blaauw, 1961; Gvaramadze & Gualandris, 2011). These high velocity stars are termed runaways (Blaauw, 1961), and currently there are two methods proposed to describe the ejection of these objects from their origins. The first method is the Binary Supernova Scenario (BSS; Blaauw 1961), where the runaway was ejected from a binary system when its companion has exploded as a supernova. The second method is the Dynamical Ejection Scenario (DES; Gies & Bolton 1986); here the runaway has been ejected after a single or $n$–body encounter in its original association.

As these massive stars move at high velocity through the ISM their strong stellar winds sweep up gas and dust to form a shell, where the ram pressures of the wind and ISM balance each other. Where the relative velocity between the star and the ISM is higher than the ISM sound speed an arc shaped bow shock (hereafter referred to as the BS) will occur (Weaver et al., 1977). The standard theory of BS structure is described by Weaver et al. (1977). The basic structure consists of a reverse (or wind termination) shock, which separates the highly supersonic (in the case of OB stars) stellar wind from the shocked wind. A forward shock separates the unshocked and shocked ISM, and between which is the contact discontinuity. Inefficient cooling of the low density shocked stellar wind will create a spatially extended, hot, low density gas layer between the free flowing wind and the contact discontinuity. For the case of gas, the mean free-paths are relatively short, meaning the regions should remain well separated, and the general properties will be quite similar to colliding winds (Stevens et al., 1992). As in colliding winds, hydrodynamic instabilities in the BS will affect the structure and dynamics of the post-shock material (Dgani et al., 1996; Blondin & Koerwer, 1998; van Marle et al., 2014).

In BSs, there is an extra complication caused by the presence of dust grains, either swept up from the ISM or indeed present in the wind itself (in the case of red giants winds - this is much less likely to be the case in BSs around OB stars, as discussed here). Diffuse radiation in the Galaxy was detected in the 1940's, Henyey & Greenstein (1941), which they then attributed to small particles. These dust grains are formed in the shells around evolved stars, (in the

RGB and AGB evolutionary stages), in the ejecta of type Ia and II supernovae and in the circumstellar shells around supergiants, novae, planetary nebulae and WC stars, these grains are then dispersed by the stellar wind into the ISM, (Jones, 2005). This dust is composed mainly of grains of silicates and carbon with sizes of up to at least 100 nm with an approximate dust to mass fraction of 0.01 or 1%, (Jones, 2005).

Dust grains, being much heavier than gas particles, are much less affected by the shocks, and can pass through the shocks or contact discontinuity. They are subject to drag and also to destruction in the environment of the BS (due to hot shocked gas). The drag forces mean the dust may be carried downstream in the flow or cross the contact discontinuity and travel at a different velocity to the gas. Cox et al. (2012a) have discussed some of the dust physics in BSs in the context of interactions between AGB stars and red supergiants and the ISM (Decin et al., 2012). In this context, Cox et al. (2012a) found that the majority of the dust emission for BSs around late type supergiant stars comes from the wind of the star itself, and only a small fraction is swept up ISM dust (see also Cox et al. (2012b)). For OB stars, we do not expect to see much dust in the hot, supersonic, radiatively drive winds, meaning the dust physics and interactions with the BS will be quite different. Important hydrodynamic simulations of the role of dust (and magnetic fields) in the BS of evolved late-type stars have been presented by van Marle et al. (2011) and van Marle et al. (2014).

In the context of OB star interactions, dust will be heated by the intense radiation field, and re-radiate at infra-red (IR) wavelengths (van Buren & McCray, 1988). In addition to IR emission, the BS will potentially emit in several different ways - the shocked stellar wind will produce free-free thermal emission (at X-ray and radio wavelengths, as well as H$\alpha$ emission), shock acceleration can produce relativistic particles, which can produce non-thermal radio, X-ray and $\gamma$-ray emission (del Valle & Romero, 2012). Recently, modeling has been undertaken by del Valle & Romero (2012) into these non-thermal processes in BSs.

In this paper we consider multi-wavelength observations of a particularly well observed BS, to investigate the range of complex physics and emission processes, that will shed light on stellar winds of massive stars and their interactions with the ISM.

The observed morphology of the BS is also an important consideration, and may show evidence for instabilities and so on. The shape of a BS is related to the inclination of the motion

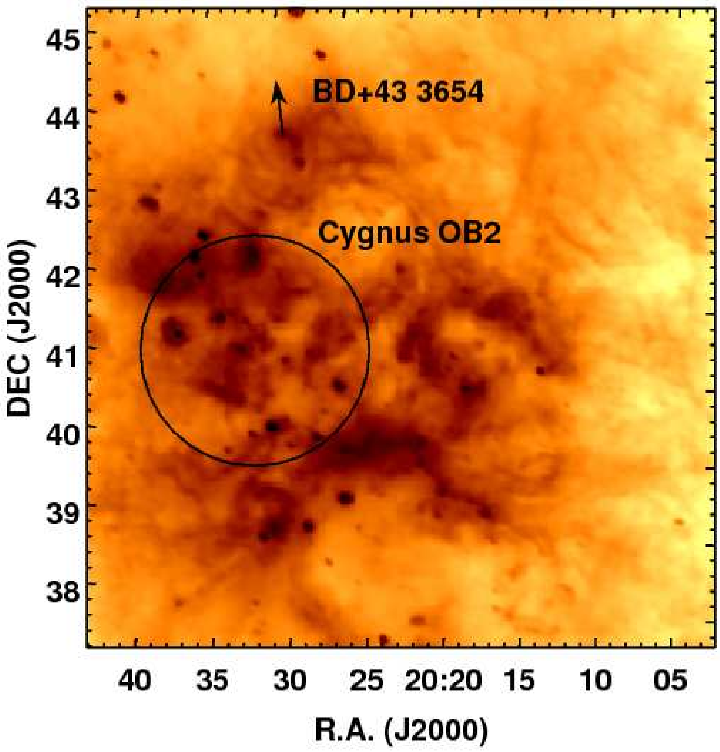

Figure 6.1: A wide angle *IRAS* 60$\mu$m image of the area surrounding BD+43° 3654. Indicated are the position of BD+43° 3654 (with the BS visible as well), the velocity vector of the stellar motion (see discussion of this in Section 6.5), and the extent of the Cygnus OB2 stellar cluster (the probable origin of BD+43° 3654).

of the star; therefore a star travelling in the plane of the sky will show an arc shaped BS, but as the stellar velocity nears the line of sight the BS will appear to become more circular - see for example Weaver et al. (1977), van Buren & McCray (1988) and del Valle & Romero (2012). Numerous studies have been made in the search for BS, see for example van Buren & McCray (1988), van Buren et al. (1995), Noriega-Crespo et al. (1997), Brown & Bomans (2005), Povich et al. (2008), Kobulnicky et al. (2010), Cox et al. (2012a) and the recent Extensive stellar Bow Shock Survey, first catalogue (E–BOSS I, Peri et al. 2012).

In this work we observe the BS shock structure around the massive O-type star, BD+43° 3654, at low radio frequencies to discover what structure can be detected and discuss the multiwavelength observations of this system. In Section 6.2 we describe the BD+43° 3654 runaway system. In Section 6.3 we describe our new GMRT observations. In Section 6.4 we discuss observations of BD+43° 3654 at other wavelengths, specifically other radio wavelengths, IR ( *WISE/Herschel* data), optical (H$\alpha$), and X-ray. In Section 6.5 we discuss the proper motion of BD+43° 3654 with respect to the local ISM and estimate the Mach number of the motion. In Section 6.6

we discuss the nature of the bow shock, temperature of the dust in the bow shock and provide constraints on the mass-loss rate of BD+43° 3654, which is important in understanding the bow shock. In Section 6.7 we discuss the nature of the Ellipsoidal Source (hereafter ES), which lies near the BS, and in Section 6.8 we summarise and conclude.

## 6.2 The Runaway Star BD+43° 3654

The massive star BD+43° 3654 has been classified as O4If by Comerón & Pasquali (2007), who estimated a mass of $70 \pm 15\ M_{\odot}$, an age of $\tau \sim 1.6$ Myr and a distance of $D = 1.45 \pm 0.4$ kpc. Comerón & Pasquali (2007) further calculated the proper motion of BD+43° 3654 with respect to its local ISM as $\Delta\mu_l \cos b = (5.3 \pm 1.1)$ mas yr$^{-1}$ and $\Delta\mu_b = (2.0 \pm 0.9)$ mas yr$^{-1}$, giving a proper motion in the plane of the sky of 5.7 mas yr$^{-1}$ with a position angle $\theta = 9.3° \pm 9.4°$ with respect to the North Galactic pole. The proper motion of BD+43° 3654 that we adopt in this paper is discussed in Section 6.5. Comerón & Pasquali (2007) also derive the component of the spatial velocity on the plane of the sky (derived from the residual proper motion at their adopted distance of $D = 1.45\,$kpc) of $39.8 \pm 9.8$ km s$^{-1}$, which corresponds to a Mach number of $\mathcal{M} = 5.7$, compared to the sound speed ($c_s$) of a warm neutral interstellar medium with a temperature of 8000 K ($c_s \sim 7\,$km s$^{-1}$).

The star was identified as a runaway by van Buren & McCray (1988) and is thought to originate from the Cygnus OB2 association where it may have been ejected by a three body encounter via the DES ejection method (Gvaramadze & Bomans, 2008). BD+43° 3654 is located at a projected distance of ∼ 3° (or ∼ 80 pc) from the centre of Cygnus OB2. For reference, a velocity of 100 km s$^{-1}$ corresponds to a motion of ∼ 100 pc Myr$^{-1}$.

Stellar parameters have also been obtained for this star by Kobulnicky et al. (2010), such as a heliocentric radial velocity of $-66.2 \pm 9.4\,$km s$^{-1}$and a very large mass loss rate of $1.6 \times 10^{-4}\,M_{\odot}$ yr$^{-1}$. We will discuss limits on the mass-loss rate of BD+43° 3654 in Section 6.6, which do suggest that BD+43° 3654 does have a very substantial wind. BD+43° 3654 also has a very fast wind, with a terminal velocity of $v_{\infty} = 2300\,$kms.

A BS like structure was first observed around this star by van Buren et al. (1995) in their *IRAS* survey of massive stars. The BS shape has now been observed at numerous IR wavelengths, several radio frequencies and has also been detected in the recent IPHAS H$\alpha$ survey

Table 6.1: Details of the GMRT observations of BD+43° 3654, with frequencies, dates and calibrators. $\sigma_{RMS}$ is the noise level in each of the observations.

| Band (GHz) | Bandwidth (MHz) | Date | Flux calibrator | Phase calibrator | Resolution ($''$) | $\sigma_{RMS}$ ($\mu$Jy beam$^{-1}$) |
|---|---|---|---|---|---|---|
| 0.610 | 16 | 2010 Nov 19 | 3C286/3C48 | 2052+3652 | 5.0 | 60 |
| 1.28 | 16 | 2010 Nov 15 | 3C286/3C48 | 2052+3652 | 2.4 | 42 |

(see Section 6.4. The region around the star contains many other bright sources and emission, for example the radio bright elliptical galaxy Cygnus A. See Fig 6.1 for a 60$\mu$m *IRAS* image of the region containing Cygnus OB2 and BD+43° 3654, showing that BD+43° 3654 is embedded in the dense interstellar material surrounding Cygnus OB2 (and which is probably connected to the BS being detectable). This image is taken from the IRAS Sky Survey Atlas (ISSA)[1] (Neugebauer et al., 1984).

## 6.3 New Low-Frequency GMRT Observations of BD+43° 3654

BD+43° 3654 was observed with the Giant Metrewave Radio Telescope (GMRT), located near Pune, India, at 1.28 GHz and 610 MHz in 2010 November 15 and 19 respectively. The pointing centre of the observations was near to the star ( $\alpha_{J2000}$= 20 33 40.0, $\delta_{J2000}$=+44 01 00), for 7.5 hr at each wavelength.

The flux density calibrators were 3C286 and 3C48, 2052+3652 was the phase calibrator. The bandwidth used for both frequencies was 16 MHz, with 128 channels. The time on source in a single scan was 30 minutes, moving to the phase calibrator for 10 minutes, with the flux calibrators observed at the beginning and end of the observations. All 30 antennas where used, giving a maximum baseline of approximately 25 km and a maximum resolution of $\sim 5.0''$ at 610 MHz and $2.4''$ at 1.28 GHz (see Table 6.1 for details).

Data reduction was performed, using standard methods, with the Astronomical Image Processing System (AIPS), then analysed using GAIA[2] and DS9 (Joye & Mandel, 2003). The images produced are shown in Fig. 6.2, with a pixel size of $1''$ for both frequencies and a synthesised

---

[1] http://irsa.ipac.caltech.edu/IRASdocs/issa.html

[2] Graphical Astronomy and Image Analysis tool, part of the Starlink software project, http://starlink.jach.hawaii.edu/starlink.

beam size of 22″ at 610 MHz and 40″ at 1.28 GHz, as indicated in the top right corner of each image.

The 610 MHz and 1.28 GHz emission from the BD+43° 3654 are shown in Fig. 6.2. The position of BD+43° 3654 is marked with a cross and the direction of proper motion indicated by the arrow (see Section 6.4 for a discussion of the velocity vector of BD+43° 3654). The arc shape of the BS is seen at both frequencies with an emission peak approximately aligned in the direction of the velocity vector of the star. We will discuss the peak of the radio emission (termed the "Hot-Spot"), which also coincides with peak of the emission at other wavelengths, in Section 6.6.5.

At 1.28 GHz the BS shows a large extension to the right, but this could be unrelated emission. At both frequencies there is a perpendicular emission feature crossing the left hand portion of the BS. From our view of the dust emission (see the later discussion associated with Fig. 6.13) this may well be unrelated to the BS. Above the BS is a prominent featured, termed the Ellipsoidal Source (ES) by Benaglia et al. (2010). We discuss the nature of this complex source in Section 6.7.

We discuss the nature of the BS, as seen in radio and other wavelengths, in Section 6.6.

## 6.4 The BD+43° 3654 Bow Shock at Other Wavelengths

### 6.4.1 Other radio data

The region around BD+43° 3654 has been previously observed at several other radio wavelengths, namely with the VLA (as pointed observations at 1.4 GHz and 4.86 GHz, Benaglia et al., 2010) and as part of the NVSS at 1.4 GHz, though at lower resolution), and by the WSRT at 325 MHz, as part of the WENSS survey.

#### VLA Pointed observations: 1.4 GHz and 4.86 GHz

Benaglia et al. (2010) used the VLA to observe this BS region at 1.42 and 4.86 GHz (observations with 50 MHz bandwidth). The BS was detected at both wavelengths, showing an arc-like morphology. The goal of this work was to look for non–thermal radio emission from the BS, as evidence of a relativistic particle population. These authors found that the emission from the BS was predominantly thermal.

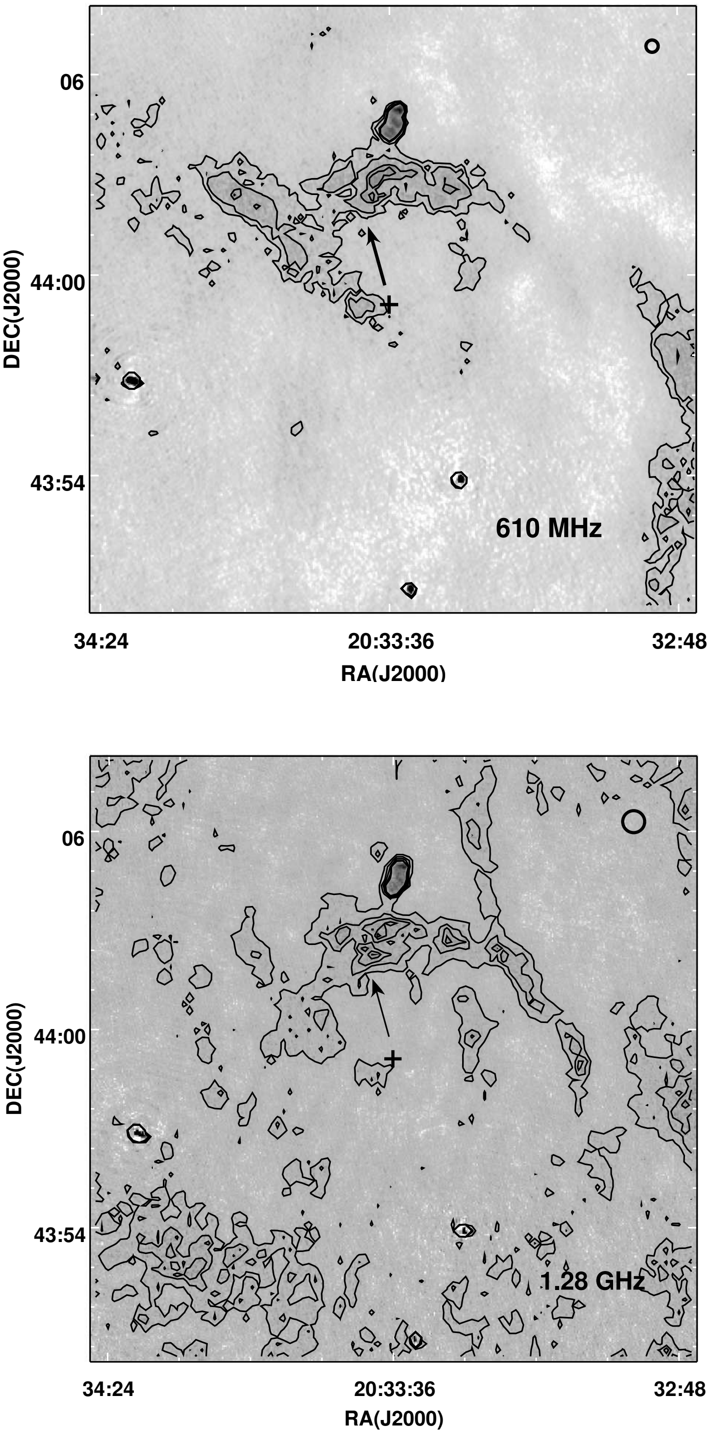

Figure 6.2: The GMRT data for the bow shock around BD+43° 3654. Top panel: The 610 MHz data, with contours shown at 0.1, 0.175, 0.25, 0.325 and 0.4 mJy beam$^{-1}$. A synthesised beam of 22" × 22" is shown in the top right of image. Lower panel: The 1.28 GHz data, with contours at 0.025, 0.07, 0.11, 0.16 and 0.2 mJy beam$^{-1}$, with a synthesised beam of 40" × 40" shown in the top right of image. For both images, the field of view is 0.3° × 0.3°, centred on the position of BD+43° 3654, marked by a cross, with the proper motion of the star indicated by a vector.

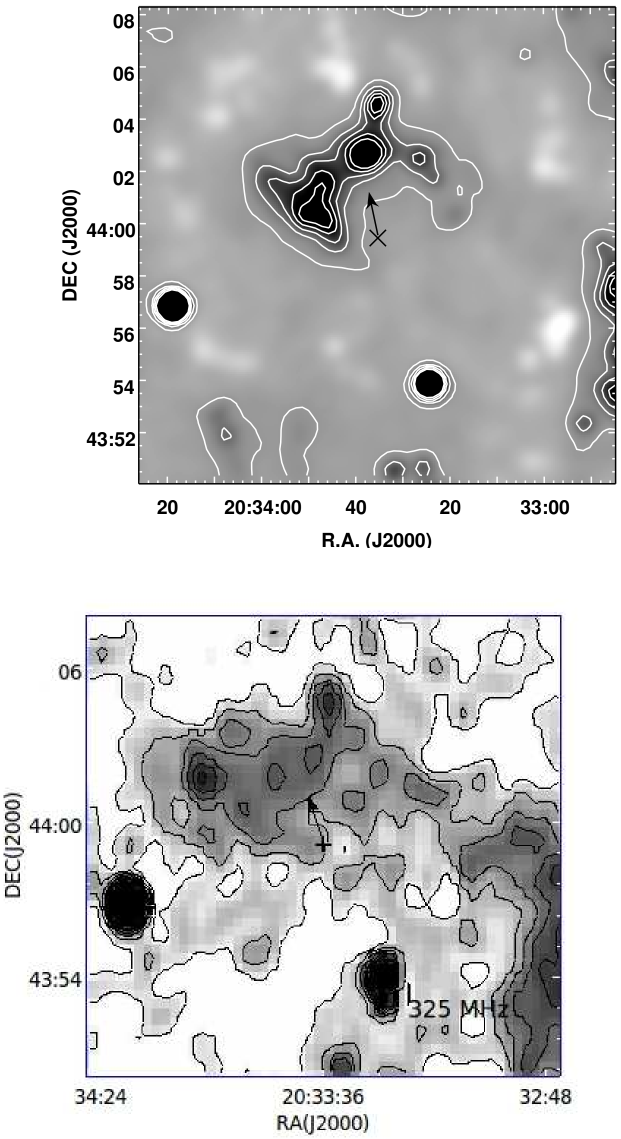

Figure 6.3: The bow shock of BD+43° 3654 observed at other radio frequencies: Top panel: Low resolution 1.4 GHz data from the NVSS. The contours shown start at 1.5 mJy beam$^{-1}$, rising with intervals of 4.625 mJy beam$^{-1}$. Lower panel, WENSS data at 325 MHz, with the lowest contour at 15 mJy beam$^{-1}$ and rising at intervals of 17.5 mJy beam$^{-1}$. The field of view is 0.3° × 0.3°, centred on the position of BD+43° 3654. The location of BD+43° 3654 is marked, along with the velocity vector.

### WENSS: 325 MHz

The BD+43° 3654 region was observed at 325 MHz by the WSRT as part of the Westerbork Northern Sky Survey (WENSS) [3], and the data is shown in Fig. 6.3. The WENSS data is of a much lower resolution than the GMRT data (with a resolution of 54 $cosec\delta$ arcsec, with $\delta$ the declination). The BS and ES are detected but the arc-like morphology is not as apparent.

### NVSS 1.4 GHz

The BD+43° 3654 BS is also detected in the NVSS at 1.4 GHz. The NVSS has lower resolution (typical $45''$) and is capable of detecting point sources with a flux greater than $\sim$ 2.5 mJy. The arc-like morphology is clearly seen in the NVSS (Fig. 6.3).

Great care must be taken when comparing derived fluxes from different arrays. The NVSS had a $45''$ beam and a total of typically 27 antennas within a distance of 1 km (observations done in the D-array configuration) and this enabled the detection of extended diffuse emission. The higher resolution GMRT observations resolved a lot of this diffuse emission out. While in principle we could taper the GMRT data to match the NVSS beam, in practice the GMRT only has a maximum of 12 antennas with the central square. The GMRT flux density at 1.28 GHz is lower than that at 1.4 GHz from NVSS, due to poor short spacing UV coverage with GMRT. We do not attempt to generate a radio spectral energy distribution (SED) using the data from the various arrays.

## 6.4.2 Infrared data

Bow shocks around massive stars can be most readily found by looking for IR emission from hot dust (Peri et al., 2012, 2015). The region around BD+43° 3654 has been observed by a number of IR satellites and we will summarise these observations here and discuss their implications on the BS structure later.

### WISE

The *WISE* satellite (Wright et al., 2010) has surveyed the entire sky at 4 different bands, which we shall refer to as W1, W2, W3 and W4. WISE Band 1 (W1) at 3.4$\mu$m; Band 2 (W2) at

---

[3] http://www.astron.nl/wow/testcode.php?survey=1

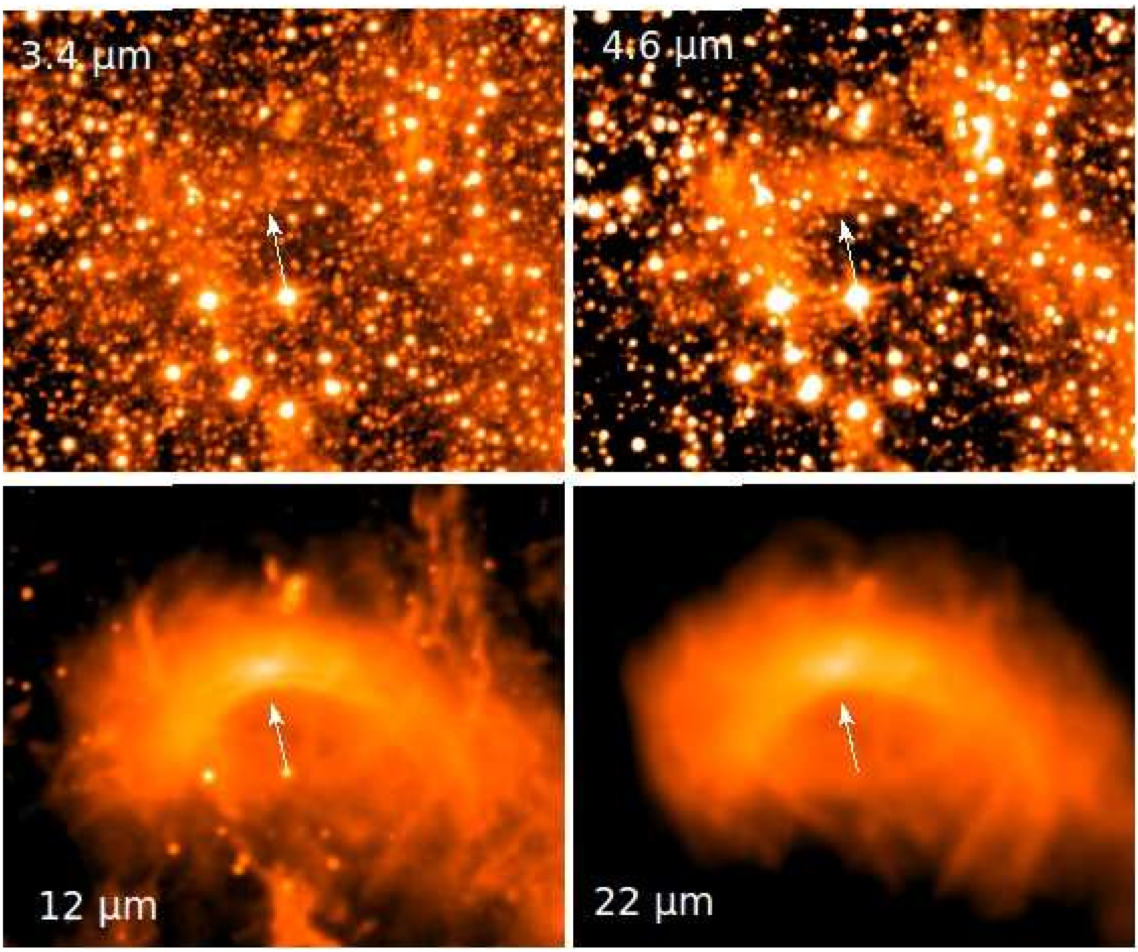

Figure 6.4: Montage of the 4 *WISE* bands centred on the position of BD+43° 3654. Top left, *WISE* W1 3.4 $\mu$m; top right, *WISE* W2 4.6 $\mu$m; bottom left, *WISE* W3 12 $\mu$m; bottom right, *WISE* W4 22 $\mu$m. The BS is clearly visible in W3 and W4, and is just visible in the W2 band. The field of view of all images is 0.3° × 0.3°.

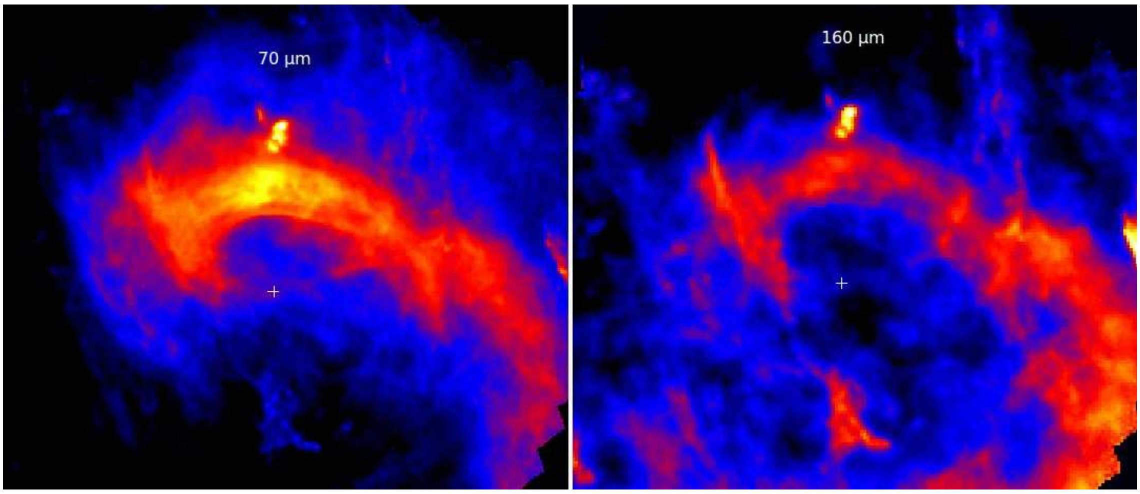

Figure 6.5: The *Herschel* data at 70$\mu$mand 160$\mu$m. The field of view of both images is 0.3° × 0.3°. The ES is clearly visible in both images.

4.6$\mu$m; Band 3 (W3) at 12$\mu$m; Band 4 (W4) at 22$\mu$m. The spatial resolution of the *WISE* data is 6.1″, 6.4″, 6.5″ and 12.0″ for bands W1–W4 respectively. As we shall see, the WISE data is very well suited to observe hot dust in the BS.

A montage of the *WISE* data in all 4 bands is shown in Fig. 6.4. The BS is very clearly seen in bands W3 and W4, showing a very clear arc-like morphology, that is broadly very similar to that seen in the GMRT data. In W3, the emission shows a considerable amount of linear substructure within the BS.

The BS is also seen very faintly in band W2 and in W1. The star BD+43° 3654 is visble in bands W1, W2 and W3, but is not apparent in band W4. We will discuss the SED of BD+43° 3654 in Section. 6.6.6. An overlay of GMRT 1.28 GHz data on top of the WISE W3 image is shown in Fig. 6.7, showing the general similarity in morphology between the 2 bands, except that the IR emission is rather broader.

### Herschel

The *Herschel Space Observatory* operated between 2009 and 2013. The BD+43° 3654 region was observed with the PACS instrument (PI N. Cox). In Fig. 6.5 we show the 70$\mu$m and 160$\mu$m images, downloaded from the IPAC database. The BS is detected clearly as a complex arc-like structure at both wavelengths. The ES is also clearly visible at both wavelengths, along with a considerable amount of additional emission. The combination of *WISE* and *Herschel* data

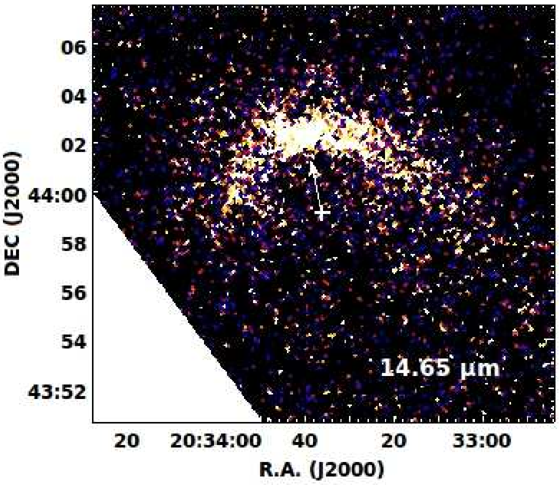

Figure 6.6: The *MSX* (14.65 $\mu$m) view of the BD+43° 3654 bow shock.

allows us to investigate the nature of the dust emission from the BS (Section 6.6).

### MSX

The region around BD+43° 3654 has also been observed at 14.65$\mu$m (bandwidth 12.88–16.34 $\mu$m) in the Mid-course Space eXperiment survey (*MSX*, Egan et al. 2003a), with a spatial resolution of 18″. The *MSX* data is shown in Fig. 6.6, and again shows an arc-like morphology.

### IRAS

The BS is also seen at low resolution in surveys using data from the *IRAS* satellite. For instance, in the Mid–Infrared Galaxy Atlas (MIGA, Kerton & Martin 2000) at 25$\mu$m (19–30$\mu$m bandwidth), the *IRAS* Galaxy Atlas (IGA, Cao et al. 1997) at 60$\mu$m (40–80$\mu$m bandwidth) and at 100$\mu$m (83–120$\mu$m bandwidth) in the Improved Reprocessing of the *IRAS* Survey (IRIS, Miville-Deschênes & Lagache 2005). We note that van Buren & McCray (1988) used *IRAS* data to search for BS around massive stars.

## 6.4.3 H$\alpha$ emission

In addition to the radio and IR regimes, BD+43° 3654 has also been observed at higher frequencies. The INT/WFC Photometric H$\alpha$ Survey of the Northern Galactic Plane (IPHAS, Drew et al. 2005), includes the area around BD+43° 3654 and shows the star and ES clearly visible,

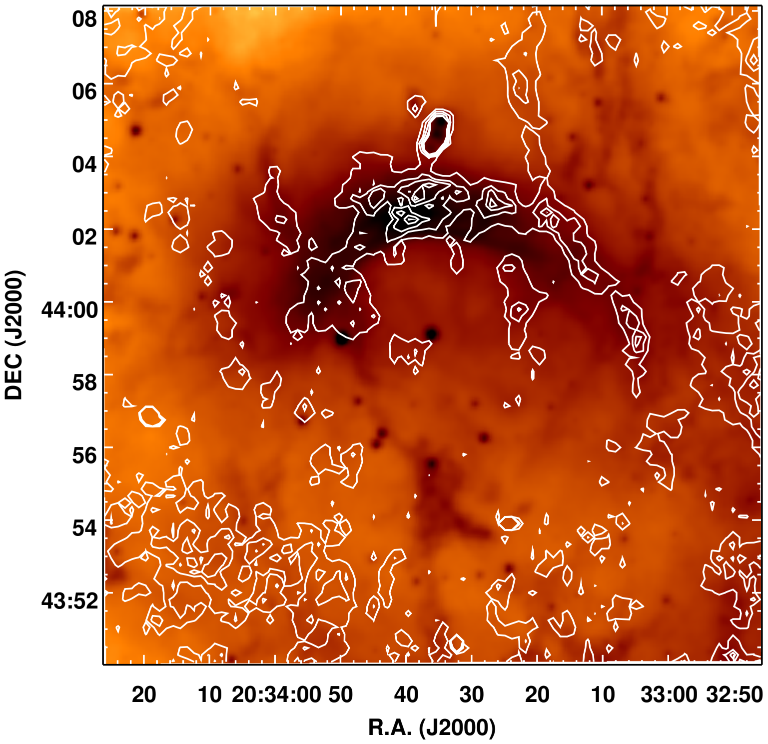

Figure 6.7: An overlay of contours from the 1.28 GHz GMRT data on the *WISE* W3 (12$\mu$m) image.

with the BS showing faint but discernible emission, particularly associated with the 'hot-spot' region discussed later. See Fig. 6.8 which also includes an image of the H$\alpha$ data overlaid with 1.28 GHz GMRT radio contours. This was compiled using ds9 after matching coordinates of both data sets. This overlay indicates possible alignment with the BS peak emission. The IPHAS images are currently not flux calibrated and we do not attempt to discuss flux values in this paper.

### 6.4.4 High–energy emission: X-ray and $\gamma$-ray

The region around BD+43° 3654 has been observed with both the *Suzaku* and *XMM-Newton* satellites, though with no clear detection of emission. We might expect such emission as the fast wind of BD+43° 3654 is shocked to high temperatures.

Terada et al. (2012) discuss observations of BD+43° 3654 with the *Suzaku* satellite. These observations shows no significant evidence of X-ray emission associated with the BS. BD+43° 3654 was detected and the X-ray spectra fitted with a thermal MEKAL model with $kT \sim 0.6$ keV and a luminosity of $L_X \sim 3.7 \times 10^{31}$ erg s$^{-1}$, values very typical of O-stars.

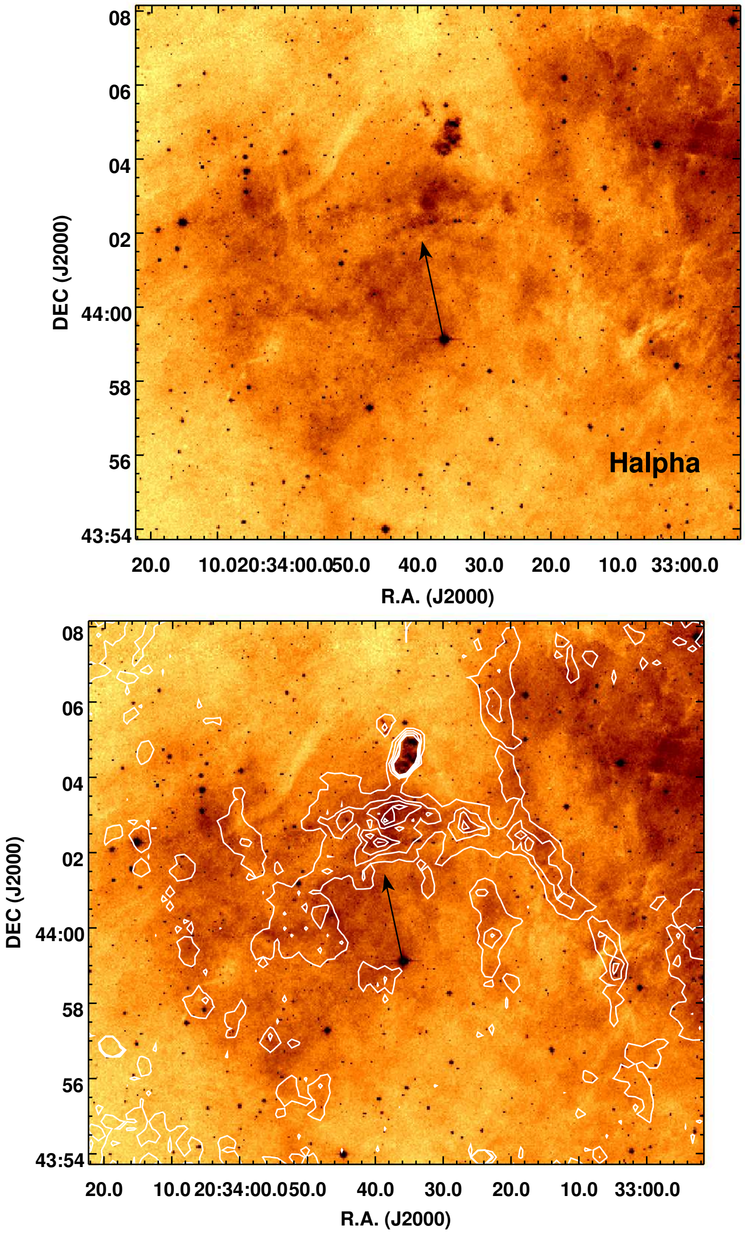

Figure 6.8: Top panel: IPHAS H$\alpha$ observations of BD+43° 3654 the field is 0.25° × 0.25° centred just above BD+43° 3654. Lower panel: GMRT 1.28 GHz radio contours overlaid onto the H$\alpha$ image. The H$\alpha$ peak emission coincides with the brightest radio emission.

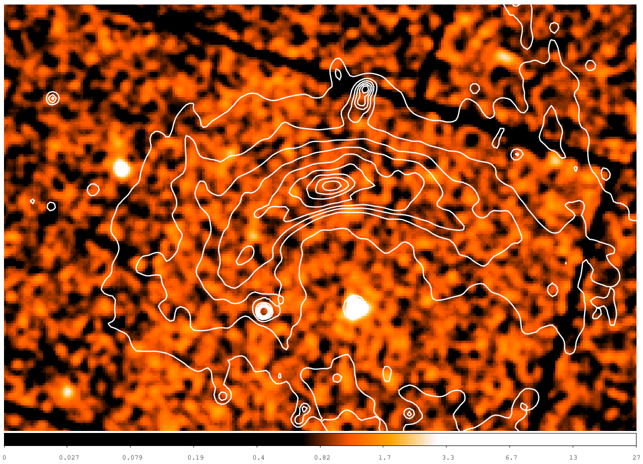

Figure 6.9: The BD+43° 3654 field as seen with *XMM-Newton*, with contours of the bow shock, as seen in the *WISE* 3 image superimposed. This is the MOS-2 data from the *XMM-Newton* XSA with minimal processing. The star BD+43° 3654 is clearly detected at X-ray energies, but the BS is not.

In addition, there is also an archival *XMM-Newton* observation of BD+43° 3654. The data were taken in 2010 (PI Zabalza). This observation was nominally for 43 ksec, however, the data was affected by flaring, reducing the usable data significantly. The *XMM Newton* image (taken straight from the *XMM-Newton* archive), with WISE W3 data overlain is shown in Fig. 6.9. BD+43° 3654 is clearly detected in the *XMM-Newton* observation as well. At even higher energies, possible detection of $\gamma$-ray emission from the BS is discussed by Benaglia et al. (2010), though no evidence has been found (see also del Valle & Romero 2012).

## 6.5 The Velocity Vector of BD+43° 3654

Before we go on to discuss the multi-wavelength structure of the BD+43° 3654 BS, it is important to estimate the speed and direction of motion of the runaway. As it apparent from Fig. 6.1, BD+43° 3654 is moving through a complex region in the vicinity of Cygnus OB2.

As discussed in Section 6.2, Comerón & Pasquali (2007) derived an estimate of the relative motion of BD+43° 3654 with respect to the local ISM, correcting for Galactic rotation. In this section, we repeat these calculations using different estimates of the relevant parameters.

There have been a number of estimates of the proper motion of BD+43° 3654 and we list those in Table 6.2 for completeness. We take as our basic data the new estimate of proper motion of BD+43° 3654 from the UCAC4 compilation (Zacharias et al. (2013)). The observed proper

Table 6.2: Observations of the proper motion of BD+43° 3654 (J2000 coordinates).

| Catalogue | $\mu_\alpha \cos\delta$ ( mas yr$^{-1}$) | $\mu_\delta$ ( mas yr$^{-1}$) | Reference |
|---|---|---|---|
| Tycho-2 | $0.5 \pm 1.3$ | $2.0 \pm 1.3$ | Høg et al. (2000) |
| NOMAD | $-0.4 \pm 0.7$ | $1.3 \pm 1.0$ | Zacharias et al. (2004) |
| PPMXL | $0.9 \pm 1.3$ | $1.6 \pm 1.3$ | Roeser et al. (2010) |
| UCAC4 | $-0.3 \pm 0.5$ | $1.1 \pm 0.9$ | Zacharias et al. (2013) |

motions of BD+43° 3654 are $\mu_\alpha \cos\delta = -0.3 \pm 0.5$ mas yr$^{-1}$ and $\mu_\delta = 1.1 \pm 0.9$ mas yr$^{-1}$. It is more convenient to work in Galactic coordinates and these values convert to $\mu_l \cos b = 0.7 \pm 0.8$ mas yr$^{-1}$ and $\mu_b = 0.9 \pm 0.7$ mas yr$^{-1}$.

We use two different models of Galactic rotation in order to investigate any difference. The first uses results from Feast & Whitelock (1997), who determined the Galactic rotation from the proper motions of Cepheid variables, using data from *Hipparcos*. This model is essentially the same as used by Comerón & Pasquali (2007), though with somewhat different values of the constants. The second uses the Galactic rotation model of Torra et al. (2000), based on data from OB stars.

### 6.5.1 The Feast & Whitelock Galactic rotation model

From Feast & Whitelock (1997), the Galactic rotation velocity field can be expressed as

$$\begin{aligned} k(\mu_l \cos b)_\odot &= A \cos 2l \cos b + B \cos b \\ &\quad + (U_\odot/D) \sin l - (V_\odot/D) \cos l \qquad (6.1) \\ k(\mu_b)_\odot &= -A \sin 2l \sin b \cos b + (U_\odot/D) \cos l \sin b \\ &\quad - (V_\odot/D) \sin l \sin b - (W_\odot/D) \cos b \qquad (6.2) \end{aligned}$$

where $U_\odot$, $V_\odot$ and $W_\odot$ are the solar peculiar motions, $A$ and $B$ are Oort constants, and $D$ is the assumed distance to BD+43° 3654 ($D = 1.45\,\mathrm{kpc}$).

We assume the following values (Feast & Whitelock, 1997):

$A = 14.82 \pm 0.84\,\mathrm{km\ s^{-1} kpc^{-1}}$

$B = -12.37 \pm 0.64\,\mathrm{km\ s^{-1} kpc^{-1}}$

$U_\odot = 9.3 \pm 0.80\,\mathrm{km\ s^{-1}}$

$V_\odot = 11.18 \pm 0.55\,\mathrm{km\ s^{-1}}$

$W_\odot = 7.61 \pm 0.64\,\mathrm{km\ s^{-1}}$,

with $k = 4.741$, the unit conversion factor between mas $\mathrm{yr^{-1}}$ and km $\mathrm{s^{-1}}$ $\mathrm{kpc^{-1}}$.

The proper motion of BD+43° 3654 with respect to the local ISM is then given by

$$\Delta\mu_l \cos b = \mu_l \cos b - (\mu_l \cos b)_\odot \tag{6.3}$$

and

$$\Delta\mu_b = \mu_b - (\mu_b)_\odot \tag{6.4}$$

with the angle of motion given by

$$\theta = \tan^{-1} \frac{\Delta\mu_l \cos b}{\Delta\mu_b} \tag{6.5}$$

with the angle $\theta$ measured from the North Galactic pole, with $\theta$ increasing with increasing $l$.

Given the large number of terms with error bars, the error analysis has been done using a Monte-Carlo method. With these assumptions we find that the corrected proper motions are $\Delta\mu_l \cos b = 5.20 \pm 0.82$ mas $\mathrm{yr^{-1}}$ and $\Delta\mu_b = 1.96 \pm 0.68$ mas $\mathrm{yr^{-1}}$, and the direction of the residual proper motion of BD+43° 3654 with respect to the local ISM is $\theta = 69.6^\circ \pm 5.9^\circ$. Here, $\theta$ is the angle between the North Galactic Pole and the proper motion vector, measured in a direction of increasing Galactic longitude $l$.

The corresponding velocity with respect to the ISM at $D = 1.45\,\mathrm{kpc}$ is then $38.4 \pm 6.2\,\mathrm{km\ s^{-1}}$, and implies a Mach number of the residual proper motion with respect to the local ISM of $\mathcal{M} \sim 5$ (assuming a warm neutral ISM with $T \sim 8000\,\mathrm{K}$).

### 6.5.2 The Torra et al. Galactic rotation model

As a check on these results, we have also used a different model for the Galactic rotation field, derived by Torra et al. (2000), using data for OB stars. Using their results for the region of $0.6\,\mathrm{kpc} < D < 2\,\mathrm{kpc}$, we have that the Galactic rotation velocity field is given by:

$$\begin{aligned} k(\mu_l \cos b)_\odot &= A\cos 2l \cos b + B\cos b - C\sin 2l \cos b \\ &\quad +(U_\odot/D)\sin l - (V_\odot/D)\cos l \qquad (6.6) \\ k(\mu_b)_\odot &= -A\sin 2l \sin b \cos b - C\cos 2l \sin b \cos b \\ &\quad -K\sin b\cos b + (U_\odot/D)\cos l \sin b \\ &\quad -(V_\odot/D)\sin l \sin b - (W_\odot/D)\cos b \qquad (6.7) \end{aligned}$$

where $U_\odot$, $V_\odot$ and $W_\odot$ (and $D$ and $k$) are as before and $A, B, C, K$ are Oort constants. We assume the following values (Torra et al., 2000): $A = 13.0 \pm 0.7\,\mathrm{km\ s^{-1}kpc^{-1}}$
$B = -12.1 \pm 0.7\,\mathrm{km\ s^{-1}kpc^{-1}}$
$C = 0.5 \pm 0.8\,\mathrm{km\ s^{-1}kpc^{-1}}$
$K = -2.9 \pm 0.6\,\mathrm{km\ s^{-1}kpc^{-1}}$
$U_\odot = 8.0 \pm 0.8\,\mathrm{km\ s^{-1}}$
$V_\odot = 13.4 \pm 0.7\,\mathrm{km\ s^{-1}}$
$W_\odot = 8.3 \pm 0.5\,\mathrm{km\ s^{-1}}$.

Given these assumptions we find that $\Delta\mu_l \cos b = 4.9 \pm 0.8$ mas yr$^{-1}$ and $\Delta\mu_b = 2.0 \pm 0.7$ mas yr$^{-1}$, and the direction of the residual proper motion of BD+43° 3654 with respect to the local ISM is $\theta = 67.8 \pm 6.1$ (defined as before).

The corresponding velocity with respect to the ISM at $D = 1.45\,\mathrm{kpc}$ is then $36.5 \pm 6.2\,\mathrm{km\ s^{-1}}$, and implies a Mach number of the residual proper motion with respect to the local ISM of $\mathcal{M} \sim 5$, assuming a warm neutral ISM with $T \sim 8000\,\mathrm{K}$.

Studies of different Galactic rotation models have revealed mainly small discrepancies (Ninkovic et al., 2002; Zhu, 2009), with similar agreement to velocities of observed stars in the Galactic disc (Ninkovic et al., 2002). In agreement with this, the conclusion from the above analysis is that the results using the model of Feast & Whitelock (1997) and Torra et al. (2000) are very similar to each other, and both are very similar to the results obtained by Comerón & Pasquali (2007). Kobulnicky et al. (2010) determined that the heliocentric radial velocity of BD+43° 3654 was $V_{LSR} = -66.2 \pm 9.4\,\mathrm{km\ s^{-1}}$ and noted that this is considerably more negative than the mean velocity of O-stars in Cyg OB2 (with $V_{LSR} = -10\,\mathrm{km\ s^{-1}}$). This opens up the possibility that BD+43° 3654 has a substantial component of motion with respect to the ISM out of the plane

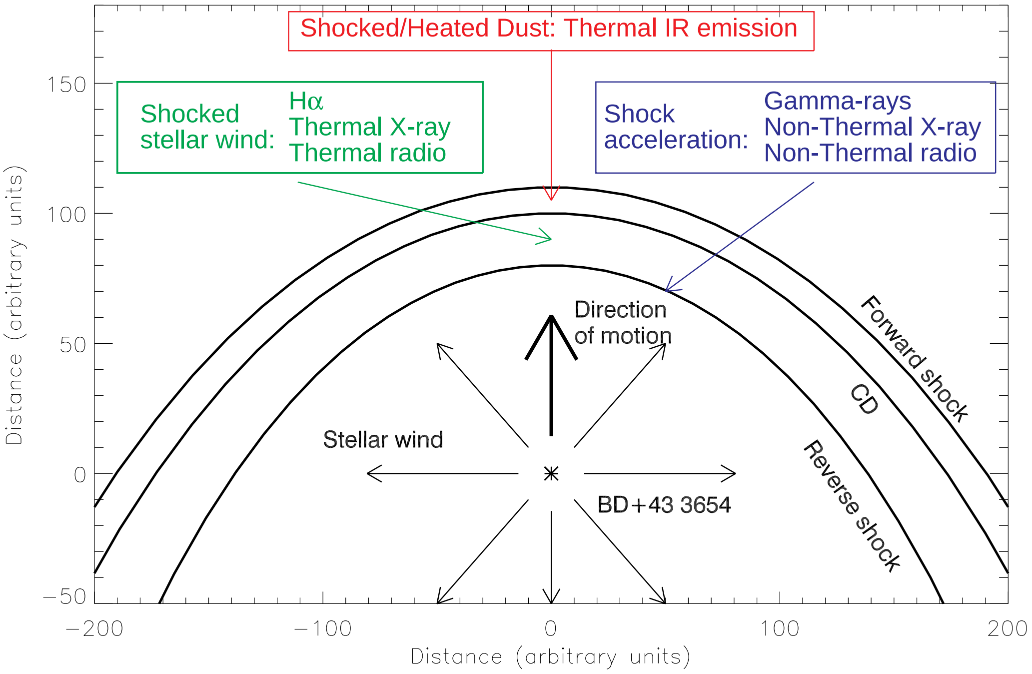

Figure 6.10: A schematic view of the structure and emission regions associated with the BS of BD+43° 3654. The sketch shows the two shocks and the contact discontinuity, and the likely location of emission regions at different wavelengths. In reality, the BS region will be more complex than this with instabilities and so on.

of the sky. On the other hand the morphology suggest the motion with respect to the ISM is predominantly in the plane of the sky, and we shall assume that in this paper.

## 6.6 The Structure of the BD+43° 3654 Bow Shock

### 6.6.1 The BD+43° 3654 bow shock: general considerations

In BD+43° 3654 we have a massive early type star that is moving supersonically through the ISM. As a consequence a BS forms, with a reverse shock, where the extremely fast stellar wind is decelerated, and a forward shock, where the incident ISM is shocked. between these two regions there is a contact discontinuity. The motion of the star sweeps up a considerable mass of the ISM.

From the observations described earlier in this paper, we have several different emission phases. We see dust emission in the IR. This material is most likely swept up ISM dust that is heated by passing through the shock and then heated by the UV radiation field of the star. In addition, we have ionised gas, that shows up in free-free radio emission and in H$\alpha$ emission.

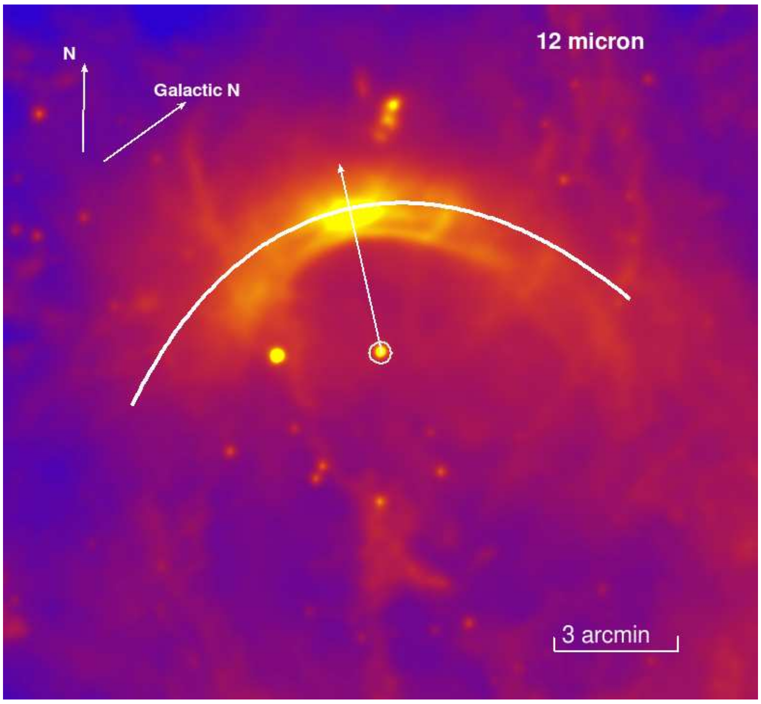

Figure 6.11: An overlay of the Wilkin model interaction zone onto the WISE 3 data of BD+43° 3654.

We also expect X-ray emission from the hot shocked stellar wind material, though that has not been detected. We also expect non-thermal emission due to shock acceleration (at radio, X-ray and $\gamma$-ray energies). A schematic overview of the different emission regimes likely to be present in BS is shown in Fig. 6.10.

Because we have a considerable body of data we can investigate the detailed structure of the BS around BD+43° 3654, estimating the dust mass, the ionised gas mass and so on, as well as looking at the distribution of emission through the BS.

If BD+43° 3654 has a wind mass-loss rate of $\dot{M}$, and a wind terminal velocity of $v_\infty$, and is moving through a static ISM with a velocity $V_{ISM}$, which has a uniform density of $\rho_{\rm ISM}$, then the theoretical standoff distance ($R_0$) from the star to the BS is given by Wilkin (1996) as:

$$R_0 = \left[ \frac{\dot{M}\, v_\infty}{4\pi \rho_{ISM} V_{ISM}^2} \right]^{1/2} . \tag{6.8}$$

For BD+43° 3654 we assume, using Howarth & Prinja (1989) and Comerón & Pasquali (2007) that $\dot{M} = 5.50 \times 10^{-6}\, M_\odot\ {\rm yr}^{-1}$, $v_\infty = 2300\,{\rm km\ s}^{-1}$.

For the ISM we assume a warm neutral medium, so that the mean mass per particle is $\sim m_p$. For $R_0 = 1.4\,{\rm pc}$, $\dot{M} = 5.50 \times 10^{-6}\, M_\odot\ {\rm yr}^{-1}$, $v_\infty = 2300\,{\rm km\ s}^{-1}$and $V_{ISM} = 38.4\,{\rm km\ s}^{-1}$, we find that the ISM number density is $n_{ISM} = 13.9\,\mathrm{cm}^{-3}$. Clearly, the inferred ISM density will scale with the assumed $\dot{M}$ for BD+43° 3654.

We have not detected BD+43° 3654 at radio wavelengths (which would enable a determination of the mass-loss rate). The assumed values of $\dot{M}$ and $v_\infty$ imply expected thermal radio fluxes of 0.23 mJy at 4.8 GHz and 0.1 mJy at 1.28 GHz. Both values are close to the respective noise levels for the observations (and suggest that the mass-loss rate cannot be substantially larger than these values).

In addition to estimating $R_0$, Wilkin (1996) derived the shape of a BS, under the assumption of the star moving through a medium of constant density. Importantly, the BS shape is independent of the detailed stellar parameters, with

$$R(\theta) = R_0 \csc\theta \left[3\left(1 - \theta\cot\theta\right)\right]^{1/2} \tag{6.9}$$

where $R(\theta)$ is the distance to the BS from the star at an angle $\theta$ to the direction of stellar motion. This means that the apex of the BS is when $\theta = 0$ and $R(\theta) = R_0$. when $\theta = \pi/2$ then $R(\theta) = 1.73R_0$.

We have overlain the Wilkin derived shape for the BS onto the WISE 3 data (which also detects the star) and find that an ideal fit to the BS shape and coinciding with the hotspot occurs when the velocity vector is at $\theta = 65.5°$ E of Galactic N, as displayed in Fig. 6.11.

The degree of post-shock cooling that the material suffers in the BS region is also of importance. From the results of Stevens et al. (1992), in the context of cooling in the post-shock region of colliding stellar winds, we can easily show that the shocked O-star wind will be of very low density and hence adiabatic. In colliding wind systems, the post-shock region tends to be adiabatic in very windy binary systems, and in this case the BS stand-off distance is very large and so the post-shock gas is low density. From this, and using the results of Luo et al. (1990), again from colliding winds, we can estimate the thickness of the region from the reverse shock to the contact discontinuity to be $h = R_0/8$. This results comes from consideration of the momentum flux in the post-shock flow.

On the other hand, the region between the forward shock and the contact discontinuity is likely to not be adiabatic (as it is a much slower shock. This region is then likely to be quite a dense shell. As discussed in the context of colliding winds by Stevens et al. (1992) this situation is likely to be strongly unstable to instabilities (see also (Dgani et al., 1996)).

A series of slices through the BS at different wavelengths are shown in Fig. 6.12, showing the different morphologies. There are some clear differences between the morphologies, for example the *Herschel* 70$\mu$m emission is brighter further away from the star than the 12$\mu$m emission.

To illustrate this further, in Fig. 6.13 we show a 2 colour image combining WISE W3 (12$\mu$m) data with the *Herschel* 160$\mu$m data, which shows cooler regions of dust underlying the BS (and possibly unrelated), while the BS itself contains both hotter regions closer to the star and cooler regions further away.

Analysis of the GMRT data has revealed a BS like structure around BD+43° 3654 at both frequencies in a position coincident with previous studies. Images of both frequencies are shown in Fig. 6.2. Slices across the BS and the position of the star at radio, IR and H$\alpha$ are shown in Fig. 6.12, indicating possible alignment of radio and H$\alpha$ emission with IR emission from the dust appearing to emit nearer the reverse shock front of the BS. Other radio emission in the area may or may not be related to the BS emission, for example, the linear feature roughly perpendicular to the BS, to the left side of the BS (Fig. 6.2).

### 6.6.2 Bow shock IR fluxes

Integrated flux values of the BS and the ES have been measured, using AIPS and GAIA, at multiple wavelengths, using the aperture photometry method used by Anderson et al. (2012a) in their IR study of HII and PNe regions.

For each wavelength we generated flux within a BS source aperture and flux for four background apertures. As with Anderson et al. (2012a), we selected apertures to enclose the BS emission at each different wavelength, however, we chose different background apertures at each wavelength according to low emission regions rather than exactly the same background regions used by Anderson et al. (2012a). This provided more robust data over the broader spectrum of our study. Background subtraction was then calculated according to:

$$S_\nu = S_{\nu,0} - \frac{B_\nu}{N_B} \times N_S \tag{6.10}$$

where $S_\nu$ is the BS source integrated flux after background subtraction, $S_{\nu,0}$ is the integrated BS flux within the source aperture before background subtraction, $B_\nu$ is the integrated flux within the background aperture, $N_B$ is the number of pixels in the background aperture and $N_S$ is the

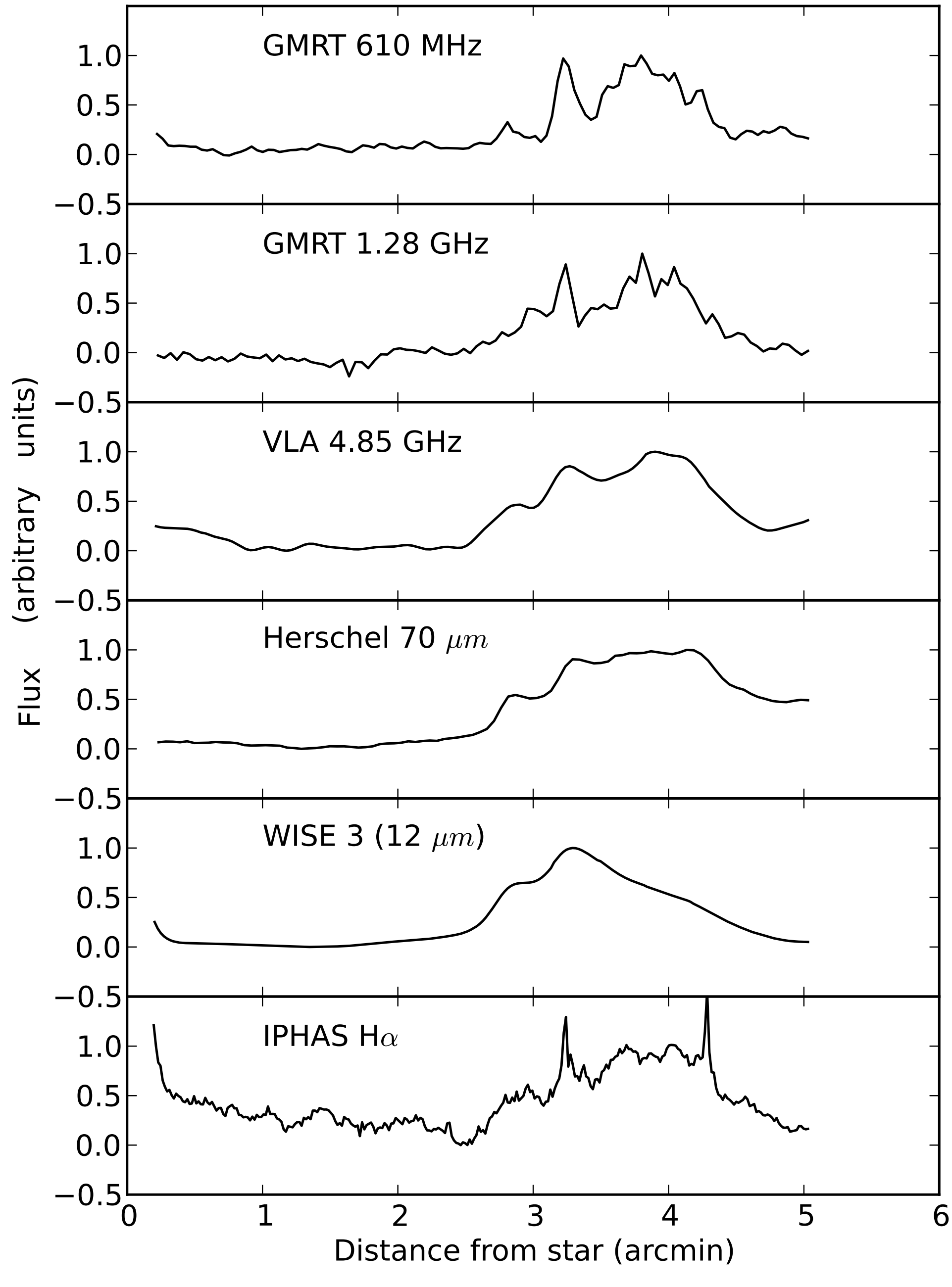

Figure 6.12: Multi-wavelength slices through the bow shock of BD+43° 3654. The width of the slice is 10″ and runs from the location of the BD+43° 3654 through the 'hot-spot' in the BS. The 6 panels are for the GMRT data at 610 MHz and 1.28 GHz, the VLA at 4.85 GHz, the *Herschel* 70$\mu$m data, the WISE 3 band (12$\mu$m) and the H$\alpha$ IPHAS data at the bottom (including emission from 2 point sources). All the flux values are arbitrary, the slices being scaled so that the maximum flux is unity. The star is positioned at zero.

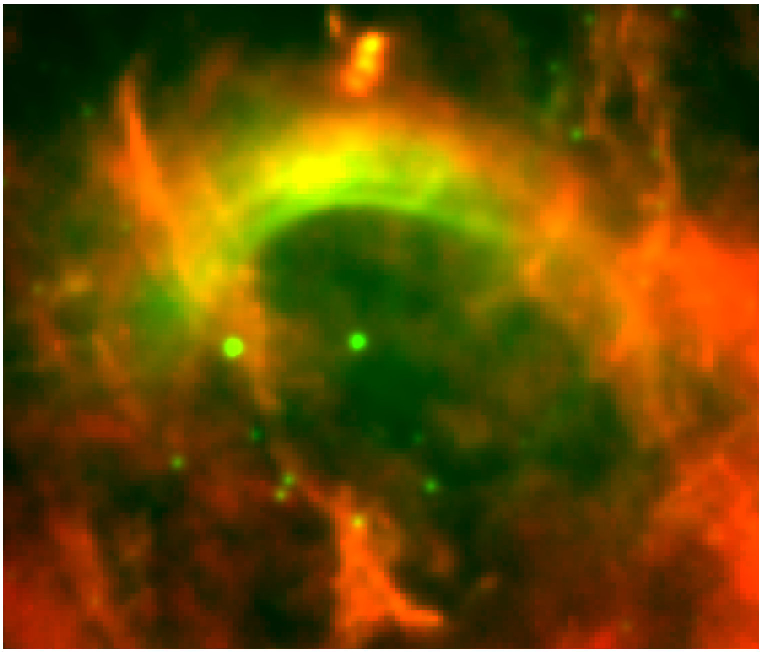

Figure 6.13: Two colour image of the IR emission from the bow shock, showing the WISE W3 data (green) and the *Herschel* (160$\mu$m) data (red). The hotter dust appears to be more concentrated towards BD+43° 3654 while the cooler dust is distributed further away.

pixel number in the BS source aperture, (Anderson et al., 2012a). An average of the four $S_\nu$ values gives the BS flux at each wavelength, and the standard deviation of the four background subtracted results gives the uncertainty in the background apertures used for each wavelength ($\sigma_\nu$). These flux values are shown in Table 6.3. The IR SED of the BS is shown in Fig. 6.14.

### 6.6.3 Bow shock: ionised gas mass

For the GMRT radio data, and assuming optically thin free-free emission, we can estimate the ionised gas mass in the BS, and estimate the density.

The free-free emissivity $\epsilon_{ff}$ is given by (Allen, 1973)

$$\epsilon_{ff} = 6.8 \times 10^{-38} Z^2 n_i n_e T^{-1/2} e^{-h\nu/kT} g_{ff} \tag{6.11}$$

with $\epsilon_{ff}$ in units of erg s$^{-1}$ cm$^{-3}$ Hz$^{-1}$. $Z$ is the mean ionic charge, $n_i$ and $n_e$ are the ionic and electron number densities (in cm$^{-3}$), $T$ is the gas temperature (K), $\nu$ is the frequency (Hz) and $g_{ff}$ the Gaunt factor, with

$$g_{ff} = 10.6 + 1.9\ \log_{10}(T) - 1.26\ \log_{10}(\nu Z). \tag{6.12}$$

Assuming that the emitting material has cosmic abundances, with $Z = 1$, the ratio of particle densities $n_e/n_i = \gamma \sim 1$, $T = 10^4$ K, $\nu = 1.3$ GHz. We approximate the volume of BS as a disk of radius $r$ and thickness $h$ so that $V = \pi r^2 h$. From Fig. 6.2 we estimate $r = 3.5'$ or $r = 1.48$pc. We estimate $h = R_0/8$ (Luo et al., 1990), so that $V = 3.2 \times 10^{55}$ cm$^3$.

From the observed 1.3 GHz flux (21.2 mJy) we can estimate the ionised mass as $M_{ion} = 0.51\,M_\odot$, with $n_e \sim n_i \sim 19$ cm$^{-3}$. We stress these numbers are indicative only, as we have assumed a constant density throughout the BS and ignored clumping effects, which are likely to be important (and will reduce the overall mass).

Studies of the BS of Betelgeuse by Mohamed et al. (2012) have modeled a BS mass of ~0.05 $M_\odot$, with BS mass from 60 $\mu$m flux of 0.042 $M_\odot$. A survey of BSs by Cox et al. (2012a) revealled BS dust+gas masses in the region of $10^{-4}$ $M_\odot$. The above estimates of the BD+43° 3654 BS mass are much greater than these, though the BD+43° 3654 BS is assumed to be swept up material and the above studies are of AGB stars with mass contributions from their wind.

With the assumptions above outlined, we can calculate the emission $EM$ and optical depth (using Eq. 4.4) for the ionised gas in the BS, assuming we are viewing the disc from the side, and find $EM \sim$ 1100 cm$^{-6}$ pc. This means that the free-free opacity at 610 MHz and 1.3 GHz is very small, justifying the optically thin approximation.

### 6.6.4 Bow shock dust temperature

The dust swept up by the stellar wind, which then interacts with the BS is assumed to be interstellar amorphous silicate dust. The radius of interstellar dust (ISD) grains is in the order of microns and the temperature is typically 20 K, whilst dust in molecular clouds is just a few K, (Coupeaud et al., 2011). The dust in the BS of BD+43° 3654 is assumed to be heated by the UV radiation from the star and to be in thermal equilibrium.

#### Dust temperature and masses: SED fitting

The emission from the BS has been observed at several different IR wavelengths from several satellites, and we have measured integrated fluxes using aperture analysis (with the GAIA software package). In order to estimate the temperature of the dust in the BS we fit the SED of the BS with a modified black body function. Assuming optically thin emission from a population of dust grains we can write that the flux $S_\nu$ at a frequency $\nu$ can be written as (Anderson et al., 2012b):

$$S_\nu \propto \kappa_\nu B_\nu(T) \tag{6.13}$$

In this paper we shall assume a simplified model for the dust opacity and have $\kappa_\nu = \kappa_0(\nu/\nu_0)^\beta$, where $\kappa_0$ is the dust opacity at a frequency $\nu_0$ and we shall assume $\beta = 2$. From Draine & Li (2007), we assume $\kappa_0(160\mu\text{m}) = 1.00\ \text{m}^2\ \text{kg}^{-1}$ ($10\ \text{cm}^2\ \text{g}^{-1}$).

For emission from a region of solid angle $\Omega$ and a dust surface density of $\Sigma_d$ we can write that the total flux is

$$S_\nu = \Sigma_d \Omega B_\nu(T) \kappa_0 (\nu/\nu_0)^\beta\,. \tag{6.14}$$

We can also estimate the mass of the dust from Hildebrand (1983). The assumption of $\beta = 2$ is better at longer wavelengths and the assumption of $\beta = 2$ at wavelengths of $\sim 10\mu$m is questionable (due to emission from PAHs etc, though the WISE bands are quite broad; (Wright et al., 2010)).

From fitting this function to the SED from the BS (see Fig. 6.14) we find that we could not find a single temperature that the fits the *WISE* and *Herschel* data points and we adopt a two temperature model, with $T_1 = 90\,\text{K}$ and $T_2 = 30\,\text{K}$.

Note that there was no colour correction made to the *WISE* data, though we estimate that this would be a small error. Colour correction is applied to the fluxes across each *WISE* bandwidth to correct for differences from the standard Vega spectrum, see Table 1 in Wright et al. (2010) where these corrections are of the order of unity. The *Herschel* data has similar unity corrections (Poglitsch et al., 2010).

We can estimate the dust mass from the observed flux. From Cox et al. (2012a); Li (2005) we estimate the dust mass, $M_{dust}$:

$$M_{dust} = \frac{d^2 S_\nu}{\kappa_\nu B_\nu(T)} \tag{6.15}$$

where $d$ is the distance to the BS, $S_\nu$ is the measured flux at frequency $\nu$ (in cm), $\kappa_\nu$ is the dust opacity at the observed wavelengths and $B_\nu(T)$ is the Planck function in frequency units at the dust temperature, $T$. We adopt a value of $\kappa_\nu$ of 940 cm$^2$ g$^{-1}$ for the 90 K dust and 12 cm$^2$ g$^{-1}$ for the 30 K dust from Li & Draine (2001). Assuming a uniform dust density and grain radius and using the fluxes in Table 6.3, we estimate the dust masses to be 0.0105 $M_\odot$ for the 90 K component and 0.263 $M_\odot$ for the 30 K component.

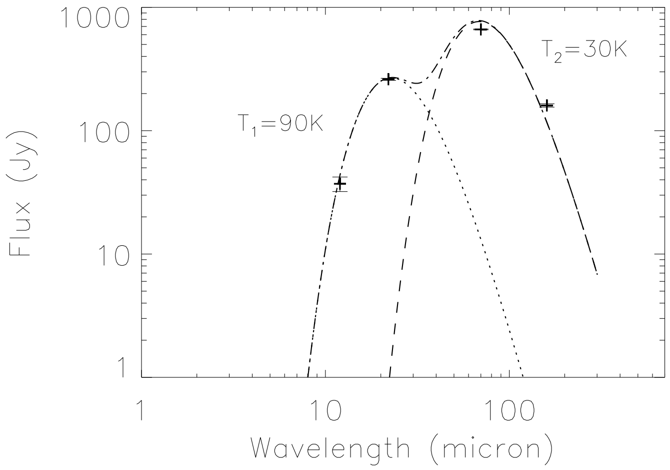

Figure 6.14: The IR SED from the BS fitted with a 2 temperature dust model.

We can provide an order-of-magnitude estimate of the amount of swept-up material in the BS by assuming the swept up mass of the ISM in the BS ($M_{ISM}$) is:

$$M_{ISM} \sim \frac{4\pi}{3} R_{BS}^3 \, \rho_{ISM} \tag{6.16}$$

where $R_{BS}$ is the effective radius of the BS which we assume to be 1.4 pc. With $n_{ISM}$ = 13.9 cm$^{-3}$, we have $M_{ISM} = 3.9\,M_\odot$. For comparison, in a study of the dust mass in the wind blown bubble of N49 (an O5 V type star) by Everett & Churchwell (2010), a 'dusty gas' mass of 2.4 $M_\odot$ is estimated.

The typical dust to gas ratio for the Galaxy is 0.01 (Draine & Li, 2007), whilst the above estimates give a mass ratio in the BS of ~0.07. The above mass estimates suggest that the BS material has a higher than typical ISM ratio. This may indicate that the BS has a higher ratio than the local ISM or that the BD+43° 3654 is travelling through an ISM with a higher dust ratio. We also can see that there are two regions of dust emission, one cooler zone in the forward, shocked ISM region where the bulk of the mass appears. Also a hotter zone within the shocked stellar wind region where ~4 per cent of the dust appears to have travelled through the contact discontinuity to reach this region.

### Theoretical Dust Properties: Temperature

We can estimate the expected dust temperature using simple thermal equilibrium considerations. If we consider that the dust is optically thin, and is located at a distance $R_0$ from BD+43° 3654, then the dust will be heated by the stellar radiation field to a temperature $T_d$ given by (Herman et al., 1986; Evans, 1993):

$$T_d = \left( \frac{L_{bol}\ T_{\rm eff}^{\beta}}{16\pi\sigma R_0^2} \right)^{1/(4+\beta)} \quad . \tag{6.17}$$

Here, $L_{bol}$ and $T_{eff}$ are the total luminosity and effective temperature of BD+43° 3654, $\sigma$ the Stefan-Boltzmann constant and $\beta$ the dust emissivity power function. Clearly, the BS is an extended feature, but we assume a distance $R_0$ for the dust to be a representative value.

For $L_{bol} = 10^6\, L_\odot$ and $T_{eff} = 42,464$ K (Comerón & Pasquali, 2007) and $\beta = 2$, we find $T_d = 225\,$K, rather hotter than we observe. However, the derived temperature depends sensitively on $\beta$, and for $\beta = 1.7$, then $T_d = 171\,$K

If the dust were predominantly amorphous silicate dust, then we could use the expression given by Draine & Lee (1984) to derive a value for the theoretical silicate dust temperature ($T_{\rm sil}$).

From Draine & Lee (1984), we have

$$T_{\rm sil} = 27 a_{\mu{\rm m}}\ ^{-1/6} L_{UV.38}\ ^{1/6} r_{pc}\ ^{-1/3}\ (K)\,. \tag{6.18}$$

This expressions is derived using a dust emissivity law $j = \lambda^{-\beta} B(T)$, with $\beta = 2$.

The dust grain radius is $a$ (in $\mu$m), $L_{UV,38}$ is the UV luminosity of the star (units of $10^{38}$ erg s$^{-1}$) and $r$ is the distance from the star (which we assume to be $R_0$, in units of pc). We assume $L_{UV} = L_{bol}$.

For the dust in the BS, these values give $T_{\rm sil} = 141\,$K for $a = 0.001\mu$m and $T_{\rm sil} = 96\,$K for $a = 0.01\mu$m. Comparing these values with the results from the SED fitting above which give $T_d$= 30 and 90 K, suggests that the hotter dust is composed of silicates.

### 6.6.5 The Hot-Spot

A feature of note in the BS is the 'hot-spot' located near the apex of the motion of BD+43° 3654. In Fig. 6.15 we show this region at six different frequencies, and the 'hot-spot' feature has quite

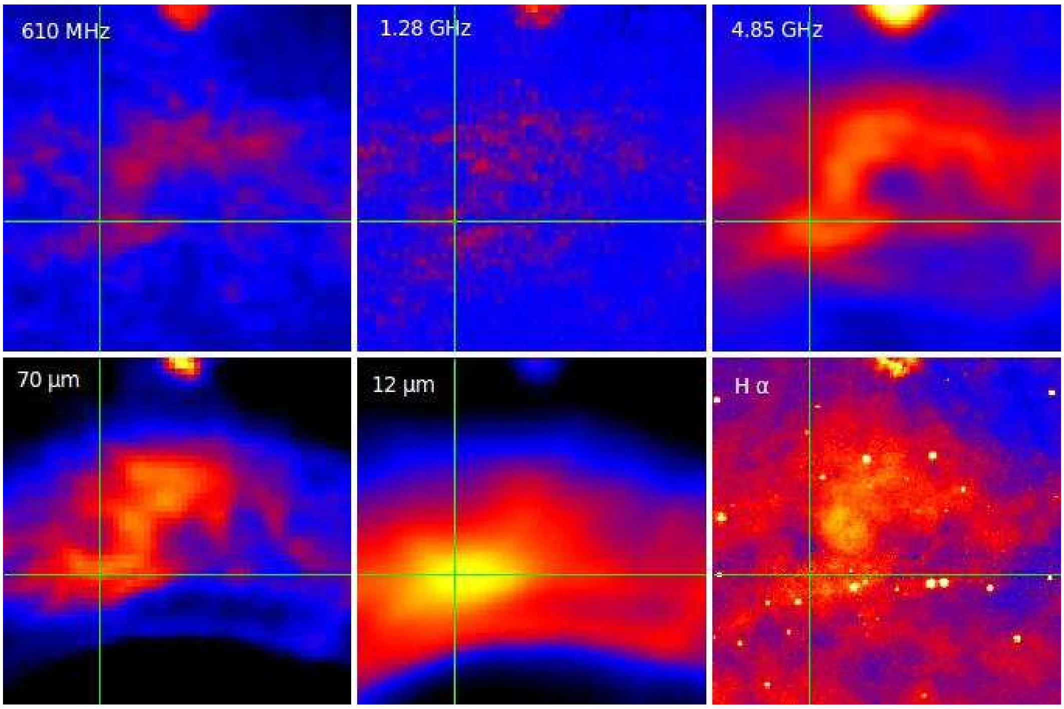

Figure 6.15: Zoomed in 'hot-spot'. The cross-hairs in all the diagrams are centred at the peak of of emission in the *WISE* W3 band ($\alpha_{J2000}$=20 33 40.0, $\delta_{J2000}$=+44 02 24.15).

a different morphology at different wavelengths. Quite what is causing this feature is unclear, but it could be related to instabilities in the BS or the BS overrunning a distinct denser region of the ISM.

### 6.6.6 BD+43° 3654, the star

The star has not been detected at radio frequencies but is observed in the IR by *WISE* bands and also in H$\alpha$ in the IPHAS survey. We infer a stellar mass-loss rate for BD+43° 3654, assuming thermal emission, using luminosity values and mass–loss rate predictor from Howarth & Prinja (1989), of $5.5 \times 10^{-6}\,M_{\odot}$ yr$^{-1}$. This value is an order of magnitude lower than that given by Kobulnicky et al. (2010).

Using the optical magnitudes and IR fluxes, the SED of BD+43° 3654 is shown in Fig. 6.16, assuming a value of $A_V = 5.1$. We also show a 40kK CMFGEN model (Hillier & Miller, 1998).

For the thermal radio emission from the wind, we assume a wind terminal velocity of 2300 km s$^{-1}$ and a distance of $D = 1.45$ kpc. With these values (and $\mu = 1.26$, $\gamma = 1$ and $Z = 1$) we can estimate a 5 GHz flux of 0.24 mJy, and a 1.4 GHz flux of 0.11 mJy. We also show the expected thermal flux for the higher mass-loss rate. Also shown are the $3\sigma$ upper limits from

Table 6.3: Multiwavelength integrated flux of the bow shock (BS) associated with BD+43° 3654 and nearby ellipsoidal source (ES), (See text for details).

| Satellite/ Survey | Waveband | $\log f$ | Bandwidth | BS region | | ES region | |
|---|---|---|---|---|---|---|---|
| | | | | Flux (Jy) | $\sigma$ (Jy) | Flux (Jy) | $\sigma$ (Jy) |
| WENSS | 325 MHz | 8.51 | 4.5 MHz | 3.43 | 0.435 | – | – |
| GMRT | 610 MHz | 8.79 | 16 MHz | 0.167 | 0.0376 | 0.019 | 0.0012 |
| GMRT | 1.28 GHz | 9.11 | 16 MHz | 0.0212 | 0.0034 | 0.0032 | 0.00018 |
| VLA | 1.42 GHz | 9.15 | 50 MHz | 0.66 | 0.05 | 0.12 | 0.012 |
| VLA | 4.8 GHz | 9.68 | 50 MHz | 0.37 | 0.06 | 0.12 | 0.0072 |
| *Herschel* | 160$\mu$m | 12.3 | | 160 | 18.8 | – | – |
| *Herschel* | 70$\mu$m | 12.6 | | 662 | 40.6 | – | – |
| *IRAS* | 60$\mu$m | 12.7 | 40$\mu$m | $4.25 \times 10^3$ | $0.32 \times 10^3$ | – | – |
| *IRAS* | 25$\mu$m | 13.08 | 11$\mu$m | $1.07 \times 10^2$ | 33.9 | – | – |
| *WISE* W4 | 22$\mu$m | 13.13 | 5.2$\mu$m | $2.61 \times 10^2$ | 16.9 | 3.66 | 0.025 |
| *MSX* | 14.65$\mu$m | 13.3 | 4$\mu$m | 90.4 | 5.8 | – | – |
| *WISE* W3 | 12$\mu$m | 13.4 | 9$\mu$m | 37.1 | 3.9 | 0.79 | 0.13 |
| *WISE* W2 | 4.6$\mu$m | 13.81 | 1.3$\mu$m | – | – | 0.052 | 0.003 |
| *WISE* W1 | 3.4$\mu$m | 13.94 | 1$\mu$m | – | – | 0.053 | 0.004 |

the VLA and GMRT observations. This suggests that the mass-loss rate is $< 10^{-5}\, M_\odot\ \mathrm{yr}^{-1}$.

However, a very useful thing would be to directly detect the wind of BD+43° 3654 and that can either be done with sub-mm observations (such as from Plateau de Bure observations, as ALMA cannot observe BD+43° 3654) or more sensitive VLA observations.

## 6.7 The Ellipsoidal Source

The ES detected in the GMRT data adjacent to the BS was also detected by Benaglia et al. (2010) in the VLA data. The recent release of the *WISE* all sky survey also shows emission from this object. The emission in 6 different bands from low frequency radio through to H$\alpha$ is shown in Fig. 6.18. Slices through the different data all show 3 distinct broad peaks of emission (Fig. 6.18). The peaks generally increase in intensity away from the BS (and BD+43° 3654). See Table 6.3 for ES flux values calculated in the same manner as the BS.

As suggested by Benaglia et al. (2010), this object is likely an HII region. A study by Anderson et al. (2012a) of HII regions at different IR wavelengths reveals considerable structure,

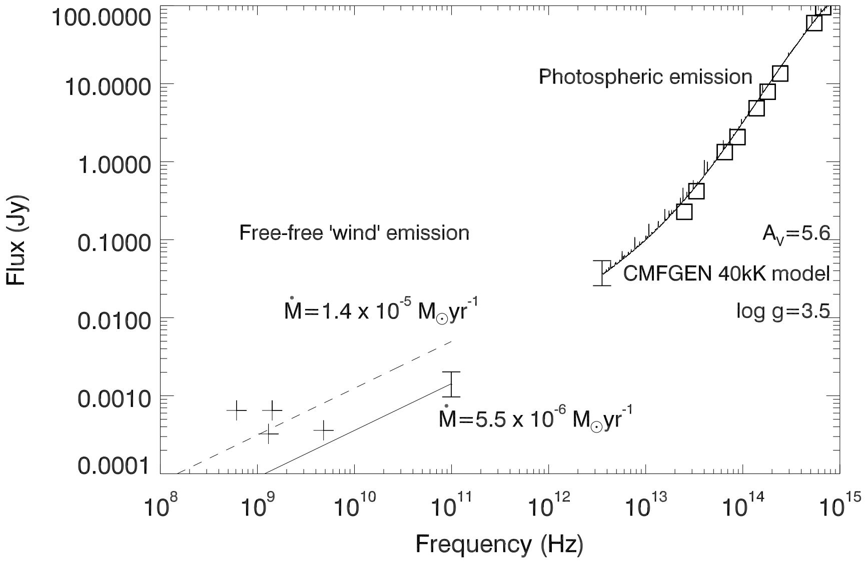

Figure 6.16: The SED of BD+43° 3654. Shown are the optical and IR fluxes, assuming an $A_V = 5.1$. Also shown is a 40kK CMFGEN model (Hillier & Miller, 1998). For the radio portion we show the expected thermal emission for two assumed values of the mass-loss rate (see text for details) along with the $3\sigma$ upper limits (marked by cross points) for the GMRT and VLA data.

some linear. On the basis of the radio emission, this could be an extragalactic jet source, but the fact that it is seen at IR and H$\alpha$ wavelengths rules this out.

The radio spectral index map for the ES is shown in Fig. 6.17, showing the distribution of $\alpha$, where the flux at a frequency $\nu$ is defined as $S_\nu \propto \nu^\alpha$. In generating this map, only pixels were included where the signal was 5× the rms value (or around 0.2 mJy/beam). Also, included in Fig. 6.17 is a spectral index error map. Only pixels were considered for which the spectral index error $\leq 0.1$.

The mean value for the spectral index is $\alpha \sim -0.7$, implying non-thermal emission. The spectral index map of the VLA observations also indicate negative spectral index across the non-thermal emission in the range of $\alpha = -0.8$ to $+0.3$ (Benaglia et al., 2010).

## 6.8 Summary and Conclusion

When comparing the GMRT data with other observations there does appear to be a consistent emission indicating a BS in the forward direction of the motion of BD+43° 3654. Images at other wavelengths are shown in Fig. 6.3 and Fig. 6.6. The recent release of the *WISE* all sky

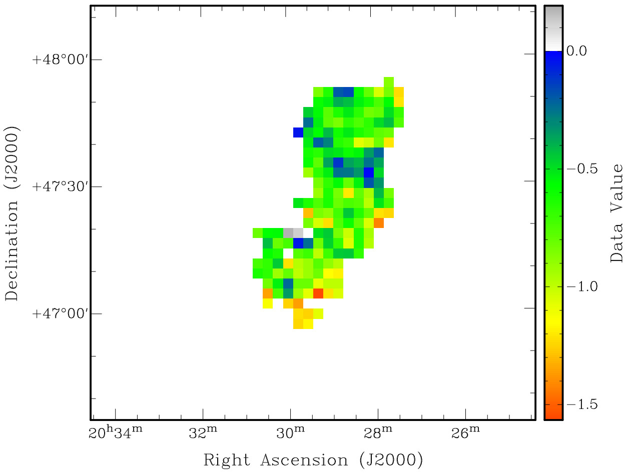

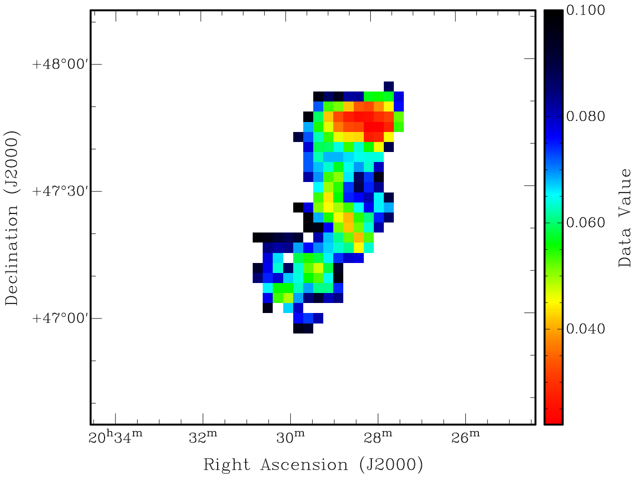

Figure 6.17: Top panel: The GMRT spectral index map of the ES. Lower panel: The errors on the spectral index map.

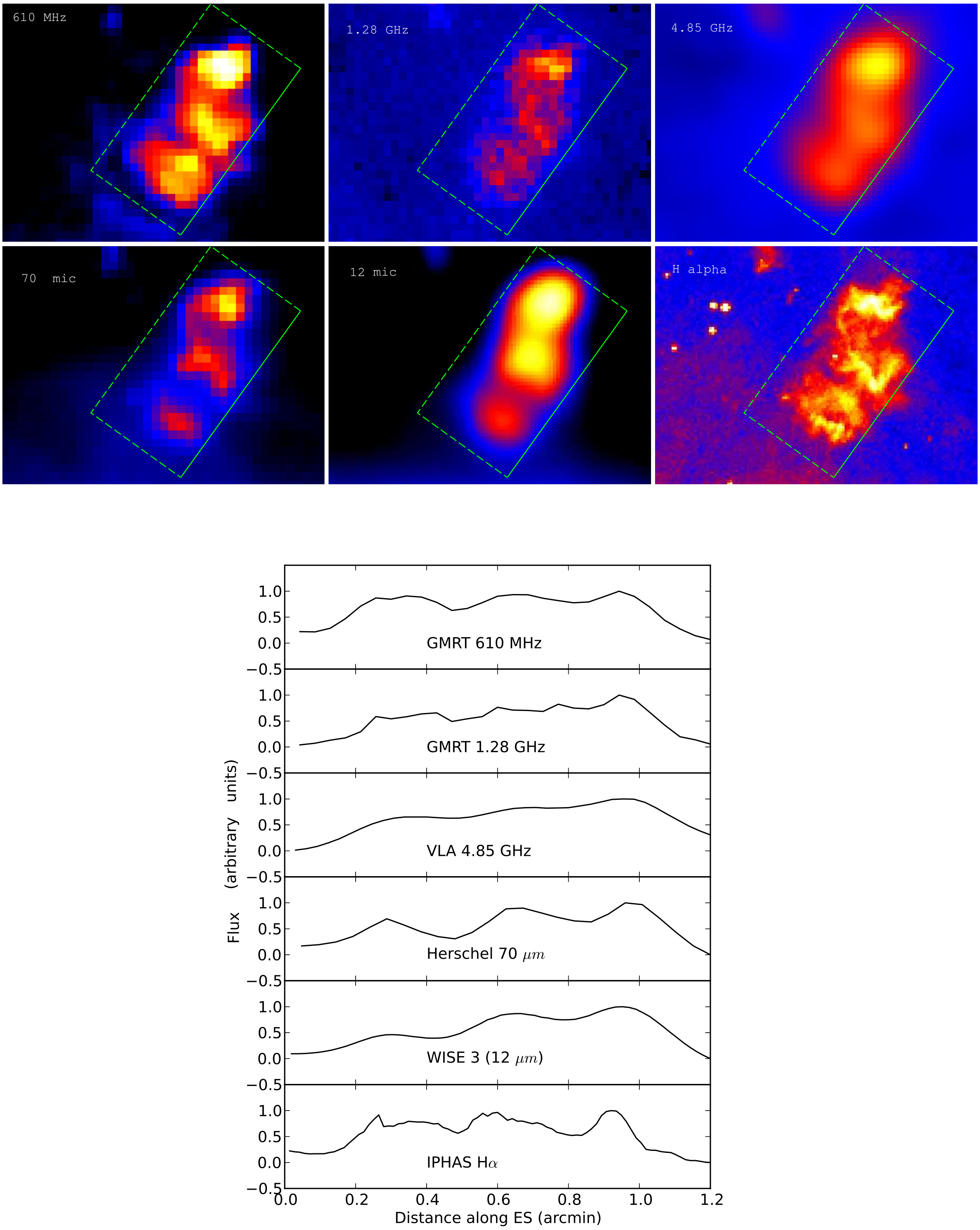

Figure 6.18: The ellipsoidal source (ES) near to the BD+43° 3654 bow shock. Upper panel: Top row: radio data at 610 MHz, 1.28 GHz and 4.85 GHz. Bottom row: IR data at 70$\mu$m(*Herschel*), 12$\mu$m(*WISE* 3) and H$\alpha$ emission. The box shows the region used for data slices (see below). The images are all 1.2 arcmin × 0.7 arcmin. Lower diagram: slices through the ES illustrating the 3 peaks in the emission. Flux levels are arbitrary, with distance shown along the length of the ES.

survey has included emission from the BS around BD+43° 3654 in W3 and W4, (see Fig. 6.4), with W3 data, at 12$\mu$m also detecting the star. A slice through this data shows the detail of the star and the BS structure, (see Fig. 6.12). From this figure the IR emission is seen to plateau then peak near to the reverse edge of the BS and the radio and H$\alpha$ emission appears coincident.

We have studied the velocity vector of BD+43° 3654 and concluded that our results are similar to previous studies, with the velocity with respect to the ISM of 36.5$\pm$6.2 km s$^{-1}$with the direction at angle $\theta = 67.8^\circ \pm 6.1^\circ$ and $38.4 \pm 6.2\,$km s$^{-1}$with $\theta = 69.6^\circ \pm 5.9^\circ$ from the two models used. We also model the BS interaction zone from Wilkin (1996) and fit to the shape of the BS to give an apparent velocity angle of 65.5°.

From the IR data we estimate the temperature and mass of the dust and detect two different emitting regions of dust; a cooler 30 K zone in the region of the forward shocked ISM with $\sim$ 96 per cent of the dust mass and a hotter, 90 K zone in the region of the shocked stellar wind with $\sim$ 4 per cent of the dust mass. This suggests that some small portion of the dust passes straight through the contact discontinuity into the hotter reverse shocked stellar wind region.

Why some stars, like BD+43° 3654, show strong BSs and other do not is still a bit of mystery. The local velocity with respect to the ISM is clearly important and BS formation may be affected by local motions of the ISM (such as outflows from young star clusters). The structure of the ISM is also going to be important - for example, regions of hot ISM will tend not to show BSs (because the motion of the runaway stars will be subsonic). In this paper we have assumed the BD+43° 3654 is running through a region of the Warm Neutral ISM, with a sound speed of $\sim$ 7 km s$^{-1}$. If instead, the star was running through a regions of the hot ISM ($T \sim 10^6\,$K), where the sound is closer to 100 km s$^{-1}$, in this case no BS would be present. Clearly, low density regions of the ISM will also make detection less likely as well.

Detailed studies of the internal structure of a sample of bow shocks like here for BD+43° 3654 will further help out understanding of these objects and the interaction of massive stars and their winds with the ISM.

# Chapter 7

# E-BOSS: an Extensive stellar BOw Shock Survey I

*"In the starry expanse that has no dwellings: forces of the universe, interior virtues, harmonious union of earth and heaven that delights the mind and the ear and the eye, that offers an attainable ideal to all wise men and a visible splendour to the beauty of the soul."* Hypatia of Alexandria, circa 370-415 A.D. From a dramatic work by Leconte de Lisle, 1857.

## 7.1 Introduction

This chapter contains a description of my contribution to the Extensive stellar BOw Shock Survey, I, (E-BOSS) Peri et al. (2012). This survey involved searching through current catalogues of candidate stars at various wavelengths to compile a catalogue of those that may reveal stellar bow shocks. Section 7.2 details the E-BOSS sample of candidate stars, Section 7.3 details the catalogue search, Section 7.4 shows the results of the survey and Section 7.5 concludes.

## 7.2 The E-BOSS Sample Stars

The candidate stars were selected according to several criteria:

1. The surroundings of massive runaway stars (runaway stars are described in Section 1.5.4) were examined as these stars have high luminosities, strong winds and high spatial velocities, hence can sweep up and heat interstellar matter.
2. Stars within a distance of 3 kpc were selected, which would have brighter bow shocks.

These candidates were then selected from two sources. First from bow shocks detected in a previous survey of data from the Infra-Red Astronomical Satellite (IRAS) by Noriega-Crespo et al. (1997) and secondly from a catalogue of runaway stars by Tetzlaff et al. (2010). This gave a list of 283 candidates to search.

## 7.3 A Multi-Wavelength Search for Stellar Bow Shocks

The IRAS survey was at 60$\mu$m, our infra-red (IR) search included other archive data from IRAS, together with data from the Midcourse Space eXperiment (MSX, Egan et al. 2003b) and the preliminary release of images from the Wide-field Infra-red Survey Explorer satellite (WISE, Wright et al. 2010). Other wavelengths that were searched were H$\alpha$ using the Virginia Tech. Spectral Survey (VTSS) [1] and the Southern Hemispheric H$\alpha$ Sky Survey Atlas (SHASSA, Gaustad et al. 2001), with searches also at radio frequencies.

My contribution to the survey was the sorting of some of the stellar candidates, and subsequent searches through the various IR and radio archives. The data that proved most useful, i.e. revealed recognisable bow shock shapes, was the IR, particularly the WISE data. At IR wavelengths the emission detected originates from the bow shock dust which has been heated by UV radiation from the parent massive star, this is then re-emitted in the IR. The searches through the other data bases did prove that the more recent, better resolution of the WISE data was better able to confirm the emission from any faint stellar bow shocks.

## 7.4 The E-BOSS Results

The results of the searches by all contributors were that 28 new bow shocks were identified. A sample of the published objects is shown in Fig. 7.1, where the proper motion of the parent star is indicated by the thicker vector, and the thinner vector indicating the proper motion corrected for the effects of Galactic rotation. Further studies were made by other contributors to analyse the frequency of bow shocks by spectral type, mass, terminal wind speed, mass loss rate, etc. of the parent star. No trend, however, was detected. Further studies have since been made by other colleagues on a larger database.

---

[1] The Virginia Tech Spectral-Line Survey (VTSS), which is supported by the National Science Foundation.

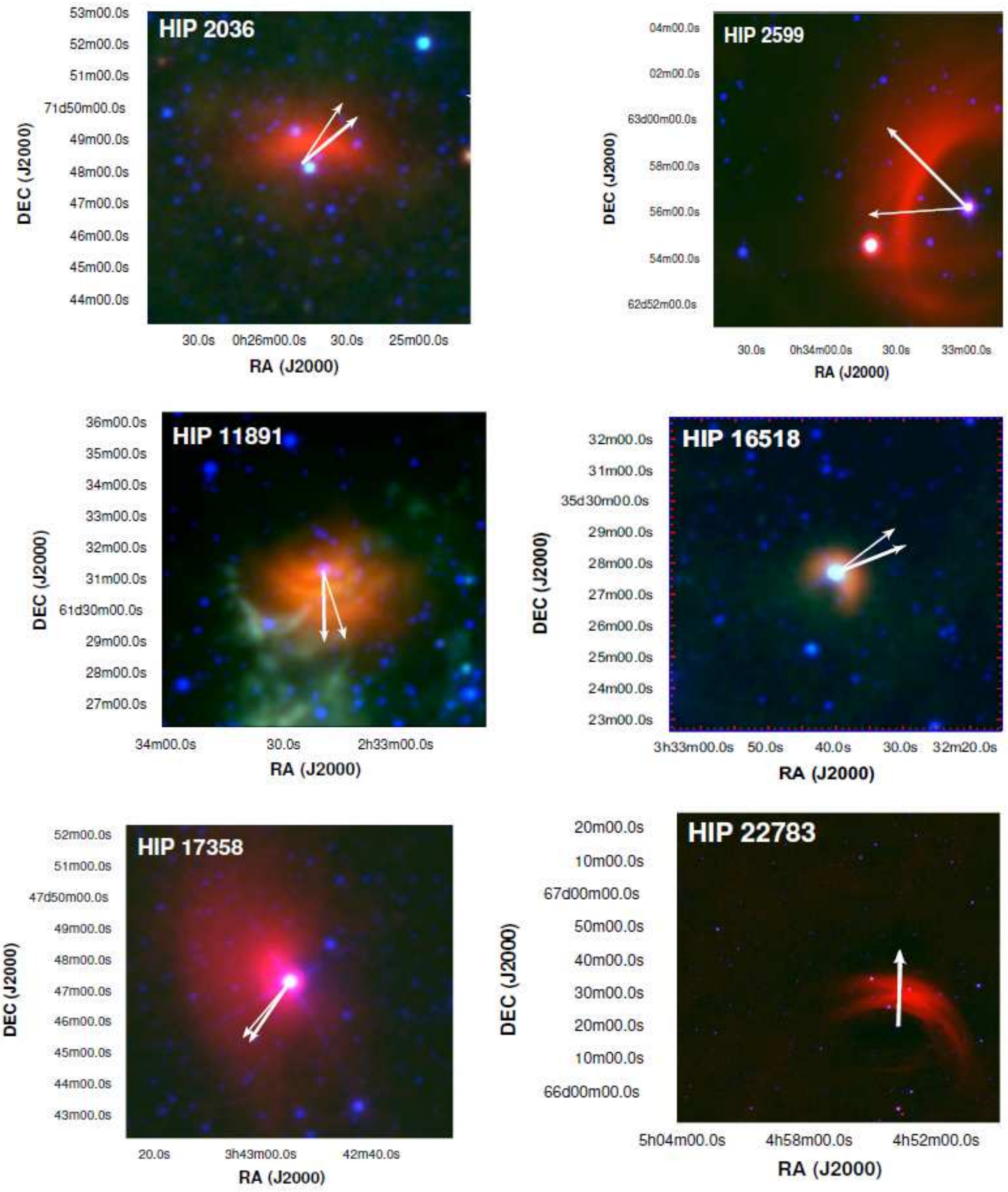

Figure 7.1: A selection of stellar bow shocks identified in the E-BOSS survey, Peri et al. (2012).

## 7.5 Conclusion

The survey results from the candidate stars revealed 28 new bow shocks. The success of this study was continued in a further study of a wider range of candidate stars. These surveys have now produced a catalogue of bow shock candidates for future reference and to further the study of these dramatic structures.

# Chapter 8

# Conclusion and Further Work

*"When it comes to astronomy, you never come to the end of anything. You have to reach out farther and farther into the universe. If it's infinite, then there is no limit."* Dorrit Hoffleit 1907-2007.

## 8.1 Summary

This research has involved the study of the interactive winds of massive stars and their interaction with their local environment. This has included the study of individual, high velocity, runaway stars with strong winds that interact with the ISM that they are passing through and massive stars in binary systems whose powerful winds interact with each other.

## 8.2 Massive Runaway Stars - Bow Shocks

In Chapter 6 a multi-wavelength analysis has been undertaken of the bow shock formed by the massive runaway BD+43° 3654. This has revealed for the first time a multi-wavelength picture of the structure of this bow shock.

At IR it was discovered that the dust emitting at this wavelength is stratified, with cool interstellar dust building up at the head of the shock, but some, possibly larger dust particles being able to pass through the forward shock and contact discontinuity into the region of the shock dominated by the hot stellar wind of the runaway. Here the dust is emitting at a higher temperature, suggesting that it is probably being destroyed within this more energetic environment.

At H$\alpha$ wavelengths the structure of the bow shock emission is very turbulent suggesting instabilities within this environment for the gas and plasma. The emission suggests a turbulent region and this is confirmed by the structure of the emission detected at radio frequencies. At radio frequencies the bow shock structure is seen across a range of frequencies with some structure replicated and with the central hot spot being a prominent ‘S’ shaped feature.

An estimate of the swept up material in the BS, $M_{ion}$=0.51 $M_{\odot}$ and the dust mass, $M_{dust}$, for the 90 K component of 0.0105 $M_{\odot}$ and for the 30 K component 0.263 $M_{\odot}$, suggests a dust to gas ratio in the BS of ∼0.07, considerably greater than the Galactic typical value of 0.01.

A study of the velocity vector of BD+43° 3654 suggests agreement with current published values and a fit of a model interaction zone to the emission suggests a velocity direction angle, $\theta = 65.5^{\circ}$ east of Galactic north.

Chapter 7 includes work completed with colleagues on a survey of bow shocks. The results of this survey were that 28 new bow shock candidates were found in the archive data bases, increasing the number of runaway bow shocks for further study.

## 8.3 Massive Binary Systems - Colliding Wind Regions at 5 GHz

In Chapter 3 are details of observations made with the recently upgraded e-MERLIN array. These observations, at 5 GHz, have resolved two radio sources, the southern Wolf-Rayet star and the northern wind interaction zone. The observation did not, however, reveal the binary companion star.

Radio fluxes measured from the data have been used to derive mass-loss rates for the WR-star, with an upper flux limit estimated for the undetected companion O-star. From this upper flux limit a range of O-star upper limit mass-loss rates were derived for a range of $v_{\infty}$ values. Due to the high resolution of the e-MERLIN data, measurements between the two resolved sources were possible. Measurements of the distances from the WR-star and the deduced position of the O-star to the WCR revealed a value of $\eta$=0.003. This allowed the study of the momentum flux of the system and suggest a range of values to limit the mass-loss rate and terminal velocity of the O-star.

Analysis of the emission has revealed some tentative structure within the wind of the WR-star with some possible elongation, though this may be a function of data reduction. The collision zone displays a typical curved shape which approximately fits with theoretical models of these interaction zones, but without the detection of the companion O-star and without any knowledge of inclination or ellipticity, the accurate positioning of the interaction zone is problematic.

The data does reveal some emission between the radio sources, the previously detected ‘bridge’ feature. This is a curious anomaly, as the winds of the two stars are unaware of each other until they collide, therefore, emission in this region is impossible from any wind interaction. In this chapter a solution is proposed to explain this emission, that of the ionising radiation from the O-star, which is suggested may be capable of ionising helium in the WR stellar wind (and or clumps in the wind) creating the observed ‘bridge’ feature.

## 8.4 Massive Binary Systems - Colliding Wind Regions at Low-Frequency

In Chapter 4 and 5 are details of a low-frequency study of massive stars. This study was undertaken to search for details of the non-thermal emission at previously unobserved low-frequencies to understand the absorption processes and turn-over in the NT emission.

In Chapter 4 the observations detected the colliding wind binary WR 147 at 610 MHz but not at 235 MHz. An upper limit at 235 MHz was derived and from these fluxes the NT emission was modelled, these fluxes were added to previous radio detections at higher frequencies and simple absorption models were fitted to the data. From this modelling it was deduced that more than one absorbing region was affecting the emission and that a two-component absorption model can best describe the region.

In Chapter 5 the observation of the much brighter colliding wind binary WR 146, also studied at low-frequency, is detailed. This system was detected at both 610 and 235 MHz, enabling a more accurate low-frequency flux to be used for the modelling. WR 146 does display a similar NT spectral energy distribution to WR 147, with a two-component absorption model best able to fit the data.

These observations, then, have revealed a complex region where the turn-over occurs at approximately 1-5 GHz. The NT emission has been fitted to models to represent two or more emitting regions from the wind collision zone, illustrating the different absorbing regions observed along our line of sight.

## 8.5 Conclusion and Future Work

The obvious conclusion from this work is that the interactive regions of massive stellar winds are very complex. In order to increase our understanding of them, observation in greater detail and number are required. The greater detail to understand the structure and the processes occurring in these complex regions. The greater number of observations is required to increase the number of objects being studied to compare and analyse similarities and differences between different shock regions, to better enable us to model these interaction zones. The greater resolution of future telescopes, such as SKA and further upgrades of the e-MERLIN array, etc., will increase observable resolution and sensitivity, enabling more interactions zones to be observed and subsequently allow such comparisons to be made.

# References

Abbott, D. C., Bieging, J. H., & Churchwell, E. 1981, ApJ, 250, 645

—. 1984, ApJ, 280, 671

Abbott, D. C., Bieging, J. H., Churchwell, E., & Cassinelli, J. P. 1980, ApJ, 238, 196

Aldoretta, E. J., Caballero-Nieves, S. M., Gies, D. R., Nelan, E. P., Wallace, D. J., Hartkopf, W. I., Henry, T. J., Jao, W.-C., Maíz Apellániz, J., Mason, B. D., Moffat, A. F. J., Norris, R. P., Richardson, N. D., & Williams, S. J. 2015, AJ, 149, 26

Allen, C. W. 1973, Astrophysical Quantities (3rd ed., London: Athlone Press)

Allen, R. J. 1968, ApJ, 153, 389

Anderson, L. D., Zavagno, A., Barlow, M. J., García-Lario, P., & Noriega-Crespo, A. 2012a, A&A, 537, A1

Anderson, L. D., Zavagno, A., Deharveng, L., Abergel, A., Motte, F., André, P., Bernard, J.-P., Bontemps, S., Hennemann, M., Hill, T., Rodón, J. A., Roussel, H., & Russeil, D. 2012b, A&A, 542, A10

Avison, A. & George, S. J. 2013, European Journal of Physics, 34, 7

Baranov, V. B., Krasnobaev, K. V., & Kulikovskii, A. G. 1971, Soviet Physics Doklady, 15, 791

Beals, C. S. 1929, MNRAS, 90, 202

Bell, A. R. 1978, MNRAS, 182, 147

Benaglia, P. 2010, in Astronomical Society of the Pacific Conference Series, Vol. 422, High Energy Phenomena in Massive Stars, ed. J. Martí, P. L. Luque-Escamilla, & J. A. Combi, 111

Benaglia, P., Koribalski, B., & Albacete Colombo, J. F. 2006, PASA, 23, 50

Benaglia, P., Marcote, B., Moldón, J., Nelan, E., De Becker, M., Dougherty, S. M., & Koribalski, B. S. 2015, A&A, 579, A99

Benaglia, P., Romero, G. E., Martí, J., Peri, C. S., & Araudo, A. T. 2010, A&A, 517, L10

Bieging, J. H., Abbott, D. C., & Churchwell, E. B. 1989, ApJ, 340, 518

Blaauw, A. 1961, BAIN, 15, 265

Black, D. C. & Bodenheimer, P. 1975, ApJ, 199, 619

Blandford, R. D. & Ostriker, J. P. 1978, ApJL, 221, L29

Blomme, R. & Volpi, D. 2014, A&A, 561, A18

Blondin, J. M. & Koerwer, J. F. 1998, NewA, 3, 571

Bonnell, I. A. & Bate, M. R. 2002, MNRAS, 336, 659

Brandner, W., Grebel, E. K., Chu, Y.-H., Dottori, H., Brandl, B., Richling, S., Yorke, H. W., Points, S. D., & Zinnecker, H. 2000, AJ, 119, 292

Brown, D. & Bomans, D. J. 2005, A&A, 439, 183

Caballero-Nieves, S. M., Nelan, E. P., Gies, D. R., Wallace, D. J., DeGioia-Eastwood, K., Herrero, A., Jao, W.-C., Mason, B. D., Massey, P., Moffat, A. F. J., & Walborn, N. R. 2014, AJ, 147, 40

Caillault, J.-P., Chanan, G. A., Helfand, D. J., Patterson, J., Nousek, J. A., Takalo, L. O., Bothun, G. D., & Becker, R. H. 1985, Nature, 313, 376

Cannon, A. J. & Pickering, E. 1925, The Henry Draper (HD) Catalogue. Vol.100: HD extension, ed. Cannon, A. J. & Pickering, E. (Cambridge, Mass.: Astronomical Observatory of Harvard College)

Cantiello, M. & Braithwaite, J. 2011, A&A, 534, A140

Canto, J., Raga, A. C., & Wilkin, F. P. 1996, ApJ, 469, 729

Cao, Y., Terebey, S., Prince, T. A., & Beichman, C. A. 1997, ApJS, 111, 387

Castor, J., McCray, R., & Weaver, R. 1975a, ApJL, 200, L107

Castor, J. I., Abbott, D. C., & Klein, R. I. 1975b, ApJ, 195, 157

Charbonneau, P. & MacGregor, K. B. 2001, ApJ, 559, 1094

Christiansen, W. N. & Högbom, J. A. 1987, Radio telescopes (Cambridge: Cambridge University Press), ed. Edgington, E. S.

Churchwell, E., Bieging, J. H., van der Hucht, K. A., Williams, P. M., Spoelstra, T. A. T., & Abbott, D. C. 1992, ApJ, 393, 329

Comerón, F. & Pasquali, A. 2007, A&A, 467, L23

Contreras, M. E. & Rodríguez, L. F. 1999, ApJ, 515, 762

Contreras, M. E., Rodriguez, L. F., Gomez, Y., & Velazquez, A. 1996, ApJ, 469, 329

Corcoran, M. F., Pollock, A. M. T., Hamaguchi, K., & Russell, C. 2011, in Proc. Stellar Winds in Interaction, ed. T. Eversberg and J. H. Knap, ArXiv:1101.1422

Corcoran, M. F., Stevens, I. R., Pollock, A. M. T., Swank, J. H., Shore, S. N., & Rawley, G. L. 1996, ApJ, 464, 434

Coupeaud, A., Demyk, K., Meny, C., Nayral, C., Delpech, F., Leroux, H., Depecker, C., Creff, G., Brubach, J.-B., & Roy, P. 2011, A&A, 535, A124

Cox, N. L. J., Kerschbaum, F., van Marle, A.-J., Decin, L., Ladjal, D., Mayer, A., Groenewegen, M. A. T., van Eck, S., Royer, P., Ottensamer, R., Ueta, T., Jorissen, A., Mecina, M., Meliani, Z., Luntzer, A., Blommaert, J. A. D. L., Posch, T., Vandenbussche, B., & Waelkens, C. 2012a, A&A, 537, 35

Cox, N. L. J., Kerschbaum, F., van Marle, A. J., Decin, L., Ladjal, D., Mayer, A., Groenewegen, M. A. T., van Eck, S., Royer, P., Ottensamer, R., Ueta, T., Jorissen, A., Mecina, M., Meliani, Z., Luntzer, A., Blommaert, J. A. D. L., Posch, T., Vandenbussche, B., & Waelkens, C. 2012b, A&A, 543, 1

Crowther, P. 2012, Astronomy and Geophysics, 53, 30

Crowther, P. A. 2007, ARA&A, 45, 177

Crowther, P. A. 2008, in IAU Symposium, Vol. 250, IAU Symposium, ed. F. Bresolin, P. A. Crowther, & J. Puls, 47–62

Crowther, P. A. & Hadfield, L. J. 2006, A&A, 449, 711

Crowther, P. A., Hillier, D. J., Evans, C. J., Fullerton, A. W., De Marco, O., & Willis, A. J. 2002, ApJ, 579, 774

Crowther, P. A., Schnurr, O., Hirschi, R., Yusof, N., Parker, R. J., Goodwin, S. P., & Kassim, H. A. 2010, MNRAS, 408, 731

Crowther, P. A., Smith, L. J., Hillier, D. J., & Schmutz, W. 1995, A&A, 293, 427

De Becker, M. 2007, A&AR, 14, 171

De Becker, M. & Raucq, F. 2013, A&A, 558, A28

De Becker, M., Rauw, G., & Manfroid, J. 2004, A&A, 424, L39

De Becker, M., Rauw, G., Pittard, J. M., Sana, H., Stevens, I. R., & Romero, G. E. 2007, A&A, 472, 905

de Mink, S. E., Langer, N., Izzard, R. G., Sana, H., & de Koter, A. 2013, ApJ, 764, 166

Decin, L., Cox, N. L. J., Royer, P., Van Marle, A. J., Vandenbussche, B., Ladjal, D., Kerschbaum, F., Ottensamer, R., Barlow, M. J., Blommaert, J. A. D. L., Gomez, H. L., Groenewegen, M. A. T., Lim, T., Swinyard, B. M., Waelkens, C., & Tielens, A. G. G. M. 2012, A&A, 548, A113

del Valle, M. V. & Romero, G. E. 2012, A&A, 543, A56

Dessart, L., Crowther, P. A., Hillier, D. J., Willis, A. J., Morris, P. W., & van der Hucht, K. A. 2000, MNRAS, 315, 407

Dgani, R., van Buren, D., & Noriega-Crespo, A. 1996, ApJ, 461, 372

Dougherty, S. M., Beasley, A. J., Claussen, M. J., Zauderer, B. A., & Bolingbroke, N. J. 2005, ApJ, 623, 447

Dougherty, S. M., Clark, J. S., Negueruela, I., Johnson, T., & Chapman, J. M. 2010, A&A, 511, A58

Dougherty, S. M., Pittard, J. M., Kasian, L., Coker, R. F., Williams, P. M., & Lloyd, H. M. 2003, A&A, 409, 217

Dougherty, S. M., Trenton, V., & Beasley, A. J. 2011, Bulletin de la Societe Royale des Sciences de Liege, 80, 658

Dougherty, S. M. & Williams, P. M. 1999, in IAU Symposium, Vol. 193, Wolf-Rayet Phenomena in Massive Stars and Starburst Galaxies, ed. K. A. van der Hucht, G. Koenigsberger, & P. R. J. Eenens, 346

Dougherty, S. M. & Williams, P. M. 2000, MNRAS, 319, 1005

Dougherty, S. M., Williams, P. M., & Pollacco, D. L. 2000, MNRAS, 316, 143

Dougherty, S. M., Williams, P. M., van der Hucht, K. A., Bode, M. F., & Davis, R. J. 1996, MNRAS, 280, 963

Draine, B. T. & Lee, H. M. 1984, ApJ, 285, 89

Draine, B. T. & Li, A. 2007, ApJ, 657, 810

Draine, B. T. & McKee, C. F. 1993, ARA&A, 31, 373

Drake, J. J., Wright, N., & Guarcello, M. 2015, IAU General Assembly, 22, 58134

Drew, J. E., Greimel, R., Irwin, M. J., Aungwerojwit, A., Barlow, M. J., Corradi, R. L. M., Drake, J. J., Gänsicke, B. T., Groot, P., Hales, A., Hopewell, E. C., Irwin, J., Knigge, C., Leisy, P., Lennon, D. J., Mampaso, A., Masheder, M. R. W., Matsuura, M., Morales-Rueda, L., Morris, R. A. H., Parker, Q. A., Phillipps, S., Rodriguez-Gil, P., Roelofs, G., Skillen, I., Sokoloski, J. L., Steeghs, D., Unruh, Y. C., Viironen, K., Vink, J. S., Walton, N. A., Witham, A., Wright, N., Zijlstra, A. A., & Zurita, A. 2005, MNRAS, 362, 753

Dyson, J. E. 1975, Ap&SS, 35, 299

Dzib, S. & Rodríguez, L. F. 2009, RMxAA, 45, 3

Eenens, P. R. J. & Williams, P. M. 1994, MNRAS, 269, 1082

Egan, M. P., Price, S. D., & Kraemer, K. E. 2003a, in Bulletin of the American Astronomical Society, Vol. 35, American Astronomical Society Meeting Abstracts, 1301

Egan, M. P., Price, S. D., & Kraemer, K. E. 2003b, in Bulletin of the American Astronomical Society, Vol. 35, American Astronomical Society Meeting Abstracts, 1301

Egan, M. P., Shipman, R. F., Price, S. D., Carey, S. J., Clark, F. O., & Cohen, M. 1998, ApJL, 494, L199

Eichler, D. & Usov, V. 1993, ApJ, 402, 271

Ekström, S., Georgy, C., Eggenberger, P., Meynet, G., Mowlavi, N., Wyttenbach, A., Granada, A., Decressin, T., Hirschi, R., Frischknecht, U., Charbonnel, C., & Maeder, A. 2012, A&A, 537, A146

Evans, A. 1993, The Dusty Universe (New York: Ellis Horwood)

Evans, C. J., Walborn, N. R., Crowther, P. A., Hénault-Brunet, V., Massa, D., Taylor, W. D., Howarth, I. D., Sana, H., Lennon, D. J., & van Loon, J. T. 2010, ApJL, 715, L74

Everett, J. E. & Churchwell, E. 2010, ApJ, 713, 592

Eversberg, T., Lépine, S., & Moffat, A. F. J. 1998, ApJ, 494, 799

Farnier, C., Walter, R., & Leyder, J.-C. 2011, A&A, 526, A57

Feast, M. & Whitelock, P. 1997, MNRAS, 291, 683

Felli, M. & Massi, M. 1991, in IAU Symposium, Vol. 143, Wolf-Rayet Stars and Interrelations with Other Massive Stars in Galaxies, ed. K. A. van der Hucht & B. Hidayat, 87

Ferland, G. J., Porter, R. L., van Hoof, P. A. M., Williams, R. J. R., Abel, N. P., Lykins, M. L., Shaw, G., Henney, W. J., & Stancil, P. C. 2013, RMxAA, 49, 137

Fermi, E. 1949, Physical Review, 75, 1169

Frank, J., King, A., & Raine, D. J. 2002, Accretion Power in Astrophysics: (Third Edition, Cambridge: Cambridge University Press)

Fullerton, A. W., Massa, D. L., & Prinja, R. K. 2006, ApJ, 637, 1025

Gaustad, J. E., McCullough, P. R., Rosing, W., & Van Buren, D. 2001, PASP, 113, 1326

Georgy, C., Ekström, S., Hirschi, R., Meynet, G., Groh, J. H., & Eggenberger, P. 2015, in Wolf-Rayet Stars: Proceedings of an International Workshop held in Potsdam, Germany, 1-5 June 2015. Edited by Wolf-Rainer Hamann, Andreas Sander, Helge Todt. Universitätsverlag Potsdam, 2015., p.229-232, ed. W.-R. Hamann, A. Sander, & H. Todt, 229–232

Gerola, H. & Seiden, P. E. 1978, ApJ, 223, 129

Gies, D. R. & Bolton, C. T. 1986, ApJS, 61, 419

Giommi, P., Colafrancesco, S., Cavazzuti, E., Perri, M., & Pittori, C. 2006, A&A, 445, 843

Gordon, K. D., Clayton, G. C., Misselt, K. A., Landolt, A. U., & Wolff, M. J. 2003, ApJ, 594, 279

Gurnett, D. A., Kurth, W. S., Burlaga, L. F., & Ness, N. F. 2013, Science, 341, 1489

Gvaramadze, V. V. & Bomans, D. J. 2008, A&A, 485, L29

Gvaramadze, V. V. & Gualandris, A. 2011, MNRAS, 410, 304

Hamann, W.-R., Gräfener, G., & Liermann, A. 2006, A&A, 457, 1015

Hamann, W.-R. & Koesterke, L. 1998, A&A, 333, 251

Hanson, M. M. 2003, ApJ, 597, 957

Henyey, L. G. & Greenstein, J. L. 1941, ApJ, 93, 70

Herbig, G. H. & Mendoza, E. E. 1960, Boletin de los Observatorios Tonantzintla y Tacubaya, 2, 21

Herman, J., Burger, J. H., & Penninx, W. H. 1986, A&A, 167, 247

Hervé, A., Rauw, G., & Nazé, Y. 2013, A&A, 551, A83

Hildebrand, R. H. 1983, QJRAS, 24, 267

Hillier, D. J. & Miller, D. L. 1998, ApJ, 496, 407

Hirv, A., Annuk, K., Eenmäe, T., Liimets, T., Pelt, J., Puss, A., & Tempel, M. 2006, Baltic Astronomy, 15, 405

Høg, E., Fabricius, C., Makarov, V. V., Urban, S., Corbin, T., Wycoff, G., Bastian, U., Schwekendiek, P., & Wicenec, A. 2000, A&A, 355, L27

Högbom, J. A. 1974, A&AS, 15, 417

Horch, E. P., van Altena, W. F., Howell, S. B., Sherry, W. H., & Ciardi, D. R. 2011, AJ, 141, 180

Howarth, I. D. & Prinja, R. K. 1989, ApJS, 69, 527

Jansky, K. G. 1933, Popular Astronomy, 41, 548

Johnston, K. G., Robitaille, T. P., Beuther, H., Linz, H., Boley, P., Kuiper, R., Keto, E., Hoare, M. G., & van Boekel, R. 2015, ApJL, 813, L19

Johnstone, C. P., Zhilkin, A., Pilat-Lohinger, E., Bisikalo, D., Güdel, M., & Eggl, S. 2015, A&A, 577, A122

Jones, A. P. 2005, in ESA Special Publication, Vol. 577, ESA Special Publication, ed. A. Wilson, 239–244

Joye, W. A. & Mandel, E. 2003, in Astronomical Society of the Pacific Conference Series, Vol. 295, Astronomical Data Analysis Software and Systems XII, ed. H. E. Payne, R. I. Jedrzejewski, & R. N. Hook, 489

Kauffmann, J. & Pillai, T. 2010, ApJL, 723, L7

Kennedy, M., Dougherty, S. M., Fink, A., & Williams, P. M. 2010, ApJ, 709, 632

Kennicutt, R. C. 2005, in IAU Symposium, Vol. 227, Massive Star Birth: A Crossroads of Astrophysics, ed. R. Cesaroni, M. Felli, E. Churchwell, & M. Walmsley, 3–11

Kerton, C. R. & Martin, P. G. 2000, ApJS, 126, 85

Klein, R. I., Fisher, R., & McKee, C. F. 2004, in Revista Mexicana de Astronomia y Astrofisica Conference Series, Vol. 22, Revista Mexicana de Astronomia y Astrofisica Conference Series, ed. G. Garcia-Segura, G. Tenorio-Tagle, J. Franco, & H. W. Yorke, 3–7

Kobulnicky, H. A., Gilbert, I. J., & Kiminki, D. C. 2010, ApJ, 710, 549

Kobulnicky, H. A., Kiminki, D. C., Lundquist, M. J., Burke, J., Chapman, J., Keller, E., Lester, K., Rolen, E. K., Topel, E., Bhattacharjee, A., Smullen, R. A., Vargas Alvarez, C. A., Runnoe, J. C., Dale, D. A., & Brotherton, M. M. 2014, VizieR Online Data Catalog, 221, 30034

Kraus, S., Hofmann, K.-H., Menten, K. M., Schertl, D., Weigelt, G., Wyrowski, F., Meilland, A., Perraut, K., Petrov, R., Robbe-Dubois, S., Schilke, P., & Testi, L. 2010, Nature, 466, 339

Kroupa, P. 2008, in Astronomical Society of the Pacific Conference Series, Vol. 388, Mass Loss from Stars and the Evolution of Stellar Clusters, ed. A. de Koter, L. J. Smith, & L. B. F. M. Waters, 271

Lamers, H. J. G. L. M. & Cassinelli, J. P. 1999, Introduction to Stellar Winds, (Cambridge: Cambridge University Press)

Lamers, H. J. G. L. M. & Leitherer, C. 1993, ApJ, 412, 771

Lépine, S. & Moffat, A. F. J. 2008, AJ, 136, 548

Lépine, S., Wallace, D., Shara, M. M., Moffat, A. F. J., & Niemela, V. S. 2001, AJ, 122, 3407

Leutenegger, M. A., Kahn, S. M., & Ramsay, G. 2003, ApJ, 585, 1015

Li, A. 2005, in American Institute of Physics Conference Series, Vol. 761, The Spectral Energy Distributions of Gas-Rich Galaxies: Confronting Models with Data, ed. C. C. Popescu & R. J. Tuffs, 123–133

Li, A. & Draine, B. T. 2001, ApJ, 554, 778

Luo, D., McCray, R., & Mac Low, M.-M. 1990, ApJ, 362, 267

Mackey, J., Gvaramadze, V. V., Mohamed, S., & Langer, N. 2015, A&A, 573, A10

Maeder, A. & Meynet, G. 1987, A&A, 182, 243

—. 1989, A&A, 210, 155

—. 2010, NAR, 54, 32

Maíz Apellániz, J., Pellerin, A., Barbá, R. H., Simón-Díaz, S., Alfaro, E. J., Morrell, N. I., Sota, A., Penadés Ordaz, M., & Gallego Calvente, A. T. 2012, in Astronomical Society of the Pacific Conference Series, Vol. 465, Proceedings of a Scientific Meeting in Honor of Anthony F. J. Moffat, ed. L. Drissen, C. Robert, N. St-Louis, & A. F. J. Moffat, 484

Martí, J., Paredes, J. M., Ishwara Chandra, C. H., & Bosch-Ramon, V. 2007, A&A, 472, 557

Martins, F., Mahy, L., Hillier, D. J., & Rauw, G. 2012, A&A, 538, A39

Mason, B. D., Hartkopf, W. I., Gies, D. R., Henry, T. J., & Helsel, J. W. 2009, AJ, 137, 3358

Massey, P. 2003, ARA&A, 41, 15

Matzner, C. D. 2002, ApJ, 566, 302

Matzner, R. A. 2001, Dictionary of Geophysics, Astrophysics, and Astronomy, ed. Matzner, R. A., (Boca Raton: CRC Press)

McKee, C. F. & Hollenbach, D. J. 1980, ARA&A, 18, 219

McKee, C. F. & Tan, J. C. 2003, ApJ, 585, 850

McKee, C. F., van Buren, D., & Lazareff, B. 1984, ApJL, 278, L115

Melrose, D. B. 1972, Ap&SS, 18, 267

Meynet, G. & Maeder, A. 2000, A&A, 361, 101

Miville-Deschênes, M.-A. & Lagache, G. 2005, ApJS, 157, 302

Mohamed, S., Mackey, J., & Langer, N. 2012, A&A, 541, A1

Monnier, J. D., Greenhill, L. J., Tuthill, P. G., & Danchi, W. C. 2002, in Astronomical Society of the Pacific Conference Series, Vol. 260, Interacting Winds from Massive Stars, ed. A. F. J. Moffat & N. St-Louis, 331

Moran, J. P., Davis, R. J., Spencer, R. E., Bode, M. F., & Taylor, A. R. 1989, Nature, 340, 449

Moravveji, E. 2016, MNRAS, 455, L67

Morris, P. W., van der Hucht, K. A., Crowther, P. A., Hillier, D. J., Dessart, L., Williams, P. M., & Willis, A. J. 2000, A&A, 353, 624

Morton, D. C. 1967, ApJ, 150, 535

Najarro, F. 2001, in Astronomical Society of the Pacific Conference Series, Vol. 233, P Cygni 2000: 400 Years of Progress, ed. M. de Groot & C. Sterken, 133

Nazé, Y. 2009, A&A, 506, 1055

Neugebauer, G., Habing, H. J., van Duinen, R., Aumann, H. H., Baud, B., Beichman, C. A., Beintema, D. A., Boggess, N., Clegg, P. E., de Jong, T., Emerson, J. P., Gautier, T. N., Gillett, F. C., Harris, S., Hauser, M. G., Houck, J. R., Jennings, R. E., Low, F. J., Marsden, P. L., Miley, G., Olnong, F. M., Pottasch, S. R., Raimond, E., Rowan-Robinson, M., Soifer, B. T., Walker, R. G., Wesselius, P. R., & Young, E. 1984, ApJL, 278, L1

Niemela, V. S., Shara, M. M., Wallace, D. J., Zurek, D. R., & Moffat, A. F. J. 1998, AJ, 115, 2047

Ninkovic, S., Orlov, V. V., & Petrova, A. V. 2002, Astronomy Letters, 28, 163

Noriega-Crespo, A., van Buren, D., & Dgani, R. 1997, AJ, 113, 780

O'Connor, E. P., Dougherty, S. M., Pittard, J. M., & Williams, P. M. 2005, in Massive Stars and High-Energy Emission in OB Associations, ed. G. Rauw, Y. Nazé, R. Blomme, & E. Gosset, 81–84

Owocki, S. 2014, Theory of Winds from Hot, Luminous Massive Stars, in Proc of the 39th Liège Astrophysical Colloquium, eds. G. Rauw, M. De Becker, Y. Nazé, J.-M. Vreux, P. Williams, ArXiv:1409.2084

Owocki, S. P. 1994, Ap&SS, 221, 3

Pandey, J. C., Pandey, S. B., & Karmakar, S. 2014, ApJ, 788, 84

Parkin, E. R. & Gosset, E. 2011, A&A, 530, A119

Pauldrach, A., Puls, J., & Kudritzki, R. P. 1986, A&A, 164, 86

Pauldrach, A. W. A., Vanbeveren, D., & Hoffmann, T. L. 2012, A&A, 538, A75

Peri, C. S., Benaglia, P., Brookes, D. P., Stevens, I. R., & Isequilla, N. L. 2012, A&A, 538, A108

Peri, C. S., Benaglia, P., & Isequilla, N. L. 2015, VizieR Online Data Catalog, 357

Pfalzner, S. 2009, A&A, 498, L37

Phillips, A. C. 1999, The Physics of Stars, (2nd Edition, Chichester: Wiley)

Pittard, J. M., Dougherty, S. M., Coker, R. F., O'Connor, E., & Bolingbroke, N. J. 2006, A&A, 446, 1001

Pittard, J. M., Stevens, I. R., Williams, P. M., Pollock, A. M. T., Skinner, S. L., Corcoran, M. F., & Moffat, A. F. J. 2002, A&A, 388, 335

Poglitsch, A., Waelkens, C., Geis, N., Feuchtgruber, H., Vandenbussche, B., Rodriguez, L., Krause, O., Renotte, E., van Hoof, C., Saraceno, P., Cepa, J., Kerschbaum, F., Agnèse, P., Ali, B., Altieri, B., Andreani, P., Augueres, J.-L., Balog, Z., Barl, L., Bauer, O. H., Belbachir, N., Benedettini, M., Billot, N., Boulade, O., Bischof, H., Blommaert, J., Callut, E., Cara, C., Cerulli, R., Cesarsky, D., Contursi, A., Creten, Y., De Meester, W., Doublier, V., Doumayrou, E., Duband, L., Exter, K., Genzel, R., Gillis, J.-M., Grözinger, U., Henning, T., Herreros, J., Huygen, R., Inguscio, M., Jakob, G., Jamar, C., Jean, C., de Jong, J., Katterloher, R., Kiss, C., Klaas, U., Lemke, D., Lutz, D., Madden, S., Marquet, B., Martignac, J., Mazy, A., Merken, P., Montfort, F., Morbidelli, L., Müller, T., Nielbock, M., Okumura, K., Orfei, R., Ottensamer, R., Pezzuto, S., Popesso, P., Putzeys, J., Regibo, S., Reveret, V., Royer, P., Sauvage, M., Schreiber, J., Stegmaier, J., Schmitt, D., Schubert, J., Sturm, E., Thiel, M., Tofani, G., Vavrek, R., Wetzstein, M., Wieprecht, E., & Wiezorrek, E. 2010, A&A, 518, L2

Portegies Zwart, S. & van den Heuvel, E. P. J. 2015, ArXiv:1511.06889

Poveda, A., Ruiz, J., & Allen, C. 1967, Boletin de los Observatorios Tonantzintla y Tacubaya, 4, 86

Povich, M. S., Benjamin, R. A., Whitney, B. A., Babler, B. L., Indebetouw, R., Meade, M. R., & Churchwell, E. 2008, ApJ, 689, 242

Prinja, R. K., Barlow, M. J., & Howarth, I. D. 1990, ApJ, 361, 607

Raassen, A. J. J., van der Hucht, K. A., Mewe, R., Antokhin, I. I., Rauw, G., Vreux, J.-M., Schmutz, W., & Güdel, M. 2003, A&A, 402, 653

Rauw, G., Blomme, R., Waldron, W. L., Corcoran, M. F., Pittard, J. M., Pollock, A. M. T., Runacres, M. C., Sana, H., Stevens, I. R., & Van Loo, S. 2002, A&A, 394, 993

Rauw, G., Crowther, P. A., De Becker, M., Gosset, E., Nazé, Y., Sana, H., van der Hucht, K. A., Vreux, J.-M., & Williams, P. M. 2005, A&A, 432, 985

Rauw, G., Nazé, Y., Wright, N. J., Drake, J. J., Guarcello, M. G., Prinja, R. K., Peck, L. W., Albacete Colombo, J. F., Herrero, A., Kobulnicky, H. A., Sciortino, S., & Vink, J. S. 2015, ApJS, 221, 1

Reber, G. 1944, ApJ, 100, 279

Reitberger, K., Kissmann, R., Reimer, A., & Reimer, O. 2014, ApJ, 789, 87

Roeser, S., Demleitner, M., & Schilbach, E. 2010, AJ, 139, 2440

Runacres, M. C. & Owocki, S. P. 2002, A&A, 381, 1015

Sana, H., de Mink, S. E., de Koter, A., Langer, N., Evans, C. J., Gieles, M., Gosset, E., Izzard, R. G., Le Bouquin, J.-B., & Schneider, F. R. N. 2012, Science, 337, 444

Sana, H., Le Bouquin, J.-B., Lacour, S., Berger, J.-P., Duvert, G., Gauchet, L., Norris, B., Olofsson, J., Pickel, D., Zins, G., Absil, O., de Koter, A., Kratter, K., Schnurr, O., & Zinnecker, H. 2014, ApJS, 215, 15

Sana, H., Momany, Y., Gieles, M., Carraro, G., Beletsky, Y., Ivanov, V. D., de Silva, G., & James, G. 2010, A&A, 515, A26

Sawicki, M. 2012, PASP, 124, 1208

Schaller, G., Schaerer, D., Meynet, G., & Maeder, A. 1992, A&AS, 96, 269

Scuderi, S., Panagia, N., Stanghellini, C., Trigilio, C., & Umana, G. 1998, A&A, 332, 251

Seaquist, E. R. & Gregory, P. C. 1973, Nature Physical Science, 245, 85

Setia Gunawan, D. Y. A., de Bruyn, A. G., van der Hucht, K. A., & Williams, P. M. 2000, A&A, 356, 676

—. 2001, A&A, 368, 484

—. 2003, ApJS, 149, 123

Shakeshaft, J. R., Ryle, M., Baldwin, J. E., Elsmore, B., & Thomson, J. H. 1955, MmRAS, 67, 106

Shu, F. H. 1991, The Physics of Astrophysics. Volume 1: Radiation (Mill Valley, CA (USA): University Science Books)

—. 1992, The Physics of Astrophysics. Volume II: Gas Dynamics (Mill Valley, CA (USA): University Science Books)

Silk, J. 1997, ApJ, 481, 703

Skinner, S. L., Itoh, M., Nagase, F., & Zhekov, S. A. 1999, ApJ, 524, 394

Skinner, S. L., Zhekov, S. A., Güdel, M., & Schmutz, W. 2007, MNRAS, 378, 1491

Smith, L. F., Shara, M. M., & Moffat, A. F. J. 1996, MNRAS, 281, 163

Smith, N. 2014, ARA&A, 52, 487

Spruit, H. C. 2002, A&A, 381, 923

Stevens, I. R. 2005, in Massive Stars and High-Energy Emission in OB Associations, ed. G. Rauw, Y. Nazé, R. Blomme, & E. Gosset, 3–12

Stevens, I. R., Blondin, J. M., & Pollock, A. M. T. 1992, ApJ, 386, 265

Stevens, I. R. & Howarth, I. D. 1999, MNRAS, 302, 549

Stevens, I. R., Skinner, S. L., Nagase, F., Corcoran, M. F., Willis, A. J., Pollock, A. M. T., & Koyama, K. 1995, Ap&SS, 224, 569

Taylor, A. R., Goss, W. M., Coleman, P. H., van Leeuwen, J., & Wallace, B. J. 1996, ApJS, 107, 239

Terada, Y., Tashiro, M. S., Bamba, A., Yamazaki, R., Kouzu, T., Koyama, S., & Seta, H. 2012, PASJ, 64, 138

Tetzlaff, N., Neuhaeuser, R., & Hohle, M. M. 2010, VizieR Online Data Catalog, 741, 190

Tielens, A. G. G. M. 2005, The Physics and Chemistry of the Interstellar Medium (Cambridge: Cambridge University Press)

Torra, J., Fernández, D., & Figueras, F. 2000, A&A, 359, 82

Tuthill, P. G., Monnier, J. D., Lawrance, N., Danchi, W. C., Owocki, S. P., & Gayley, K. G. 2008, ApJ, 675, 698

Usov, V. V. 1992, ApJ, 389, 635

van Buren, D. & McCray, R. 1988, ApJL, 329, L93

van Buren, D., Noriega-Crespo, A., & Dgani, R. 1995, AJ, 110, 2914

van der Hucht, K. A. 2001, NAR, 45, 135

van Marle, A. J., Cox, N. L. J., & Decin, L. 2014, A&A, 570, A131

van Marle, A. J., Meliani, Z., Keppens, R., & Decin, L. 2011, ApJL, 734, L26

Vine, S. G., Bonnell, I. A., & Bate, M. R. 2004, in Astronomical Society of the Pacific Conference Series, Vol. 322, The Formation and Evolution of Massive Young Star Clusters, ed. H. J. G. L. M. Lamers, L. J. Smith, & A. Nota, 359

Vink, J. S. 2015, ArXiv:1510.00227

Vink, J. S., de Koter, A., & Lamers, H. J. G. L. M. 1999, A&A, 350, 181

—. 2000, A&A, 362, 295

—. 2001, A&A, 369, 574

Walder, R., Folini, D., & Meynet, G. 2012, Space Sci. Rev., 166, 145

Wallace, D. J. 2003, PhD thesis, GEORGIA STATE UNIVERSITY

Watson, S. K., Davis, R. J., Williams, P. M., & Bode, M. F. 2002, MNRAS, 334, 631

Weaver, R., McCray, R., Castor, J., Shapiro, P., & Moore, R. 1977, ApJ, 218, 377

Wendker, H. J., Higgs, L. A., & Landecker, T. L. 1996, Astronomische Nachrichten, 317, 35

White, R. L. 1985, ApJ, 289, 698

White, R. L. & Becker, R. H. 1983, ApJL, 272, L19

Wilkin, F. P. 1996, ApJL, 459, L31

Williams, P. 2011, Bulletin de la Societe Royale des Sciences de Liege, 80, 595

Williams, P. M., Dougherty, S. M., Davis, R. J., van der Hucht, K. A., Bode, M. F., & Setia Gunawan, D. Y. A. 1997, MNRAS, 289, 10

Willis, A. J., Dessart, L., Crowther, P. A., Morris, P. W., Maeder, A., Conti, P. S., & van der Hucht, K. A. 1997, MNRAS, 290, 371

Woosley, S. E. & Bloom, J. S. 2006, ARA&A, 44, 507

Wright, A. E. & Barlow, M. J. 1975, MNRAS, 170, 41

Wright, E. L., Eisenhardt, P. R. M., Mainzer, A. K., Ressler, M. E., Cutri, R. M., Jarrett, T., Kirkpatrick, J. D., Padgett, D., McMillan, R. S., Skrutskie, M., Stanford, S. A., Cohen, M., Walker, R. G., Mather, J. C., Leisawitz, D., Gautier, III, T. N., McLean, I., Benford, D., Lonsdale, C. J., Blain, A., Mendez, B., Irace, W. R., Duval, V., Liu, F., Royer, D., Heinrichsen, I., Howard, J., Shannon, M., Kendall, M., Walsh, A. L., Larsen, M., Cardon, J. G., Schick, S., Schwalm, M., Abid, M., Fabinsky, B., Naes, L., & Tsai, C.-W. 2010, AJ, 140, 1868

Wright, N. J., Drew, J. E., & Mohr-Smith, M. 2015, MNRAS, 449, 741

Wright, N. J., Parker, R. J., Goodwin, S. P., & Drake, J. J. 2014, MNRAS, 438, 639

Yoon, S.-C. & Cantiello, M. 2010, ApJL, 717, L62

Zacharias, N., Finch, C. T., Girard, T. M., Henden, A., Bartlett, J. L., Monet, D. G., & Zacharias, M. I. 2013, AJ, 145, 44

Zacharias, N., Monet, D. G., Levine, S. E., Urban, S. E., Gaume, R., & Wycoff, G. L. 2004, in Bulletin of the American Astronomical Society, Vol. 36, American Astronomical Society Meeting Abstracts, 1418

Zeilik, M., Gregory, S. A., & Smith, E. V. P. 1992, Introductory Astronomy and Astrophysics (Fort Worth : Saunders College Pub.)

Zhekov, S. A. & Park, S. 2010a, ApJ, 721, 518

—. 2010b, ApJL, 709, L119

Zhu, Z. 2009, Research in Astronomy and Astrophysics, 9, 1285

Zinnecker, H., McCaughrean, M. J., & Wilking, B. A. 1993, in Protostars and Planets III, ed. E. H. Levy & J. I. Lunine, 429–495

Zinnecker, H. & Yorke, H. W. 2007, ARA&A, 45, 481

Zoonematkermani, S., Helfand, D. J., Becker, R. H., White, R. L., & Perley, R. A. 1990, ApJS, 74, 181